BEILSTEIN JOURNAL OF NANOTECHNOLOGY

Biomimetic materials

Edited by Wilhelm Barthlott and Kerstin Koch

Imprint

Beilstein Journal of Nanotechnology
www.bjnano.org
ISSN 2190-4286
Email: journals-support@beilstein-institut.de

The *Beilstein Journal of Nanotechnology* is published by the Beilstein-Institut zur Förderung der Chemischen Wissenschaften.

Beilstein-Institut zur Förderung der Chemischen Wissenschaften
Trakehner Straße 7–9
60487 Frankfurt am Main
Germany
www.beilstein-institut.de

Beilstein Journal of Nanotechnology

Biomimetic materials

Wilhelm Barthlott[1] and Kerstin Koch[*2]

Editorial

Open Access

Address:
[1]Nees Institute for Biodiversity of Plants, Rheinische Friedrich-Wilhelms University of Bonn, Meckenheimer Allee 170, 53115 Bonn, Germany and [2]Rhine-Waal-University of Applied Sciences, Landwehr 4, 47533 Kleve, Germany

Email:
Kerstin Koch[*] - Kerstin.Koch@hochschule-rhein-waal.de

* Corresponding author

Beilstein J. Nanotechnol. **2011,** *2,* 135–136.
doi:10.3762/bjnano.2.16

Received: 02 March 2011
Accepted: 02 March 2011
Published: 10 March 2011

Guest Editors: W. Barthlott and K. Koch

Life is a specific characteristic of our planet. The diversity of life, biodiversity, is one of the most fascinating phenomena. We know some 1.8 million different species, but all extrapolations show that probably 20 million or more species exist: We know less than 10% of the plants, animals and micro-organisms living on the planet Earth. The editors, who are both biologists, are well acquainted with these figures whilst for non-biologists this fact is most surprising and even unbelievable. The process of life started more than one billion years ago, it is a continuous process of evolution, of mutation and selection, of structures and materials. Put another way, this means one billion years of trial, error and optimization. The diversity of life thus created a breath taking diversity of materials and structures based on an extremely restricted number of elements.

It took a surprisingly long time until we understood what we can learn from one billion years of biological development work. No doubt, Daedalus and Icarus in Greek mythology copied biological models – without, however, great success. This is an unbroken tradition from past epochs to the era of Leonardo da Vinci up to the present day. However, systematic research of biological systems for a technical application began astonishingly quite late: Bionics and biomimetics became important only after 1960, and it was only in the new millennium they became worldwide disciplines with high potentials for innovation. An apparently simple observation can lead to new materials, structures and design principles, but the technical transformation and realization may take a much longer time. Our own example of the self cleansing abilities of lotus leaves clearly demonstrates this point: Published for the first time in 1976, patented as a technical feasibility in 1994, facade paints only appeared on the market in 1999.

Bionics concentrated in the first decades, in particular, on highly complex biomechanic problems: the hovering of humming birds and robot locomotion. Today a focal point is the incredibly specific diversity of biological materials, materials with micro and nano structures, often self-assembling. Another change of paradigm was caused by lotus leaves: surfaces and boundary layers. All interactions between an organism and its environment take place via its surface – be it the interaction between a solid (biological species), a liquid (e.g., water), a gas (e.g., air) and radiation (e.g., sunlight). Boundary layers and, in particular, superhydrophobic surfaces and their interactions with the environment were thus the focus of this Thematic Series on *Biomimetic materials*.

The most interesting phenomena happen on boundary layers: from the biosphere at the boundary layer of our planet down to the surfaces of lotus leaves or Salvinia water ferns. And these

are only two out of the 20 million species which all have secrets to be revealed: Biomimetic materials provide innovative solutions for the design of a new generation of bio inspired functional materials.

Wilhelm Barthlott and Kerstin Koch

Bonn, Kleve, March 2011

Beilstein Journal of Nanotechnology

Biomimetics inspired surfaces for drag reduction and oleophobicity/philicity

Bharat Bhushan

Review

Open Access

Address:
Nanoprobe Laboratory for Bio- & Nanotechnology and Biomimetics (NLB²), The Ohio State University, 201 W. 19th Avenue, Columbus, OH 43210-1142, USA

Email:
Bharat Bhushan - Bhushan.2@osu.edu

Keywords:
aquatic animals; biomimetics; drag; lotus plants; shark skin; superhydrophobicity; superoleophobicity

Beilstein J. Nanotechnol. **2011,** *2,* 66–84.
doi:10.3762/bjnano.2.9

Received: 01 October 2010
Accepted: 20 January 2011
Published: 01 February 2011

This article is part of the Thematic Series "Biomimetic materials".

Guest Editors: W. Barthlott and K. Koch

Abstract

The emerging field of biomimetics allows one to mimic biology or nature to develop nanomaterials, nanodevices, and processes which provide desirable properties. Hierarchical structures with dimensions of features ranging from the macroscale to the nanoscale are extremely common in nature and possess properties of interest. There are a large number of objects including bacteria, plants, land and aquatic animals, and seashells with properties of commercial interest. Certain plant leaves, such as lotus (*Nelumbo nucifera*) leaves, are known to be superhydrophobic and self-cleaning due to the hierarchical surface roughness and presence of a wax layer. In addition to a self-cleaning effect, these surfaces with a high contact angle and low contact angle hysteresis also exhibit low adhesion and drag reduction for fluid flow. An aquatic animal, such as a shark, is another model from nature for the reduction of drag in fluid flow. The artificial surfaces inspired from the shark skin and lotus leaf have been created, and in this article the influence of structure on drag reduction efficiency is reviewed. Biomimetic-inspired oleophobic surfaces can be used to prevent contamination of the underwater parts of ships by biological and organic contaminants, including oil. The article also reviews the wetting behavior of oil droplets on various superoleophobic surfaces created in the lab.

Introduction

Biologically inspired design, adaptation, or derivation from nature is referred to as 'biomimetics.' It means mimicking biology or nature. Nature has gone through evolution over the 3.8 billion years since life is estimated to have appeared on the Earth [1]. Nature has evolved objects with high performance using commonly found materials. These function on the macroscale to the nanoscale. The understanding of the functions provided by objects and processes found in nature can guide us to imitate and produce nanomaterials, nanodevices, and processes [2]. There are a large number of objects (bacteria, plants, land and aquatic animals, seashells etc.) with properties of commercial interest.

Natural superhydrophobic, self-cleaning, low adhesion, and drag reduction surfaces

Drag reduction in fluid flow is of interest in various commercial applications. These include transportation vehicles and micro/nanofluidics based biosensor applications [3]. To reduce pressure drop and volume loss in micro/nanochannels used in micro/nanofluidics, it is desirable to minimize the drag force at the solid–liquid interface. A model surface for superhydrophobicity, self-cleaning and low adhesion is the leaves of water-repellent plants such as *Nelumbo nucifera* (lotus) [2,4-11]. The leaf surface is very rough due to so-called papillose epidermal cells, which form papillae or microasperities. In addition to the microscale roughness, the surface of the papillae is also rough, with nanoscale asperities composed of three-dimensional epicuticular waxes which are long chain hydrocarbons and hydrophobic. The waxes on lotus leaves exist as tubules [10,11]. Water droplets on these hierarchical structured surfaces readily sit on the apex of the nanostructures because air bubbles fill the valleys of the structure under the droplet (Figure 1a). Therefore, these leaves exhibit considerable superhydrophobicity. Static contact angle and contact angle hysteresis of a lotus leaf are about 164° and 3°, respectively [12,13]. The water droplets on the leaves remove any contaminant particles from their surfaces when they roll off, leading to self-cleaning [5] and show low adhesive force [14-16].

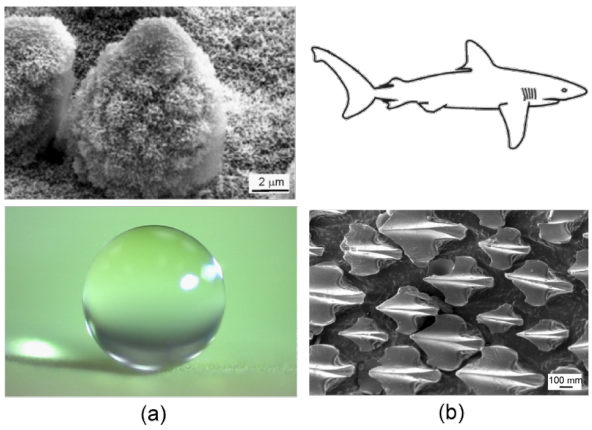

Figure 1: Two examples from nature: (a) Lotus effect [12], and (b) scale structure of shark reducing drag [21].

Natural superoleophobic, self-cleaning, and drag reduction surfaces

A model surface for superoleophobicity and self-cleaning is provided by fish which are known to be well protected from contamination by oil pollution although they are wetted by water [15,17]. Fish scales have a hierarchical structure consisting of sector-like scales with diameters of 4–5 mm covered by papillae 100–300 μm in length and 30–40 μm in width [18]. Shark skin, which is a model from nature for a low drag surface, is covered by very small individual tooth-like scales called dermal denticles (little skin teeth), ribbed with longitudinal grooves (aligned parallel to the local flow direction of the water) (Figure 1b). These grooved scales reduce vortice formation present on a smooth surface, resulting in water moving efficiently over their surface [2,19-22]. The water surrounding these complex structures can lead to protection from marine fouling and play a role in defense against adhesion and growth of marine organisms, e.g., bacteria and algae [11,23]. If oil is present on the surfaces in air or water, surfaces are known to be oleophobic and may exhibit self-cleaning and anti-fouling properties. Many sea animals including fish and shark are known to be oleophobic under water. Superoleophobic surfaces can also reduce significant losses of residual fuel in fuel tanks and pipes [15,24].

Roughness-induced superhydrophobicity, self-cleaning, low adhesion, and drag reduction

Jung and Bhushan [21] created artificial surfaces inspired by the lotus leaf and shark skin and studied the influence of structure on pressure drop and fluid drag. One of the basic properties of interest in fluid flow is slip. The relative velocity between a solid wall and liquid is believed to be zero at the solid–liquid interface, which is the so called no-slip boundary condition (Figure 2, left) [25,26]. However, for hydrophobic surfaces, fluid film exhibits a phenomenon known as slip, which means that the fluid velocity near the solid surface is not equal to the velocity of the solid surface (Figure 2, right) [27-33]. The degree of boundary slip at the solid–liquid interface is characterized by a slip length. The slip length b is defined as the length of the vertical intercept along the axis orthogonal to the interface when a tangent line is drawn along the velocity profile

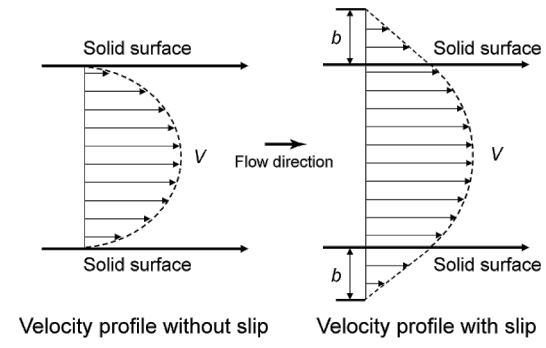

Figure 2: Schematic of velocity profiles of fluid flow without and with boundary slip. The definition of slip length b characterizes the degree of boundary slip at the solid–liquid interface. The arrows represent directions of fluid flow.

at the interface (Figure 2, right). Recent experiments with surface force apparatus (SFA) [34-36], atomic force microscopy (AFM) [32,33,37], and particle image velocimetry (PIV) [38] techniques have reported slip lengths on hydrophobic surfaces: No slip was observed on hydrophilic surfaces [34,36-40]. Theoretical studies [41-44] and experimental studies [33,45-47] suggest that the presence of nanobubbles at the solid-liquid interface is responsible for boundary slip on hydrophobic surfaces.

Roughness-induced superoleophobicity

The surface tension of oil and organic liquids is lower than that of water, so to create a superoleophobic surface, the surface energy of the solid surface in air should be lower than that of oil. For underwater applications, if an oil droplet is placed on a solid surface in water, the solid–water–oil interface exists. The nature of oleophobicity/philicity of an oil droplet in water can be determined from the values of surface energies of various interfaces and contact angles of water and oil in air.

Many superoleophobic surfaces have been developed by modifying the surface chemistry with a coating of extreme low surface energy materials [20,48-54]. Tuteja et al. [54] showed that surface curvature, in conjunction with chemical composition and roughened texture, can be used for liquids with low surface tension, including alkanes such as decane and octane. Liu et al. [18] performed experiments in a solid-water-oil interface. They found that hydrophilic and oleophilic surfaces (solid–air–water interface and solid–air–oil interface) can switch to an oleophobic surface in water (solid–water–oil interface). As a result, oil contaminants are washed away when immersed in water. This effect can be employed for underwater oleophobicity and self-cleaning that can be used against marine ship fouling [17]. Jung and Bhushan [20] proposed a model for predicting the oleophobic/philic nature of surfaces and showed how the water and oil droplets in three phase interfaces influence the wetting behavior on micropatterned surfaces with varying pitch values as well as the shark skin replica as an example from an aquatic animal.

Article objective

This article reviews drag data on artificial surfaces inspired from shark skin and lotus leaf. Oleophobic and self-cleaning surfaces inspired from aquatic animals are then discussed.

Fabrication and Characterization of Biomimetic Structures for Fluid Drag Reduction

In this section, we discuss drag reduction efficiency on biomimetic structured surfaces in channels.

Experimental techniques

For the measurement of pressure drop using water and air flows, an experimental flow channel with a rectangular channel was designed and fabricated as shown in Figure 3 [21]. The fabricated surfaces were used for the upper and lower walls of the flow channel. Two pieces of plastic were glued between the upper and lower samples and at each end to prevent flow leak. For the measurement of pressure drop, the upper sample had two opening holes connected with a differential manometer (Model A 1000-13, Differential Pressure Plus Inc., USA). The thickness, width, and length of the resulting channel are designated as H, W, and L, respectively.

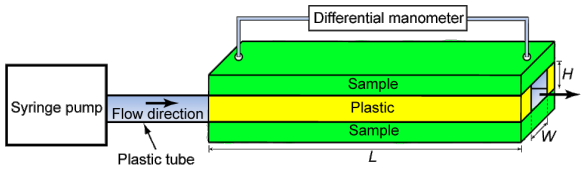

Figure 3: Schematic of the experimental flow channel connected with a differential manometer. The thickness, width, and length of the channel are H, W, and L, respectively.

The inlet and outlet ports were machined and connected with plastic tubes. To introduce water into the channel in laminar flow, a syringe pump (Model NE-300, New Era Pump Systems Inc., USA) was used at a range of flow rates between 50 μL/s and 400 μL/s (a range of flow velocity between 0.03 m/s and 0.23 m/s). The Reynolds number of the flow applied by the syringe pump was less than 300, which is the laminar flow. To create a turbulent flow, a larger flow rate is needed that cannot be accomplished with the syringe pump. To accomplish high fluid flow, a separate plastic chamber filled with a measured amount of water was used to allow flow through the channel under the force of gravity. By measuring the amount of water and time for the water to flow from a starting fluid level to an end fluid level, the Reynolds number was calculated as 4200 (flow velocity of 3.8 m/s), which indicates that the flow is turbulent using this setup. In order to make air flow a laboratory air outlet was connected to the channel. A flowmeter (Model FL-1478-G, Omega Engineering, Inc., USA) was used to measure the air flow rate between laboratory air outlet and channel. For the experimental measurements of air flow, the calculated range of Reynolds number was between 200 and 4600, which indicates both laminar and turbulent flows [21].

Model for calculation of pressure drop and slip length

The pressure drop Δp of an incompressible fluid flow between two points along the channel of thickness H, width W, and length L for a hydrophilic flat surface can be calculated by [55]

$$\Delta p = \frac{\rho V^2 f L}{2D_H} \quad (1)$$

where ρ is the fluid density, V is the flow velocity obtained from flow rate Q divided by cross section area of the channel, and f is the friction factor which specifies the loss in pressure required to impel a flow over the surface or through the channel. The friction factor is generally a function of Reynolds number, surface roughness, and the geometry of the surface. D_H is the hydraulic diameter which is proportional to four times the flow area divided by the perimeter of the surface containing the flow. For the rectangular channel, the hydraulic diameter is

$$D_H = \frac{2WH}{W+H} \quad (2)$$

The friction factor for laminar flow is inversely proportional to the Reynolds number Re as [55]

$$f = \frac{k}{Re} \quad \text{(for laminar flow)} \quad (3)$$

$$Re = \frac{\rho V D_H}{\eta} \quad (4)$$

where η is the dynamic fluid viscosity. The Reynolds number can be used to determine whether the fluid flow will be within the laminar, turbulent, or transitional flow regimes. Since the Reynolds number is proportional to flow velocity, the pressure drop in laminar flow increases with flow velocity. k is the friction coefficient which can be found by the solution of Poisson's equation over the cross section as [55]

$$k = \frac{64}{\frac{2}{3} + \frac{11}{23}\frac{H}{W}\left(2 - \frac{H}{W}\right)} \quad (5)$$

From Equation 5, the friction coefficient is dependent only on the shapes of the cross section and independent of the surface roughness.

To improve the calculation of the friction factor for turbulent flow in a rectangular channel, Jones [56] developed an improved equivalent diameter, $D_e = 64D_H/k$, thus the friction factor for turbulent flow can be modified as

$$f = \frac{64}{Re} \quad \text{(for turbulent flow)} \quad (6)$$

Next, we present an analysis to calculate slip length in laminar flow. Using the Navier slip boundary condition, the slip length b of the two infinite parallel and smooth plates can be expressed as [45,55]

$$b = \frac{4\eta QL}{\Delta p WH^2} - \frac{H}{3} \quad (7)$$

For a rectangular channel, the slip length would have the following general form [45]

$$b = \frac{c\eta QL}{\Delta p WH^2} - \frac{H}{3} \quad (8)$$

where c is a constant which must be obtained empirically. In order to obtain the constant, pressure drop measurements on a hydrophilic channel must be made. Equation 8 is then fitted under the assumption of zero slip length with the measured pressure drop data to obtain c and was equal to 5 for the channel (H = 0.7 mm, W = 2.5 mm, L = 60 mm) used in this study. This equation was now used to calculate the slip length for hydrophobic surfaces [21].

Fabrication and characterization of biomimetic structures

A shark (*Squalus acanthias*, L. Squalidae) was used for creating a shark skin replica [21]. A shark is an aquatic animal, and its skin is permanently exposed to contamination from marine organisms, e.g., bacteria and algae. The shark was conserved in FAA (formaldehyde/acetic acid/ethanol) solution. The detailed structure varies from one location to another for the shark. The scales are present over most of the shark's body. To create a replica, the right front of shark body was selected. Before replicating the conserved shark skin, the selected area was first cleaned with acetone and then washed with deionized water. This process was repeated twice. The cleaned skin was placed in air for 1 hour for drying. For the negative replica, a polyvinylsiloxane dental wax was applied via a dispenser on the upper side of the shark skin and immediately pressed down with a glass plate. After complete hardening of the molding mass (at room temperature 3–5 minutes), the master surface and the mold (negative) were separated. The first negative replica was made only to remove any remaining contaminations from the shark surface by embedding the dirt into the replica material. A second and third replica of the same area was made to obtain negatives without contamination. For the positive replica, a liquid epoxy resin was used in the molding process.

To simulate a shark skin structure, a rib-patterned surface was created using a FlashCut CNC milling machine [21]. Bechert et al. [57] and Dean and Bhushan [22] have reported that optimal groove depth for the rib surface should be about half of the lateral rib spacing for low drag. In the rib pattern design selected here, multiple stacks of ribs oriented along an axis were fabricated. For the fabrication, first a model of a rib-patterned surface was designed in SolidWorks, and then the code for the rib's height, width, spacing and lengths, and channel dimensions was written with FeatureCAM in order to fabricate structures using the CNC milling machine. An acrylic resin was clamped onto the table of the CNC mill, and a fly cutter was used to make the top of the surface flat. The code was opened with FlashCut CNC and then the rib patterns were milled using an endmill with 130 μm bit.

Figure 4a shows the scanning electron microscope (SEM) micrographs of the shark skin (*Squalus acanthias*) replica taken at a top view, a 45° tilt angle side view, and a 45° tilt angle top view. The shark skin replica shows that scales are lifted up at the end, and there are only three ribs on each scale. It is clearly visible that the V-shaped riblets' height varies between 200 and 500 μm, and their space varies between 100 and 300 μm. The ribs are oriented nearly parallel to swimming direction of the shark. Figure 4b shows the optical microscope images of the rib-patterned surface fabricated as a model of artificial shark skin surfaces. The height, width, and length of the created ribs were 90, 38, and 850 μm, respectively. The spacing between the ribs was 180 μm.

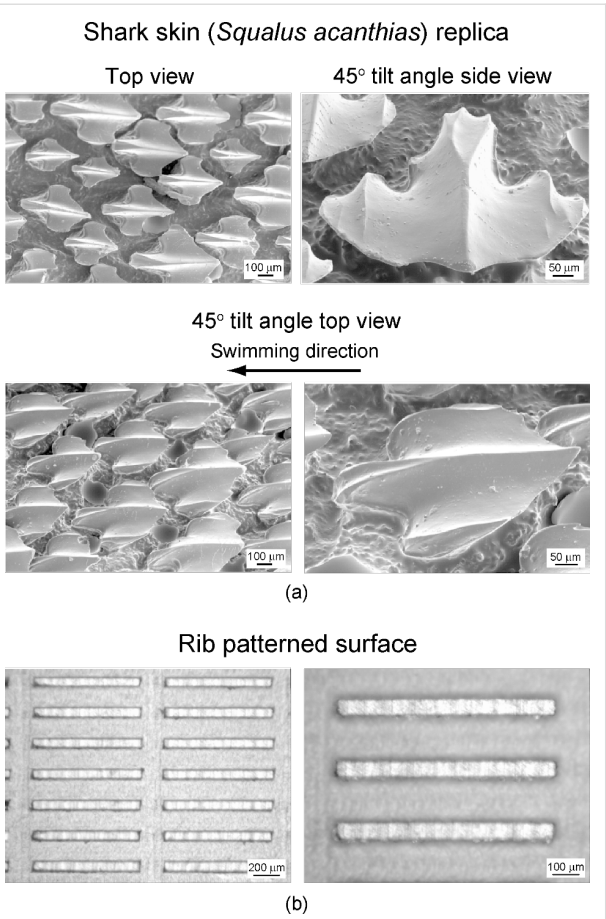

Figure 4: (a) SEM micrographs taken at top view, 45° tilt angle side view and 45° tilt angle top view, show shark skin (*Squalus acanthias*) replica. The shark skin replica shows only three ribs on each scale. (b) optical microscope images (shown at two magnifications) show the rib-patterned surface fabricated as a model of artificial shark skin surfaces [21].

To investigate drag reduction efficiency on the surfaces with superhydrophobicity, self-cleaning, and low adhesion described earlier, Jung and Bhushan [21] used nano-, micro-, and hierarchical structures [12,13]. Microstructures were fabricated using a two step molding process (soft lithography). A microstructured Si surface with pillars of 14 μm diameter and 30 μm height with 23 μm pitch fabricated by photolithography was used as a master template. A negative replica of the template was generated by applying a polyvinylsiloxane dental wax (President Light Body® Gel, ISO 4823, Polyvinylsiloxan (PLB), Coltene Whaledent, Hamburg, Germany), via a dispenser on the surface and immediately pressing down with a glass plate. After complete hardening of the molding mass (3–5 minutes at room temperature), the silicon master surface and the mold (negative) were separated. After a relaxation time of 30 minutes for the molding material, the negative replicas were filled with a liquid epoxy resin (Epoxydharz L®, No. 236349, Conrad Electronics, Hirschau, Germany) with hardener (Harter S, Nr 236365, Conrad Electronics, Hirschau, Germany). Specimens with microstructures were immediately transferred into a vacuum chamber at 750 mTorr (100 Pa) pressure for 10 seconds to remove trapped air and to increase the resin infiltration through the structures. After hardening at room temperature (24 h at 22 °C), the positive replica was separated from the negative replica. To generate several replicas the second step of replication was repeated twenty times for each surface type.

Nanostructures were created by self-assembly of plant wax deposited by thermal evaporation [12,13]. Tubule forming wax, which was isolated from a leaf of *Nelumbo nucifera,* in the following referred to as Lotus, was used to create tubule structures. Lotus wax with 0.8 μg/mm^2 was deposited on the specimen surfaces by thermal evaporation. The specimens with Lotus wax were exposed to ethanol vapor for three days at 50 °C, and then left in the oven at 50 °C for seven days in total. Hierarchical structures were fabricated by creating of nanostructures on top of microstructured surfaces, as described above. Flat epoxy resin and microstructure were covered with

flat Lotus wax. Flat thin wax layer was made by melting the deposited wax (3 min at 120 °C) and subsequent rapid cooling of the specimen to 5 °C. Then the specimens were stored for seven days at 21 °C in a desiccator. The fast cooling of the wax prevents the formation of nanostructure roughness. Figure 5 shows the SEM micrographs of nanostructure on flat replica, microstructures, and hierarchical structure. SEM micrographs show an overview (left column), a detail in higher magnification (middle column), and a large magnification of the created flat wax layers and tubules nanostructures (right column).

Table 1 summarizes the static contact angle and contact angle hysteresis measured on shark skin replica, rib-patterned surface, and the structured surfaces with Lotus wax. The shark skin

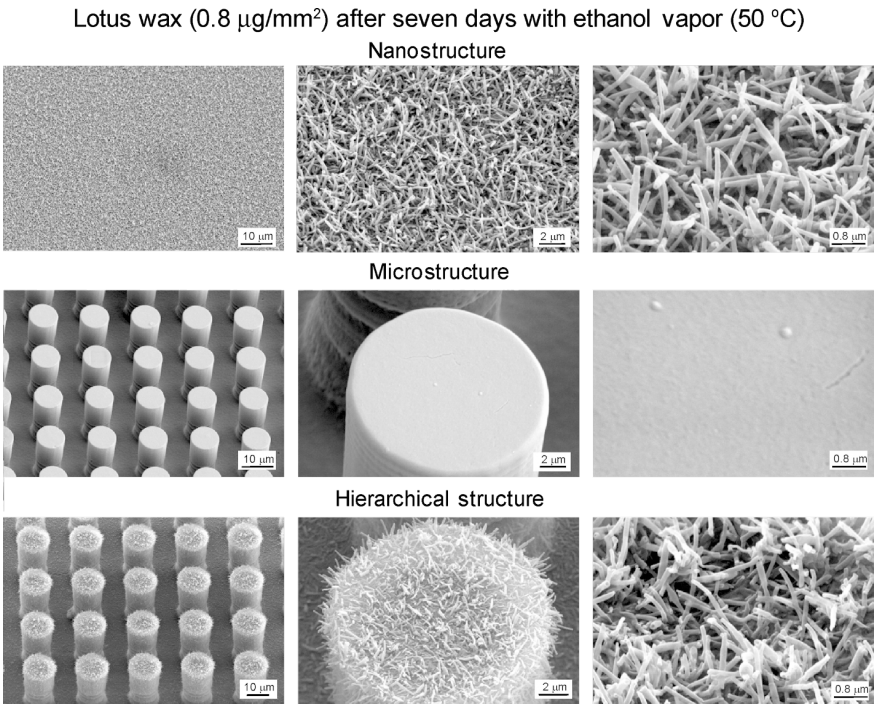

Figure 5: SEM micrographs taken at 45º tilt angle (shown using three magnifications) of nanostructure on flat replica, microstructures, and hierarchical structure. Nano and hierarchical structures coated with 0.8 μg/mm^2 of Lotus wax after storage for seven days at 50 °C with ethanol vapor. Flat epoxy resin and microstructure were covered with flat Lotus wax [21].

Table 1: Summary of the static contact angles and contact angle hysteresis measured on the various surfaces. Nanostructures and hierarchical structures were fabricated with 0.8 μg/mm^2 of Lotus wax after storage at 50 °C with ethanol vapor. Flat epoxy resin and microstructure were covered with flat Lotus wax. The variations represent one standard deviation [21].

	Static contact angle (°)	Contact angle hysteresis (°)
(a) Epoxy resin		
Flat epoxy resin	76 ± 0.9	67 ± 2.9 (151[a], 84[b])
Flat with thin wax layer	119 ± 2.4	56 ± 3.2 (148[a], 92[b])
Nanostructure	167 ± 0.7	6 ± 1.1 (170[a], 164[b])
Microstructure	160 ± 1.8	27 ± 2.1 (169[a], 142[b])
Hierarchical structure	173 ± 0.8	1 ± 0.6 (174[a], 173[b])
Shark skin replica	89 ± 1.7	66 ± 3.4 (155[a], 89[b])
(b) Acrylic resin		
Flat acrylic resin	82 ± 1.8	71 ± 2.6 (122[a], 51[b])
Rib-patterned surface	146 ± 1.2	43 ± 1.2 (158[a], 115[b])

[a]advancing contact angle; [b]receding contact angle.

replica had a static contact angle of 89° and a contact angle hysteresis of 66° for a water droplet. For acrylic resin material, a static contact angle of 82° was found for flat acrylic resin. Introduction of the rib patterns on the flat surface led to a much higher static contact angle of 146° and lower contact angle hysteresis of 43°. A static contact angle of 76° was found for flat epoxy resin. The microstructure (covered with a Lotus wax film) has a static contact angle of 160° but shows a much higher contact angle hysteresis of 27° than found in the hierarchical structure. Superhydrophobicity with a static contact angle of 167° and a contact angle hysteresis of 6° was also found in the nanostructured surface. Melting of the wax led to a flat surface with a flat wax film and a much lower static contact angle of 119° and higher contact angle hysteresis of 56°. The data of a flat Lotus wax film on a flat replica show that the Lotus wax by itself is hydrophobic. For the hierarchical structure, the highest static contact angles of 173° and lowest contact angle hysteresis of 1° were found. The recrystallized wax tubules are very similar to those of the original lotus leaf, but are 0.5 to 1 μm longer, and the static contact angle is higher, and the contact angle hysteresis is lower than reported for the original lotus leaf (static contact angle of 164° and contact angle hysteresis of 3°).

Pressure drop in the channel using water flow and calculated slip length. To observe the fluid drag reduction in the channel using water flow, experiments on flat epoxy resin, flat with thin wax layer, nanostructure, microstructure, hierarchical structure, and shark skin replica were performed [21]. In Figure 3, the rectangular channels with these surfaces had thickness H = 0.7 mm, width W = 2.5 mm, and length L = 60 mm. For calculation of the pressure drop using Equation 1, the mass density ρ and viscosity η for water were taken to be 1000 kg/m^3 and 0.001 Pa·s, respectively [58]. Figure 6 shows the pressure drop as a function of flow rate in the channel with various surfaces using water flow. The measured data are compared with the predicted pressure drop values for a hydrophilic surface obtained using Equation 1 for laminar and turbulent flows (solid lines). The figure in the bottom is magnified in

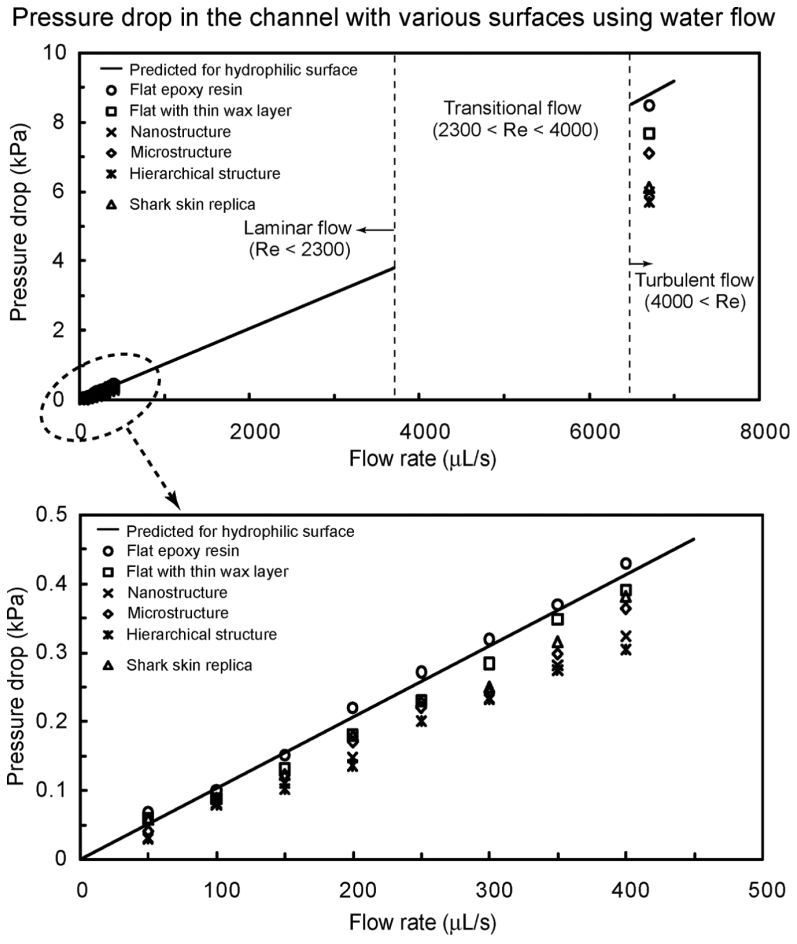

Figure 6: Pressure drop as a function of flow rate in the channel with various surfaces using water flow. The figure in the bottom is magnified in flow rate between 0 and 500 μL/s. Data are compared with predicted pressure drop values for a hydrophilic surface obtained using Equation 1 for laminar and turbulent flows (solid lines) [21].

flow rate between 0 and 500 µL/s. In both laminar and turbulent flows, the pressure drop increased linearly with flow rate for all samples. It was found that the pressure drop for the flat epoxy resin was similar to the value predicted by Equation 1, while structured surfaces had values lower than the predicted. As mentioned earlier and shown in Table 1, the introduction of roughness increases the hydrophobicity of the surfaces responsible for reduction in drag or pressure drop. The hierarchical structure with highest contact angle and lowest static contact angle hysteresis provided the lowest pressure drop. It is believed that air pockets inside the grooves underneath the fluid reduce the contact area between fluid and surface, resulting in lower pressure drop. These results indicate that superhydrophobicity can lead to drag reduction in fluid flow [21].

As shown in Figure 6, for shark skin replica, it was found that the pressure drop in laminar flow was higher than those of the nanostructure and hierarchical structure and the reduction of pressure drop was about 12% as compared to the theoretical pressure drop. However, in turbulent flow, the reduction of pressure drop was similar to those of nanostructure and hierarchical structure. Bechert et al. [19] showed that a turbulent boundary layer on the shark skin surface with ribs can help to reduce turbulent shear stress (also see Dean and Bhushan [22]). The results of experimental measurements on shark skin replica showed that a reduction of pressure drop was obtained up to 30% in turbulent flow. It can be concluded that the surfaces with ribs are more beneficial in providing drag reduction in turbulent flow than in laminar flow.

Based on the pressure drop data, the slip length on the surfaces with different wettabilities was calculated using Equation 8. For calculations, it was assumed that there is a no-slip boundary condition on flat epoxy resin as verified from the experiments [40]. Figure 7 shows the bar chart showing the slip length in the channel with various surfaces using water flow in laminar flow ($0 < Re < 300$). The average values of slip length on the surfaces were calculated over all the experimental flow rates. A slip length of 24 µm was found for the flat surface with thin wax layer. The microstructure (covered with a flat Lotus wax film) and shark skin replica had slip lengths of 56 and 35 µm, but the nanostructure and hierarchical structures show much higher slip lengths of 91 and 103 µm, respectively, which implies the boundary slip increases with increasing hydrophobicity of solid surfaces.

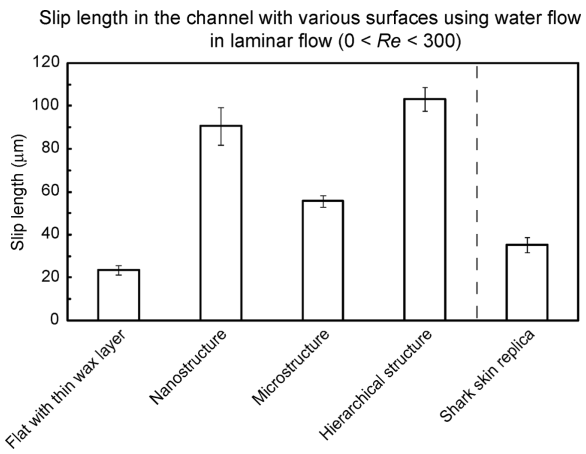

Figure 7: Bar chart showing the slip length in the channel with various surfaces using water flow in laminar flow ($0 < Re < 300$). The slip length was calculated using Equation 8 and the pressure drop measured on various surfaces. The error bars represent one standard deviation [21].

Slip length measurements have also been made on the nanoscale on hydrophilic and hydrophobic surfaces with various degrees of hydrophobicity using a dynamic AFM method [16,33]. Data on one hydrophilic, one hydrophobic, and one superhydrophobic surface are presented in Table 2. Mica was taken as the hydrophilic surface. Hydrophobic and superhydrophobic surfaces were fabricated by deposition of evaporated plant wax on smooth epoxy substrates following the procedure described earlier in this section. Hydrophilic surface was produced without any recrystallization (rather flat surface) whereas to produce a superhydrophobic surface, the wax was recrystallized to produce a tubular nanostructure [13]. The data presented in Table 2 shows increasing boundary slip from the hydrophobic surface to the superhydrophobic one. We note that slip length on the nanoscale is much lower than that on the macroscale reported in Figure 7. Zhu and Granick [59] have reported that the slip length increases from nanometer range to micrometer range as the flow rate increases.

Table 2: RMS roughness (AFM, scan size = 5 µm × 5 µm), static contact angle and slip length measured using tapping mode of three different surfaces [16,33].

Surfaces	RMS roughness (nm)	Static contact angle (°)	Slip length with tapping AFM (nm)
hydrophilic	0.20	~0	~0
hydrophobic	11.0	91 ± 2.0	43 ± 10
superhydrophobic	178	167 ± 0.7	236 ± 18

The fluid drag measurements were also made on flat acrylic resin and rib-patterned surfaces fabricated as a model of artificial shark skin [21]. In Figure 3, the rectangular channels with these surfaces had thickness H = 1 mm, width W = 2 mm, and length L = 100 mm. Figure 8 shows the pressure drop as a function of flow rate in the channel using water flow. The measured data are compared with predicted pressure drop values for a hydrophilic surface obtained using Equation 1 for laminar and turbulent flows (solid lines). The figure at the bottom is magnified for flow rate between 0 and 500 μL/s. In laminar flow, it was found that the pressure drop increased linearly with flow rate and was similar to the value predicted by Equation 1. However, in turbulent flow, the reduction in pressure drop was up to 23% as compared to the theoretical pressure drop. This result shows a similar trend to that of the shark skin replica.

Pressure drop in the channel using air flow. To investigate the effect of air flow in the channel and compare them to water drag reduction, experiments with air flow on various surfaces were performed [21]. In Figure 3, the rectangular channels had thickness H = 0.7 mm, width W = 2.5 mm, and length L = 60 mm. For calculation of pressure drop using Equation 1, the mass density ρ and viscosity η for air were taken to be 1.204 kg/m^3 and 1.837×10^{-5} Pa·s, respectively [58]. Figure 9 shows the pressure drop as a function of flow rate in the channel with various surfaces using air flow. The measured data are compared with predicted pressure drop values for a hydrophilic surface obtained using Equation 1 for laminar and turbulent flows (solid lines). The figure at the bottom is magnified for flow rate between 0 and 50 mL/s. The pressure drop of the structured surfaces is higher than that of the hydrophilic surface in the turbulent flow which is opposite to that in liquid flow. In both laminar and turbulent flows, the pressure drop increased linearly with flow rate for all samples. As mentioned earlier, in the case of water flow, air pockets between the structures reduce the contact area between liquid and surface, resulting in reduction of the flow drag. The data shows that the structures are not beneficial for drag reduction in air flow. The introduc-

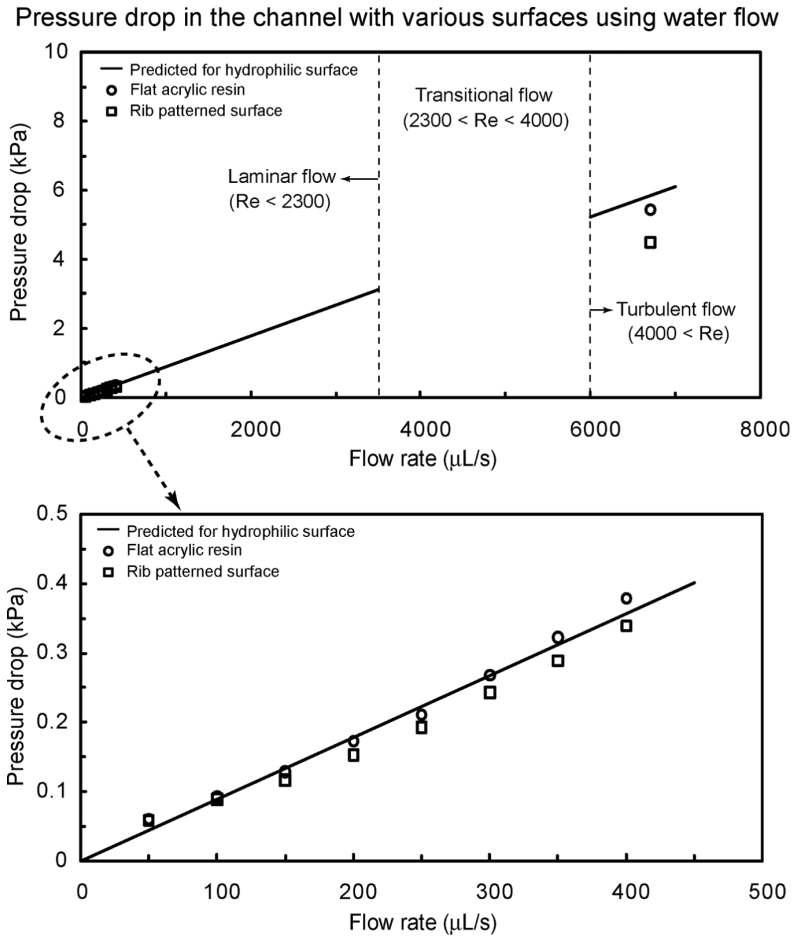

Figure 8: Pressure drop as a function of flow rate in the channel with flat acrylic resin and rib-patterned surface using water flow. The figure in the bottom is magnified for flow rate between 0 and 500 μL/s. Data are compared with predicted pressure drop values for a hydrophilic surface obtained using Equation 1 for laminar and turbulent flows (solid lines) [21].

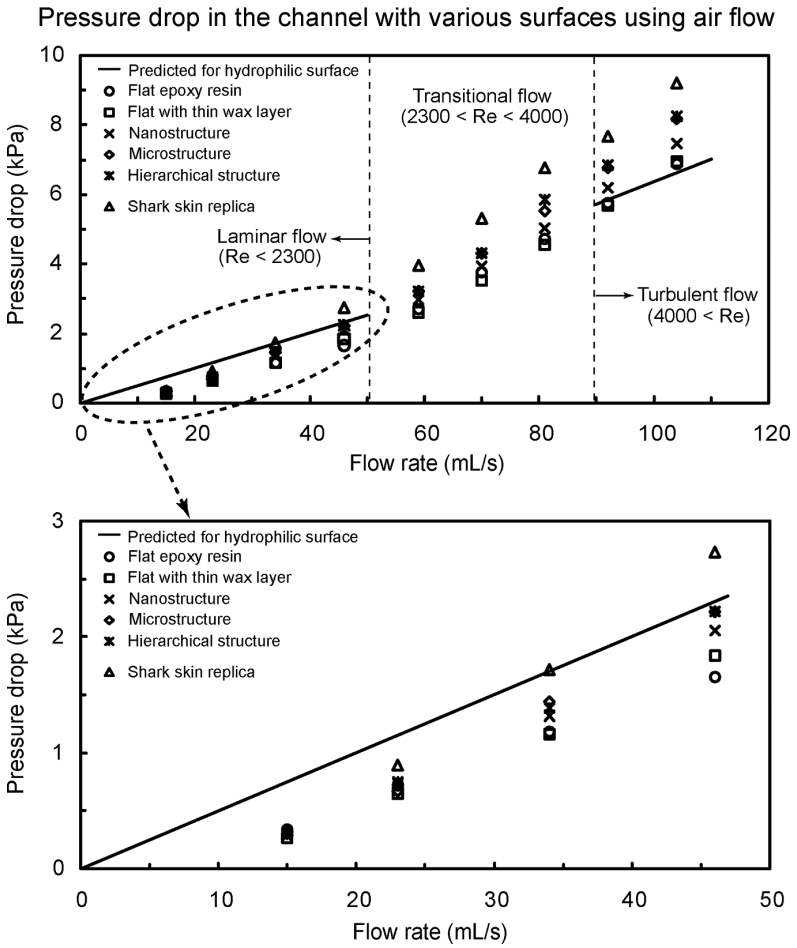

Figure 9: Pressure drop as a function of flow rate in the channel with various surfaces using air flow. The figure at the bottom is magnified for flow rate between 0 and 50 mL/s. Data are compared with predicted pressure drop values for a hydrophilic surface obtained using Equation 1 for laminar and turbulent flows (solid lines) [21].

tion of roughness on the surfaces increases the pressure drop in the channel in the turbulent flow. It is generally known that surfaces with a streamlined body can produce dramatic reductions of the fluid pressure drag with only a slight increase in shear stress in air flow [60]. It is also known that as the Reynolds number increases, the pressure drop becomes very large, resulting in larger pressure drag. The roughness of structures on surfaces may cause air to move around them, resulting in the formation of vortices and large fluid drag.

To observe the fluid drag reduction in the channel using air flow, experiments on flat acrylic resin and fabricated rib-patterned surface were also performed [21]. The rectangular channels with these surfaces had thickness H = 1 mm, width W = 2 mm, and length L = 100 mm. Figure 10 shows the pressure drop as a function of flow rate in the channel with flat acrylic resin and rib-patterned surface using air flow. The measured data are compared with predicted pressure drop values for a hydrophilic surface obtained using Equation 1 for laminar and turbulent flows (solid lines). The experimental results show a similar trend to the data as shown in Figure 9. It was found that the pressure drop of the rib-patterned surface slightly increased due to the vortices formed at the end of the ribs in turbulent flow as compared to the theoretical pressure drop.

Modeling, Fabrication and Characterization of Oleophobic/philic Surfaces

Oleophobic surfaces have the potential for self-cleaning and anti-fouling from biological and organic contaminants both in air and underwater applications. In this section, we discuss a model for predicting the oleophobic/philic nature and experimental measurements of the wetting properties of the surfaces.

Modeling of contact angle for various interfaces

If a water droplet is placed on a solid surface in air, the solid–air and water–air interfaces come together with a static contact

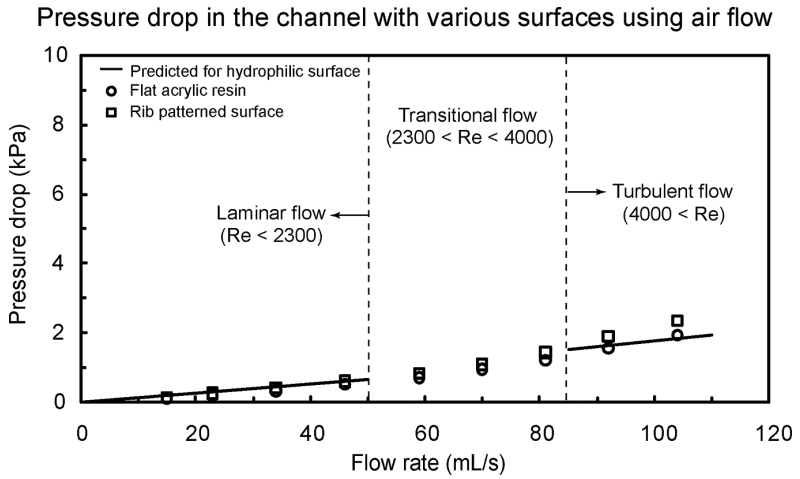

Figure 10: Pressure drop as a function of flow rate in the channel with flat acrylic resin and rib-patterned surface using air flow. Data are compared with predicted pressure drop values for a hydrophilic surface obtained using Equation 1 for laminar and turbulent flows (solid lines) [21].

angle, θ_W. The value of θ_W can be determined from the condition of the total energy of the system being minimized [61-63] and is given by Young's equation for the contact angle θ_W

$$\cos\theta_W = \frac{\gamma_{SA} - \gamma_{SW}}{\gamma_{WA}} \tag{9}$$

where γ_{SW}, γ_{SA}, and γ_{WA} are the surface tensions of the solid–water, solid–air, and water–air interfaces, respectively. If an oil droplet is placed on a solid surface in air, the Young's equation for the contact angle, θ_O, can be expressed by

$$\cos\theta_O = \frac{\gamma_{SA} - \gamma_{SO}}{\gamma_{OA}} \tag{10}$$

where γ_{SO}, γ_{SA}, and γ_{OA} are surface tensions of the solid–oil, solid–air, and oil–air interfaces, respectively. As predicted by Equation 10, if γ_{SO} is higher than γ_{SA}, an oleophobic surface can be achieved.

To create an oleophobic surface in water, let us consider the solid–water–oil interface. If an oil droplet is placed on a solid surface in water, the contact angle of an oil droplet in water, θ_{OW}, is given by Young's equation

$$\cos\theta_{OW} = \frac{\gamma_{SW} - \gamma_{SO}}{\gamma_{OW}} \tag{11}$$

where γ_{SO}, γ_{SW}, and γ_{OW} are surface tensions of the solid–oil, solid–water, and oil–water interfaces, respectively. Combining Equation 9, Equation 10 and Equation 11, the equation for the contact angle, θ_{OW}, of an oil droplet in water is given as

$$\cos\theta_{OW} = \frac{\gamma_{OA}\cos\theta_O - \gamma_{WA}\cos\theta_W}{\gamma_{OW}} \tag{12}$$

Based on Jung and Bhushan [20], as predicted by Equation 12, for a hydrophilic surface ($\gamma_{SA} > \gamma_{SW}$), an oleophobic surface in the solid–water–oil interface can be created if $\gamma_{OA}\cdot\cos\theta_O$ is lower than $\gamma_{WA}\cdot\cos\theta_W$. Since the surface tension of oil and organic liquids is much lower than that of water, most hydrophilic surfaces can be made oleophobic in a solid–water–oil interface. For a hydrophobic surface ($\gamma_{SA} < \gamma_{SW}$) and an oleophobic surface in a solid–air–oil interface ($\gamma_{SA} < \gamma_{SO}$), an oleophobic surface in a solid–water–oil interface can be created if $\gamma_{OA}\cdot\cos\theta_O$ is higher than $\gamma_{WA}\cdot\cos\theta_W$ and vice versa. For a hydrophobic and an oleophilic surface in solid–air–oil interface, an oleophobic surface in solid–water–oil interface cannot be created. Schematics are shown in Figure 11, and the summary of philic/phobic nature in various interfaces is shown in Table 3. For an oleophobic surface, oil contaminants are washed away when immersed in water. This effect leads to self-cleaning that can be used against ship fouling.

Experimental techniques

For the measurement of the static contact angle, deionized water was used for the water droplet and hexadecane was used for oil droplets [20]. The surface tensions of the water–air interface (γ_{WA}), oil–air interface (γ_{OA}), and oil–water interface (γ_{OW}) are 73 [58], 27.5 [58], and 51.4 [64] mN/m, respectively. The mass densities are 1000 and 773 kg/m^3 for water and hexadecane, respectively. Water and oil droplets of about 5 μL in volume (with radius of a spherical droplet about 1 mm) in an air environment were gently deposited on the specimen using a microsyringe. The process of wetting behavior of an oil droplet in water was obtained in a solid–water–oil interface system as

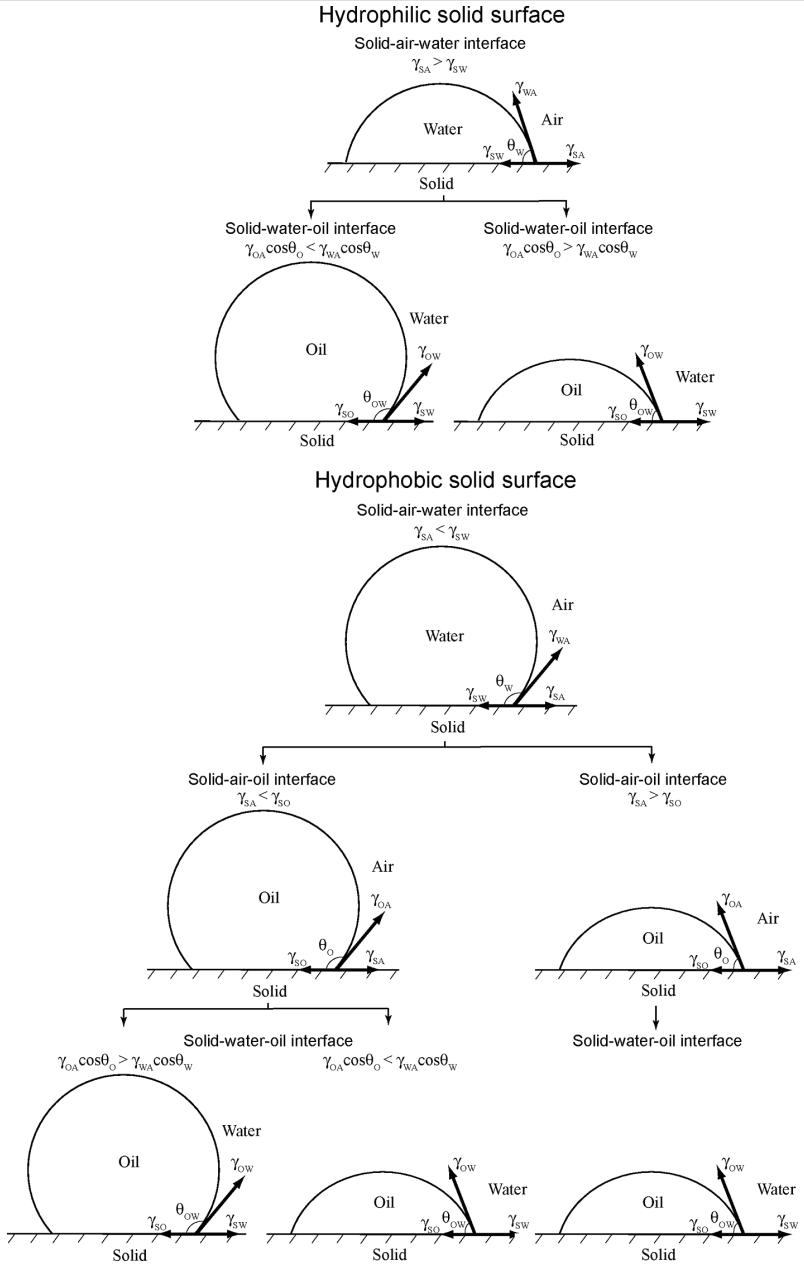

Figure 11: Schematics of a droplet of liquid showing philic/phobic nature in three different phase interface on the surface – θ_W, θ_O, and θ_{OW} are the static contact angles of a water droplet, an oil droplet, and an oil droplet in water, respectively [20].

Table 3: Summary of philic/phobic nature in various interfaces [20].

solid–air–water interface		solid–water–oil interface
hydrophilic ($\gamma_{SA} > \gamma_{SW}$)	→	oleophobic if $\gamma_{OA}\cos\theta_O < \gamma_{WA}\cos\theta_W$ oleophilic if $\gamma_{OA}\cos\theta_O > \gamma_{WA}\cos\theta_W$

solid–air–water interface	solid–air–oil interface	solid–air–water interface
hydrophobic ($\gamma_{SA} < \gamma_{SW}$) →	oleophobic if $\gamma_{SA} < \gamma_{SO}$	→ oleophobic if $\gamma_{OA}\cos\theta_O > \gamma_{WA}\cos\theta_W$ → oleophilic if $\gamma_{OA}\cos\theta_O > \gamma_{WA}\cos\theta_W$
	oleophilic if $\gamma_{SA} > \gamma_{SO}$ →	oleophilic

shown in Figure 12 [20]. A specimen was first immersed in water phase. Then an oil droplet was gently deposited using a microsyringe from the bottom of the system because the density of oil (hexadecane) is lower than that of water. The image of the droplet was obtained by a digital camcorder (Sony, DCRSR100, Tokyo, Japan) with a 10× optical and 120× digital zoom. Images obtained were analyzed for the contact angle using Imagetool® software (University of Texas Health Science Center). The measurements were reproducible to within ± 2°.

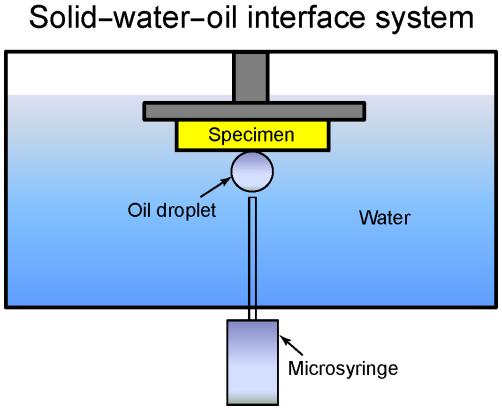

Figure 12: Schematics of a solid–water–oil interface system. A specimen is first immersed in water phase, then an oil droplet is gently deposited using a microsyringe, and the static contact angle in the system measured [20].

Fabrication and characterization of oleophobic surfaces

As presented earlier, a two-step molding process was used to replicate microstructures with varying pitch values. As a master template for flat and micropatterned surfaces, a flat Si surface and micropatterned Si surfaces with pillars of 14 µm diameter and 30 µm height with different pitch values (21, 23, 26, 35, 70, 105, 126, 168 and 210 µm), fabricated by photolithography, were used [20].

To study surfaces with some oleophobicity, a surface coating which has a lower surface tension than that of oil is required. For this purpose, Jung and Bhushan [20] deposited *n*-perfluoroeicosane ($C_{20}F_{42}$) (268828, Sigma-Aldrich, USA) on the specimen surfaces by thermal evaporation. The surface energy of *n*-perfluoroeicosane is 6.7 mJ/m^2 (6.7 mN/m) [65]. The specimens were mounted on a specimen holder with double-sided tape and placed in a vacuum chamber at 30 mTorr (4 kPa pressure), 2 cm above a heating plate loaded with 6000 µg *n*-perfluoroeicosane [16]. The *n*-perfluoroeicosane was evaporated by heating it to 170 °C. In a vacuum chamber the evaporation from the point source to the substrate occurs in straight line; thus, the amount of sublimated material is equal in a hemispherical region over the point of source [66]. In order to estimate the amount of sublimated mass, the surface area of the half sphere was calculated by using the formula $2\pi r^2$, whereby the radius r represents the distance between the specimen to be covered and the heating plate with the substance to be evaporated. The calculated amount of *n*-perfluoroeicosane deposited on the surfaces was 2.4 µg/mm^2 (amount of *n*-perfluoroeicosane loaded on a heating plate divided by surface area).

Hierarchical structures were fabricated using a two step fabrication process, including the production of microstructured surfaces by soft lithography and the subsequent development of nanostructures on top by self assembly of *n*-hexatriacontane with the amounts of 0.2 µg/mm^2 deposited by thermal evaporation, as described previously [16,67]. Jung and Bhushan [20] also used a shark skin replica described previously.

Figure 13a shows the SEM micrographs taken at a 45° tilt angle, showing two magnifications of the micropatterned surface. Figure 13b shows the hierarchical structures and nanostructures covered with *n*-hexatriacontane platelets. The nano-

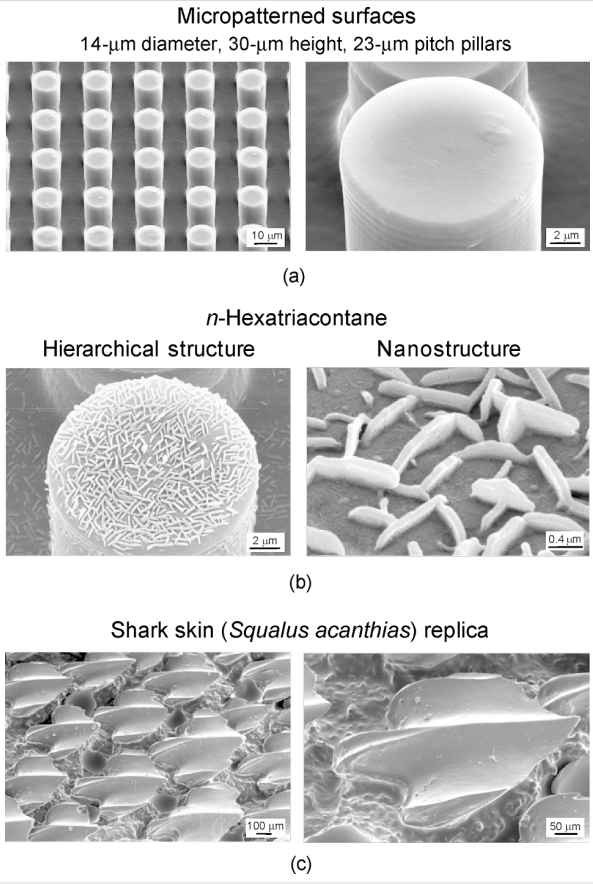

Figure 13: SEM micrographs taken at a 45° tilt angle showing two magnifications of (a) the micropatterned surface, (b) hierarchical structure and nanostructure with three-dimensional platelets on the surface fabricated with 0.2 µg/mm^2 mass of *n*-hexatriacontane, and (c) shark skin (*Squalus acanthias*) replica. [20].

structure is formed by three-dimensional platelets of *n*-hexatriacontane. Platelets are flat crystals, grown perpendicular to the substrate surface. The platelet thickness varied between 50 and 100 nm, and their length varied between 500 and 1000 nm. Figure 13c, the shark skin replica, shows only three ribs on each scale. It is clearly visible that the V-shaped riblets' height varies between 200 and 500 µm, and their space varies between 100 and 300 µm [20].

Wetting behavior on flat and micropatterned surfaces. To observe the wetting behavior of water and oil droplets for philic/phobic nature in three phase interfaces, Jung and Bhushan [20] performed experiments with droplets on both hydrophilic and hydrophobic, and oleophilic surfaces in air. Figure 14 shows the optical micrographs of droplets in three different phase interfaces on flat epoxy resin and micropatterned surfaces. In a solid–air–water interface, the water droplet was hydrophilic for the flat epoxy resin and was superhydrophobic for the micropatterned surface with 23 µm pitch. It is known that air pocket formation between the pillars makes a high static contact angle for micropatterned surface. However, in a solid–air–oil interface, the oil droplet was oleophilic for both surfaces. In the solid–water–oil interface system, in which the oil droplet sits on water trapped in the pillars, it is observed that the oil droplet in water was oleophobic and had contact angles of 109° and 151° for flat epoxy resin and micropatterned surface with 23 µm pitch, respectively.

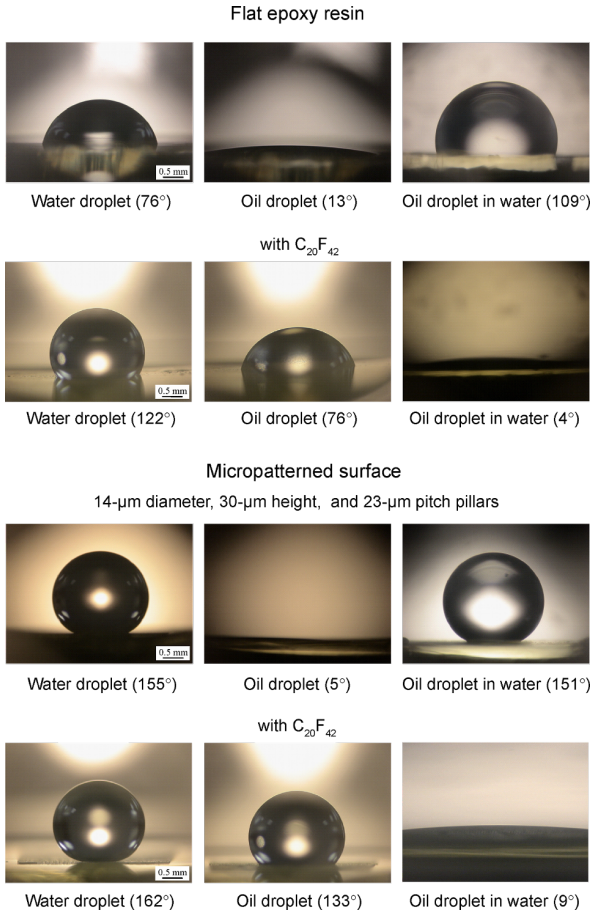

Figure 14: Optical micrographs of droplets in three different phase interfaces on flat epoxy resin and micropatterned surface without and with $C_{20}F_{42}$. Left images: a water droplet is placed on a surface in air. Middle images: an oil droplet is placed on a surface in air. Right images: an oil droplet is placed on a solid surface in water [20].

To study optimization of oleophobicity in the two solid–air–water and solid–air–oil interfaces, the static contact angles for water and oil droplets were measured on the micropatterned surfaces [20]. Figure 15 (top) shows the measured static contact angle as a function of pitch between the pillars for a water droplet (circle) and an oil droplet (cross) in air. The data are compared with predicted static contact angle values obtained using Wenzel and Cassie–Baxter equations [20] (solid lines) with a measured value of θ_0 for the micropatterned surfaces. In a solid-air-water interface for a water droplet, the flat epoxy resin showed a static contact angle of 76°. The static contact angle on micropatterned surfaces is higher than that of the flat surfaces. It first increases with an increase in the pitch values, then starts to drop rapidly to a value slightly higher than that of the flat surfaces. In the first portion, it jumps to a high value of 150° corresponding to a superhydrophobic surface and continues to increase to 160° at a pitch of 26 µm because open air space increases with an increase in pitch responsible for the propensity of air pocket formation. The sudden drop at a pitch value of about 30 µm corresponds to the transition from the Cassie–Baxter to the Wenzel regime. The experimental observations for the transition are comparable to the value predicted from Wenzel and Cassie–Baxter equations.

At a solid–air–oil interface for an oil droplet, the flat epoxy resin showed a static contact angle of 13°. As shown in Figure 15 (top), the oil droplets on all micropatterned surfaces were oleophilic, and the contact angle was lower than that of the flat surfaces. It increases with an increase in the pitch values as predicted from Wenzel equation. As mentioned earlier, the surface tension of the oil–air interface is very low for hexadecane. Therefore, it is observed that from Equation 11 the surface tension of solid–oil interface (γ_{SO}) is lower than that of solid–water interface (γ_{SW}), resulting in oleophilic state for all micropatterned surfaces.

To study optimization of oleophobicity in a solid–water–oil interface, the static contact angles for oil droplets in water were measured on the micropatterned surfaces [20]. Figure 15 (bottom) shows the measured static contact angle as a function of pitch between the pillars for an oil droplet in water (triangles). The data are compared with the predicted static

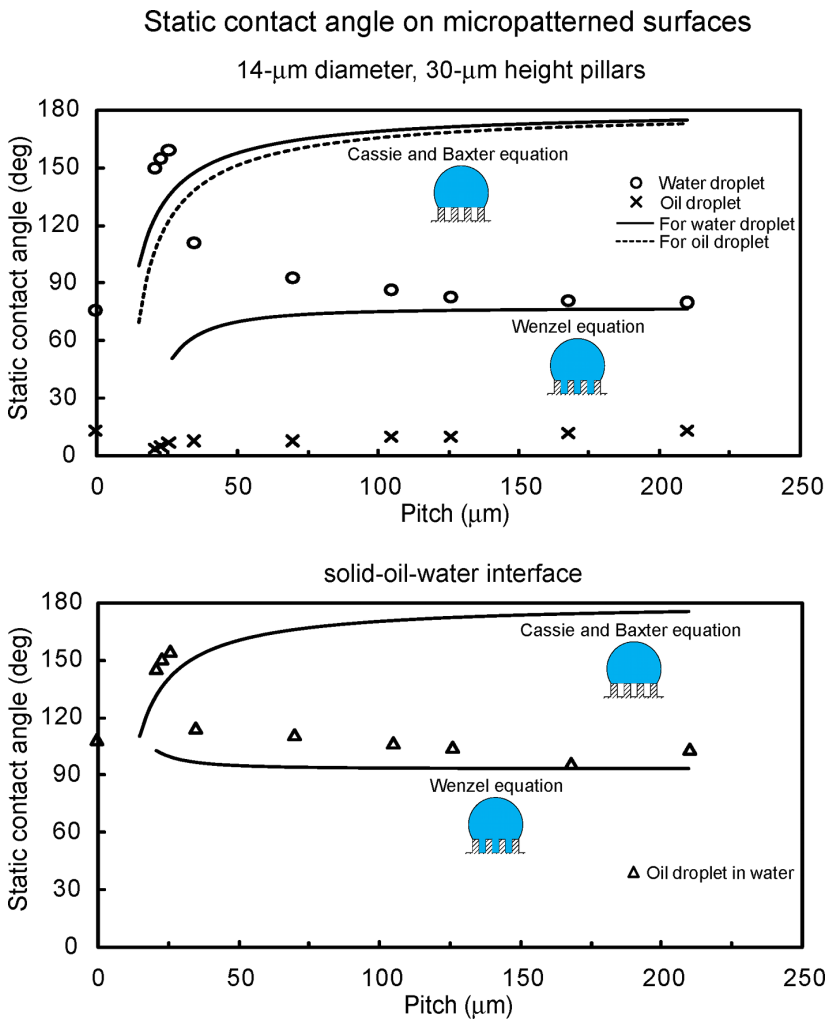

Figure 15: Static contact angle as a function of geometric parameters for water droplet (circle) and oil droplet (cross) in air (top), and oil droplet in water (triangle) (bottom) compared with predicted static contact angle values obtained using Wenzel and Cassie–Baxter equations (solid lines) with a measured value of θ_0 for the micropatterned surfaces [20].

contact angle values obtained using the Wenzel and Cassie–Baxter equations [9] (solid lines), with a measured value of θ_0 for the micropatterned surfaces. In a solid–water–oil interface, the oil droplet on the flat epoxy resin was oleophobic and had a static contact angle of 109°. The static contact angle of micropatterned surfaces in the solid–water–oil interface showed a similar trend to that in the solid–air–water interface. As the pitch increases up to 26 μm, the static contact angle first increases gradually from 146° to 155° because the oil droplet sits on water trapped in the pillars, and open space increases with an increase in pitch. The contact angle then starts to decrease rapidly due to the transition from the Cassie–Baxter to the Wenzel regime. The experimental observations for the transition are comparable to the values predicted from Wenzel and Cassie–Baxter equations. The micropatterned surfaces studied here were either hydrophilic or hydrophobic and both were oleophilic. In the solid–water–oil interface, they were oleophobic. It is observed that the data are not consistent with the model for hydrophobic surfaces shown in Figure 11 and Table 3. However, hydrophilic surfaces became oleophobic in the solid–water–oil interface because $\gamma_{OA}\cdot\cos\theta_O$ is higher than $\gamma_{WA}\cdot\cos\theta_W$.

Wetting behavior on flat and micropatterned surfaces with $C_{20}F_{42}$. To study surfaces with some oleophobicity, *n*-perfluoroeicosane ($C_{20}F_{42}$), which has lower surface tension than that of oil, was deposited on the surfaces, and experiments with droplets on hydrophobic and both oleophilic and oleophobic surfaces in air were performed [20]. Figure 14 shows the optical micrographs of droplets in three different phase interfaces on a flat epoxy resin and a micropatterned surface with $C_{20}F_{42}$. In a solid–air–water interface and a solid–air–oil interface, the water

droplet and oil droplet showed contact angles of 122° and 76° for the flat epoxy resin with $C_{20}F_{42}$ and contact angles of 162° and 133° for the micropatterned surface with 23 μm pitch with $C_{20}F_{42}$, respectively. However, in a solid–water–oil interface, the oil droplet in water was oleophilic and had contact angles of 4° and 9° for both surfaces, respectively. To explain why the oleophobic surfaces in air became oleophilic in water, the theoretical values for both surfaces were calculated using Equation 12. For the calculations, the surface tensions of the water–air interface (γ_{WA}), oil–air interface (γ_{OA}), and oil–water interface (γ_{OW}) were taken to be 73, 27.5, and 51.4 mN/m, and the contact angles for water and oil droplets in air were the measured values. The theoretical values for the flat epoxy resin and the micropatterned surface with 23 μm pitch with $C_{20}F_{42}$ are 28° and 10°, respectively. These values are similar to those from the experiments. This indicates that the oleophobic surfaces become oleophilic in water.

To study optimization of oleophobicity in two solid–air–water and solid–air–oil interfaces, the static contact angles for water and oil droplets were measured on the micropatterned surfaces with different pitch values and with $C_{20}F_{42}$ [20]. Figure 16 shows the measured static contact angle as a function of pitch between the pillars for a water droplet (circle) and an oil droplet (cross) in air. The data are compared with the predicted static contact angle values obtained using the Wenzel and Cassie–Baxter equations [20] (solid lines) with a measured value of θ_0 for the micropatterned surfaces with $C_{20}F_{42}$. In a solid–air–water interface for the water droplet, the flat epoxy resin with $C_{20}F_{42}$ showed a static contact angle of 122°. The static contact angle of micropatterned surfaces with $C_{20}F_{42}$ first increases from 158° to 169° with an increase in the pitch values, then starts to drop rapidly at a pitch value of 110 μm. From a comparison of the experimental data with the Wenzel and Cassie–Baxter equations, this corresponds to the transition from

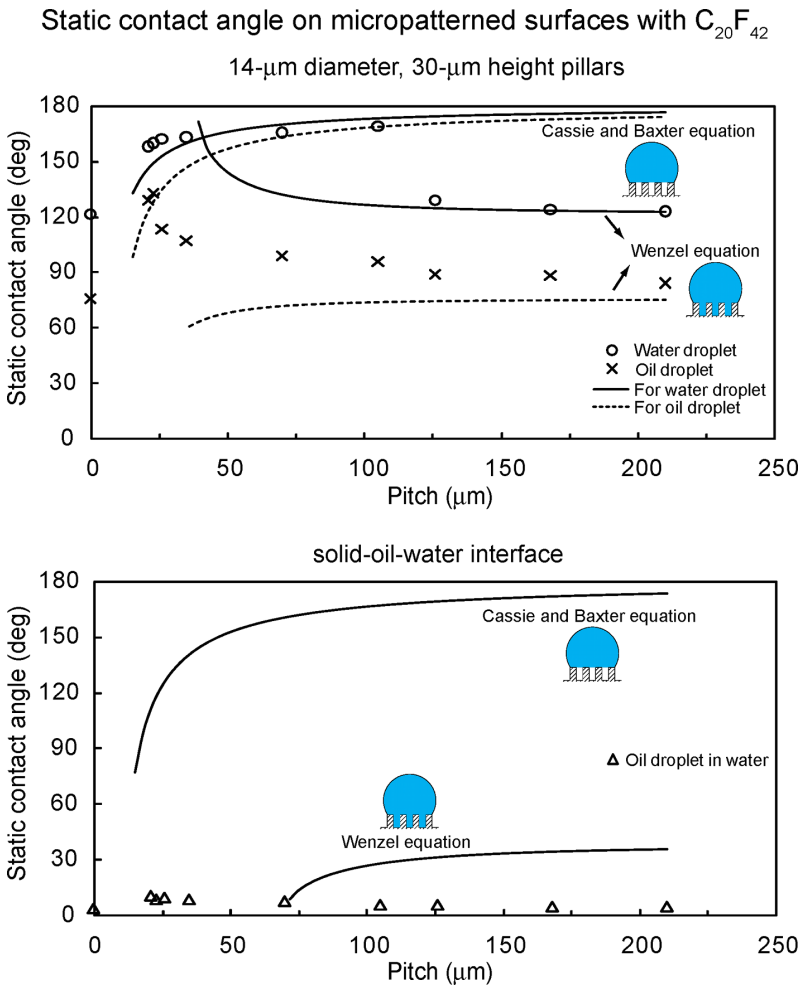

Figure 16: Static contact angle as a function of geometric parameters for water droplet (circle) and oil droplet (cross) in air, and oil droplet in water (triangles) compared with predicted static contact angle values obtained using the Wenzel and Cassie–Baxter equations (solid lines) with a measured value of θ_0 for the micropatterned surfaces with $C_{20}F_{42}$ [20].

the Cassie–Baxter to the Wenzel regime. All surfaces with $C_{20}F_{42}$ had an increase in contact angle, and the transition took place at higher pitch value than that of the micropatterned surfaces (Figure 15).

At a solid–air–oil interface for an oil droplet, the flat epoxy resin with $C_{20}F_{42}$ showed a static contact angle of 76°. As shown in Figure 16, the highest contact angle of micropatterned surfaces with $C_{20}F_{42}$ was 133° at a pitch value of 23 μm. Then, it decreases with an increase in the pitch values, and these values are comparable with the values predicted by the Wenzel equation. The contact angles of all micropatterned surfaces with $C_{20}F_{42}$ are higher than that of the flat surfaces.

To study optimization of oleophobicity in a solid–water–oil interface, the static contact angles for oil droplets in water were measured on the micropatterned surfaces with different pitch values and with $C_{20}F_{42}$ [20]. Figure 16 shows the measured static contact angle as a function of pitch between the pillars for an oil droplet in water (triangles). The data are compared with the predicted static contact angle values obtained using the Wenzel and Cassie–Baxter equations [20] (solid lines) with a measured value of θ_0 for the micropatterned surfaces with $C_{20}F_{42}$. In a solid–water–oil interface, the flat epoxy resin with $C_{20}F_{42}$ was oleophilic and had a static contact angle of 4°. All micropatterned surfaces with $C_{20}F_{42}$ were oleophilic and had contact angle lower than 10°. The reason why hydrophobic and oleophobic surfaces in air became oleophilic in water can be explained from Figure 11 and Table 3. The contact angle for a water droplet is higher than that for an oil droplet on all surfaces with $C_{20}F_{42}$, and the surface tension of the water–air interface (γ_{WA}) is higher than that of the oil–air interface (γ_{OA}). Therefore, it is observed that $\gamma_{WA}\cdot\cos\theta_W$ is higher than $\gamma_{OA}\cdot\cos\theta_O$, and then the surfaces become oleophilic in the solid–water–oil interface.

Wetting behavior on nano- and hierarchical structures and shark skin replica. To observe the wetting behavior of water and oil droplets for nano- and hierarchical structures found from lotus plant surfaces, experiments with the droplets on the surfaces were performed in the three phase interface [20]. Figure 17 shows the optical micrographs of droplets in three different phase interfaces on a nanostructure and a hierarchical structure fabricated with 0.2 μg/mm^2 mass of *n*-hexatriacontane. Both nano- and hierarchical structures were superhydrophobic and had a static contact angle of 158° and 169° in the solid–air–water interface, respectively. However, they are oleophilic in the solid–air–oil interface because the surface energy of *n*-hexatriacontane is 31.4 mJ/m^2 (31.4 mN/m) [68], and this value is higher than that of an oil droplet (hexadecane). In the solid–water–oil interface, nano- and hierarchical structures had a static contact angle of 10° and 5°, respectively. As shown in Figure 11 and Table 3, it is observed that both surfaces are oleophilic in solid–water–oil interface.

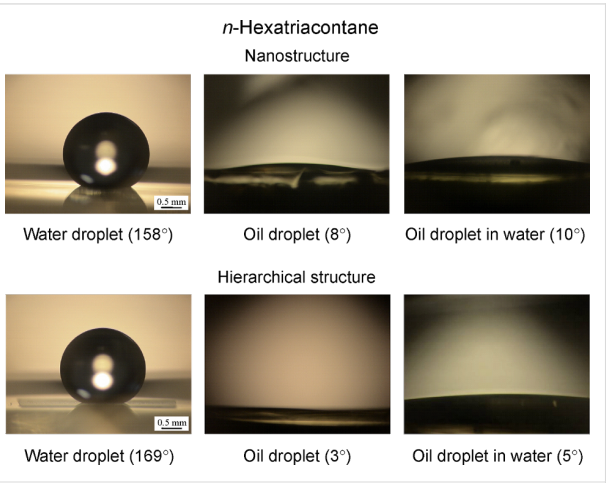

Figure 17: Optical micrographs of droplets in three different phase interfaces on nanostructure and hierarchical structure fabricated with 0.2 μg/mm^2 mass of *n*-hexatriacontane. Left images: a water droplet is placed on a surface in air. Middle images: an oil droplet is placed on a surface in air. Right images: an oil droplet is placed on a solid surface in water [20].

To study the surface structure of an aquatic animal, experiments with water and oil droplets on the shark skin replica were performed in a three phase interface [20]. Figure 18 shows the optical micrographs of droplets in three different phase interfaces on a shark skin replica without and with $C_{20}F_{42}$. First, the shark skin replica had contact angles of 89° and ~0° for water and oil droplets, respectively. After the surface was coated with $C_{20}F_{42}$, the contact angles of water and oil droplets became

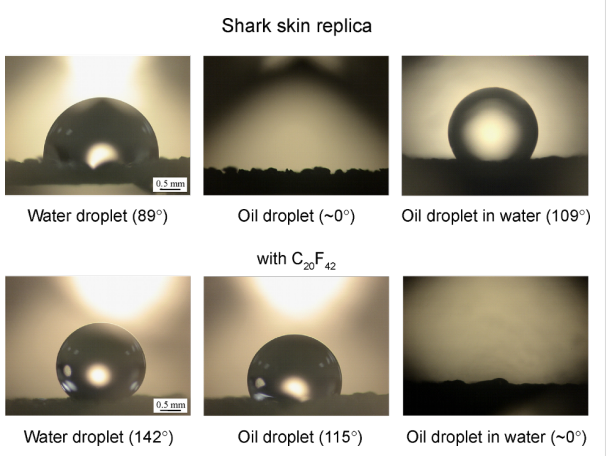

Figure 18: Optical micrographs of droplets in three different phase interfaces on shark skin replica without and with $C_{20}F_{42}$. Left images: a water droplet is placed on a surface in air. Middle images: an oil droplet is placed on a surface in air. Right images: an oil droplet is placed on a solid surface in water [20].

142° and 115°, respectively. In the solid–water–oil interface, the oil droplet in water on the shark skin replica became oleophobic and had a contact angle of 109°. Based on Equation 12, the calculated value was 59° for the oil droplet in water on a shark skin replica. This difference may arise from the open space under the scales of the shark skin replica responsible for the propensity of trapped water pocket formation as reported by Jung and Bhushan [21]. Shark skin replica with $C_{20}F_{42}$ was oleophilic and had a contact angle of ~0°. This state is the same as the micropatterned surfaces with $C_{20}F_{42}$ as shown in Figure 11 and Table 3.

Conclusion

Biomimetics allows one to mimic biology or nature and for engineers to develop materials and devices of commercial interest. Properties of biological materials and surfaces result from a complex interplay between surface morphology and physical and chemical properties. Hierarchical structures with dimensions of features ranging from the macroscale to the nanoscale are extremely common in nature and possess properties of interest. There are a large number of objects including bacteria, plants, land and aquatic animals and seashells, with properties of commercial interest.

One focus of this article is on biomimetics inspired structured surfaces for low fluid drag. One of the models from nature is the lotus leaf with a surface covered with wax and with hierarchical structure which provides superhydrophobicity, self cleaning, and low adhesion. An aquatic animal, such as a shark, is another model from nature. Shark skin is covered by very small individual tooth-like scales called dermal denticles (little skin teeth), ribbed with longitudinal grooves (aligned parallel to the local flow direction of the water). These grooved scales reduce vortices formation present on a smooth surface, resulting in water moving efficiently over their surface. The artificial surfaces inspired by the shark skin and the lotus leaf have been created and the influence of structure has been reviewed by measurement of pressure drop and fluid drag for drag reduction efficiency.

Oleophobic surfaces have the potential for self-cleaning and anti-fouling from biological and organic contaminants both in air and underwater applications. A model for predicting the contact angle of water and oil droplets has been reviewed. The surface tension of oil and organic liquids is lower than that of water, so to make the surface oleophobic in a solid–air–oil interface, a material with surface energy lower than that of oil should be used. The wetting behavior of water and oil droplets for hydrophobic/philic and oleophobic/philic surfaces in three phase interfaces is reviewed. For underwater applications, we have reviewed oleophobicity/philicity of an oil droplet in water on surfaces with different surface energies of various interfaces and contact angles of water and oil droplets in air.

This article provides a useful guide for the development of biomimetic artificial surfaces with either low drag or self-cleaning/anti-fouling properties.

References

1. Gordon, J. E. *The New Science of Strong Materials, or Why You Don't Fall Through the Floor,* 2nd ed.; Princeton University Press: Princeton, 1984.
2. Bhushan, B. *Philos. Trans. R. Soc. London, Ser. A* **2009,** *367,* 1445–1486. doi:10.1098/rsta.2009.0011
3. Bhushan, B. *Springer Handbook of Nanotechnology,* 3rd ed.; Springer: Heidelberg, Germany, 2010. doi:10.1007/978-3-642-02525-9
4. Barthlott, W.; Neinhuis, C. *Planta* **1997,** *202,* 1–8. doi:10.1007/s004250050096
5. Neinhuis, C.; Barthlott, W. *Ann. Bot. (Oxford, U. K.)* **1997,** *79,* 667–677. doi:10.1006/anbo.1997.0400
6. Wagner, P.; Furstner, R.; Barthlott, W.; Neinhuis, C. *J. Exp. Bot.* **2003,** *54,* 1295–1303. doi:10.1093/jxb/erg127
7. Burton, Z.; Bhushan, B. *Ultramicroscopy* **2006,** *106,* 709–719. doi:10.1016/j.ultramic.2005.10.007
8. Bhushan, B.; Jung, Y. C. *Nanotechnology* **2006,** *17,* 2758–2772. doi:10.1088/0957-4484/17/11/008
9. Bhushan, B.; Jung, Y. C. *Prog. Mater. Sci.* **2011,** *56,* 1–108. doi:10.1016/j.pmatsci.2010.04.003
10. Koch, K.; Bhushan, B.; Barthlott, W. *Soft Matter* **2008,** *4,* 1943–1963. doi:10.1039/b804854a
11. Koch, K.; Bhushan, B.; Barthlott, W. *Prog. Mater. Sci.* **2009,** *54,* 137–178. doi:10.1016/j.pmatsci.2008.07.003
12. Bhushan, B.; Jung, Y. C.; Koch, K. *Philos. Trans. R. Soc. London, Ser. A* **2009,** *367,* 1631–1672. doi:10.1098/rsta.2009.0014
13. Koch, K.; Bhushan, B.; Jung, Y. C.; Barthlott, W. *Soft Matter* **2009,** *5,* 1386–1393. doi:10.1039/b818940d
14. Bhushan, B.; Jung, Y. C. *J. Phys.: Condens. Matter* **2008,** *20,* 225010. doi:10.1088/0953-8984/20/22/225010
15. Nosonovsky, M.; Bhushan, B. *Multiscale Dissipative Mechanisms and Hierarchical Surfaces: Friction, Superhydrophobicity, and Biomimetics;* Springer: Heidelberg, Germany, 2008.
16. Bhushan, B.; Wang, Y.; Maali, A. *Langmuir* **2009,** *25,* 8117–8121. doi:10.1021/la900612s
17. Nosonovsky, M.; Bhushan, B. *Philos. Trans. R. Soc. London, Ser. A* **2009,** *367,* 1511–1539. doi:10.1098/rsta.2009.0008
18. Liu, M.; Wang, S.; Wei, Z.; Song, Y.; Jiang, L. *Adv. Mater.* **2009,** *21,* 665–669. doi:10.1002/adma.200801782
19. Bechert, D. W.; Bruse, M.; Hage, W. *Exp. Fluids* **2000,** *28,* 403–412. doi:10.1007/s003480050400
20. Jung, Y. C.; Bhushan, B. *Langmuir* **2009,** *25,* 14165–14173. doi:10.1021/la901906h
21. Jung, Y. C.; Bhushan, B. *J. Phys.: Condens. Matter* **2010,** *22,* 035104. doi:10.1088/0953-8984/22/3/035104
22. Dean, B.; Bhushan, B. *Philos. Trans. R. Soc. London, Ser. A* **2010,** *368,* 4775–4806. doi:10.1098/rsta.2010.0201
23. Genzer, J.; Efimenko, K. *Biofouling* **2006,** *22,* 339–360. doi:10.1080/08927010600980223

24. Nosonovsky, M.; Bhushan, B. *J. Adhes. Sci. Technol.* **2008,** *22,* 2105–2115.
25. Stokes, S. G. G. *Trans. Cambridge Philos. Soc.* **1851,** *9,* 8–106.
26. Batchelor, G. K. *An Introduction to Fluid Dynamics;* Cambridge University Press: Cambridge, U.K., 1967.
27. Goldstein, S. *Modern Development in Fluid Dynamics;* Clarendon: Oxford, 1938.
28. Goldstein, S. *Annu. Rev. Fluid Mech.* **1969,** *1,* 1–28. doi:10.1146/annurev.fl.01.010169.000245
29. Lauga, E.; Brenner, M. P.; Stone, H. A. Microfluidics: The No-Slip Boundary Condition. In *Handbook of Experimental Fluid Dynamics;* Tropea, C.; Yarin, A.; Foss, J. F., Eds.; Springer: New York, 2007; pp 1219–1240.
30. Neto, C.; Evans, D. R.; Bonaccurso, E.; Butt, H.-J.; Carig, V. S. J. *Rep. Prog. Phys.* **2005,** *68,* 2859–2897. doi:10.1088/0034-4885/68/12/R05
31. Maali, A.; Bhushan, B. *J. Phys.: Condens. Matter* **2008,** *20,* 315201. doi:10.1088/0953-8984/20/31/315201
32. Wang, Y.; Bhushan, B.; Maali, A. *J. Vac. Sci. Technol., A* **2009,** *27,* 754–760. doi:10.1116/1.3086637
33. Wang, Y.; Bhushan, B. *Soft Matter* **2010,** *6,* 29–66. doi:10.1039/b917017k
34. Baudry, J.; Charlaix, E.; Tonck, A.; Mazuyer, D. *Langmuir* **2001,** *17,* 5232–5236. doi:10.1021/la0009994
35. Zhu, Y.; Granick, S. *Phys. Rev. Lett.* **2002,** *88,* 106102. doi:10.1103/PhysRevLett.88.106102
36. Cottin-Bizonne, C.; Cross, B.; Steinberger, A.; Charlaix, E. *Phys. Rev. Lett.* **2005,** *94,* 056102. doi:10.1103/PhysRevLett.94.056102
37. Vinogradova, O. I.; Yakubov, G. E. *Langmuir* **2003,** *19,* 1227–1234. doi:10.1021/la026419f
38. Tretheway, D. C.; Meinhart, C. D. *Phys. Fluids* **2002,** *14,* L9–L12. doi:10.1063/1.1432696
39. Honig, C. D. F.; Ducker, W. A. *Phys. Rev. Lett.* **2007,** *98,* 028305. doi:10.1103/PhysRevLett.98.028305
40. Maali, A.; Wang, Y.; Bhushan, B. *Langmuir* **2009,** *25,* 12002–12005. doi:10.1021/la902934j
41. Watts, E. T.; Krim, J.; Widom, A. *Phys. Rev. B* **1990,** *41,* 3466–3472. doi:10.1103/PhysRevB.41.3466
42. Lauga, E.; Stone, H. A. J. *Fluid Mech.* **2003,** *489,* 55–77. doi:10.1017/S0022112003004695
43. Cottin-Bizonne, C.; Barentin, C.; Charlaix, E.; Bocquet, L.; Barrat, J. L. *Eur. Phys. J. E* **2004,** *15,* 427–438. doi:10.1140/epje/i2004-10061-9
44. Sbragaglia, M.; Prosperetti, A. J. *Fluid Mech.* **2007,** *578,* 435–451. doi:10.1017/S0022112007005149
45. Ou, J.; Perot, B.; Rothstein, J. P. *Phys. Fluids* **2004,** *16,* 4635–4643. doi:10.1063/1.1812011
46. Choi, C.-H.; Kim, C.-J. *Phys. Rev. Lett.* **2006,** *96,* 066001. doi:10.1103/PhysRevLett.96.066001
47. Joseph, P.; Cottin-Bizonne, C.; Benoit, J. M.; Ybert, C.; Journet, C.; Tabeling, P.; Bocquet, L. *Phys. Rev. Lett.* **2006,** *97,* 156104. doi:10.1103/PhysRevLett.97.156104
48. Shibuichi, S.; Yamamoto, T.; Onda, T.; Tsujii, K. *J. Colloid Interface Sci.* **1998,** *208,* 287–294. doi:10.1006/jcis.1998.5813
49. Li, H.; Wang, X.; Song, Y.; Liu, Y.; Li, Q.; Jiang, L.; Zhu, D. *Angew. Chem., Int. Ed.* **2001,** *40,* 1743–1746. doi:10.1002/1521-3773(20010504)40:9<1743::AID-ANIE17430>3.0.CO;2-#
50. Kiuru, M.; Alakoski, E. *Mater. Lett.* **2004,** *58,* 2213–2216. doi:10.1016/j.matlet.2004.01.024
51. Xie, Q.; Xu, J.; Feng, L.; Jiang, L.; Tang, W.; Luo, X.; Han, C. C. *Adv. Mater.* **2004,** *16,* 302–305. doi:10.1002/adma.200306281
52. Nicolas, M.; Guittard, F.; Geribaldi, S. *Angew. Chem., Int. Ed.* **2006,** *45,* 2251–2254. doi:10.1002/anie.200503892
53. Hoefnagels, H. F.; Wu, D.; de With, G.; Ming, W. *Langmuir* **2007,** *23,* 13158–13163. doi:10.1021/la702174x
54. Tuteja, A.; Choi, W.; Ma, M.; Mabry, J. M.; Mazzella, S. A.; Rutledge, G. C.; McKinley, G. H.; Cohen, R. E. *Science* **2007,** *318,* 1618–1622. doi:10.1126/science.1148326
55. Blevins, R. D. *Applied Fluid Dynamics Handbook;* Van Nostrand Reinhold: New York, 1984.
56. Jones, O. C. J. *Fluids Eng.* **1976,** *98,* 173–180. doi:10.1115/1.3448250
57. Bechert, D. W.; Bruse, M.; Hage, W.; van der Hoeven, J. G. T.; Hoppe, G. *J. Fluid Mech.* **1997,** *338,* 59–87. doi:10.1017/S0022112096004673
58. Lide, D. R. *CRC Handbook of Chemistry and Physics,* 89th ed.; CRC Press: Boca Raton, FL, 2009.
59. Zhu, Y.; Granick, S. *Phys. Rev. Lett.* **2001,** *87,* 096105. doi:10.1103/PhysRevLett.87.096105
60. Bertin, J. J.; Smith, M. L. *Aerodynamics for Engineers;* Prentice Hall: New Jersey, 1979.
61. Adamson, A. W. *Physical Chemistry of Surfaces;* Wiley: New York, 1990.
62. Israelachvili, J. N. *Intermolecular and Surface Forces,* 2nd ed.; Academic Press: London, U.K., 1992.
63. Bhushan, B. *Principles and Applications of Tribology;* Wiley: New York, 1999.
64. Tajima, K.; Tsutsui, T.; Murata, H. *Bull. Chem. Soc. Jpn.* **1980,** *53,* 1165–1166. doi:10.1246/bcsj.53.1165
65. Nishino, T.; Meguro, M.; Nakamae, K.; Matsushita, M.; Ueda, Y. *Langmuir* **1999,** *15,* 4321–4323. doi:10.1021/la981727s
66. Bunshah, R. F., Ed. *Handbook of Deposition Technologies for Films and Coatings: Science, Technology and Applications;* Applied Science Publishers: Westwood, New Jersey, 1994.
67. Bhushan, B.; Koch, K.; Jung, Y. C. *Soft Matter* **2008,** *4,* 1799–1804. doi:10.1039/b808146h
68. Wu, S. *J. Colloid Interface Sci.* **1979,** *71,* 605–609. doi:10.1016/0021-9797(79)90332-1

License and Terms

Beilstein Journal of Nanotechnology

Superhydrophobic surfaces of the water bug *Notonecta glauca*: a model for friction reduction and air retention

Petra Ditsche-Kuru[*1,2], Erik S. Schneider[1], Jan-Erik Melskotte[3], Martin Brede[3], Alfred Leder[3] and Wilhelm Barthlott[*1]

Full Research Paper

Open Access

Address:
[1]Nees Institute for Biodiversity of Plants, Rheinische Friedrich-Wilhelms University of Bonn, Meckenheimer Allee 170, Bonn, 53115, Germany, [2]Department of Zoology: Functional Morphology and Biomechanics, Christian-Albrechts-University of Kiel, Am Botanischen Garten 1–9, Kiel, 24098, Germany and [3]Lehrstuhl Strömungsmechanik, Universität Rostock, Albert Einstein Str. 2, Rostock, 18051, Germany

Email:
Petra Ditsche-Kuru[*] - pditschekuru@zoologie.uni-kiel.de; Erik S. Schneider - eschneid@uni-bonn.de; Jan-Erik Melskotte - jan-erik.melskotte2@uni-rostock.de; Martin Brede - martin.brede@uni-rostock.de; Alfred Leder - alfred.leder@uni-rostock.de; Wilhelm Barthlott[*] - lotus@uni-bonn.de

* Corresponding author

Keywords:
air film; aquatic insects; backswimmer; drag reduction; superhydrophobic surfaces

Beilstein J. Nanotechnol. **2011,** *2,* 137–144.
doi:10.3762/bjnano.2.17

Received: 07 January 2011
Accepted: 01 March 2011
Published: 10 March 2011

This article is part of the Thematic Series "Biomimetic materials".

Guest Editors: W. Barthlott and K. Koch

Abstract

Superhydrophobic surfaces of plants and animals are of great interest for biomimetic applications. Whereas the self-cleaning properties of superhydrophobic surfaces have been extensively investigated, their ability to retain an air film while submerged under water has not, in the past, received much attention. Nevertheless, air retaining surfaces are of great economic and ecological interest because an air film can reduce friction of solid bodies sliding through the water. This opens perspectives for biomimetic applications such as low friction fluid transport or friction reduction on ship hulls. For such applications the durability of the air film is most important. While the air film on most superhydrophobic surfaces usually lasts no longer than a few days, a few semi-aquatic plants and insects are able to hold an air film over a longer time period. Currently, we found high air film persistence under hydrostatic conditions for the elytra of the backswimmer *Notonecta glauca* which we therefore have chosen for further investigations. In this study, we compare the micro- and nanostructure of selected body parts (sternites, upper side of elytra, underside of elytra) in reference to their air retaining properties. Our investigations demonstrate outstanding air film persistence of the upper side

of the elytra of *Notonecta glauca* under hydrostatic and hydrodynamic conditions. This hierarchically structured surface was able to hold a complete air film under hydrostatic conditions for longer than 130 days while on other body parts with simple structures the air film showed gaps (underside of elytra) or even vanished completely after a few days (sternites). Moreover, the upper side of the elytra was able to keep an air film up to flow velocities of 5 m/s. Obviously the complex surface structure with tiny dense microtrichia and two types of larger specially shaped setae is relevant for this outstanding ability. Besides high air film persistence, the observation of a considerable fluid velocity directly at the air–water interface indicates the ability to reduce friction significantly. The combination of these two abilities makes these hierarchically structured surfaces extremely interesting as a biomimetic model for low friction fluid transport or drag reduction on ship hulls.

Introduction

Superhydrophobic surfaces are of great economic interest because of their amazing properties. In nature they occur in many species of animals and plants [1,2]. These surfaces combine a special topography at the micro- and nanoscale with a superhydrophobic surface chemistry [3,4]. Transferred to technical surfaces, superhydrophobic surfaces have successfully entered the markets of the world [5,6]. The effective self-cleaning mechanism of the Lotus flower *Nelumbo nucifera* is especially well known [3]. Granting of a patent in 1998 [7], followed by the introduction of the trade mark Lotus-Effect® was the start of the realisation of biomimetic self-cleaning surfaces. Another highly interesting property of superhydrophobic surfaces, which did not receive so much attention in the past, is the ability to retain an air film while submerged under water. This air film cover can reduce drag of solid bodies sliding through water [8,9]. Therefore, air retaining surfaces are of great economic and ecological interest for low friction fluid transport and friction reduction on ship hulls [10-12]. On some technical superhydrophobic surfaces extremely high drag reduction of up to 50% was measured, but on these surfaces the air film lasted only a short time [13-15].

Biological air retaining superhydrophobic surfaces in the past were primarily examined in the context of their respiratory function [16-21], while some recent publications deal more with their functional morphology and their suitability for technical application [11,22-24]. For biomimetic applications of air retaining surfaces for low friction fluid transport and drag reduction on ship hulls, the durability of the air film is most important. While on many superhydrophobic surfaces the air film usually lasts no longer than a few days, some semi-aquatic plants and insects are able to hold an air film for a longer time period [19,24,25]. Very high air film persistence was observed on the water bug *Notonecta glauca* under hydrostatic conditions on their elytra [24]. Based on this comparative study about the correlation of surface morphology and air film persistence on different semi-aquatic insects, we chose *Notonecta glauca* as the model organism for further investigations on air film persistence and drag reduction. The backswimmer *Notonecta glauca* is surrounded by a thin film of air covering most body parts and causing a silvery sheen (Figure 1).

Figure 1: Lateral view on the water bug *Notonecta glauca*.

Notonecta spp. can dive and swim quickly through water, but most of the time it supports itself from underneath against the water surface with both pairs of fore legs and the tip of the abdomen [26]. The surface of the elytra is covered by a hierarchical structure of larger setae and very small microtrichia. Balmert et al. hypothesized that the dense microtrichia cover is relevant for the high air film persistence of the elytra measured under hydrostatic conditions [24]. In the present study we will prove this assumption by comparing the different structures on the body parts of *Notonecta*. Moreover, we measure the persistence of the air film of the elytra under hydrodynamic conditions and its effect on friction drag. By carrying out scanning electron microscopy, particle image velocimetry and air film persistence tests, we will answer the following questions: (1) Do the air retaining surface structures vary on the different body parts? (2) Is there a correlation between surface structure and air film persistence? (3) How is it possible to hold the air film under hydrodynamic conditions? (4) How much is the friction on the elytron surface reduced?

Results and Discussion

Characteristics of air retaining surfaces

Notonecta glauca is covered with hairy structures over almost all its body with exception of head, pronotum and legs. The body parts show a large variety of surface structures, but in general two types of surface protuberances occur: Large and sparse setae as well as small and dense microtrichia. Setae have a socket originating from an adjacent cell and are classified as true hairs, while microtrichia originating from one cell and are, by definition, not really hairs [27,28]. Three different body parts of *Notonecta glauca* with different surface structures were selected for further investigations; a pure setae structure, a pure microtrichia structure and a hierarchical structure with setae and microtrichia (Figure 2). On the abdominal sternites a pure setae structure can be observed. About 2,300 setae per mm^2 cover the surface up to a height of approximately 30 µm. The basis of these setae points in the caudal direction while the tips are bent in the distal direction (Figure 2B). These surfaces are inside of the area of the air pockets on the abdomen.

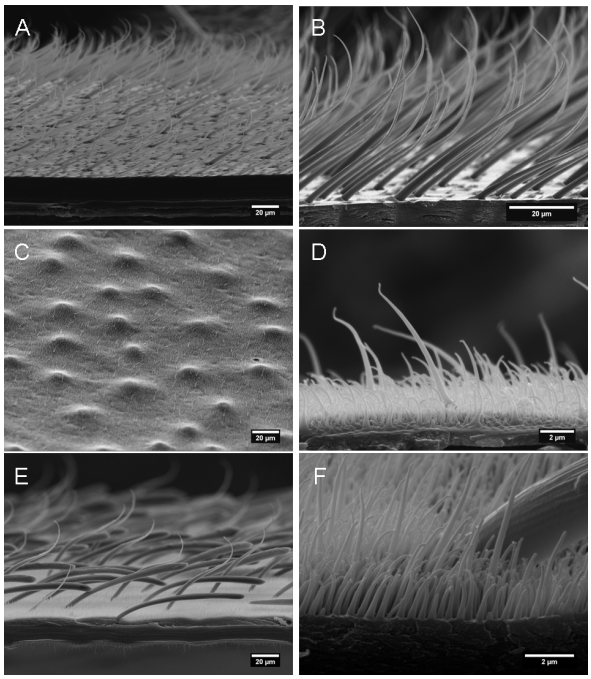

Figure 2: Selected air retaining body parts of *Notonecta glauca*: A,B) setae on the abdominal sternites; C,D) underside of the elytra with a dense cover of microtrichia; E,F) upper side of elytra with a hierarchical double structure of microtrichia and setae. Two different types of setae occur. In all pictures the caudal direction of the insect is on the right side.

In contrast, the underside of the elytra is covered only with microtrichia. These tiny protuberances of an average height of 1.2 µm show a large variation in height (Figure 2D) and reach a density of approximately 5.8×10^6 mm^{-2}. The underside of the elytra is only able to hold a very small volume of air due to their minor height. The little air film, however, might primarily help to keep the wings dry.

The upper side of the elytra is hierarchically structured by larger setae and tiny microtrichia (Figure 2E and Figure 2F). The microtrichia cover shows a similar density (6.0×10^6 mm^{-2} on average) as the underside of the elytra, but the height is somewhat larger (2.3 µm). On these surfaces two different types of setae occur. The first seta-type (ST 1) is tapered and bent while the tips point more or less in the anterio–distal direction. In contrast, the second seta-type (ST 2) is clubbed and points in the posterior direction. The combined density of both setae-types is approximately 250 mm^{-2}. The air film on the upper side of the elytra might help to keep the wings dry and save air for respiration, but friction reduction might also be an additional advantage for the backswimmer while hunting. An overview of the structural parameters of the investigated surfaces is given in Table 1.

Table 1: Structural parameters of the investigated body parts of *Notonecta glauca* (mean ± 95% confidence interval, N = 6).

	sternites	elytra (underside)	elytra (upper side)		
			ST 1 (pins)	ST 2 (clubs)	total
setae					
height [µm]	30 ± 3	—	60 ± 15	17 ± 5	39 ± 7
length [µm]	51 ± 6	—	85 ± 4	95 ± 5	90 ± 4
density [mm^{-2}]	2,332 ± 359	—	90 ± 14	163 ± 30	253 ± 18
diameter [µm]	2.3 ± 0.2	—	3.1 ± 0.2	3.4 ± 0.2	3.3 ± 0.1
microtrichia					
height [µm]	—	1.2 ± 0,2	—	—	2.3 ± 0,8
density [mm^{-2}]	—	$(5.8 \pm 0.3) \times 10^6$	—	—	$(5.9 \pm 0.2) \times 10^6$
diameter [µm]	—	0.32 ± 0.05	—	—	0.38 ± 0.05

All investigated surfaces are more or less superhydrophobic (Table 2). Contact angles ranged between 154° and 158°. The tilting angles were less than 5° on the sternites (not measurable) and the underside of the elytra. On the upper side of the elytra the tilting angle was higher (15°), which might be explained by the distant shape of the first seta-type (ST 1). However, in all cases a Cassie–Baxter regime [29] can be assumed so that the applied drop rests on an air layer in between the cover of surface protuberances. These hydrophobic structures enable the animal to trap an air film between the bottom surface and the tips of the surface protuberances.

Table 2: Contact and tilting angle of the investigated body parts of *Notonecta glauca* (mean ± 95% confidence interval, N = 10).

body part	contact angle [°]	tilting angle [°]
elytra (upper side)	154.2 ± 1.6	15.0 ± 4.3
elytra (underside)	155.3 ± 4.9	<5
sternites	157.5 ± 32	<5

Air film persistence under hydrostatic conditions

Submerged in an aquarium with freshwater, the three described surface structures showed large differences in air film persistence. Experiments were performed with natural surfaces as well as with an additional superhydrophobic coating ("Antispread") on the original surfaces in order to exclude an influence of a possibly different surface chemistry. The results show similar air film persistence on untreated and treated surfaces (Table 3). Consequently, the surface structure can be identified as the relevant feature.

The air covering the surfaces can be identified by its silvery sheen [30-32]. On both sides of the elytra the air film remained for months, whereas it vanished after 1–2 days on the pure setae

Table 3: Air film persistence of the submerged body parts of *Notonecta glauca* (N = 10).

body part	untreated surface [d]	surfaces treated with "Antispread" [d]
elytra (upper side)	>130	>130
elytra (underside)	>130	>130
sternites	<2	<1

structures of the sternites (Table 3, Figure 2). On the upper and underside of the elytra air was still present after 130 days. This time span is much longer than that reported for *Salvinia* species, which are able to hold air for only weeks. Nevertheless, the quality of the air film was not the same on both surfaces of the elytra. After 130 days, the upper side of the elytra was still covered with air, almost totally. In contrast, the underside of the elytra was no longer completely covered with air (Figure 3 and Figure 4). In the latter, little gaps in the air film cover were identified after a few days or a week, which increased with time.

The different air retaining abilities of the investigated body parts of the backswimmer indicate an optimization for different functions. The short air film persistence of the pure setae structure (about 2 d) corresponds with the air retaining properties described for more or less similar structures on the abdominal sternites of other water bugs (*Ilyocoris*, *Corixa*) [24]. These surfaces might be optimized to hold additional air for respiration. The volume of the air might be more relevant than long term stability of the air film because the air store in this area is frequently renewed.

The underside of the elytra with a dense but pure microtrichia cover showed high air film persistence. This observation underlines the high relevance of the dense cover of surface protuberances previously assumed by Crisp in 1949 and proved by

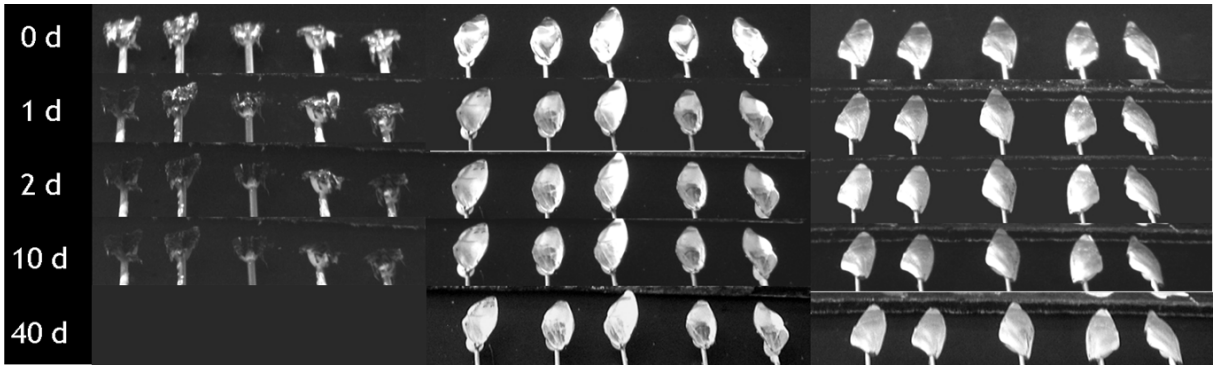

Figure 3: Submerged body parts of *Notonecta glauca* in the course of time. All surfaces were treated with a hydrophobic coating. Left side: sternites; middle: underside of elytra; right side: upper side of elytra.

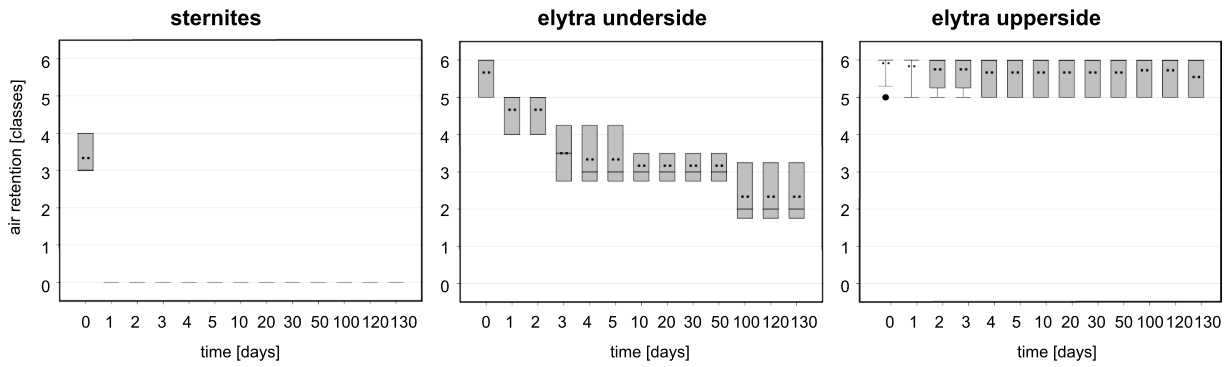

Figure 4: Air retention [classes] of the submerged surfaces of *Notonecta glauca* vs time. All surfaces were treated with a hydrophobic coating. Air retention classes define the air retaining portion (X) of the surface, with 0: X = 0%; 1: 0% < X < 20%; 2: 20% ≤ X < 40%; 3: 40% ≤ X < 60%; 4: 60% ≤ X < 80%; 5: 80% ≤ X < 100%; 6: X = 100%.

Balmert [24,33]. The wetting of the microtrichia cover will require a significant amount of energy due to the density of the structures. A dense cover of surface protuberances leads to a smaller radius of curvature of the air–water interface between the structures: More energy is necessary to displace an interface with a smaller radius [19,24]. Furthermore, the variable height of microtrichia leads to an increased density of microtrichia with decreasing distance to the body surface. Also the decreased air–water interface itself leads to a higher resistance against water pressure according to the model of Crisp and Thorpe [17]. The tiny, but stable, air film on the underside of the elytra seems to be more relevant to keep the wings dry rather than playing a role in the storage of air required for respiration.

Nevertheless, our results show that the quality of the air film was not the same as for the upper side of the elytra. Therefore, it can be hypothesized that the presence of setae in addition to the microtrichia cover not only contributes to the storage of a higher volume of air, but also stabilizes the air film itself by a kind of two barrier system. Also the reduced height of the microtrichia on the underside (1.2 µm) in comparison to the upper side of the elytra (2.3 µm) might contribute to the reduced air film persistence. In contrast to the underside of elytra in the living animal, the upper side stays in direct contact with the water. It therefore may have developed further adaptations to stabilize the air film. Obviously, the hierarchical double structure of the upper side of the elytra with a dense microtrichia cover and two different kinds of setae is most advantageous for long term air film persistence. Both types of setae are more or less tilted in the posterior direction at their bases. Therefore, a directional choice is forced when the setae are bent and a more stable air film can be expected according to Blow and Yeomans in comparison to setae bent in different directions [34].

Air film persistence under hydrodynamic conditions

Due to their outstanding properties in air film persistence under hydrostatic conditions, the upper side of the elytra was chosen for hydrodynamic experiments. Impressively the upper side of the elytron was able to hold an air film up to a fluid velocity of 5 m/s (Figure 5).

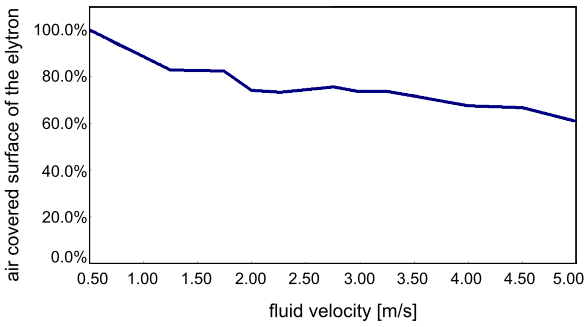

Figure 5: Air covered surface on the upper side of the elytron at increasing inflow velocity.

The experiment started at low flow velocities of 0.5 m/s where no wetting was visible. At increasing flow velocities the fraction of the surface on the elytron covered with air decreased slightly (80% at 1.5 m/s). It is remarkable that at inflow velocities between 1.5 m/s and 3.5 m/s the fraction of air covered surface is reduced only marginally by 10% (70% at 3.5 m/s). Even at high flow velocities of 5.0 m/s, 61% of the surface initially covered with air is still intact. In comparison, the water fern *Salvinia molesta,* which is another model organism for air retention, had about 60% of the initial area covered with air at a flow velocity of 2.25 m/s [35]. Obviously, the surface structure of the upper side of the elytra of the backswimmer is optimally adapted to hold an air film under hydrodynamic conditions.

Beneath the dense microtrichia cover the special shape of the two different seta-types seems to contribute to this remarkable property. The angular positioning of the setae in the direction of flow leads to an increased contact area between setae and water when the setae are bent by increased pressure due to pressure fluctuation. Therefore, a similar mechanism as described for the eggbeater shaped structures of *Salvinia molesta* [12] occurs. The penetration of the water requires energy for creating the larger contact area between the hydrophobic setae and water. The bending of the setae might also enable a flexible adaptation of the air water interface to the oscillation of the water flow. On the elytron surface, moreover, the microtrichia cover is present as an additional effective backup-system, if water is pressed close to the body surface between the setae.

Velocity field above the elytron surface under hydrodynamic conditions

Next to the persistence of the air film at the surface, the quantification of the velocity field and the friction reduction at the water–air interface are most important. The velocity field above the elytron surface was investigated by means of particle image velocimetry (PIV), which is a contactless method to measure the velocity field in fluids by analysing the particle movement. The measurement of the flow on the elytron surface were performed at a flow velocity of 0.5 m/s parallel to the surface. To represent the mean flow field above the elytron surface, the average of the velocity vector measurements using PIV is presented in Figure 6. For a better survey only every second velocity vector in the vertical and horizontal directions is plotted. Along the red line velocity vectors were selected to assemble a profile perpendicular to the surface. The resulting profile is depicted in Figure 7, the values being normalized with the mean velocity of the oncoming flow. The profile shows that the flow velocity in the vicinity of the surface differs significantly from zero due to the air retained on the surface. Since wall bonding is not possible at the water–air interface, slippage can be observed.

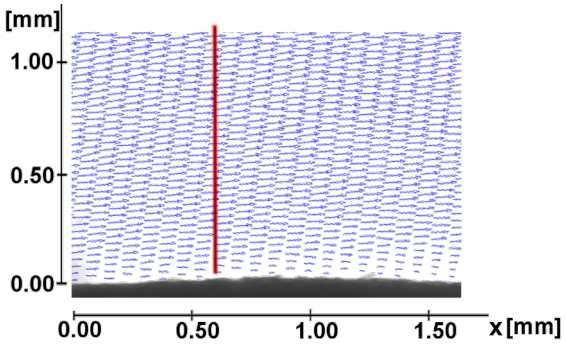

Figure 6: Averaged velocity field over the elytron surface (upper side).

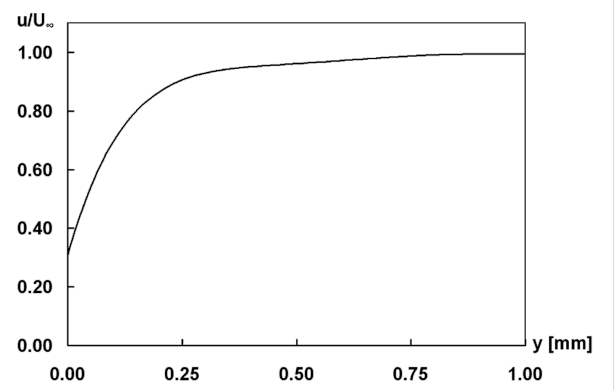

Figure 7: Velocity component u parallel to the elytron surface recorded along path in Figure 6.

The velocity measurements indicate that the fluid moves over the interface at nearly one third of the inflow velocity. Hence, it can be assumed, that a considerable friction reduction is present. Next to the effect of the air film itself on friction reduction, we assume that the special shape of the setae on the upper side of the elytra might contribute to this property.

Conclusion

Our investigations showed outstanding air film persistence under hydrostatic and hydrodynamic conditions of the upper side of the elytra of *Notonecta glauca*. Moreover, a considerable reduction of the friction on the elytron surface was measured. The combination of these two abilities makes these hierarchically structured surfaces extremely interesting for biomimetic applications such as low friction fluid transport or drag reduction on ship hulls.

Experimental

Animals. Freshly killed insects were dissected and the air retaining surfaces were processed immediately after taxidermy.

Scanning electron microscopy. Isolated body parts were glued on insect pins, sputter-coated with 20 nm gold on the upper and underside (Balzers Union SCD 040 Sputter-Coater, Baltec AG, Liechtenstein) and screwed to a custom made holder [25,36], which allowed the examination of all sides. The specimens were examined with a Cambridge Stereoscan 200 scanning electron microscope (SEM) (Cambridge Instruments Ltd., Cambridge, UK) using a tungsten cathode and accelerating voltages between 5 and 15 kV. To determine structural surface parameters, SEM images of 10 areas of each of the 6 investigated individuals were analysed with the digital image processing software ImageJ.

Contact angle (CA) measurements. To characterise the wetting behaviour of the biological surfaces, contact (CA) and tilting

angle (TA) measurements were performed with a DataPhysics Contact Angle System OCA, TBU 90 E (DataPhysics GmbH, Filderstadt, Germany), which was operated by the software SCR 20 (DataPhysics). CA measurements were performed with the "needle-in-drop" method by application of 5 µL droplets of pure water. CA and TA were measured for ten drops to each of ten individuals.

Measurement of air film persistence under hydrostatic conditions. For this experiment, three different body parts of *Notonecta glauca* with different surface structures were selected. Ten samples of each surface were fixed on insect pins glued onto thin plates of polyvinyl chloride by a water resistant two-component adhesive (Pattex Powerkleber Kraft Mix Extrem Schnell, Henkel AG & Co. KGaA, Düsseldorf, Germany). Specimens were submerged in an aquarium filled with pure water to a depth of 15 cm at room temperature. Air film persistence was detected optically by light reflection at the air–water interface. Digital images of the submerged specimens were recorded using a Canon Power Shot SX110IS digital camera (Canon Inc., Japan).

To compare the air film persistence of the three investigated surfaces with regard to the different surface structures, we covered them with a uniform hydrophobic surface coating. For that purpose the surfaces were dipped in Antispread (F2/200 Fluorcarbon 60, Horb-Ahldorf, Germany) for 10 s which forms approximately 40 nm thin layers on the substrate surfaces (product information). After drying for 30 minutes, the hydrophobized specimens were treated like the native surfaces as described above.

Measurement of the velocity field above the surface and air film persistence under hydrodynamic conditions. Experiments under hydrodynamic conditions were performed for the upper side of the elytra by particle image velocimetry. Neutrally buoyant particles were added to the flow and then digital images were recorded in selected planes [37]. For macroscopic setups, the location of the plane was defined by illuminating the particles with a thin laser-light sheet whereas for microscopic experiments the plane was selected by the depth of focus in a completely illuminated volume [38].

The experiment was performed in a closed circuit water channel with a cross-section of 15 × 30 mm^2. A single elytron of *Notonecta* was fixed to an exchangeable retainer which was placed inside the channel using a streamlined base plate on a wall mounted post (Plastik Fermit weiß, Fermit). For the observation of the flow, a microscope with a Leica lens (planapo 2.0) was used resulting in an observation area orthogonal to the elytron surface of 2.6 × 1.4 mm^2. Within the focal plane of the lens, the particle images could then be observed. Double-frame image pairs were generated by a HiSense PIV camera (Dantec Dynamics, Copenhagen, Denmark) while the flow-field was completely illuminated by a pulsed 5 W LED. The in-plane velocity vector components were then calculated using an average correlation scheme with an interrogation area size of 64 × 32 pixels and an overlap of 50%. Finally, the velocity profiles of the flow along a path perpendicular to the air retaining surface were evaluated.

In addition to the analysis of the velocity field the persistence of the air film under dynamic conditions was determined. To quantify the air film coverage on the elytron, images of the surface of the elytron were taken with a digital SLR camera (Nikon D80, Japan) at different flow velocities in the channel. Additional illumination was achieved by a Cold-light source KL 1500 LCD (Zeiss, Germany). The dimension of the air film on the surface was subsequently derived from the images using the area of total light reflection on the elytron.

Acknowledgements

We are grateful to the German Federal Ministry of Education and Research (BMBF) and the German Research Foundation (DFG) for the financial support of the work. Moreover, we thank Thomas Schimmel and Stefan Walheim for inspiring discussions during the course of the whole topic.

References

1. Wagner, T.; Neinhuis, C.; Barthlott, W. *Acta Zoologica (Stockholm)* **1996,** *77,* 213–225. doi:10.1111/j.1463-6395.1996.tb01265.x
2. Neinhuis, C.; Barthlott, W. *Ann. Bot. (Oxford, U. K.)* **1997,** *79,* 667–677. doi:10.1006/anbo.1997.0400
3. Barthlott, W.; Neinhuis, C. *Planta* **1997,** *202,* 1–8. doi:10.1007/s004250050096
4. Callies, M.; Quéré, D. *Soft Matter* **2005,** *1,* 55–61. doi:10.1039/b501657f
5. Koch, K.; Bhushan, B.; Barthlott, W. *Soft Matter* **2008,** *4,* 1943–1963. doi:10.1039/b804854a
6. Roach, P.; Shirtcliffe, N. J.; Newton, M. I. *Soft Matter* **2008,** *4,* 224–240. doi:10.1039/b712575p
7. Barthlott, W. Self-cleaning surfaces of objects and process for producing same. European Patent EP 0772514 B1, Dec 23, 1998.
8. McHale, G.; Shirtcliffe, N. J.; Evans, C. R.; Newton, M. I. *Appl. Phys. Lett.* **2009,** *94,* 0641041. doi:10.1063/1.3081420
9. McHale, G.; Newton, M. I.; Shirtcliffe, N. J. *Soft Matter* **2010,** *6,* 714–719. doi:10.1039/b917861a
10. Corbett, J. J.; Koehler, H. W. *J. Geophys. Res.* **2003,** *108,* 4650. doi:10.1029/2003JD003751
11. Eyring, V.; Köhler, H. W.; van Aardenne, J.; Lauer, A. *J. Geophys. Res.* **2005,** *110,* D17305. doi:10.1029/2004JD005619
12. Barthlott, W.; Schimmel, T.; Wiersch, S.; Koch, K.; Brede, M.; Barczewski, M.; Walheim, S.; Weis, A.; Kaltenmaier, A.; Leder, A.; Bohn, H. F. *Adv. Mater.* **2010,** *22,* 2325–2328. doi:10.1002/adma.200904411

13. Balasubramanian, A. K.; Miller, A. C.; Rediniotis, O. K. *AIAA J.* **2004,** *42,* 411–414. doi:10.2514/1.9104
14. Jung, Y. C.; Bhushan, B. *J. Phys.: Condens. Matter* **2010,** *22,* 035104. doi:10.1088/0953-8984/22/3/035104
15. Lee, C.; Kim, C. J. *Langmuir* **2009,** *25,* 12812–12818. doi:10.1021/la901824d
16. Ege, R. Z. *Allg. Physiol.* **1915,** *17,* 81–124.
17. Thorpe, W. H.; Crisp, D. J. J. *Exp. Biol.* **1947,** *24,* 227–269.
18. Thorpe, W. H. *Biol. Rev. Cambridge Philos. Soc.* **1950,** *25,* 344–390. doi:10.1111/j.1469-185X.1950.tb01590.x
19. Heckman, C. W. *Int. Rev. Gesamten Hydrobiol.* **1983,** *68,* 715–736. doi:10.1002/iroh.3510680515
20. Chapman, R. F. *The insects: structure and function,* 4th ed.; Cambridge University Press: Cambridge, 1998.
21. Merritt, R. W.; Cummins, K. W., Eds. *An introduction to the aquatic insects of North America,* 3rd ed.; Kendall Hunt: Dubuque, Iowa, 1996.
22. Perez Goodwyn, P.; De Souza, E.; Fujisaki, K.; Gorb, S. *Acta Biomater.* **2008,** *4,* 766–770. doi:10.1016/j.actbio.2008.01.002
23. Perez Goodwyn, P. Anti-wetting surfaces in Heteroptera (insecta): hairy solutions to any problem. In *Functional Surfaces in Biology: little structures with big effects;* Gorb, S. N., Ed.; Springer: Dordrecht, 2009; Vol. 1, pp 55–76.
24. Balmert, A.; Bohn, H. F.; Ditsche-Kuru, P.; Barthlott, W. *J. Morphol.*, in press. doi:10.1002/jmor.10921
25. Cerman, Z.; Striffler, B. F.; Barthlott, W. Dry in the water: the superhydrophobic water fern *Salvinia* - a model for biomimetic surfaces. In *Functional Surfaces in Biology: little structures with big effects;* Gorb, S. N., Ed.; Springer: Dordrecht, 2009; Vol. 1, pp 97–111.
26. Wichard, W.; Arens, W.; Eisenbeis, G. *Biological Atlas of Aquatic Insects;* Apollo Books: Stenstrup, Denmark, 2002.
27. Richards, A. G.; Richards, P. A. *Int. J. Insect Morphol. Embryol.* **1979,** *8,* 143–157. doi:10.1016/0020-7322(79)90013-8
28. Gorb, S. N. J. *Morphol.* **1997,** *234,* 1–10. doi:10.1002/(SICI)1097-4687(199710)234:1<1::AID-JMOR1>3.0.CO;2-I
29. Cassie, A. B. D.; Baxter, S. *Trans. Faraday Soc.* **1944,** *40,* 546–551. doi:10.1039/tf9444000546
30. Johnson, R. E., Jr.; Dettre, R. H. Contact Angle Hysteresis. Study of an Idealized Rough Surface. In *Contact Angle, Wettability, and Adhesion;* Fowkes, F. M., Ed.; Advances in Chemistry, Vol. 43; American Chemical Society: Washington, 1964; pp 112–135. doi:10.1021/ba-1964-0043.ch007
31. Herminghaus, S. *EPL* **2000,** *52,* 165. doi:10.1209/epl/i2000-00418-8
32. Marmur, A. *Langmuir* **2006,** *22,* 1400–1402. doi:10.1021/la052802j
33. Crisp, D. J. *Trans. Faraday Soc.* **1949,** *46,* 228–235. doi:10.1039/tf9504600228
34. Blow, M. L.; Yeomans, J. M. *Langmuir* **2010,** *26,* 16071–16083. doi:10.1021/la101847b
35. Ditsche-Kuru, P.; Mayser, M.; Schneider, E.; Bohn, H.; Koch, K.; Melskotte, J.-E.; Brede, M.; Leder, A.; Barczewski, M.; Weiß, A.; Kaltenmeier, A.; Walheim, S.; Schimmel, T.; Barthlott, W. Eine Lufthülle für Schiffe – Können Schwimmfarn und Rückenschwimmer helfen Sprit zu sparen?. In *Bionik: Patente aus der Natur, Tagungsbeiträge des 5. Bionik-Kongresses der Hochschule Bremen;* Kesel, A. B.; Zehren, D., Eds.; Hochschule Bremen: Bremen, 2010; pp 159–165.
36. Ditsche-Kuru, P.; Koop, J. H. E. *Aquatic Insects* **2009,** *31* (Suppl. S1), 495–506. doi:10.1080/01650420903106731
37. Adrian, R. J. *Annu. Rev. Fluid Mech.* **1991,** *23,* 261–304. doi:10.1146/annurev.fl.23.010191.001401
38. Nguyen, N.-T.; Wereley, S. T. *Fundamentals and Applications of Microfluidics,* 2nd ed.; Artec House: Boston, 2002.

License and Terms

The definitive version of this article is the electronic one which can be found at: doi:10.3762/bjnano.2.17

Beilstein Journal of Nanotechnology

Capillary origami: superhydrophobic ribbon surfaces and liquid marbles

Glen McHale*§, Michael I. Newton, Neil J. Shirtcliffe and Nicasio R. Geraldi

Full Research Paper

Open Access

Address:
School of Science and Technology, Nottingham Trent University, Clifton Lane, Nottingham NG11 8NS, UK

Email:
Glen McHale* - glen.mchale@ntu.ac.uk

* Corresponding author
§ Tel: +44 (0)115 8483383

Keywords:
capillary origami; Cassie; contact angle; superhydrophobic; Wenzel

Beilstein J. Nanotechnol. **2011,** *2,* 145–151.
doi:10.3762/bjnano.2.18

Received: 18 December 2010
Accepted: 10 February 2011
Published: 10 March 2011

This article is part of the Thematic Series "Biomimetic materials".

Guest Editors: W. Barthlott and K. Koch

Abstract

In the wetting of a solid by a liquid it is often assumed that the substrate is rigid. However, for an elastic substrate the rigidity depends on the cube of its thickness and so reduces rapidly as the substrate becomes thinner as it approaches becoming a thin sheet. In such circumstances, it has been shown that the capillary forces caused by a contacting droplet of a liquid can shape the solid rather than the solid shaping the liquid. A substrate can be bent and folded as a (pinned) droplet evaporates or even instantaneously and spontaneously wrapped on contact with a droplet. When this effect is used to create three dimensional shapes from initially flat sheets, the effect is called *capillary origami* or *droplet wrapping*.

In this work, we consider how the conditions for the spontaneous, capillary induced, folding of a thin ribbon substrate might be altered by a rigid surface structure that, for a rigid substrate, would be expected to create Cassie–Baxter and Wenzel effects. For smooth thin substrates, droplet wrapping can occur for all liquids, including those for which the Young's law contact angle (defined by the interfacial tensions) is greater than 90° and which would therefore normally be considered relatively hydrophobic. However, consideration of the balance between bending and interfacial energies suggests that the tendency for droplet wrapping can be suppressed for some liquids by providing the flexible solid surface with a rigid topographic structure. In general, it is known that when a liquid interacts with such a structure it can either fully penetrate the structure (the Wenzel case) or it can bridge between the asperities of the structure (the Cassie–Baxter case).

In this report, we show theoretically that droplet wrapping should occur with both types of solid–liquid contact. We also derive a condition for the transition between the Cassie–Baxter and Wenzel type droplet wrapping and relate it to the same transition condition known to apply to superhydrophobic surfaces. The results are given for both droplets being wrapped by thin ribbons and for solid grains encapsulating droplets to form liquid marbles.

Introduction

In wetting, the usual implicit assumption is that a solid substrate is sufficiently thick or rigid, that it does not deform or change shape due to the interfacial forces that arise when it contacts a droplet of a liquid, however, in many natural systems this is not the case. Depositing a small droplet onto a smooth substrate and measuring the contact angle in side-profile view gives the contact angle, θ, which is assumed (to within contact angle hysteresis) to approximate to the Young's law value, θ_e, given by the interfacial tensions, i.e., $\cos\theta_e = (\gamma_{SV} - \gamma_{SL})/\gamma_{LV}$ where the γ_{ij} are the interfacial tensions between the solid, liquid and vapor phases. However, the bending rigidity of a solid elastic plate scales with the cube of its thickness and this assumption can become erroneous [1]. When a droplet has a radius, R, larger than the elastocapillary bending length [2], $L_{EC} = (\kappa_b/\gamma_{LV})^{1/2}$ the solid can become deformed and shaped by the liquid. In practice, this effect has been given the name "*capillary origami*" based on experiments showing how films of polydimethylsiloxane (PDMS) shaped in two-dimensions can be folded by evaporating droplets of water to produce a designed three-dimensional shape [3,4]; an effect stronger than the dimpling of an elastomer surface by a deposited droplet [5]. *Capillary origami* is more than a curiosity and has implications for technological applications in creating three-dimensional structures from initially flat films through the capillary forces during liquid evaporation and drying [6-8]. The effect of capillary forces due to nanodroplets in activating and guiding the folding of planar graphene ribbons has recently been simulated [9].

Figure 1 illustrates *capillary origami* concepts and effects based on original ideas by Py et al [3,4]. When a PDMS (Sylgard 184) substrate of reduced thickness is contacted by a droplet of water (containing blue food dye) capillary forces bend it out of its initial planar shape (Figure 1a). When the substrate thickness is reduced to 45 μm and cut into a triangular shape (10 mm side lengths) and scored with a laser (Universal Laser Systems 30W CO_2 laser cutter) to create fold-lines (Figure 1b), contact with a large droplet of water can create a three-dimensional shape (Figure 1d). On contact by the droplet the sheet is bent (Figure 1c) and after droplet evaporation a tetrahedron is formed (Figure 1d). Whilst this is an example of the shaping of a solid substrate by capillary forces, the final shape relies on evaporation to complete the process.

Figure 2 illustrates a number of effects as a droplet contacts a thin PDMS strip substrate ("ribbon") hanging vertically. If a droplet is deposited on a long ribbon it causes substrate deformation, but is unable to wrap or fold the substrate around itself and, as evaporation proceeds, the deformation decreases (Figure 2a). However, when the length of ribbon below the

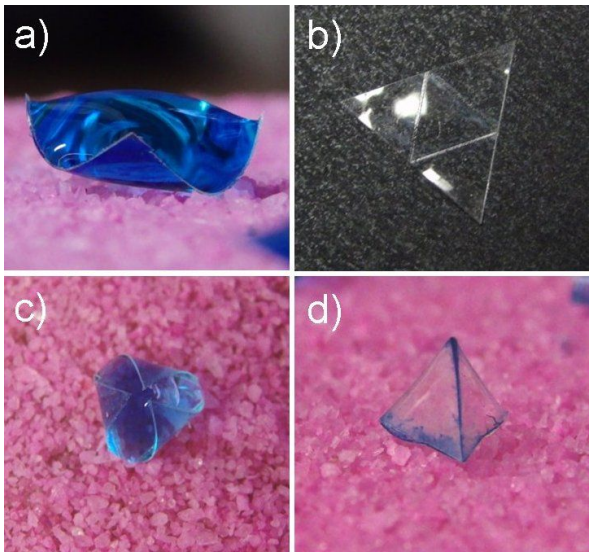

Figure 1: Effect of droplets of blue-dyed water on a thin polydimethylsiloxane (PDMS) membrane: a) droplet causing bending of the substrate, b) initial shaped substrate with the three score lines for folding, c) droplet induced folding, and d) three-dimensional shape left after completion of evaporation.

droplet contact point is sufficiently short, the contacting droplet can quickly fold the ribbon up against gravity and wrap itself. Figure 1 and Figure 2 are illustrative of the ability of capillary forces to deform, fold and bend substrates. The concepts of *capillary origami* and *droplet wrapping* also have implications for our understanding of the definition of hydrophobicity and its relationship to adhesion. Gao and McCarthy demonstrated that spontaneous and complete droplet wrapping occurs, without the need for evaporation, with a thin film of Teflon® even though this material would normally have a contact angle to water greater than 90° and so be regarded as hydrophobic [10]; an effect one of the current authors explained on the basis of the changes in the balance between interfacial and bending energies [11].

In a previous report, McHale argued from surface free energy considerations that, when the bending energy is small, all solids should demonstrate droplet wrapping and so can, in an absolute sense, be considered hydrophilic [11]. That work also discussed why for a partially wetting droplet to be observed there is necessarily an assumption of some rigidity of the substrate, so that the usual definition of relative hydrophobicity (and relative hydrophilicity) through contact angle measurement includes a structural non-surface chemistry based assumption about the solid. It was also suggested that a set of loose spherical grains could be considered to be the extreme case of a solid with no bending energy, thus relating the concept of droplet wrapping to

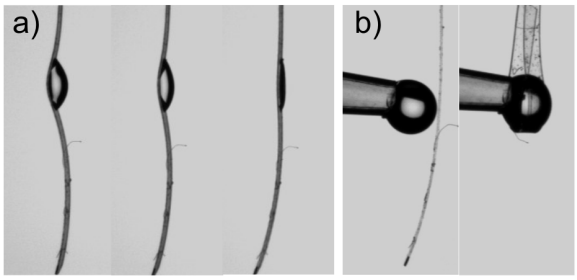

Figure 2: Effect of droplets of water on a thin polydimethylsiloxane (PDMS) membrane ribbon substrate hanging vertically: a) droplet causing a bending of the substrate which disappears as evaporation proceeds (three frames), b) spontaneous wrapping as a droplet touches a membrane ribbon (initial and final states).

that of the formation of liquid marbles [12,13]. It was further argued that when the flexible solid surface possessed rigid surface roughness or the solid grains had a rigid surface roughness, droplet wrapping might, under defined conditions for the surface chemistry defined contact angle, be suppressed. Since wrapping a spherical droplet requires both bending and stretching of the solid, in this report, we consider the simpler, but experimentally realizable, cases of wrapping of a droplet of water by a thin ribbon and the assembly of solid grains to form a liquid marble. For both cases, we extend the previous theoretical consideration to ribbon-type substrates and disconnected solid grains with a rigid surface structure. We review the case for surface roughness that has low aspect ratio so that the liquid can penetrate into the structure – the Wenzel case [14,15]. We then consider whether droplet wrapping can occur without penetration into the surface structure – the Cassie–Baxter case [16,17]. We show that droplet wrapping should occur with both types of configuration and we derive a condition for the transition between these two cases; this condition is the same as for the Wenzel to Cassie–Baxter transition on a superhydrophobic surface [18,19].

Results and Discussion

1. Droplet wrapping theory

To assess whether it is energetically favourable for a liquid to become wrapped in a solid we consider the change in interfacial energy as the solid–vapor interface is replaced by a solid–liquid interface together with the increase in bending energy as the solid deforms from a planar ribbon, similar to those shown in Figure 2, of width $w << R$, where R is the droplet radius. The use of a ribbon substrate allows the problem to be simplified to a quasi-two dimensional situation. Assuming there is no spontaneous curvature of the solid film, the initial energy is given by the sum of the energy associated with the liquid in contact with the vapor and the surfaces of the solid in contact with the vapor (Figure 3a),

$$F^{\mathrm{i}} = A^{\mathrm{i}}_{\mathrm{LV}}\gamma_{\mathrm{LV}} + r_{\mathrm{W}}A^{\mathrm{p}}_{\mathrm{SV}}\gamma_{\mathrm{SV}} + A^{\mathrm{lower}}_{\mathrm{SV}}\gamma_{\mathrm{SV}} \qquad (1)$$

where $A^{\mathrm{i}}_{\mathrm{LV}}$ is the initial liquid–vapor interfacial area, $A^{\mathrm{p}}_{\mathrm{SV}}$ is the initial planar projection of the area of the upper surface of the solid film, r_{W} is the Wenzel roughness of the surface, and the γ_{ij} are the interfacial tensions; the lower surface of the film is assumed to have an area $A^{\mathrm{lower}}{}_{\mathrm{SV}}$. The initial liquid-vapor area is $A^{\mathrm{i}}{}_{\mathrm{LV}} = 4\pi R^2$, where R is the droplet radius, and after wrapping it is assumed that the shape is spherical with the same radius R. This means that a planar projected area $2\pi Rw$ of the ribbon's area is involved in the wrapping. For simplicity in the following, we limit the initial ribbon length to $2\pi R$, so that $A^{\mathrm{p}}{}_{\mathrm{SV}} = 2\pi Rw$ is assumed.

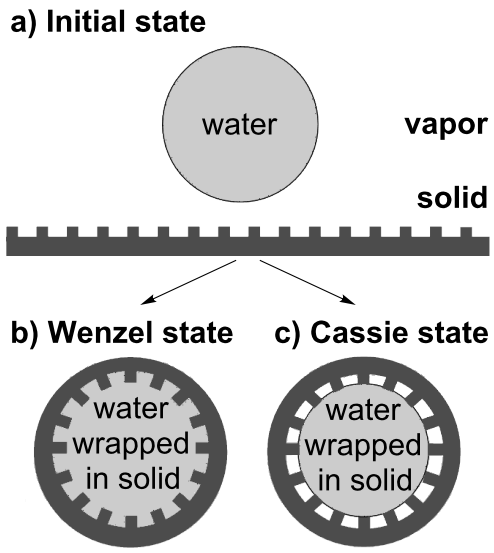

Figure 3: Initial and final states involved in a droplet wrapping event for a flexible ribbon membrane with rigid roughness. In the Wenzel case the liquid penetrates between features and in the Cassie case it bridges between them.

The energy per unit area, f_{b}, associated with bending and stretching a thin membrane substrate is related to the principal radii of curvatures of the substrate,

$$f_{\mathrm{b}} = \frac{\kappa_{\mathrm{b}}\left(c_1 + c_2\right)^2}{2} + \kappa_{\mathrm{G}}c_1c_2 \qquad (2)$$

where κ_{b} is the elastic bending rigidity and κ_{G} is the Gaussian bending modulus [20]. For a film of thickness h, the bending rigidity is given by $\kappa_{\mathrm{b}} = Eh^3/12(1-\nu^2)$, where E is Young's modulus and ν is Poisson's ratio; the Gaussian bending modulus relates to any stretching or compression of the film. The coefficients c_1 and c_2 are the principal radii of curvature, which for a

spherical droplet are $c_1 = c_2 = 1/R$. For a ribbon bending only along its length $c_1 = 1/R$ and $c_2 = 0$ so that for a radius of R the bending energy per unit area is,

$$f_b = \frac{\kappa_b c_1^2}{2} = \frac{\kappa_b}{2R^2} \tag{3}$$

When the liquid comes into contact with the ribbon, assuming the ribbon can bend, and that the roughness remains unchanged, we can imagine two types of wrapping scenarios. In the Wenzel case, the liquid may penetrate between the surface features and retain contact with the ribbon at all points along its surface (Figure 3b). In the alternative Cassie–Baxter case, the surface structure combined with the surface chemistry may be such that the liquid bridges between the tops of the surface features leaving vapor between them (Figure 3c).

1.1 Wenzel case

In the Wenzel case, the liquid penetrates between surface features (Figure 3b) and the difference in energy between the final and the initial state related to the attachment of the droplet to the ribbon is given by,

$$\frac{\Delta F_W}{2\pi R w} = r_W\left(\gamma_{SL} - \gamma_{SV}\right) - \gamma_{LV} + \frac{\kappa_b c_1^2}{2} \tag{4}$$

which can be rewritten using the definition of the Young's law equilibrium contact angle on a rigid surface of $\cos\theta_e = (\gamma_{SV} - \gamma_{SL})/\gamma_{LV}$, as,

$$\frac{\Delta F_W}{2\pi R w} = -\gamma_{LV}\left(r_W \cos\theta_e + 1\right) + \frac{\kappa_b c_1^2}{2} \tag{5}$$

For liquids which on a rigid smooth solid substrate are considered to be partially wetting the cosine satisfies $-1 < \cos\theta_e < 1$ and θ_e gives a finite Young's law contact angle. However, for those liquids which completely wet and form films, the combination $(\gamma_{SV} - \gamma_{SL})/\gamma_{LV}$ has a value greater than 1. The combination of the roughness, r_W, multiplying $\cos\theta_e$ immediately introduces the Wenzel contact angle,

$$\frac{\Delta F_W}{2\pi R w} = -\gamma_{LV}\left(\cos\theta_W + 1\right) + \frac{\kappa_b c_1^2}{2} \tag{6}$$

One assumption in Equation 6 is that the final radius of the wrapped portion of the droplet is approximately the same as the initial droplet radius.

1.2 Cassie–Baxter case

In the Cassie–Baxter case, complete penetration of liquid between surface features does not occur (Figure 3c). The liquid only contacts a fraction φ_s of the surface thus leaving a fraction $(r_W - \varphi_s)$ of the solid surface in contact with the vapor. In addition, the liquid bridges between surface features, thus providing a set of menisci, here approximated by a fraction $(1 - \varphi_s)$ of the surface with a liquid–vapor interface. The difference in energy between the final and the initial state related to the attachment of the droplet to the ribbon is then given by,

$$\frac{\Delta F_{CB}}{2\pi R w} = \varphi_s\gamma_{SL} + \left(1-\varphi_s\right)\gamma_{LV} + \left(r_W - \varphi_s\right)\gamma_{SV} - r_W\gamma_{SV} - \gamma_{LV} + \frac{\kappa_b c_1^2}{2} \tag{7}$$

Cancelling terms involving the roughness factor r_W and using the definition of the equilibrium contact angle on a rigid substrate of $\cos\theta_e = (\gamma_{SV} - \gamma_{SL})/\gamma_{LV}$ gives,

$$\frac{\Delta F_{CB}}{2\pi R w} = -\gamma_{LV}\left(\varphi_s\cos\theta_e - \left(1-\varphi_s\right) + 1\right) + \frac{\kappa_b c_1^2}{2} \tag{8}$$

Defining the Cassie–Baxter combination $\cos\theta_{CB} = \varphi_s\cos\theta_e - (1-\varphi_s)$, which is familiar from the modelling of droplets on superhydrophobic surfaces, gives,

$$\frac{\Delta F_{CB}}{2\pi R w} = -\gamma_{LV}\left(\cos\theta_{CB} + 1\right) + \frac{\kappa_b c_1^2}{2} \tag{9}$$

The similarity of Equation 6 and Equation 9 can be revealed by writing,

$$\frac{\Delta F_T}{2\pi R w} = -\gamma_{LV}\left(\cos\theta_T + 1\right) + \frac{\kappa_b c_1^2}{2} \tag{10}$$

where the subscript T defines the topographic assumption of the liquid either in a Wenzel ("penetrating") or Cassie–Baxter ("skating") state. In the form presented by Equation 10, the principal radius of curvature c_1 is given by $1/R$ and so the energy change per unit area of the ribbon substrate depends on the droplet size.

1.3 Wrapping and transitions with roughness

The wrapping state will be stable provided the energy change given by Equation 10 is negative, i.e.,

$$\cos\theta_T > -1 + \frac{\kappa_b c_1^2}{2\gamma_{LV}} \quad (11)$$

Defining the dimensionless curvature elastocapillary number $n_{EC} = \kappa_b {c_1}^2/2\gamma_{LV}$, Equation 11 can be written as,

$$\cos\theta_T > -1 + n_{EC} \quad (12)$$

A ribbon substrate that is unable to bend in response to contact with the liquid will have an elastocapillary number that tends to infinity and so wrapping will not occur. When the elastocapillary number has a finite value, wrapping will occur, but will depend on the volume and shape of the liquid. For a droplet with a spherical shape of radius R, the elastocapillary number is $n_{EC} = \kappa_b/2\gamma_{LV}R^2 = ½(L_{EC}/R)^2$, where $L_{EC} = (\kappa_b/\gamma_{LV})^{1/2}$ is the characteristic elastocapillary length. Equation 12 then becomes,

$$\cos\theta_T > -1 + 2\left(\frac{L_{EC}}{R}\right)^{1/2} \quad (13)$$

This condition for droplet wrapping depends upon the state of contact of the wrapped liquid with the solid surface, i.e., penetrating or skating. For the Cassie–Baxter state with its air-pockets to be thermodynamically stable compared to the Wenzel state, requires $\Delta F_{CB} < \Delta F_W$ in addition to $\Delta F_{CB} < 0$. Since the curvature energy contributes the same to both, Equation 10 implies $\cos\theta_W < \cos\theta_{CB}$, which gives a condition on the relationship between the Young's law contact angle θ_e, and the roughness r_W and solid surface fraction φ_s,

$$\cos\theta_e < -\left(\frac{1-\varphi_s}{r_W - \varphi_s}\right) = \cos\theta_c \quad (14)$$

where θ_c is a critical contact angle for thermodynamic stability of the Cassie–Baxter state; when the Young's law contact angle exceeds the critical contact angle the Cassie–Baxter state is favoured over the Wenzel state. Equation 14 is exactly the same as the condition derived by Bico et al., for the thermodynamic stability of the Cassie–Baxter state on a superhydrophobic surface [18,19]. As noted by these authors, when $90° < \theta_e < \theta_c$, the Cassie–Baxter state may exist due to, e.g., pinning on sharp edges of features, but it is a metastable state.

Here we have also only considered a simple model that assumes either a Wenzel state or a Cassie–Baxter state. However, surfaces with curvature can effectively have a combination of both Wenzel and Cassie–Baxter properties with the solid surface fraction becoming a function of the Young's law contact angle [21]. Re-entrant surfaces have been shown to be particularly effective in producing suspended droplets of liquids with low surface tensions [22]. Following the superhydrophobic literature, we can also anticipate that if the surface chemistry tends towards hydrophilic (i.e., $\theta_e < 90°$) there might be a hemi-wicking effect with the liquid invading the surface texture, but wetting the asperities of the topographic features. A simple two-dimensional model consideration of the energy changes as a liquid invades a structure on a thin substrate suggests that the critical Young's law contact angle for hemi-wicking will be shifted to values lower than θ_c due to the contribution of bending energy.

1.4 Drop size and contact angle effects

The inclusion of the energy associated with the curvature of a substrate introduces a characteristic elastocapillary length and results in drop size effects. For a ribbon film substrate, Equation 10 implies wrapping requires the droplet radius R to be greater than a critical radius, R_c, given by,

$$R_c = \left(\frac{\kappa_b}{2\gamma_{LV}\left(\cos\theta_T + 1\right)}\right)^{1/2} = \left(\frac{1}{2\left(\cos\theta_T + 1\right)}\right)^{1/2} L_{EC} \quad (15)$$

which can be compared to the condition $R > L_{EC}/\sqrt{2}$ given by Py et al [3]. Thus, there is a critical radius which depends on the Young's law contact angle, θ_e, and the topographic structure via the surface roughness, r_W, or solid surface fraction, φ_s.

In the Cassie–Baxter case, $\cos\theta_T = \cos\theta_{CB}$, and θ_{CB} can approach 180° from below and, as it does so, the critical radius for wrapping tends to infinity; a strongly superhydrophobic ribbon will not result in droplet wrapping because the energy gain cannot overcome the bending energy. In the Wenzel case, $\cos\theta_T = \cos\theta_W$, and this is positive when $\theta_e < 90°$, but negative when $\theta_e > 90°$. In the former case, the critical radius becomes smaller as the Young's law contact angle tends to zero or as the roughness increases; a film can be wrapped in a tighter curve and, hence, a smaller droplet radius is needed. It should also be noted that $\cos\theta_e$ is defined by a combination of the interfacial tensions and this combination can be greater than unity; this corresponds to a film of liquid on a smooth and rigidly flat surface. In the considerations above, no account has been taken of the finite mass of the substrate on the critical volume of liquid required for wrapping; a problem recently considered experimentally and theoretically for square and triangular sheets of PDMS by Chen et al [23].

2. Liquid marbles and topographically structured grains

When a solid in the form of a thin ribbon wraps around a droplet it only needs to bend, whereas when the solid is a sheet it needs to either stretch and deform or to crumple and fold. Such a situation could be considered, but additional energies relating to these effects would need to be included unless the contribution from these is at no energy cost. One possible situation that conceptually is similar to a substrate able to deform and conform to a liquid surface, but without any bending or stretching energy cost, is the adhesion of a collection of solid grains to a liquid surface to encapsulate it and form a liquid marble (Figure 4a and Figure 4b) [12,13,24]. In an abstract sense, a collection of grains assembled in a close-packed form onto a liquid–vapor interface is the extreme limit of a flexible solid possessing no curvature (or stretching) energy and, hence, a vanishing elastocapillary length. In the study of liquid marbles, the simplest assumption is that each grain is spherical in shape and has no particular surface topography. As a consequence all grains, irrespective of their surface chemistry, will adhere to the water-air interface; a similar conclusion to that regarding the absolute hydrophilicity of solids when their curvature energy is zero. The effect of surface chemistry, characterised through the Young's law contact angle, is to determine the strength of the adhesion to the air-water interface with maximum strength corresponding to $\theta_e = 90°$; if $\theta_e > 90°$ more than half the grain projects out of the interface into the air. In practice, the surfaces of the grains do not need to be smooth and can have a topographic structure. For example, pollen grains come in a variety of shapes, commonly spherical, ovoid or disc-like with lengths in the order of 10–100 μm and their surfaces (exine) under scanning electron microscopy vary from relatively smooth to mesh-like and ones adorned with sharp spikes (see, e.g., [25]).

By considering the changes in interfacial areas as a spherical grain of radius R_g with a roughness r_W attaches to a droplet of radius R (Figure 4c), we deduce the change in surface free energy ΔF^M_T,

$$\Delta F_T^M = -A_{cap}\gamma_{LV}\left(1+\cos\theta_T\right) \qquad (16)$$

where $A_{cap} = \pi R_g^2(1 + \cos\theta_T)$ is the spherical cap area of the solid grain of radius R_g intersecting the droplet and θ_T is either the Wenzel contact angle or the Cassie–Baxter contact angle, depending on whether the liquid penetrates between the topographic features on the surface of the grain or whether it bridges between the asperities (and is therefore only in contact with a fraction of the solid area, φ_s). In a similar manner to droplet wrapping, Equation 14 defines a minimum Young's law contact angle for the Cassie–Baxter state to be thermodynamically stable over the Wenzel state. The idea of a solid film that tends to a non-adhesive surface for liquids can be extended to non-stick granular or powder systems. All smooth spherical grains adhere to the liquid interface because $(1 + \cos\theta_e)$ can never be negative. However, when the surface of a grain is structured it can become superhydrophobic and it will then only weakly attach to the surface of the liquid.

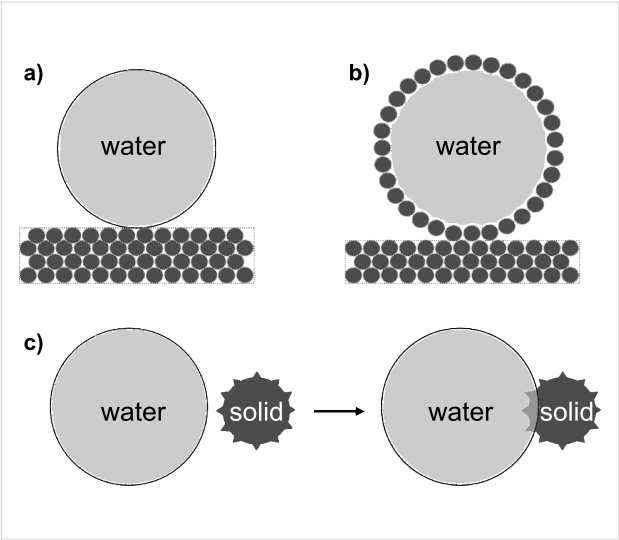

Figure 4: Formation of a liquid marbles: a) droplet contacting substrate composed of loose grains, b) attachment of grains to encapsulate a droplet, c) minimisation of surface free energy by replacement of a portion of the liquid–vapor interface by a portion of the rough solid surface from an attaching grain.

Conclusion

In this work, we have focused on a rigid surface structure on a thin flexible substrate, but the inverse situation of a flexible surface structure on a rigid substrate has recently also been modelled [26,27]. A result of that work is an understanding that elastocapillary effects can provide additional stability for Cassie-type suspended liquid states involved in, e.g., plastron respiration [27-29]. It therefore seems likely that to fully understand superhydrophobic surfaces, the flexible nature of elements of surfaces needs to be understood. Using a model of a thin ribbon (strip) substrate we have shown that relaxing the assumption of a rigid substrate allows a contacting droplet to shape and bend the substrate provided the droplet radius is larger than a critical value. When the flexible substrate has a surface with a rigid topographic structure, the critical droplet radius at which droplets wrap depends on both the elastocapillary length and a function of either the Wenzel or the Cassie–Baxter contact angle dependent on the state of the contact. We have argued that liquid marbles can be thought of as such a system, but with a vanishing elastocapillary length. Manipulating the surface structure therefore provides a method,

complementary to control of substrate thickness, to tune the balance of adhesive forces between liquids and solids both within *capillary origami* and granular systems.

Acknowledgements

One of the authors (NG) is grateful to Nottingham Trent University for providing a PhD scholarship.

References

1. Olives, J. *J. Phys.: Condens. Matter* **1993,** *5,* 2081–2094. doi:10.1088/0953-8984/5/14/007
2. Bico, J.; Roman, B.; Moulin, L.; Boudaoud, A. *Nature* **2004,** *432,* 690. doi:10.1038/432690a
3. Py, C.; Reverdy, P.; Doppler, L.; Bico, J.; Roman, B.; Baroud, C. N. *Phys. Rev. Lett.* **2007,** *98,* No. 156103. doi:10.1103/PhysRevLett.98.156103
4. Py, C.; Reverdy, P.; Doppler, L.; Bico, J.; Roman, B.; Baroud, C. N. *Eur. Phys. J. Special Topics* **2009,** *166,* 67–71. doi:10.1140/epjst/e2009-00880-4
5. Pericet-Camara, R.; Auernhammer, G. K.; Koynov, K.; Lorenzoni, S.; Raiteri, R.; Bonaccurso, E. *Soft Matter* **2009,** *5,* 3611–3617. doi:10.1039/b907212h
6. De Volder, M.; Tawfick, S. H.; Park, S. J.; Copic, D.; Zhao, Z.; Lu, W.; Hart, A. J. *Adv. Mater.* **2010,** *22,* 4384–4389. doi:10.1002/adma.201001893
7. Ahn, B. Y.; Shoji, D.; Hansen, C. J.; Hong, E.; Dunand, D. C.; Lewis, J. A. *Adv. Mater.* **2010,** *22,* 2251–2254. doi:10.1002/adma.200904232
8. van Honschoten, J. W.; Berenschot, J. W.; Ondarçuhu, T.; Sanders, R. G. P.; Sundaram, J.; Elwenspoek, M.; Tas, N. R. *Appl. Phys. Lett.* **2010,** *97,* No. 014103. doi:10.1063/1.3462302
9. Patra, N.; Wang, B.; Král, P. *Nano Lett.* **2009,** *9,* 3766–3771. doi:10.1021/nl9019616
10. Gao, L.; McCarthy, T. J. *Langmuir* **2008,** *24,* 9183–9188. doi:10.1021/la8014578
11. McHale, G. *Langmuir* **2009,** *25,* 7185–7187. doi:10.1021/la900597a
12. Aussillous, P.; Quéré, D. *Nature (London)* **2001,** *411,* 924–927. doi:10.1038/35082026
13. McHale, G.; Herbertson, D. L.; Elliott, S. J.; Shirtcliffe, N. J.; Newton, M. I. *Langmuir* **2007,** *23,* 918–924. doi:10.1021/la061920j
14. Wenzel, R. N. *Ind. Eng. Chem.* **1936,** *28,* 988–994. doi:10.1021/ie50320a024
15. Wenzel, R. N. *J. Phys. Colloid Chem.* **1949,** *53,* 1466–1467. doi:10.1021/j150474a015
16. Cassie, A. B. D.; Baxter, S. *Trans. Faraday Soc.* **1944,** *40,* 546–551. doi:10.1039/tf9444000546
17. Cassie, A. B. D. *Discuss. Faraday Soc.* **1948,** *3,* 11–16. doi:10.1039/df9480300011
18. Bico, J.; Thiele, U.; Quéré, D. *Colloids Surf., A* **2002,** *206,* 41–46. doi:10.1016/S0927-7757(02)00061-4
19. Quéré, D. *Annu. Rev. Mater. Res.* **2008,** *38,* 71–99. doi:10.1146/annurev.matsci.38.060407.132434
20. Boal, D. H. *Mechanics of the Cell;* Cambridge University Press: New York, 2002.
21. Shirtcliffe, N. J.; McHale, G.; Atherton, S.; Newton, M. I. *Adv. Colloid Interface Sci.* **2010,** *161,* 124–138. doi:10.1016/j.cis.2009.11.001
22. Tuteja, A.; Choi, W.; Ma, M.; Mabry, J. M.; Mazzella, S. A.; Rutledge, G. C.; McKinley, G. H.; Cohen, R. E. *Science* **2007,** *318,* 1618–1622. doi:10.1126/science.1148326
23. Chen, L.; Wang, X.; Wen, W.; Li, Z. *Appl. Phys. Lett.* **2010,** *97,* No. 124103. doi:10.1063/1.3492834
24. Shirtcliffe, N. J.; McHale, G.; Newton, M. I.; Pyatt, F. B.; Doerr, S. H. *Appl. Phys. Lett.* **2006,** *89,* No. 094101. doi:10.1063/1.2339072
25. Shaheen, N.; Khan, M. A.; Hayat, M. Q.; Yasmin, G. J. *Med. Plants Res.* **2009,** 3.
26. Bernardino, N. R.; Blickle, V.; Dietrich, S. *Langmuir* **2010,** *26,* 7233–7241. doi:10.1021/la904345r
27. Blow, M. L.; Yeomans, J. M. *Langmuir* **2010,** *26,* 16071–16083. doi:10.1021/la101847b
28. McHale, G.; Newton, M. I.; Shirtcliffe, N. J. *Soft Matter* **2010,** *6,* 714–719. doi:10.1039/b917861a
29. Shirtcliffe, N. J.; McHale, G.; Newton, M. I.; Perry, C. C.; Pyatt, F. B. *Appl. Phys. Lett.* **2006,** *89,* No. 104600. doi:10.1063/1.2347266

License and Terms

Beilstein Journal of Nanotechnology

Superhydrophobicity in perfection: the outstanding properties of the lotus leaf

Hans J. Ensikat*[1], Petra Ditsche-Kuru[1], Christoph Neinhuis[2] and Wilhelm Barthlott[1]

Full Research Paper

Open Access

Address:
[1]Nees Institute, University of Bonn, Meckenheimer Allee 170, 53115 Bonn, Germany and [2]Institut für Botanik, Technische Universität Dresden, Zellescher Weg 20b, 01069 Dresden, Germany

Email:
Hans J. Ensikat* - ensikat@uni-bonn.de

* Corresponding author

Keywords:
epicuticular wax; leaf surface; Lotus effect; papillae; water repellency

Beilstein J. Nanotechnol. **2011,** *2,* 152–161.
doi:10.3762/bjnano.2.19

Received: 07 January 2011
Accepted: 17 February 2011
Published: 10 March 2011

This article is part of the Thematic Series "Biomimetic materials".

Guest Editors: W. Barthlott and K. Koch

Abstract

Lotus leaves have become an icon for superhydrophobicity and self-cleaning surfaces, and have led to the concept of the 'Lotus effect'. Although many other plants have superhydrophobic surfaces with almost similar contact angles, the lotus shows better stability and perfection of its water repellency. Here, we compare the relevant properties such as the micro- and nano-structure, the chemical composition of the waxes and the mechanical properties of lotus with its competitors. It soon becomes obvious that the upper epidermis of the lotus leaf has developed some unrivaled optimizations. The extraordinary shape and the density of the papillae are the basis for the extremely reduced contact area between surface and water drops. The exceptional dense layer of very small epicuticular wax tubules is a result of their unique chemical composition. The mechanical robustness of the papillae and the wax tubules reduce damage and are the basis for the perfection and durability of the water repellency. A reason for the optimization, particularly of the upper side of the lotus leaf, can be deduced from the fact that the stomata are located in the upper epidermis. Here, the impact of rain and contamination is higher than on the lower epidermis. The lotus plant has successfully developed an excellent protection for this delicate epistomatic surface of its leaves.

Introduction

Since the introduction of the 'Lotus concept' in 1992 [1,2], the lotus leaf became the archetype for superhydrophobicity and self-cleaning properties of plant surfaces and a model for technical analogues [3,4] . Lotus (*Nelumbo nucifera*) is a semi-aquatic plant and develops peltate leaves up to 30 cm in diameter with remarkable water repellency. As an adaptation to the aquatic environment – some of the leaves float occasionally on the water surface – the stomata are located in the upper

epidermis. The lower epidermis consists of convex cells covered with wax tubules and contains only few stomata. The upper epidermis features the distinctive hierarchical structure consisting of papillae with a dense coating of agglomerated wax tubules, which is the basis for the famous superhydrophobicity (Figure 1).

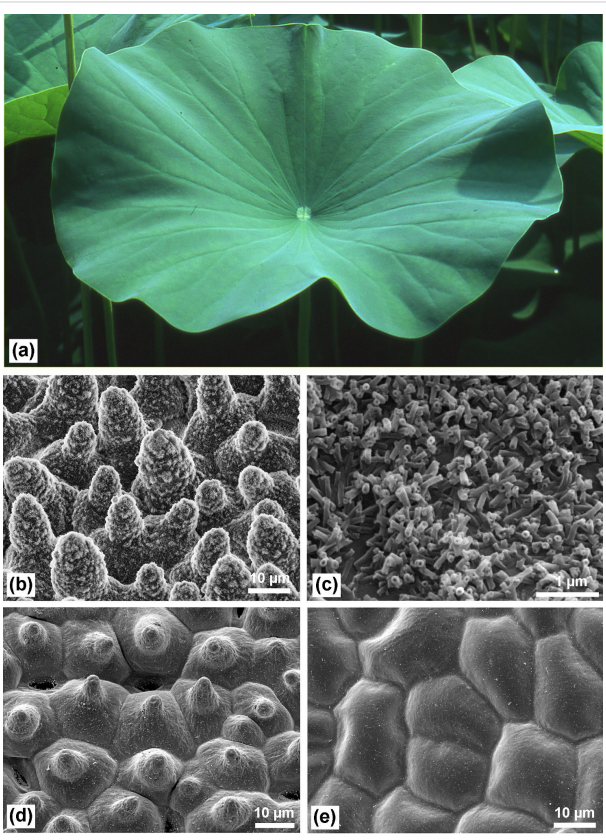

Figure 1: (a) Lotus leaves, which exhibit extraordinary water repellency on their upper side. (b) Scanning electron microscopy (SEM) image of the upper leaf side prepared by 'glycerol substitution' shows the hierarchical surface structure consisting of papillae, wax clusters and wax tubules. (c) Wax tubules on the upper leaf side. (d) Upper leaf side after critical-point (CP) drying. The wax tubules are dissolved, thus the stomata are more visible. Tilt angle 15°. (e) Leaf underside (CP dried) shows convex cells without stomata.

However, a hierarchical surface structure which induces strong water repellency and contact angles above 150° is not a special feature of lotus leaves. It has been known for a long time that plant surfaces covered with epicuticular wax crystals are water repellent, and that this feature is enhanced when the epidermis has additional structures such as papillae or hairs [5,6]. Neinhuis and Barthlott (1997) [7] presented an overview of more than 200 species with contact angles >150° and their surface morphologies. Many studies, in which the properties of lotus leaves were compared with those of other superhydrophobic plants, have shown the superiority of the upper side of the lotus leaf. A standard tool for the determination of wettability or water repellency is the measurement of the static contact angle by the 'sessile drop' method. Neinhuis and Barthlott (1997) [7] for example, measured contact angles on the lotus leaf of 162°, which are among the highest of the compared species, but many other (43%) of the tested superhydrophobic plants also showed contact angles between 160 and 163°. Even some species with flat epidermis cells but with a dense layer of epicuticular wax crystals, such as *Brassica oleracea* or some *Eucalyptus* species, can exhibit contact angles >160°. Thus, the contact angle alone is not suitable for a differentiated comparison of superhydrophobic samples. Other values such as contact angle hysteresis or roll-off (tilting) angle show more clearly the differences between the species. Mockenhaupt et al. (2008) [8] compared the tilting angles and the stability of the superhydrophobicity of various plants under moisture condensation conditions. Only the lotus leaves showed no significant loss of water repellency when water vapour condensed on the surface of the cooled samples at 5 °C. Wagner et al. (2003) [9] examined the morphology of the epidermal structures and the wettability with liquids of varying surface tension such as methanol–water mixtures. They reported the lowest wettability by these liquids for the lotus leaves in comparison to other species. They also described the unique shape of the papillae and a very high papillae density (number per area). Chemical analyses [10] and crystal structure analysis by X-ray diffraction [11] showed unique properties of the epicuticular wax of the lotus. The high content of nonacosanediols leads to a high melting point as well as a strongly disturbed crystal structure which is the basis for the formation of tubules. The visualization of the contact zone between leaves and droplets with cryo-scanning electron microscopy demonstrated the extremely reduced contact area for lotus [12]. Zhang et al. (2008) [13] made detailed measurements of the water repellency of the papillose lotus leaf surface in comparison with the non-papillose leaf margin. The importance of the nanoscopic wax crystals for the water repellency was demonstrated by Cheng et al. (2006) [14]. They reported a strong decrease of the contact angle after melting of the waxes. A limited air retaining capability of submersed lotus leaves was reported by Zhang et al. (2009) [15] after the leaves were held at a depth of 50 cm for 2 h. Bhushan et al. (2010) [4] used the surface structures of the lotus leaf as model for the development of artificial biomimetic superhydrophobic structures.

It became obvious that the outstanding and stable superhydrophobicity of the lotus leaf relies on the combination of optimized features such as the surface topography, robustness and the unique properties of the epicuticular wax. The aim of this article is to integrate the relevant features of the lotus leaf, and to compare them with superhydrophobic leaves of other plant species in order to illustrate their significance.

Results and Discussion

The properties of the lotus leaves

The lotus leaf shows an outstanding water repellency particularly on its upper (adaxial) side, which is more robust and less sensitive to mechanical damage than the under (abaxial) side. The reasons for these superior properties can be ascribed to the combination of micro- and nano-structures with optimized geometry and the unique chemical composition of the epicuticular waxes. These properties are illustrated in the following sections and compared with those of other superhydrophobic leaves. (The species are listed in the Experimental section).

Minimization of the water-to-leaf contact area: The epidermis cells of the upper leaf side form papillae of varying height and with a unique shape. The diameter of the papillae is much smaller than that of the epidermis cells and each papilla apex is not spherical but forms an ogive (Figure 2).

The whole surface is covered with short wax tubules which often accumulate in clusters. In comparison with other papillose plant surfaces, lotus has the highest density of papillae, but the lotus papillae have much smaller diameters which reduces the contact area with water drops; strictly speaking, the area of heterogeneous contact between surface and water. The contact area depends on the hydrophobicity of the surface and on the pressure of the water or on the kinetic energy or velocity of the striking water drops. At low pressures, caused by resting or rolling water droplets, the contact area is determined by the local contact angle of the surface structures. For the surface of a papilla coated with wax tubules, a superhydrophobic behavior with a local contact angle of >140° can be assumed. So, the diameter of the contact areas can be estimated from the SEM images and the cross sections of the selected samples (Figure 2).

The minimized contact area is the basic cause for the very low adhesion of water and, thus, the small roll-off (tilting) angles. Compared with lotus, the papillae on the leaves of the other plants (*E. myrsinites*, *C. esculenta*, *A. macrorrhiza*) (Figure 3, see also Figure 7) have much larger diameters and tip radii, and are covered with different wax types, wax platelets or wax film, respectively, which have a lower water repellency than wax tubules.

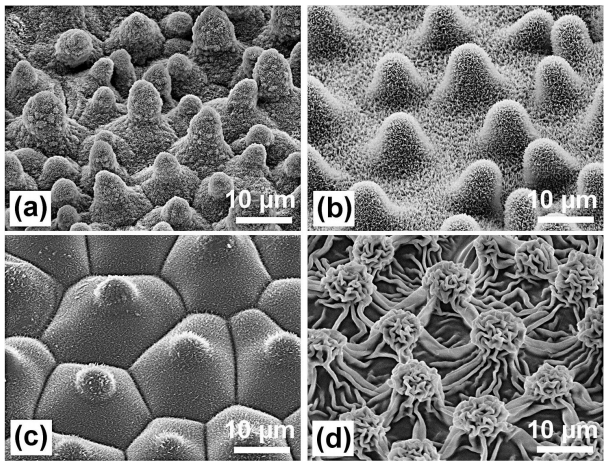

Figure 3: SEM images of the papillose leaf surfaces of *Nelumbo nucifera* (Lotus) (a), *Euphorbia myrsinites* (b), *Colocasia esculenta* (c), and *Alocasia macrorrhiza* (d). Lotus has the highest density of papillae with varying heights and the smallest diameter of the papillae. The papillae of the other species have larger diameters and are covered with different wax types: wax platelets *(E. myrsinites* and *C. esculenta*) and a wax film (*A. macrorrhiza)* which covers cuticular foldings.

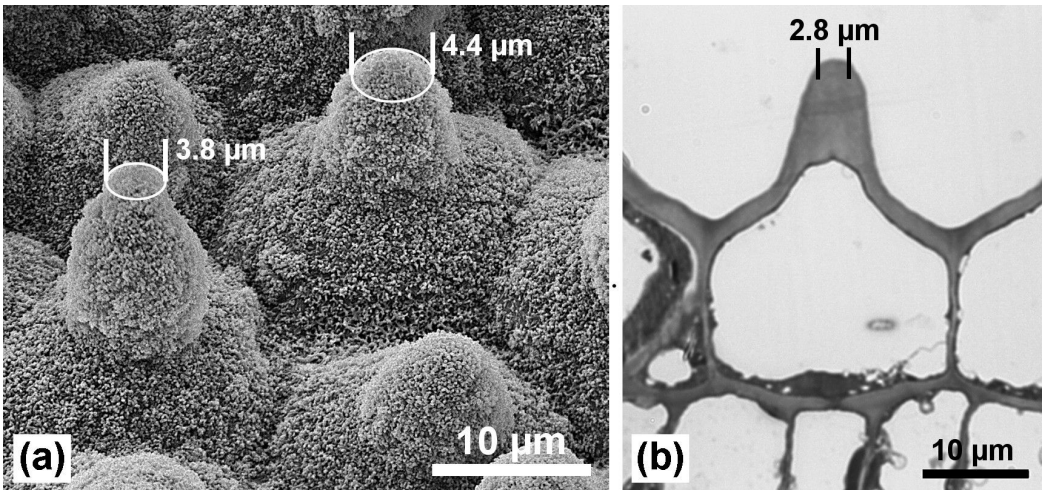

Figure 2: Epidermis cells of the leaf upper side with papillae. The surface is densely covered with wax tubules. (a) SEM image after freeze drying. (b) Light microscopy (LM) image of thin section of an embedded sample. Assuming a contact angle of >140°, for example, the area of heterogeneous contact between single papillae and water (marks) is small in comparison to the epidermis cell area.

The varying height of the papillae further reduces the adhesion between water drops and the surface (Figure 4). Small resting or sliding water drops touch only the highest papillae [12]. At higher pressures, e.g., at the impact of raindrops, the water intrudes deeper between the papillae (Figure 4a) and forms a meniscus at the still superhydrophobic wax tubules coating. The deformation of the non-wetting droplet surface due to surface tension causes a repellent force ('re', Figure 4). When the water retracts, either at the receding side of a moving drop or if the drop is lifted off the surface, the contact areas decrease and the papillae release their contact to the water one by one (Figure 4b, Figure 4c), so that only few of the papillae are simultaneously in the adhesive state ('ad'). Finally, before the drop loses contact with the leaf, only few of the papillae are still in contact and cause a small adhesive force. In contrast, artificial superhydrophobic samples with pillars of equal height lead to stronger adhesion during drop retraction when all the pillars are simultaneously in the adhesive state before the contact breaks (Figure 4d). The measurement of the adhesive and repellent forces between a superhydrophobic papilla-model (with ten times larger tip radius than a lotus papilla) and a water drop is shown in Figure 5.

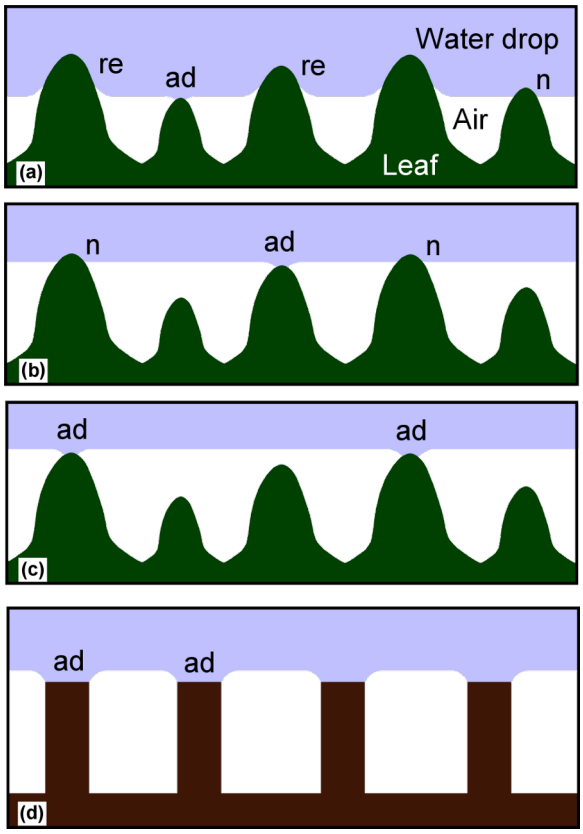

Figure 4: The contact between water and superhydrophobic papillae at different pressures. At moderate pressures the water intrudes into the space between the papillae, but an air layer remains between water and epidermis cells (a). The superhydrophobic surface of the papillae causes a repellent force ('re'). When the water recedes, then the papillae lose contact one after the other (b, c). At a certain water level, the meniscus is flat and the force is neutral ('n'). Just prior to the separation an adhesive force ('ad') arises at the almost horizontal area of the papilla tip, which is small on tips with intact wax crystals and larger when the wax is damaged or eroded. On artificial superhydrophobic structures with equal height (d) the adhesive forces during water receding occur simultaneously at all contacts.

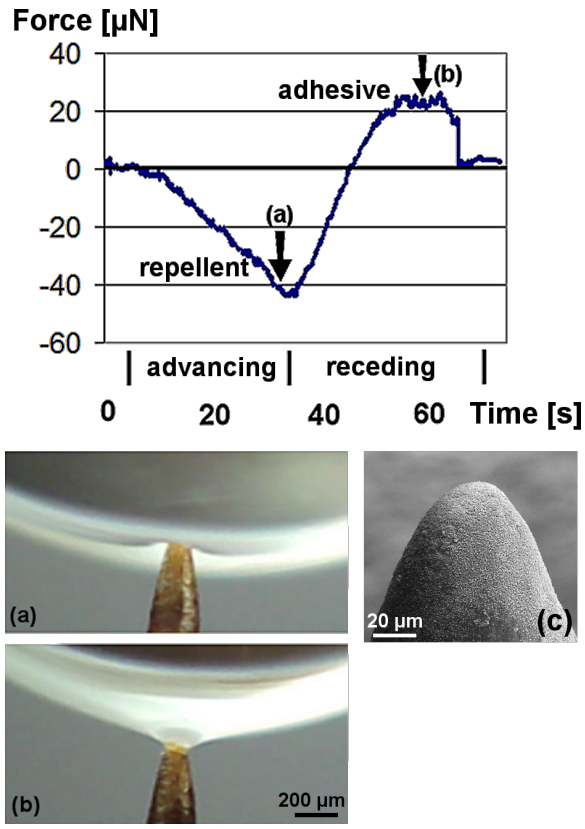

Figure 5: Measured forces between a superhydrophobic papilla-model and a water drop during advancing and receding. The images corresponding to the marks (arrows) in the diagram show the repellent (a) and adhesive (b) meniscus. (c) Papilla-model tip shown with SEM.

Contact angle measurements are the standard tool for the determination of hydrophobicity. But the measurement of very high contact angles is often inaccurate due to difficulties in the determination of the exact drop shape [16], particularly on uneven leaf surfaces. For many superhydrophobic plant surfaces, the contact angles are very close together [7] such that the inaccuracies are larger than the differences between the samples. This may prevent a meaningful comparison. A more differentiated comparison of water repellency has been achieved by the measurement of the adhesion between surface and water during retraction of a drop [13], similar to the measurement shown in Figure 5. Table 1 shows, in addition to other relevant properties, the maximal adhesion forces of water drops on fresh lotus leaves and leaves of other species with intact wax. The adhesion forces are strongly dependent on

Table 1: Comparison of water repellency relevant properties of lotus and other selected species.

	Nelumbo nucifera (Lotus) (upper side)	*Colocasia esculenta* (upper side)	*Euphorbia myrsinites* (upper side)	*Alocasia macrorrhiza* (lower side)	*Brassica oleracea* (upper side)
papillae density (per mm^2) [9]	3431	2662	1265	2002	0
contact angle (static) [7]	163°	165°	162°	157°	161°
drop adhesion force (μN)[a]	8–18	28–55	30–58	90–127	7–48
wax type	tubules	platelets	platelets	film on cuticular folds	rodlets and tubules
wax melting point (°C)	90–95	75–78	75–76	n.a.[b]	65–67
main components [11]	C_{29}-diols	C_{28}-1-ol	C_{26}-1-ol	n.a.[b]	C_{29}-ketones, C_{29}-alkanes

[a]provided by D. Mohr, Nees Institute, Bonn; [b]the wax film of *A. macrorrhiza* has not been isolated and analyzed; no data available.

surface defects which cause pinning of the drops. In contrast, advancing contact angles depend weakly on such irregularities. Thus, the adhesion data correlate better with receding contact angles and hysteresis and indicate the perfection and defects of superhydrophobic surfaces.

Mechanical protection of the wax crystals by papillae: The highest water repellency occurs when the water drops touch the tips of the epicuticular wax crystals only. Thus, the best properties are found on leaves with an intact coating of wax crystals on the epidermal cells (Figure 6). The waxes are, however, relatively soft materials so that older leaves often show patches of eroded or damaged wax (Figure 7), which cause an increased adhesion of water. Neinhuis and Barthlott (1997) [7] have reported that papillae protect the wax crystals between them. On papillose epidermis cells only the wax on the papillae tips appears damaged while the wax between the papillae remains intact (Figure 7a, Figure 7b). Thus, lotus leaves retain their water repellency up to the end of their lifetime. In contrast, the non-papillose surfaces of *Brassica oleracea* and *Yucca filamentosa* (Figure 7c, Figure 7d) often show larger damaged areas which cause a stronger pinning of water. The efficiency of the protective properties can easily be tested by wiping across the leaf with the finger, which destroys only the wax on the papillae tips (Figure 8a, Figure 8b), but the leaves remained superhydrophobic. In the case of the non-papillose surface of a *B. oleracea* leaf (Figure 8c), the waxes are completely destroyed and superhydrophobicity is lost; the contact angle decreased from 160° to ca. 130°. On a *Y. filamentosa* leaf (Figure 8d) with convex epidermis cells, most of the wax crystals were destroyed and the contact angle dropped from 150° to ca. 110°.

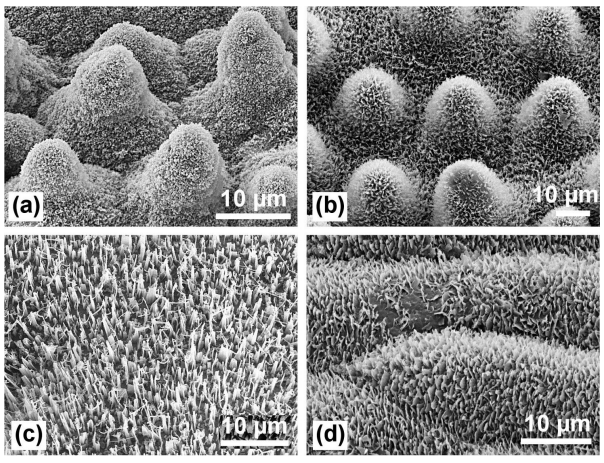

Figure 6: Papillose and non-papillose leaf surfaces with an intact coating of wax crystals: (a) *Nelumbo nucifera* (Lotus); (b) *Euphorbia myrsinites*; (c) *Brassica oleracea*; (d) *Yucca filamentosa*. Even the non-papillose leaves are superhydrophobic. The contact angle of *B. oleracea* can exceed 160°.

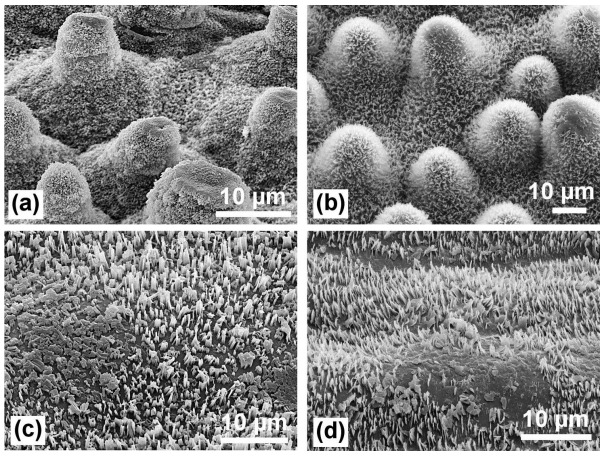

Figure 7: Traces of natural erosion of the waxes on the same leaves as in Figure 6: (a) *Nelumbo nucifera* (Lotus); (b) *Euphorbia myrsinites*; (c) *Brassica oleracea*; (d) *Yucca filamentosa*. On the papillose leaves (a,b) the eroded areas are limited to the tips of the papillae. On non-papillose cells, the damaged areas can be much larger (c,d), causing stronger pinning of water droplets.

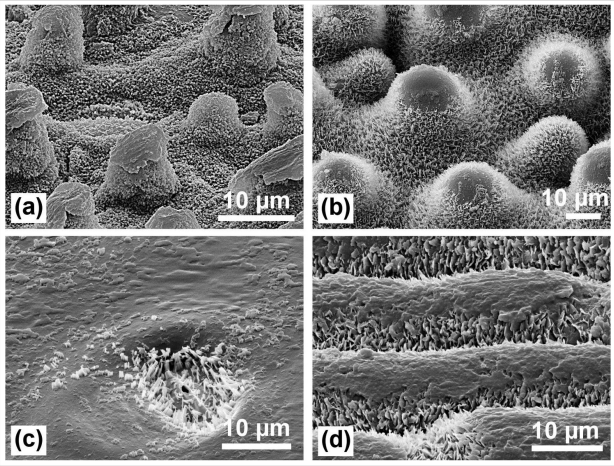

Figure 8: Test for the stability of the waxes against damaging by wiping on the same leaves: (a) *Nelumbo nucifera* (Lotus); (b) *Euphorbia myrsinites*; (c) *Brassica oleracea*; (d) *Yucca filamentosa*. On the papillose surfaces only the waxes on the tips of the papillae are destroyed. The waxes between the papillae are protected and remain intact. On the non-papillose surfaces, most of the waxes are destroyed, adhesion of water drops (pinning) is strongly increased, and the superhydrophobicity is lost.

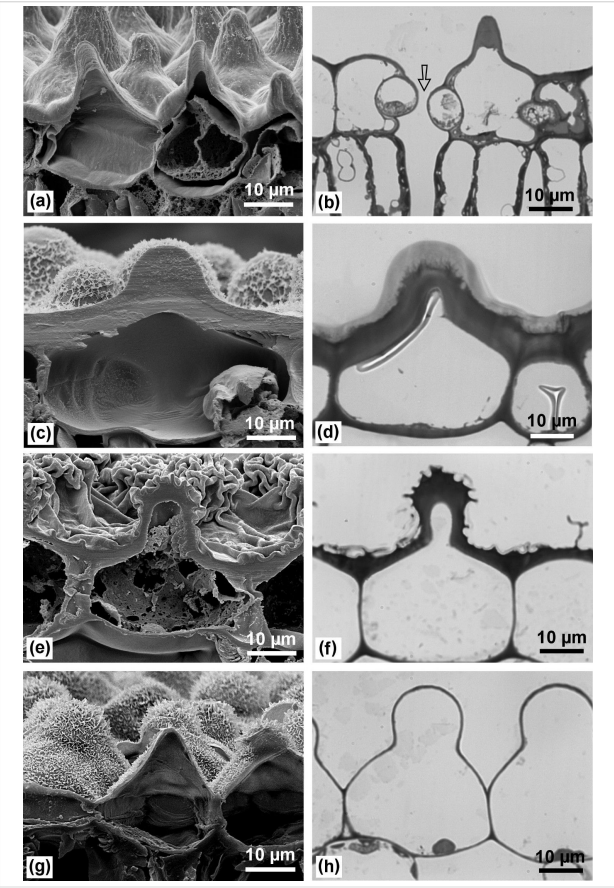

Figure 9: SEM and LM images of cross sections through the papillae. Lotus (a,b) and *Euphorbia myrsinites* (c,d) have almost massive papillae, those of *Alocasia macrorrhiza* (e,f) have a relatively thick outer wall; the epidermal cells of *Colocasia esculenta* have thin walls (g,h). The arrow in (b) marks a stoma.

The basis for the ability to protect the leaf surface in lotus is the robustness of its leaf papillae in combination with their high density. Cross sections (Figure 9) show that they are almost massive at least in the apical part, in contrast to the fragile papillose cells found on many flower petals. However, papillae of other superhydrophobic leaves show various architectures: *Euphorbia myrsinites* has completely massive papillae; those of the lower epidermis of *Alocasia macrorrhiza* have quite thick outer walls, whereas the epidermal cells of *Colocasia esculenta* have very thin walls with slight thickening at the protrusions.

Properties of the lotus wax

Both the upper side and the lower side of the lotus leaf are covered with wax tubules. But, as can be seen on the SEM images (Figure 10a, Figure 10b), the waxes of both sides look quite different. The wax tubules of the lower side are longer (1 to 2 µm) and thicker (ca. 150 nm) and are typical 'nonacosanol tubules' which commonly occur on many plant species [7]. In contrast, the wax tubules of the upper leaf side are very short (0.3–1 µm) and thin (80–120 nm) but the density is very high. Figure 10 shows on a clearly arranged area, approximately 200 tubules per 10 μm^2 on the upper side, but only about 63 tubules per 10 μm^2 on the lower side of the same leaf. The spacing between the tubules on the upper side of the lotus leaf is much smaller than that of other wax crystals such as platelets (Figure 10c, Figure 10d) and other tubular waxes (Figure 10b, Figure 10e, Figure 10f). These distances between the hydrophobic wax crystals determine the pressure (capillary pressure) which is necessary for an intrusion of a water droplet between them.

The chemical analyses of the waxes give an explanation for the different properties. It is known that the epicuticular wax of lotus contains a high percentage of nonacosanediols [10], but the older analyses were made from the entire wax of the leaves, which was obtained as a chloroform extract and also contained intracuticular lipids. The new analyses of the separately isolated waxes from both sides (Figure 11) show that the wax of the upper side contains ca. 65% of various nonacosanediols and only 22% of nonacosan-10-ol, whereas the wax of the underside contains predominantly nonacosan-10-ol (53%) and only 15% of diols, together with 18% of alkanes. The remaining 13% and 14% could not be identified.

This high content of nonacosanediols provides extraordinary properties to the upper side wax. The melting point of 90 to 95 °C is very high for normal (aliphatic) waxes and indicates the influence of hydrogen bonding in the crystal lattice which increases the stability. A comparison of different aliphatic wax components with similar chain length shows that the melting points increase with the occurrence of polar OH-groups. Strong

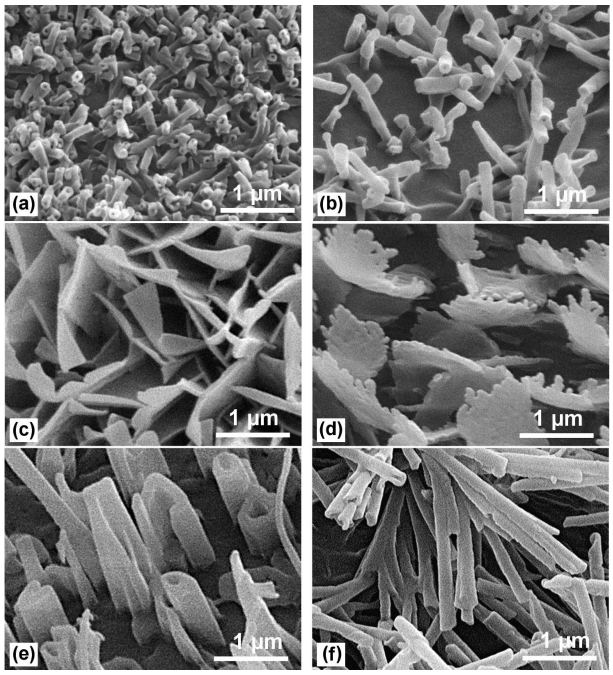

Figure 10: Epicuticular wax crystals in an area of 4 × 3 µm^2. The upper side of the lotus leaf (a) has the highest crystal density (number per area) of wax crystals and the smallest spacings between them. Lotus upper side (a) ca. 200 tubules per 10 µm^2; (b) Lotus underside ca. 63 tubules per 10 µm^2; (c) *Euphorbia myrsinites* ca. 50 platelets per 10 µm^2; (d) *Yucca filamentosa* ca. 17 platelets with over 80 jags per 10 µm^2; (e) *Brassica oleracea* ca. 22 rodlets and tubules, and (f) *Eucalyptus macrocarpa* ca. 50 tubules per 10 µm^2. The larger spacing between the wax crystals of the other surfaces compared to the lotus upper side is obvious.

hydrogen bonding effects have been measured recently by Coward (2010) [17] in nonacosanol wax using FTIR spectroscopy. The effects on the crystal structure should be even stronger for the nonacosanediols. Although the secondary alcohols (nonacosan-10-ol and nonacosanediols) contain polar OH-groups in their molecules, the resulting wax tubules are known to feature strong and relatively stable water repellency, particularly the diols of the lotus leaf. This seems paradoxical, but X-ray diffraction analyses (Figure 12) are in accordance with a layer structure model in which the OH-groups are buried deep in the layer, while the layer surface consists only of non-polar methyl groups [11,18]. In contrast, primary alcohols such as the widespread octacosan-1-ol, which occurs in many platelet-shaped epicuticular waxes, can present the OH-group on the surface, e.g., if they are in contact with a polar environment (water). Holloway (1969) [19] studied the hydrophobicity and water contact angles of various plant waxes and pure wax components. He found the highest contact angles for aliphatic waxes which present only methyl groups on the surface.

According to the layer structure model, the tubules are strongly curved helically growing layers. While straight long-chained alkane molecules form flat layers and regular platelet crystals, secondary alcohols and ketones carry lateral oxygen atoms which inhibit a tight package of the molecules. Thus the resulting layers have a strong curvature and form tubules with a circular cross-section (Figure 13). Today, the progress in molec-

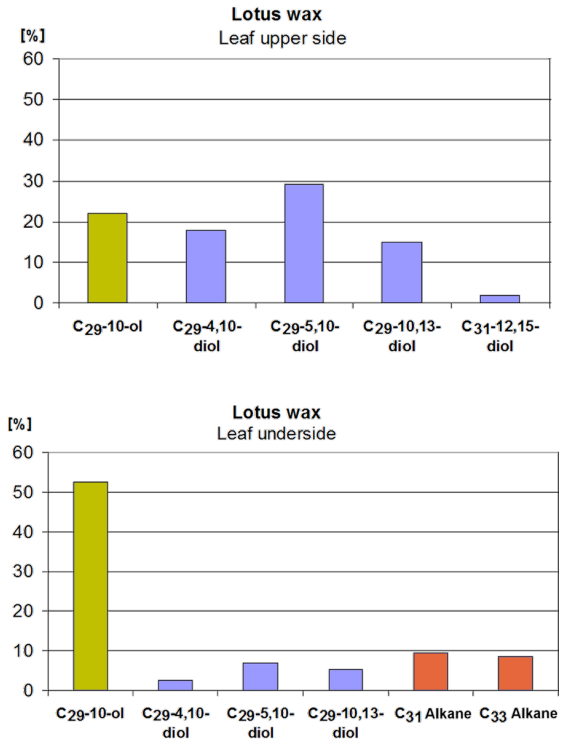

Figure 11: Chemical composition of the separated waxes of the upper and lower side of the lotus leaf. The upper side wax contains 65% of various diols and only 22% of nonacosan-10-ol (C_{29}-10-ol), 13% was unidentified; the underside wax contains 53% nonacosan-10-ol and only 15% of various diols. Alkanes (18%) were only found in the underside wax and may be an essential part of the underlying wax film.

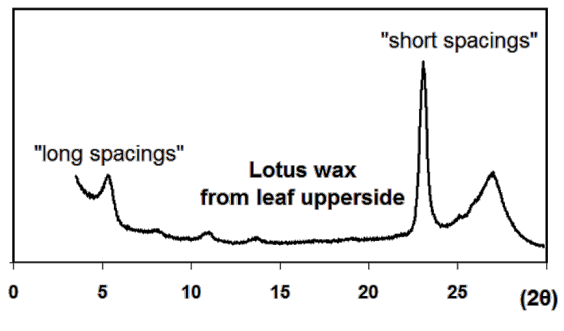

Figure 12: X-ray diffraction diagram of upperside lotus wax. The 'long spacing' peaks indicate a layer structure which is common in aliphatic waxes. The broad 'short spacing' peak at 2θ = 27° indicates a strong disorder in the lateral package of the molecules.

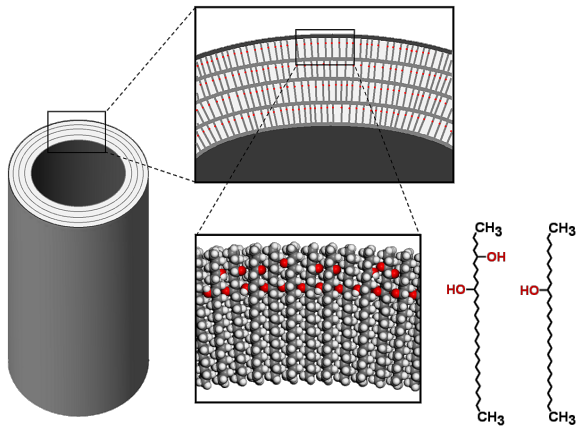

Figure 13: Model of a wax tubule composed of layers of nonacosan-10-ol and nonacosanediol molecules. The OH-groups (red) occupy additional space so that the dense package is disturbed and the layer is forced into a curvature which leads to the formation of a tubule. The polar OH-groups are hidden in the layer, only the CH_3-groups appear at the surface of the layers and tubules.

ular dynamics simulations enables the calculation of the behaviour of nano-structured surfaces in contact with water [20] and to prove the theories such as those of Wenzel or Cassie and Baxter. For precise modelling of the behaviour of natural water repellent surfaces, an exact knowledge of the chemical composition and molecular structure are essential.

Resistance against environmental stress

The excellent superhydrophobic properties of the upper side of the lotus leaf are a result of several unique optimizations. The question then arises whether this development has a certain reason or whether it is a 'freak of nature'. On most plants, the undersides of the leaves show the highest water repellency, or more precisely, those sides which are equipped with stomata. It is obvious that the water repellency serves as a protection to keep the stomata dry [7]. On some species only the cells around the stomata are covered with wax crystals. This is in accordance with the fact that the lotus leaf is epistomatic; it bears the stomata on the upper side, which possesses the higher water repellency. The upper side of a leaf is strongly exposed to environmental impacts such as rainfall and deposition of contaminations. Obviously it is a greater challenge to keep the upper side of a large leaf dry and clean than the underside or the surfaces of vertically growing leaves (grasses etc.). On most plants, the upper sides of the leaves bear no stomata and are more robust than the undersides [21]. Thus the extremely stable and durable water repellency of the lotus leaf, which persists up to the end of its lifetime in autumn, seems to be a successful evolutionary adaptation to the aquatic environment, which led to the placing of the stomata in the upper epidermis and the development of an effective protection through specialized epidermal structures.

For a stable superhydrophobicity – that means the retention of the Cassie state with only partial contact between surface and water – an intrusion of water between the surface structures must be avoided. When the air layer is displaced by water, the water repellency is lost and the surface becomes wet (Wenzel state). The pressure which is necessary to press water into the space between hydrophobic structures depends on the local contact angle and the size of the spacing. This pressure (capillary pressure) is reciprocal to the size of the spacing and can be deduced from the Young–Laplace equation. Due to the irregular spacing, it can be estimated roughly. Water droplets with a radius <100 nm may be able to intrude between the wax tubules; this curvature corresponds to a Laplace pressure of >1.4 MPa (14 bar). Varanasi et al. (2009) [22] calculated the capillary pressures of hydrophobic test samples with structure dimensions roughly similar to those of the lotus leaf: The capillary pressure for spacing of 5 µm between hydrophobic pillars is 12 kPa (120 mbar); a nanoporous structure with 90 nm pore diameter has a capillary pressure of 1.6 MPa (16 bar). Thus the capillary pressure of the lotus papillae with spacing of ca. 10 µm is sufficient to carry the load of resting or rolling water drops. But impacting raindrops generate higher pressure pulses and can intrude into the space between the papillae. The maximal pressure for a drop impact on a rigid material can be calculated from the 'water hammer' equation: $p_{WH} = 0.2\ \rho{\cdot}c{\cdot}v$, where ρ is the density of the liquid, c is the speed of sound in the liquid, and v is the velocity of the droplet. Varanasi et al. (2009) [22] calculated the 'water hammer pressure' of raindrops with a velocity of 3 m/s as 0.9 MPa (9 bar). However, drop impacts on flexible surfaces generate considerably lower pressures [23]. Due to the small spacing between the wax tubules of the lotus leaf and their strong hydrophobicity, their capillary pressure is obviously higher than the impact pressure of raindrops and sufficient to prevent water intrusion. However, it is unproven and hypothetical whether the larger spacing in other waxes causes an intrusion of raindrops. Mechanical damage to the waxes by the impacting drops is a more likely cause for degradation.

Biological models serve as an inspiration for the development of technical superhydrophobic materials [4]. So the question arises whether the lotus leaf presents an optimal architecture for superhydrophobicity. In biological surfaces, several different strategies can be found. The lotus leaf with the largely reduced contact area seems optimal for low adhesion of contaminants and water, observable as small roll-off angles. A disadvantage is the relatively soft wax material, which is too fragile for most technical applications. A different architecture is found on some species with hairy leaf surfaces. The water fern (some species of the genus *Salvinia*) and *Pistia stratioides* leaves retain a relatively thick air layer between hydrophobic hairs when sub-

mersed in water [24]. This provides sufficient buoyancy to avoid long-term submerging. Although superhydrophobic leaves retain an air layer when they are submersed, they are not designed for continuously living under water. All permanently submersed plant surfaces are hydrophilic without hydrophobic waxes [25]. Superhydrophobic surfaces which feature permanent air retention under water are found on animals (some birds, spiders and insects). An outstanding air-retention capability is found, for example, for the aquatic insect *Notonecta glauca* ('backswimmer') [26,27]. Here the water repellency is created by a two-level structure consisting of coarse hairs which can hold a relatively thick air layer, and extremely fine hairs which ensure a high capillary pressure. The biopolymers used in these structures have the advantage of a much higher strength than waxes. On the other hand, the plant surfaces have the capability to regenerate damaged or lost waxes.

Conclusion

It is true that lotus exhibits outstanding water repellency on the upper side of its leaves. The basis of this behaviour is the hierarchical surface structure. In comparison to other species with a hierarchical surface structure composed of papillae and wax crystals, the lotus leaf shows special optimization of some of its features. The morphology of the papillae, particularly the small tip radius, minimizes the contact area to water drops but also the area where erosion and damaging of the waxes occurs. The robustness of the papillae ensures protection of the wax crystals between them. The chemical composition of the epicuticular wax with the high content of nonacosanediols leads to the growth of a dense layer of very small wax tubules with a permanently hydrophobic surface. The unique combination of these properties provides the lotus leaves with unrivaled superhydrophobicity and self-cleaning properties as an effective protection of the delicate epistomatic surface.

Experimental

In addition to the data from the literature, some new examinations provided material for this publication. Plant leaves were taken from the Botanical Gardens, University of Bonn: *Alocasia macrorrhiza* (Elephant ear), *Brassica oleracea* var. *gongylodes* (Kohlrabi), *Colocasia esculenta* (Taro), *Euphorbia myrsinites*, *Nelumbo nucifera* (Lotus), *Yucca filamentosa*.

For scanning electron microscopy, a Cambridge Stereoscan S200 SEM was used. Depending on the sample properties, different preparation methods were applied: Slowly drying leaves were examined as fresh-hydrated samples (*Euphorbia myrsinites*, *Alocasia macrorrhiza*, *Brassica oleracea*, *Yucca filamentosa*). The other species were critical-point dried or freeze dried (Lotus). Air-dried samples were used for high-magnification imaging of epicuticular waxes. These preparation methods are described in detail elsewhere [28]. The samples for thin sections were prepared following a standard protocol for transmission electron microscopy preparation [29]: fixation in glutaraldehyde, dehydration with acetone, embedding in epoxy resin (Agar Low Viscosity Kit, Plano GmbH, Wetzlar, Germany). Sections of ca. 0.5 µm thickness were stained with 'Rapid dye' (Azur II and Methylene blue) for light microscopy.

Wax samples for chemical analyses were isolated mechanically using a 'cryo-adhesion'-method using triethylene glycol as preparation liquid [30]. The wax was analysed by gas chromatography (HP 5890 series II, Avondale, USA) after 'derivatization' by the reaction with *N*,*O*-bis(trimethylsilyl)trifluoroacetamide [31]. X-ray powder diffraction diagrams were recorded with a diffractometer PW 1049/10 (Philips, Eindhoven, The Netherlands) [6].

Contact angles of water drops on the sample surfaces were measured with a contact angle measurement system (OCA 30-2, Dataphysics Instruments GmbH, Filderstadt, Germany) using drops of 10 µL. The adhesion of water drops on the samples was measured with a self-developed device by recording force–distance curves while the drop was attached to and detached from the surface with constant velocity. Drops of 10 µL with a diameter of 2.5 mm were attached until the contact area was 0.7 mm in diameter. Then the maximal adhesion forces during retraction were measured and compared. Low adhesion forces correlate with strong water repellency. The robustness of the leaf surface structures was tested by wiping the leaves with a finger, with a vertical force of 1 N and a contact area of 2.5 cm^2.

Acknowledgements

Our studies were supported by the Bundesministerium für Bildung, Forschung und Technologie (BMBF), the German Science Foundation (Deutsche Forschungsgemeinschaft, DFG) and the Akademie der Wissenschaften und der Literatur zu Mainz (Project V 'Biodiversität im Wandel'). We thank Prof. Lukas Schreiber, Bonn, for the chemical analyses, Prof. Kerstin Koch (Kleve) and Ms. Divykriti Chopra for the help in the preparation of the manuscript, and Dominic Mohr (Bonn) for assistance with the measurements.

References

1. Barthlott, W. Die Selbstreinigungsfähigkeit pflanzlicher Oberflächen durch Epicuticularwachse. In *Klima- und Umweltforschung an der Universität Bonn;* Rheinische Friedrich-Wilhelms-Universität, Bonn, Ed.; Bornemann: Bonn, 1992; pp 117–120.
2. Barthlott, W.; Neinhuis, C. *Planta* **1997,** *202,* 1–8. doi:10.1007/s004250050096

3. Barthlott, W.; Neinhuis, C. *Biol. Unserer Zeit* **1998,** *28,* 314–321. doi:10.1002/biuz.960280507
4. Bhushan, B.; Jung, C. J.; Nosonovsky, M. Lotus Effect: Surfaces with Roughness-Induced Superhydrophobicity, Self-Cleaning, and Low Adhesion. In *Springer Handbook of Nanotechnology,* 3rd ed.; Bhushan, B., Ed.; Springer: New York, 2010; pp 1437–1524.
5. Rentschler, I. *Planta* **1971,** *96,* 119–135. doi:10.1007/BF00386362
6. Holloway, P. J. *Pestic. Sci.* **1970,** *1,* 156–163. doi:10.1002/ps.2780010411
7. Neinhuis, C.; Barthlott, W. *Ann. Bot. (Oxford, U. K.)* **1997,** *79,* 667–677. doi:10.1006/anbo.1997.0400
8. Mockenhaupt, B.; Ensikat, H. J.; Spaeth, M.; Barthlott, W. *Langmuir* **2008,** *24,* 13591–13597. doi:10.1021/la802351h
9. Wagner, P.; Fürstner, R.; Barthlott, W.; Neinhuis, C. *J. Exp. Bot.* **2003,** *54,* 1295–1303. doi:10.1093/jxb/erg127
10. Barthlott, W.; Neinhuis, C.; Jetter, R.; Bourauel, T.; Riederer, M. *Flora (Jena)* **1996,** *191,* 169–174.
11. Ensikat, H. J.; Boese, M.; Mader, W.; Barthlott, W.; Koch, K. *Chem. Phys. Lipids* **2006,** *144,* 45–59. doi:10.1016/j.chemphyslip.2006.06.016
12. Ensikat, H. J.; Schulte, A. J.; Koch, K.; Barthlott, W. *Langmuir* **2009,** *25,* 13077–13083. doi:10.1021/la9017536
13. Zhang, J.; Wang, J.; Zhao, Y.; Xu, L.; Gao, X.; Zheng, Y.; Jiang, L. *Soft Matter* **2008,** *4,* 2232–2237. doi:10.1039/b807857b
14. Cheng, Y. T.; Rodak, D. E.; Wong, C. A.; Hayden, C. A. *Nanotechnology* **2006,** *17,* 1359–1362. doi:10.1088/0957-4484/17/5/032
15. Zhang, J.; Sheng, X.; Jiang, L. *Langmuir* **2009,** *25,* 1371–1376. doi:10.1021/la8024233
16. Extrand, C. W.; Moon, S. I. *Langmuir* **2010,** *26,* 17090–17099. doi:10.1021/la102566c
17. Coward, J. L. *J. Biol. Phys.* **2010,** *36,* 405–425. doi:10.1007/s10867-010-9192-6
18. Mazliak, P. Chemistry of Plant Cuticles. In *Progress in Phytochemistry, Vol. 1;* Reinhold, L.; Liwschitz, Y., Eds.; Interscience Publishers: New York, 1968; pp 49–111.
19. Holloway, P. J. *J. Sci. Food Agric.* **1969,** *20,* 124–128. doi:10.1002/jsfa.2740200214
20. Leroy, F.; Müller-Plathe, F. *Langmuir* **2011,** *27,* 637–645. doi:10.1021/la104018k
21. Koch, K.; Ensikat, H. J. *Micron* **2008,** *39,* 759–772. doi:10.1016/j.micron.2007.11.010
22. Varanasi, K. K.; Deng, T.; Hsu, M.; Bhate, N. Hierarchical Superhydrophobic Surfaces Resist Water Droplet Impact. In *Nanotechnology 2009: Biofuels, Renewable Energy, Coatings, Fluidics and Compact Modeling;* Nanoscience and Technology Institute, Cambridge, Ed.; Technical Proceedings of the 2009 NSTI Nanotechnology Conference and Expo, Vol. 3; CRC Press: Boca Raton, 2009; pp 184–187.
23. Nearing, M. A.; Bradford, J. M.; Holtz, R. D. *Soil Sci. Soc. Am. J.* **1987,** *51,* 1302–1306. doi:10.2136/sssaj1987.03615995005100050038x
24. Barthlott, W.; Schimmel, T.; Wiersch, S.; Koch, K.; Brede, M.; Barczewski, M.; Walheim, S.; Weis, A.; Kaltenmeier, A.; Leder, A.; Bohn, H. F. *Adv. Mater.* **2010,** *22,* 1–4. doi:10.1002/adma.201090075
25. Koch, K.; Barthlott, W. *Philos. Trans. R. Soc., A* **2009,** *367,* 1487–1509. doi:10.1098/rsta.2009.0022
26. Bush, J. W. M.; Hu, D. L.; Prakash, M. *Adv. Insect Physiol.* **2007,** *34,* 117–192. doi:10.1016/S0065-2806(07)34003-4
27. Balmert, A.; Bohn, H. F.; Ditsche-Kuru, P.; Barthlott, W. *J. Morphol.*, in press. doi:10.1002/jmor.10921
28. Ensikat, H. J.; Ditsche-Kuru, P.; Barthlott, W. Scanning electron microscopy of plant surfaces: simple but sophisticated methods for preparation and examination. In *Microscopy: Science, Technology, Applications and Education;* Méndez-Vilas, A.; Diaz, J., Eds.; FORMATEX Microscopy series No. 4, Vol. 1; Formatex Research Center: Badajoz, Spain, 2010; pp 248–255.
29. Robinson, D. G.; Ehlers, U.; Herken, R.; Herrmann, B.; Mayer, F.; Schürmann, F. W. *Präparationsmethodik in der Elektronenmikroskopie;* Springer: Heidelberg, 1985; p 39.
30. Ensikat, H. J.; Neinhuis, C.; Barthlott, W. *Int. J. Plant Sci. (Chicago, IL, U. S.)* **2000,** *161,* 143–148. doi:10.1086/314234
31. Koch, K.; Dommisse, A.; Barthlott, W. *Cryst. Growth Des.* **2006,** *6,* 2571–2578. doi:10.1021/cg060035w

License and Terms

Beilstein Journal of Nanotechnology

Functional morphology, biomechanics and biomimetic potential of stem–branch connections in *Dracaena reflexa* and *Freycinetia insignis*

Tom Masselter[*1,2], Sandra Eckert[1] and Thomas Speck[1,2]

Full Research Paper

Open Access

Address:
[1]Plant Biomechanics Group Freiburg, Botanic Garden, Faculty of Biology, University of Freiburg, Schänzlestraße 1, 79104 Freiburg, Germany and [2]Competence Network Biomimetics and Bionics Competence Network BIOKON e.V

Email:
Tom Masselter[*] - tom.masselter@biologie.uni-freiburg.de

* Corresponding author

Keywords:
Biomimetics; branching; *Dracaena reflexa*; *Freycinetia insignis*; monocotyledons

Beilstein J. Nanotechnol. **2011,** *2,* 173–185.
doi:10.3762/bjnano.2.21

Received: 22 December 2010
Accepted: 02 March 2011
Published: 24 March 2011

This article is part of the Thematic Series "Biomimetic materials".

Guest Editors: W. Barthlott and K. Koch

Abstract

Branching in plants is one of the most important assets for developing large arborescent growth forms with complex crowns. While the form and development of branching in gymnosperms and dicotyledonous trees is widely understood, very little is known about branching patterns and the structure of branch–stem-junctions in arborescent monocotyledons. For a better and quantitative understanding of the functional morphology of branch–stem-junctions in arborescent monocotyledons, we investigated the two species *Dracaena reflexa* and *Freycinetia insignis*. While *D. reflexa* is able to develop large arborescent forms with conspicuous crowns by anomalous secondary growth, *F. insignis* remains relatively small and is only capable of primary growth. Biomechanical investigations were performed by applying vertical loads up to rupture to lateral branches of both species. This allows the analysis of the fracture mechanics and the determination of the maximal force, stress and strain at rupture as well as the fracture toughness. Functional morphology was correlated with the mechanical behaviour of these plants and compared to data of other dicotyledonous trees. The high energy absorption found in the rupture process of lateral branches of *D. reflexa* and *F. insignis* makes them promising biological concept generators with a high potential for biomimetic implementation, i.e., for the development of branched fibre-reinforced technical composites. A wide range of constructional elements with branched (sub-)structures can be optimised by using solutions inspired by plant ramifications, e.g., in automotive and aerospace engineering, architecture, sports equipment and prosthetic manufacturing.

Introduction

One of the most conspicuous features of woody plants is their ability to form branches and canopies. Some of these branches can grow continuously and be as long-lived as the stems. This has always intrigued naturalists and botanists, and therefore, branching in woody plants has been the subject of scientific studies for centuries. These studies have increased in number

over the past decades and improved our understanding of the importance and the form–structure–function-relationship of branching significantly (e.g., [1-9]). It has become evident that branching is essential for woody plants, as it allows space to be occupied and trap solar energy in an efficient way (e.g., [5]). However, these benefits are coupled with disadvantages such as increased magnitude and complexity of mechanical loads. Therefore, structural and mechanical adaptation on different hierarchical levels can be observed both in main stems as well as in lateral branches [9-12], and particularly in the region of branch–stem-junctions [4,6-8]. Due to these optimisations of form and structure, notch stresses in branch–stem-junctions can be significantly reduced or even avoided [6-8]. These ramifications are often highly stiff yet flexible enough to avoid fracture or tearing apart even under high mechanical loading.

While numerous studies exist on branching in gymnosperms and dicotyledonous trees, relatively little is known about branching in monocotyledons. This could be due to the fact that branching is observed much more frequently in broad leaved and gymnosperm trees with secondary cambial growth than in arborescent monocotyledons. Monocotyledons seldom branch, normally only after bloom with a terminal inflorescence or when the apical meristem of the axis is damaged or destroyed [13]. The ramifications of monocotyledons can vary considerably in shape and number (Figure 1). The angle between the main stem and the lateral branch can differ considerably among monocotyledons. Small monocotyledons such as *Freycinetia* often show high values for stem–branch angles of up to 90° (Figures 1G, 2B), which are comparable to the values found in many gymnosperms and broad leaved trees. Other monocotyledons, such as species of *Dracaena* or *Yucca*, can grow much higher, developing considerable stem dimensions. They develop large arborescent growth forms often with crowns (Figure 1) due to their ability to increase stem and branch diameter by anomalous secondary growth. Thus, additional fibrous bundles in an often lignified parenchymatous ground tissue are differentiated due to secondary growth processes by a cambium located in the cortex region [3,14-19]. In these monocotyledons, the stem–branch angles typically are much lower, about 60°, but can vary considerably (Figure 1 and Figure 2, see [1]). However, the degree of the branching angles is to some extent limited by the inner bauplan of these plants. In contrast to gymnosperms and dicotyledonous, trees in which the wooden

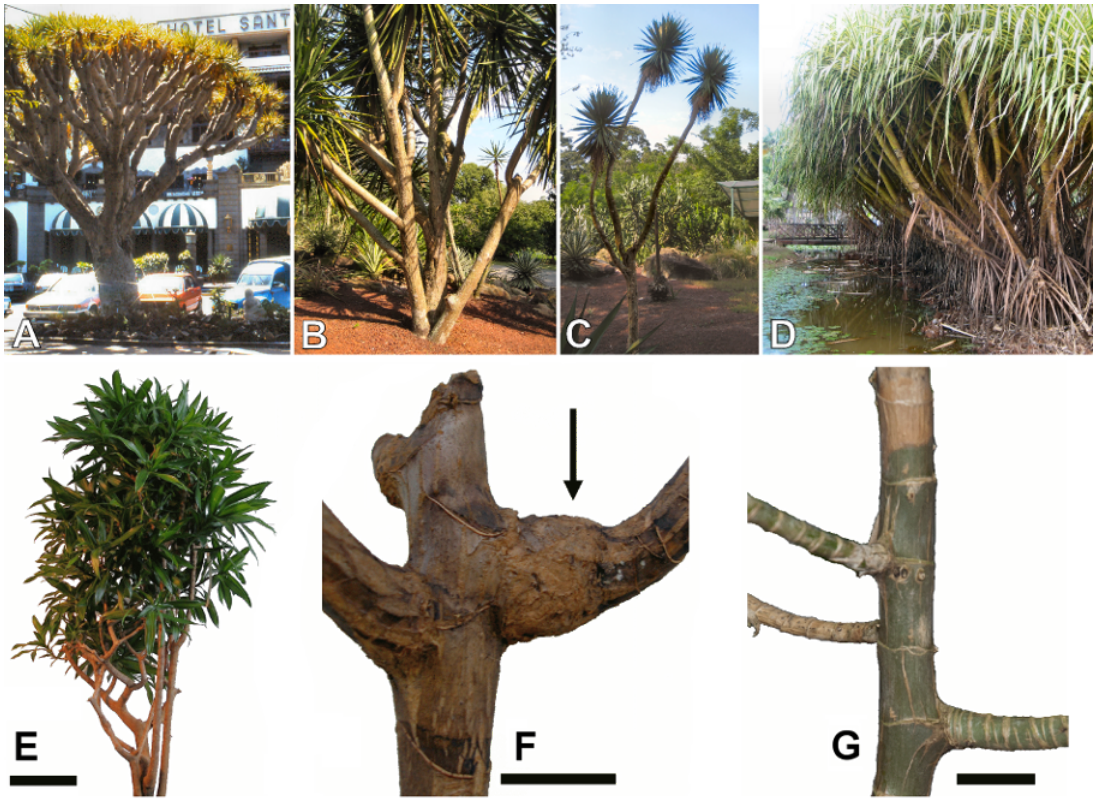

Figure 1: Arborescent monocotyledons. (A) *Dracaena draco*, (B) *Dracaena yuccaeifolia,* (C) *Yucca* sp., (D) *Pandanus* sp. © Thomas Speck. Morphology of monocotyledons analysed. (E) Branched specimen of *Dracaena reflexa.* Scale bar = 200 mm, (F) Detail of a branched specimen of *Dracaena reflexa*. Anomalous secondary growth has led to a thickened zone in the region of branch–stem-junction (arrow). Scale bar = 20 mm, (G) Branched specimen of *Freycinetia insignis.* Scale bar = 15 mm.

tissues are compact and a relatively large amount of secondary wood from the main stem is in direct connection with the branches, in arborescent monocotyledons vascular bundles with fibre caps (both summed up as 'fibrous bundles' in this study) are isolated, i.e., with no or little tangential or radial interconnection, and arranged in a parenchymatous, often lignified cellular ground tissue [14,17-25] (Figure 2). This makes the stems flexible, yet decreases their static load-bearing capacity. It can be speculated that branching angles are limited in large arborescent monocotyledons so that critical bending moments leading to fracture are avoided.

Some of the fibrous bundles run from the main stem into the lateral branches [2]. Apart from that, very little is known about their anatomy. The arrangement and course of the fibrous bundles in branch–stem-junctions of arborescent monocotyledons and the functional morphology and mechanics of branch–stem-junctions have yet not been analysed quantitatively. For our studies we chose two branched arborescent monocotyledons, *Dracaena reflexa* and *Freycinetia insignis*, in order to answer the following questions:

1. How are the fibrous bundles in the main stem connected to those in the lateral branch? and what are the structure and arrangement of the fibrous bundles in the regions of branch–stem-junctions?
2. What are the biomechanical properties of the branch–stem-junctions?
3. Does a quantifiable relationship exist between morphology/anatomy and the biomechanical properties of the branch–stem-junctions?
4. Are the values of the biomechanical properties (i.e., maximal force, fracture toughness as well as stress and strain) of the branch–stem-junctions in arborescent monocotyledons comparable to the values found in dicotyledonous trees?

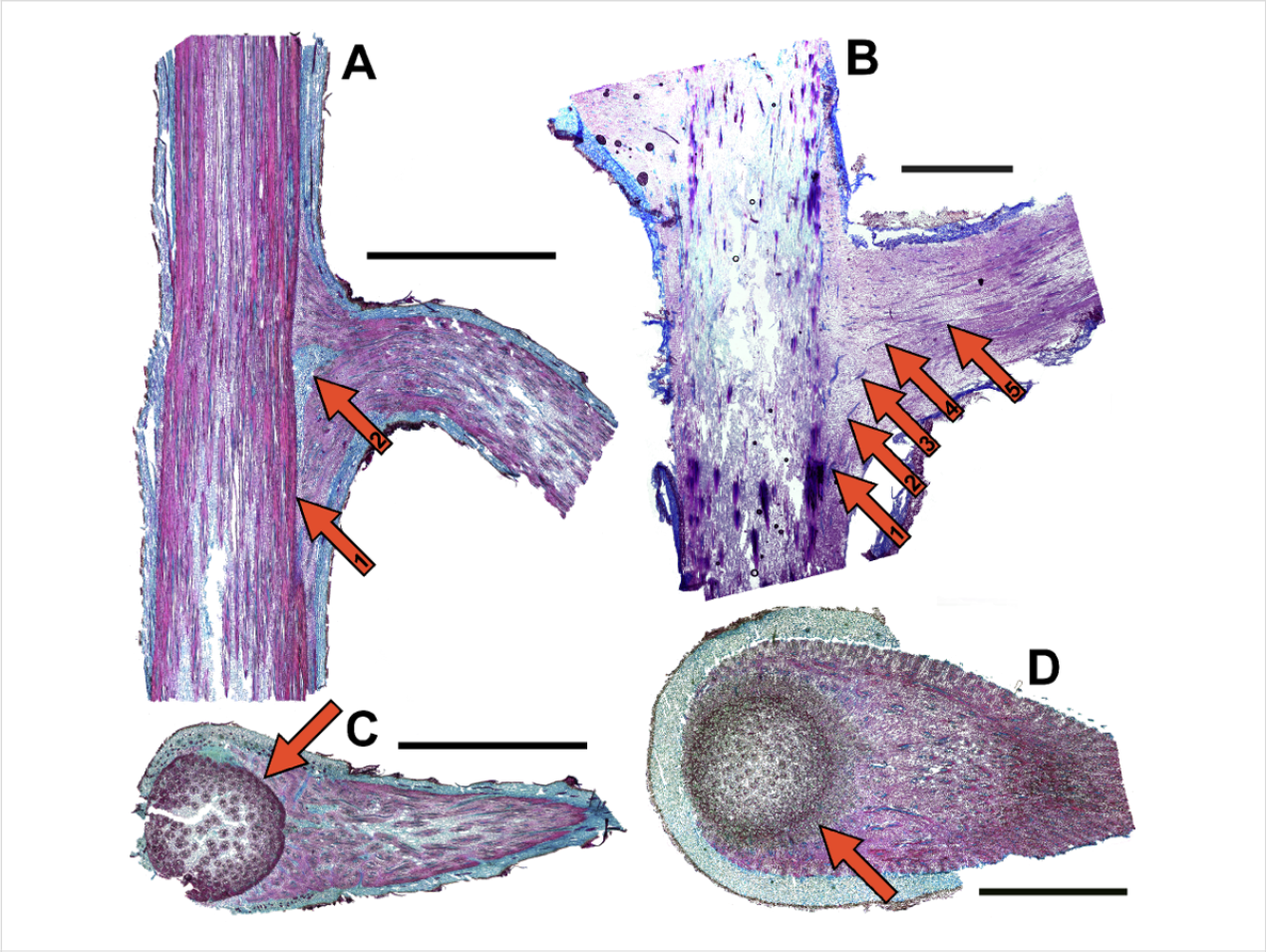

Figure 2: Branch–stem-junction of *Freycinetia insignis* and *Dracaena reflexa*. (A) *F. insignis*, longitudinal section, arrow 1: distinct border-line between fibrous bundles in the main stem and in the lateral branch, arrow 2: zone of partly lignified parenchymatous ground tissue without fibrous bundles, (B) *D. reflexa*, longitudinal section, arrows 1–5; gradual transition from fibrous bundles in the main stem (arrow 1) to fibrous bundles in the lateral branch (arrow 5), (C) *F. insignis*, cross-section, arrow: distinct border-line between fibrous bundles in the main stem and in the lateral branch, (D) *D. reflexa*, cross-section, arrow: gradual transition zone showing fibrous bundles in the main stem and fibrous bundles in the lateral branch. Scale bars = 3 mm.

Results

Morphology

In *Dracaena reflexa*, the fibrous bundles of the lateral branches clasp around the main stem resulting in a flange mounted structure (Figure 2B,D, see Supporting Information File 1). Some of the largely paraxial fibrous bundles in the main stem are connected with the predominantly fibrous bundles in the lateral branches so that there is no distinct separation boundary between the bundles in the stem and the bundles in the branch (Figure 2B,D) but rather a gradual transition. The branch bundles are also paraxial oriented with regard to the lateral branch resulting in a perpendicular orientation relative to the main stem (Figure 2B,D, see Supporting Information File 1). In *F. insignis*, the fibrous bundles are arranged in a generally similar pattern that, however, differs in several important aspects. The fibrous bundles of the lateral branches also clasp around the stem. However, the fibrous bundles of the lateral branches are not directly interconnected with the fibrous bundle system in the median section of the main stem (Figure 2A,C). Additionally, it is noticeable that there exists a purely parenchymatous region between the main stem and the lateral branches in the region of the branch–stem-junction (Figure 2A).

Biomechanical tests

Three main modes of mechanical failure (Figure 3) were found in the 31 samples of *Dracaena reflexa* when the branches were loaded with over-critical forces: (1) failure in the stem (11 samples, Figure 3A) with delamination between the fibrous bundles and the parenchymatous ground tissue resulting in longitudinal splitting of the main stem, (2) sickle-shaped detachment of the lateral branch (13 samples, Figure 3B), i.e., failure in the region where the branch is connected to the stem, and (3) failure in the branch (7 samples, Figure 3C). The different modes of failure are correlated with typical shapes of the force-displacement-curves (Figure 3D–F).

Two modes of failure occurred in the 19 samples of *Freycinetia insignis*: (1) Most often a detachment of the branch resulting in a flat fracture surface was observed (16 samples), while (2) failure in the region where the branch is connected to the stem occurred in three cases only.

Maximal force F_{max} [kN]

The maximal force F_{max} increases with increasing diameter of the lateral branches (Figure 4, Table 1). This correlation is statistically significant. It holds true for each mode of failure and the pooled data of all fracture modes in *Dracaena reflexa* (Figure 4A), and for the mode of flat detachment in *Freycinetia insignis* (Figure 4B). Due to the small sample size the correlation for the mode of failure in the branch could not be tested statistically in *F. insignis*. It is noticeable in *D. reflexa* that smaller branches tend to crack in the branch and that less force is needed than for the other modes of failure (Table 2). In *D. reflexa* the maximal force found for the failure mode 'failure in the branch' is significantly smaller than for the other modes of failure (Table 1). Maximal forces found in branches with diameters ranging from 3.5 to 5.4 mm are significantly lower in *D. reflexa* (94.30 ± 48.53 N, Table 2) than in branches of *F. insignis* with the same diameter range (199.62 ± 117.37 N, Table 2).

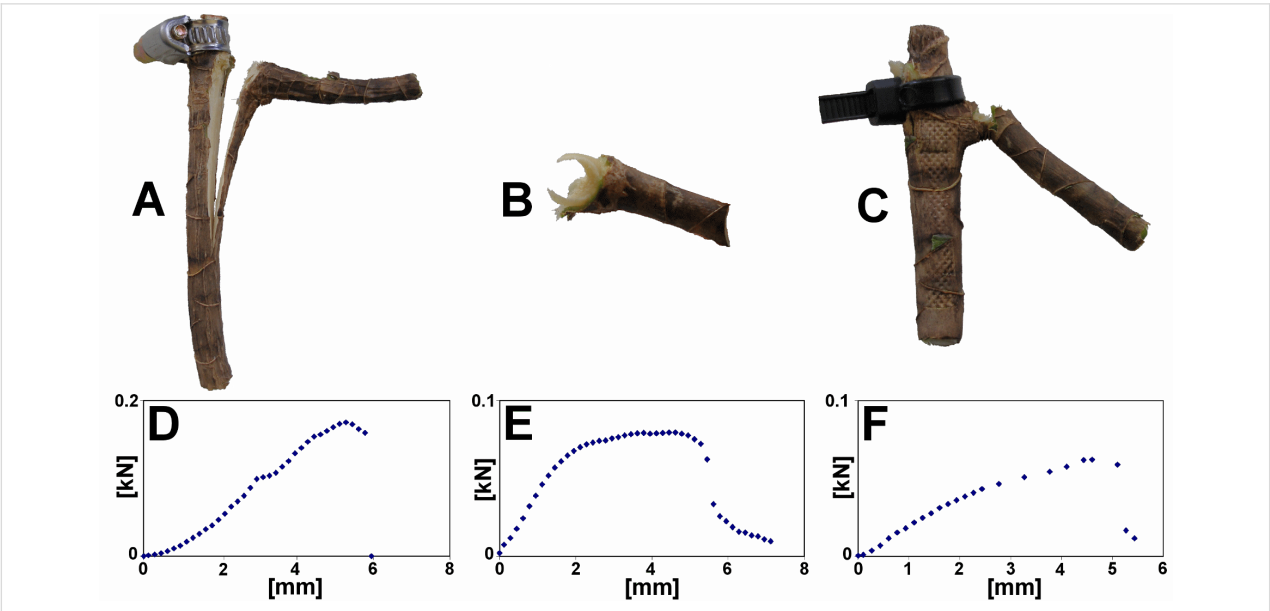

Figure 3: Breaking experiments. Different modes of fracture found in *Dracaena reflexa*. (A) Fracture in the stem, (B) sickle-shaped detachment, (C) fracture in the branch; (D, E, F) force-displacement-curves resulting from the experiments carried out in A, B, and C, respectively.

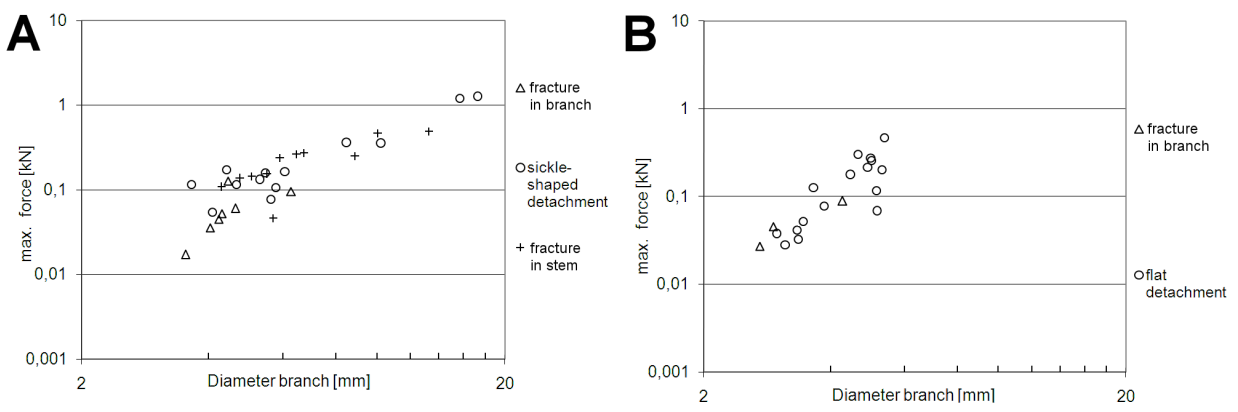

Figure 4: Bivariate, double logarithmic plot of maximal forces vs diameter of lateral branches (d_1 or d_2 depending on the mode of fracture (see 'Experimental' section) in *Dracaena reflexa* (A) and *Freycinetia insignis* (B).

Table 1: Statistical analysis of biomechanical and morphological data of *Dracaena reflexa* and *Freycinetia insignis*[a].

	Dracaena reflexa								*Freycinetia insignis*				
	failure mode	n	Normality test	KW[b]	Dunn's[c]		Correlation[c]		failure mode	n	Normality test	Correlation[d]	
					sickle	stem	failure mode	All				failure mode	All
Maximal force F_{max} [kN]	branch	7	-	+	+	+	↑	↑	branch	3	+	/	↑
	sickle	13				-	↑		flat	16		↑	
	stem	11					↑				\		
Fracture toughness until F_{max} [kJm^{-2}]	branch	7	-	-	/		-	↑	branch	3	+	/	-
	sickle	13					-		flat	16		↑	
	stem	11					-				\		
Fracture toughness until failure [kJm^{-2}]	branch	7	-	-	/		-	↑	branch	3	+	/	-
	sickle	13					-		flat	16		↑	
	stem	11					-				\		
Stress at failure [MPa]	branch	7	-	-	/		-	↓	branch	3	+	/	-
	sickle	13					-		flat	16		-	
	stem	11					-				\		
Strain at failure [/]	branch	7	-	+	-	+	↑	↓	branch	3	-	/	-
	sickle	13				-	-		flat	16		-	
	stem	11					-				\		

[a]Normality test, Kruskal–Wallis test or Dunn's test with 5% level of significance (+) or below (-). The Pearson product moment test or the Spearman rank correlation test indicate whether the increase of biomechanical data (e.g., maximal force F_{max}) is correlated with an increase (↑) or decrease (↓) of the branch diameter or whether there is no statistically significant correlation (-). [b]The Kruskal–Wallis test is a non-parametric method for testing equality of population medians among groups. [c]The Dunn's test was used. [d]The parametric Pearson product moment test was used.

Table 2: Morphological and biomechanical data of *Dracaena reflexa* and *Freycinetia insignis*[a].

	Dracaena reflexa (branch diameter 3.52–5.35 mm)						*Freycinetia insignis* (branch diameter 3.52–5.35 mm)						Stat. sign. difference
	failure mode	n	mean value	s.d.	mean value all	s.d. all	failure mode	n	mean value	s.d.	mean value all	s.d. all	
Maximal force F_{max} [kN]	branch	6	56.06	37.41	94.30	48.53	branch	1	89.02	/	199.62	117.37	+[b]
	sickle	5	118.76	42.65			flat	11	209.67	117.55			
	stem	3	130.02	19.39					\				
Fracture toughness until F_{max} [kN]	branch	6	10.41	4.91	10.53	4.92	branch	1	17.25	/	14.93	9.31	-[b]
	sickle	5	9.42	3.08			flat	11	14.72	9.74			
	stem	3	12.62	8.27					\				
Fracture toughness until failure [kN]	branch	6	10.74	5.10	11.01	5.15	branch	1	17.74	/	15.54	9.56	-[c]
	sickle	5	10.09	3.15			flat	11	15.34	10.01			
	stem	3	13.08	8.89					\				
Stress at failure [MPa]	branch	6	30.40	11.38	27.86	11.17	branch	1	42.95	/	50.11	14.26	+[c]
	sickle	5	26.54	10.93			flat	11	50.76	14.77			
	stem	3	24.96	14.57					\				
Strain at failure [/]	branch	6	0.85	0.58	0.58	0.48	branch	1	0.82	/	0.31	0.19	-[b]
	sickle	5	0.47	0.33			flat	11	0.27	0.11			
	stem	3	0.21	0.11					\				

[a]The significance of the differences in *D. reflexa* and *F. insignis* was calculated with the Kruskal–Wallis test or One Way Analysis of Variance with a 5% level of significance (+) or below (-). [b]Data tested with Kruskal–Wallis One Way Analysis of Variance on Ranks. [c]Data tested with One Way Analysis of variance.

Fracture toughness until F_{max} [kJm^{-2}]

The increase of the fracture toughness until F_{max} with increasing diameter of the lateral branches is statistically significant only for the pooled data of all fracture modes in *D. reflexa* (Figure 5A, Table 1). A similar but not statistically significant trend can also be observed in *F. insignis* (Figure 5C, Table 1). No statistically significant difference exists between the different failure modes in *D. reflexa*. Fracture toughness until F_{max} found in branches with diameters from 3.5 to 5.4 mm is not significantly different in *D. reflexa* (10.53 ± 4.92 kJm^{-2}, Table 2) compared to *F. insignis* (14.93 ± 9.31 kJm^{-2}, Table 2).

Fracture toughness until failure [kJm^{-2}]

The increase of the fracture toughness until failure also increases statistically significant with increasing diameter of the lateral branches for the pooled data of all fracture modes in *D. reflexa* (Figure 5B, Table 1). A similar but not statistically significant trend can also be observed in *F. insignis* (Figure 5D, Table 1). No statistically significant difference was found between the different failure modes in *D. reflexa*. Fracture toughness until failure found in branches with diameters from 3.5 to 5.4 mm is not significantly different in *D. reflexa* (11.01 ± 5.15 kJm^{-2}, Table 2) compared to *F. insignis* (15.54 ± 9.56 kJm^{-2}, Table 2).

Stress at failure [MPa]

The data do not show a statistical difference between the different failure modes in *D. reflexa* (Figure 6A, Table 1). A statistically significant trend only exists for the decrease of stress at failure with increasing diameter in the pooled data of all fracture modes in *D. reflexa* (Figure 6A, Table 1). No correlation between stress at failure and diameter of the lateral

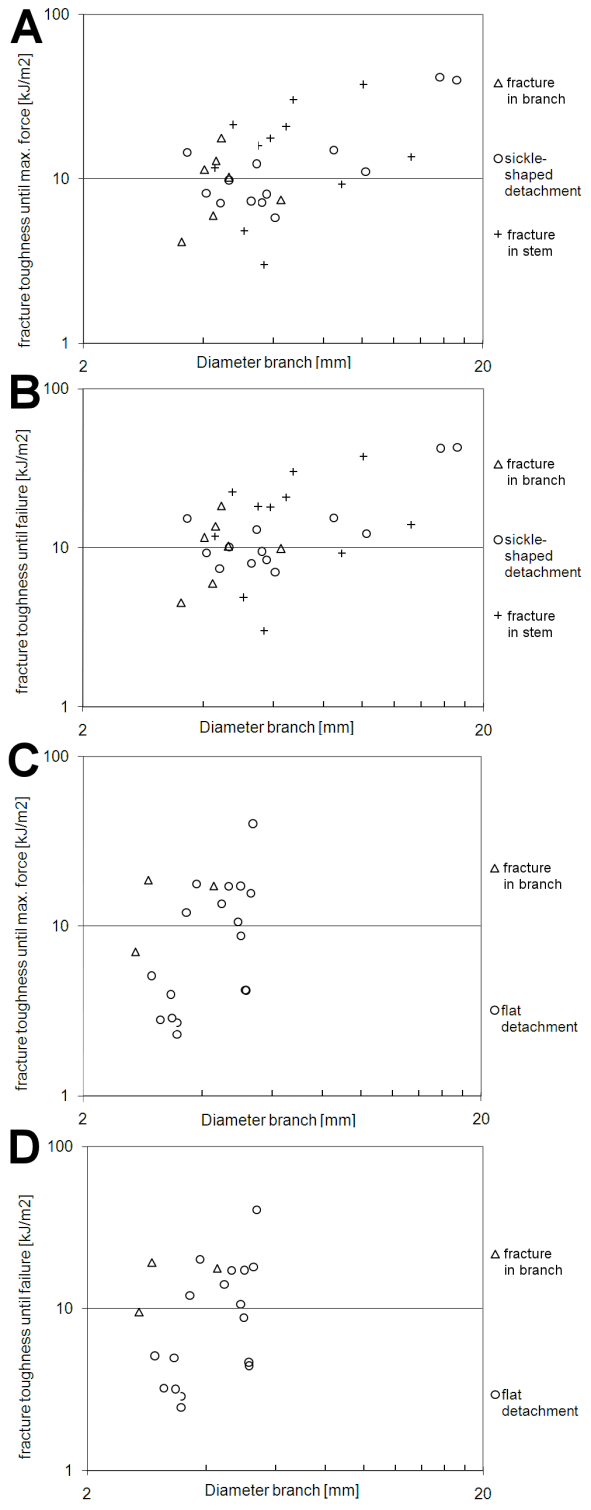

Figure 5: Bivariate, double logarithmic plot of fracture toughness until maximal force vs diameter of lateral branches (d_1 or d_2 depending on the mode of fracture (see 'Experimental' section) in *Dracaena reflexa* (A) and *Freycinetia insignis* (C). Bivariate, double logarithmic plot of fracture toughness until failure vs diameter of lateral branches (d_1 or d_2 depending on the mode of fracture (see 'Experimental' section) in *Dracaena reflexa* (B) and *Freycinetia insignis* (D).

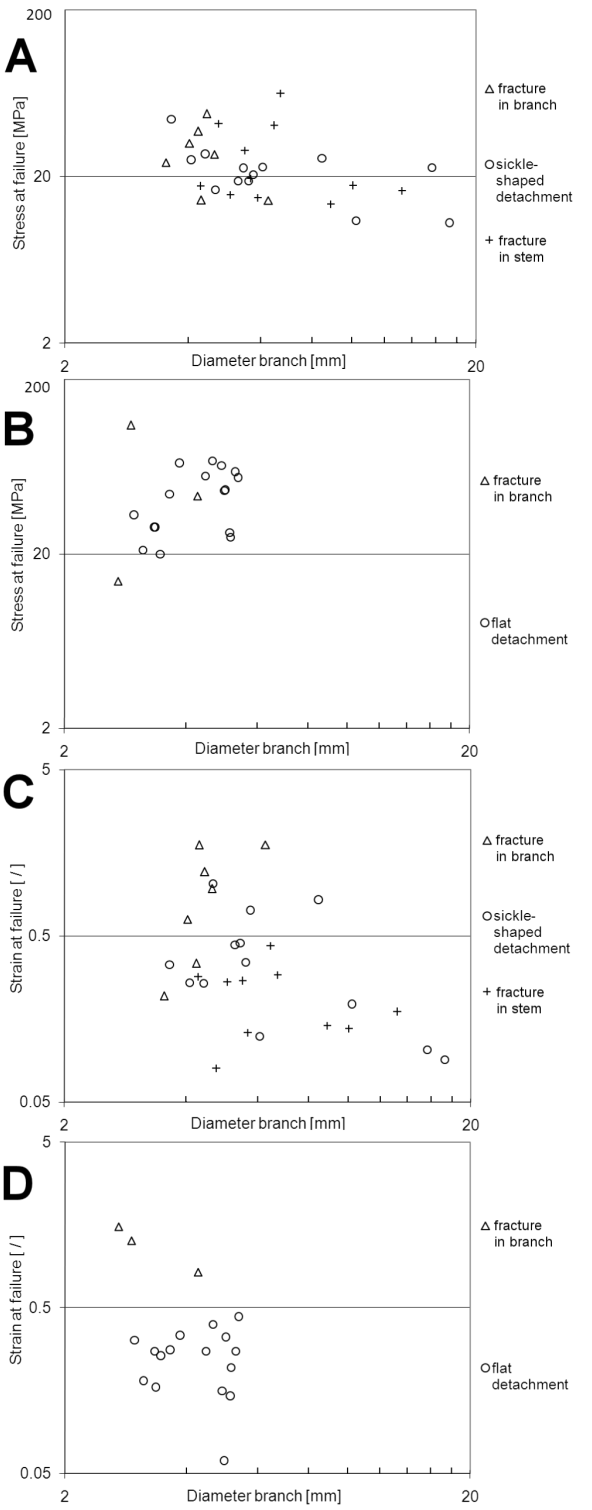

Figure 6: Bivariate, double logarithmic plot of stress at failure vs diameter of lateral branches (d_1 or d_2 depending on the mode of fracture (see 'Experimental' section) in *Dracaena reflexa* (A) and *Freycinetia insignis* (B). Bivariate, double logarithmic plot of strain at failure vs diameter of lateral branches (d_1 or d_2 depending on the mode of fracture (see 'Experimental' section) in *Dracaena reflexa* (C) and *Freycinetia insignis* (D).

branches could be observed in *F. insignis* (Figure 6B, Table 1). In branches with diameters from 3.5 to 5.4 mm stress at failure is significantly higher in *F. insignis* (50.11 ± 14.26 MPa, Table 2) than in *D. reflexa* (27.86 ± 11.17 MPa, Table 2).

Strain at failure [/]

In *D. reflexa*, strain at failure is significantly higher for the mode 'failure in the branch' than in the mode 'failure in the stem' (Figure 6C, Table 1). The failure mode 'sickle-shaped detachment' does not differ from both other failure modes. The decrease of strain at failure with increasing branch diameters is significant for the pooled data of all fracture modes in *D. reflexa* (Figure 6C, Table 1). For the mode 'failure in the branch' a significant increase of strain at failure with increasing diameter was found. No correlation between strain at failure and diameter of the lateral branches could be observed in *F. insignis* (Figure 6D, Table 1). In branches with diameters from 3.5 to 5.4 mm, no significant difference for the strain at failure could be found between *D. reflexa* (0.58 ± 0.48, Table 2 and *F. insignis* (0.31 ± 0.19, Table 2).

Discussion

Morphology and biomechanics

The monocotyledonous mode of branching has important implications for the morphology and anatomy in *Dracaena reflexa* and *Freycinetia insignis*. It determines the shape of the branch–stem-junctions, the arrangement and course of the fibrous bundles in the main stem and in the lateral branches and their interconnection. The mode of branching again depends on the apical or distal position of the branching on the stem [2]. Due to this, a certain variability of the attachment modes exists, which may account for the relatively large scatter of the biomechanical data (Figures 4–6). It can be assumed that the ability to build secondary tissues has a high impact on growth form and biomechanics. While the attachment modes of *D. reflexa* and *F. insignis* are generally similar in that the lateral branches clasp around the main stem (Figure 2), the distinct separation (in some parts by a layer of parenchymatous tissues) of lateral branches from the main stem found in *F. insignis* contrasts with the gradual transition between fibrous bundles secondarily formed in the main stem and the lateral branches observed in *D. reflexa* (Figure 2B,D). Furthermore, due to the missing ability for anomalous secondary growth, *F. insignis* is not able to form secondary tissues [26] including fibrous bundles. Therefore, this species cannot (or only to a very limited extent) 'react' adaptively to an increase in loads acting on stem, branch and branch–stem-junction when the length of the branch increases. It can therefore be assumed that the branch–stem-junctions in *F. insignis* are configured to carry high loads from the very start of their development, i.e., when these interconnections are formed by primary establishment growth. This could explain why *F. insignis* is able to carry higher loads in small branches compared to *D. reflexa* (Table 2).

Qualitative biomechanics: Failure modes

In *D. reflexa*, the fibrous bundles that are connected to the lateral branches clasp around the main stem resulting in a sickle-shaped structure (Figure 2B,D, see Supporting Information File 1). This accounts for the high number of sickle-shaped failures in which the outer fibrous bundles remain attached to the lateral branches and are detached from the main stem (Figure 3B) following the stem clasping arrangement of the fibrous bundles of the branch (Figure 2B,D, see Supporting Information File 1). Failure in the branch occurs mainly in relatively young, possibly not fully lignified branches (see below). Failure in the stem results in longitudinal cracks which very quickly reach a critical length and lead to failure of the main stem. This failure mode is the most disadvantageous one for the plant and can be lethal as the mechanical stability of the stem is drastically reduced, water and assimilate transport is seriously disturbed and germs can easily access and infect the large wound surface of the plant. It remains unclear whether and to what extent this failure mode may occur due to an experimental artefact that occurs in spite of clamping the apical cut off part of the stem circumferentially with a clip collar to avoid longitudinal splitting.

In *F. insignis*, the fibrous bundles are arranged in a different pattern with no gradual transition between the fibrous bundles in the main stem and the fibrous bundles in the lateral branches as found in *D. reflexa*. The fibrous bundles in stem and branch in *F. insignis* are anatomically strictly separated (Figure 2A,C), and the detachment modes mirror this arrangement. *F. insignis* typically (in 84% of failures) shows a detachment of the fibrous bundles of the lateral branches from those of the main stem resulting in a relatively flat fracture surface. In some cases (in 16% of failures) branch–stem-junctions with low diameters of lateral branches (under 1 mm) fail in the branch. It can be speculated that these very young branches are not yet fully lignified and therefore structurally weaker than thicker ones. Very young stems in *F. insignis* have fully lignified fibrous bundles but they lack a somewhat more densely packed zone of lignified fibrous bundles at the transition between stem and branch, also the ground tissue appears to be less lignified than the ground tissue in older axes.

(Semi-)Quantitative biomechanics

One of the most prominent results is that the values for maximal force and for stress at failure are significantly higher in *Freycinetia insignis* than in *Dracaena reflexa*. In fact all tested mechanical parameters are higher in *F. insignis*, even if not significantly. A possible reason for this may be the lack of

anomalous secondary growth in *F. insignis* which is thereby restricted to develop only comparatively thin main stems and lateral branches throughout its entire ontogenetic trajectory. It can be argued that these 'thin branchings' in *F. insignis* with diameters of lateral branches between 3.52 and 5.35 mm are fully mature and are able to take up higher loads than branches in *D. reflexa* with the same diameter. In contrast to *F. insignis*, the same diameters are relatively small for lateral branches of *D. reflexa* so that the fibrous bundles may not yet have reached a fully lignified state. This is indicated by staining experiments for lignin in which young axes of *Dracaena reflexa* (3–5 mm) are less stained than older axes (above 7 mm).

Comparison with data of branchings of dicotyledonous trees

No comparative data for maximal force or fracture toughness measured with a similar setup could be found for dicotyledonous trees in the literature. However, the maximal forces measured for branching of *D. reflexa* and *F. insignis* are intuitively high with a mean value of 199.62 ± 117.37 N and maximum values of up to 0.3 kN for *F. insignis* in a branch no thicker than 5mm (in larger stems of *Dracaena reflexa* with a branch diameter of 20 mm, the maximal force exceeded 10 kN, data not shown here). Values for fracture toughness can be also considered to be high as the maximal forces are high and large displacements are generated before the branches break off.

Values for stress at failure are comparable to values found for dicotyledonous trees, [4] reported for different species of willows with an identical experimental setup and comparable branch diameters between 2 and 6 mm, mean values for stress at failure ranging from 18 to 57 MPa.

On the other hand, the values for strain at failure are much higher than the values reported for dicotyledonous trees [4] found for different species of willows with an identical experimental setup with mean values for the strain at failure that ranged from 6% to 11%. These values are very much lower than the 58% strain at failure found in *D. reflexa* and the 31% strain at failure found in *F. insignis*.

Based on the structural data presented, one may hypothesize that one reason for the high values of strain at failure found in the two arborescent monocotyledon species is the special stem architecture with loosely interconnected fibrous bundles in a rather flexible parenchymatous ground tissue. Insertion of the fibrous bundles and gradual connection with the ground tissue as well as the intertwining arrangement of the fibrous bundles leads to a structure which allows for a high load bearing capacity combined with high fracture toughness and very high strains at failure.

Outlook: biomimetic potential and implementation

These mechanical properties make the arborescent monocotyledons studied well suited as concept generators for technical implementations in branched fibre-reinforced compound structures such as axel-carriers and frames in automotive engineering and aerospace as well as ramified supporting structures in architecture. The high potential of arborescent monocotyledons is currently being assessed in a joint project whose members include the Plant Biomechanics Group Freiburg, the Institute for Textile Technology and Process Engineering Denkendorf, the Institute of Lightweight Structures and Polymer Technology of the TU Dresden as well as the Botanical Garden of the TU Dresden [27-31]. In this project the hierarchical organisation of branch–stem-junctions of arborescent monocotyledons and columnar cacti is analysed and different biomechanical tests are performed on these plants in order to determine the mechanical parameters of stems, branches, branch–stem-junctions and the different constituent tissues in different directions. This allows for simulation of hierarchical structure and mechanical behaviour of the biological structures and thereby to identify the underlying principles of mechanical optimisation. Some of these principles have already been quantitatively understood, abstracted and first prototypes have been produced that already incorporate different structural and mechanical optimisations (Figure 7).

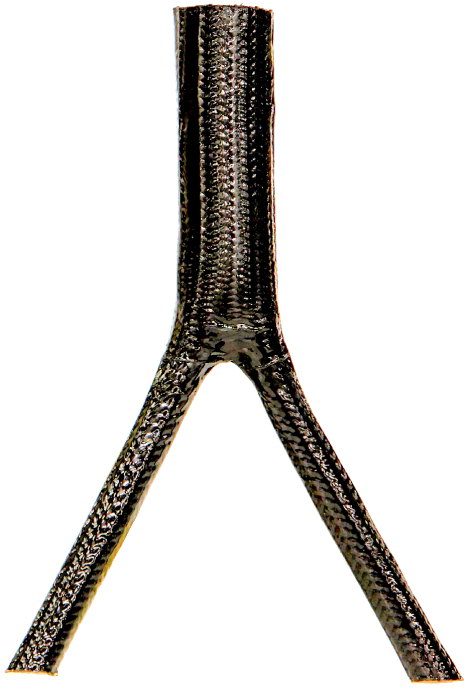

Figure 7: Prototype of biomimetically optimised, braided branched fibre reinforced technical compound structure © ITV Denkendorf.

Experimental

Sampling of *Dracaena reflexa* and *Freycinetia insignis*

The biomechanical properties of 127 branch–stem-junctions of *D. reflexa* and of 37 branch–stem-junctions of *F. insignis* were analysed. Of these, 31 ramifications of *D. reflexa* and 19 of *F. insignis* could be retained for the statistical analysis (Table 1).

The specimens used for this study originated from commercial garden centres (*D. reflexa*) and from the Botanic Garden of Freiburg (*F. insignis*). These plants were chosen as they show a relatively high number of branchings and a lignified branching region with anomalous secondary growth (*D. reflexa,* Figures 1E,F, 2B,D), or without anomalous secondary growth (*F. insignis,* Figures 1G, 2A,C). For the measurements in *D. reflexa* two varieties of *Dracaena* were used: 'Song of India' and 'Song of Jamaica'. These varieties only differ by the form and colour patterns of their leaves while morphology, anatomy and the biomechanical behaviour showed neither apparent nor statistically significant differences. Consequently, the values of these two varieties are pooled and presented as '*D. reflexa*'.

Anatomy and morphology

Thin and semi-thin sections for anatomical analysis were obtained via microtome sectioning and staining with the Fuchsin-Chrysoidin-Astrablue staining method according to Etzold [32] (Figure 2). Additionally, the three-dimensional arrangement and the course of the fibrous bundles was analysed by superimposing photographs of serial sections showing the two-dimensional arrangement of the fibrous bundles one upon the other in order to obtain a stacked sequence (following a similar technique as the one described in [33]) that could be digitized and visualised (see Supporting Information File 1).

Morphometric measurements

Different lengths, diameters, and angles were measured in the main stems and lateral branches of the selected arborescent monocotyledons (Figure 8). These measurements were also carried out in the 'swollen part' where the lateral branches are connected to the main axis. This region has developed by intense 'anomalous secondary growth', and it can be assumed that it is of (high) mechanical importance for the biomechanical performance of the branch stem-junctions.

Experimental setup

The upper part of the cut off main axis was tightly embraced by a cable strap (Figure 9). This gripping helps to avoid longitudinal fractures in the main axis that could result as artefacts from the proximity of the branching region to the point where the main axis is cut off. A steel cable connected to the testing

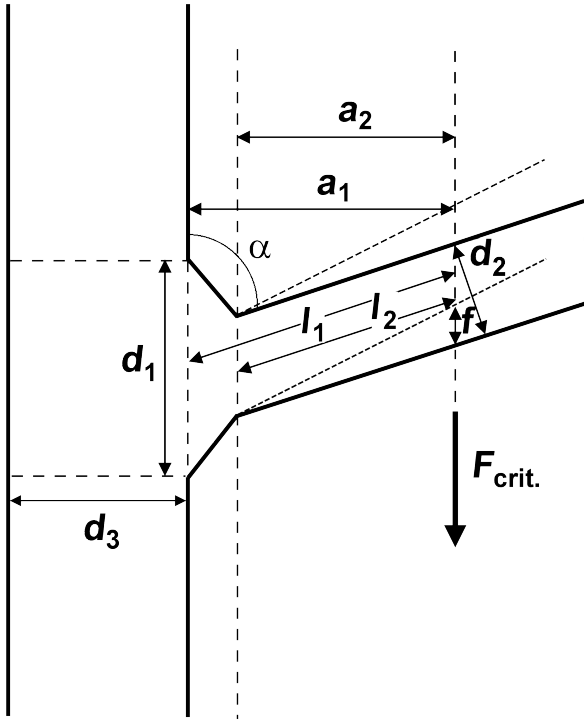

α angle just before breakage between the 'un-swollen region' of the main stem and the 'un-swollen region' of the lateral branch; the swelling is a consequence of intense anomalous secondary growth in the region of the branch–stem-junction

a_1 length of the effective lever arm shortly before fracture (from the 'un-swollen region' of the main stem to the point where the force F from an Instron testing machine is applied to the lateral branch)

a_2 length of the effective lever arm shortly before fracture (from the 'swollen region' of the main stem to the point where the force F from an Instron testing machine is applied to the lateral branch)

d_1 axial length of the 'swollen region' of the main stem

d_2 diameter of the 'un-swollen region' the lateral branch

d_3 diameter of the 'un-swollen region' of the main stem

F force applied vertically, i.e. parallel to the main stem, by the testing machine

F_{crit} critical force F at fracture of the branch

f vertical displacement until rupture of the branch at the point where the force F is applied

l_1 distance from the 'un-swollen region' of the main stem to the point where the force F is applied at the lateral branch

l_2 distance from the 'swollen region' of the main stem to the point where the force F is applied at the lateral branch

Figure 8: Breaking experiments. Schematic drawing of the geometry and parameters used for calculations. The dashed lines show a lateral branch before bending, the solid lines show a main stem and a lateral branch shortly before fracture.

machine was placed around the branch (Figure 9). When the cross-head of the testing machine moves upwards, the steel cable tears off the lateral branch from the main axis (due to the upward movement of the cross-head, the branch–stem-junctions were oriented 'upside-down' in the testing device, see Figure 9). The speed of the cross-head was set to 100 mm/min. The experiments were recorded with a high speed camera at 1000 fps in order to determine the vertical displacement until rupture of the branch at the point where the force F was applied ('f' in Figure 8). The design of the setup as well as the biomechanical calculations were carried out according to the methods described in detail in [4].

Figure 9: Breaking experiments. A critical force F_{crit} is applied to a branch of *Dracaena reflexa* by means of a steel cable connected to an Instron testing device. For technical reasons (direction of movement of the cross-head) the branch–stem-junctions are oriented 'upside-down' with regard to the original orientation in the plant.

Biomechanical calculations

Our experiment showed that three distinct modes of failure exist when tearing off lateral branches in *Dracaena reflexa* (Figure 3). When the rupture occurred in the 'un-swollen region' of the lateral branches, the parameters a_2, l_2 and d_2 (Figure 8) were used for the calculations. When the branch–stem-junctions mechanically failed either in the 'swollen region' between main stem and lateral branch or in the main stem itself, a_1, l_1 and d_1 were used; r_1 and r_2 are the radius of the main stem and the lateral branch, respectively, where:

$$r_1 = \frac{d_1}{2} \text{ and } r_2 = \frac{d_2}{2} \text{ [m]}$$

Axial second moment of area (I), assuming a circular cross-section of main stem and lateral branch which holds true in good approximation for the investigated species

$$I = \frac{\pi}{4} \cdot r^4 \text{ [m}^4\text{]}, r = r_1 \text{ or } r_2 \text{ depending on the mode of fracture}$$

Bending moment at fracture (BM)

$$BM = a \cdot F_{crit} \text{ [Nm]}$$

a is the length of the effective lever arm shortly before fracture; a_1 or a_2 are used depending on the mode of fracture, F_{crit} is the critical force at rupture

Stress at rupture (σ)

$\sigma = BM \cdot \frac{r}{I}$ [Nm^{-2}], $r = r_1$ or r_2 depending on the mode of fracture

Strain at rupture (ε)

$$\varepsilon = \frac{3 \cdot \sin\alpha_{\text{krit}} \cdot f \cdot r}{l^2} \text{ [/]}$$

f is the vertical displacement until rupture of the branch at the point where the force F is applied to the lateral branch

l is the length between the point where the force is applied to the lateral branch and the position of rupture in the main stem or the lateral branch, $l = l_1$ or l_2 depending on the mode of fracture

α_{krit} is the angle between the lateral branch and main stem at the moment of rupture

Tensile energy absorption [kJ]

The tensile energy absorption up to the maximal force or up to the force at fracture was assessed by calculating the integral under the force-displacement-curve in the force-displacement diagrams (Figure 10).

Fracture toughness [kJm^{-2}]

Fracture toughness was calculated by dividing the tensile energy absorption by the cross-sectional area calculated for the main stem of the lateral branch by using d_1 or d_2 depending on the mode of fracture (see above).

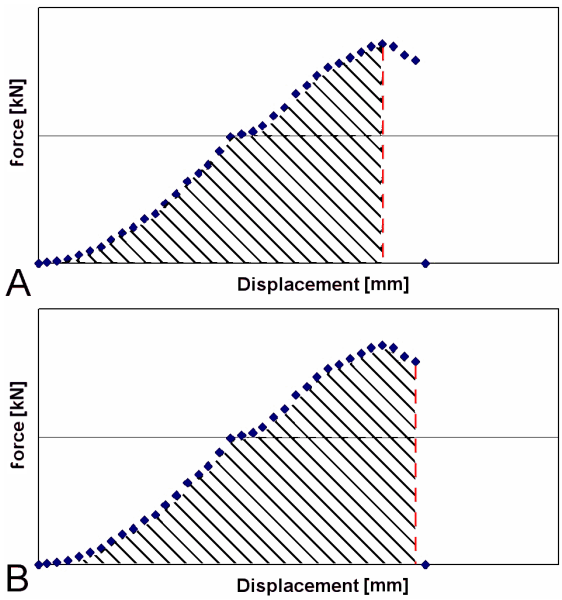

Figure 10: Breaking experiments. Exemplary force-displacement diagrams showing maximal force and displacement at maximum force (A) as well as force at fracture and displacement at fracture (B). The hatched areas were used for calculating fracture toughness until maximum force (A) and work of fracture until failure (B).

Statistical calculations

The software Sigmastat (Version 3.1) by Systat Software Inc. was used. Not all recorded data were normally distributed (Table 1). Therefore parametric tests (normal distribution) or non-parametric tests (no normal distribution) were used for calculating statistical significance of parameter correlation or difference amongst groups (Table 1).

- The (parametric) 'One Way Analysis of Variance' or the (non-parametric) 'Kruskal–Wallis One Way Analysis of Variance on Ranks' was used:

1. to verify whether the three groups of observed failure modes (in the branch, sickle-shaped, in the stem) for *D. reflexa* were statistically different as to the mechanical parameters calculated ($p < 0{,}05$, Table 1).
2. to analyse whether the biomechanical data for *D. reflexa* differed from the data of *F. insignis* (Table 2). Only specimens of *D. reflexa* that were found to be in the same range of branch diameters as *F. insignis* (3.5–5.4 mm) were used for this comparison (n = 14 for *D. reflexa*, n = 12 for *F. insignis*; Table 2).

- The Pearson Product moment correlation test was used to calculate whether there was a statistically significant correlation between tested mechanical parameters (e.g., maximum force) and the diameter of the branch (Table 1).

- No statistical significance of differences between the failure modes in *F. insignis* could be calculated, as the number of specimens in one failure mode was too low (n = 3, Table 1) in order to make a reasonable statistical evaluation.

Supporting Information

Supporting Information File 1

Three-dimensional arrangement and course of fibrous bundles in a branch–stem-junction of *Dracaena reflexa.*
[http://www.beilstein-journals.org/bjnano/content/supplementary/2190-4286-2-21-S1.zip]

Acknowledgements

We thank Tobias Haushahn for his kind permission to publish the three-dimensional visualisation of *Dracaena* (Supporting Information File 1) and (together with Samuel Fink) for competent help in microtome cutting and image processing. We gratefully acknowledge the German Research Foundation (DFG) for funding the project on branched biomimetic structures within the Priority Programme SPP 1420. We would also like to thank Markus Milwich from the ITV Denkendorf for his kind permission to publish Figure 7.

References

1. Holttum, R. E. *Phytomorphology* **1955,** *5,* 399–413.
2. Tomlinson, P. B. *Q. Rev. Biol.* **1973,** *48,* 458–466. doi:10.1086/407704
3. Fisher, J. B. *Q. Rev. Biol.* **1973,** *48,* 291–298. doi:10.1086/407591
4. Beismann, H.; Wilhelmi, H.; Baillères, H.; Spatz, H.-C.; Bogenrieder, A.; Speck, T. *J. Exp. Bot.* **2000,** *51,* 617–633. doi:10.1093/jexbot/51.344.617
5. Fleury, V.; Gouyet, J.-F.; Léonetti, M. *Branching in Nature – Dynamics and Morphogenesis of Branching structures, from Cell to River Networks;* Springer: Berlin, Germany, 2001.
6. Mattheck, C. *Design in der Natur. Der Baum als Lehrmeister;* Rombach Verlag: Freiburg, Germany, 2006.
7. Mattheck, C. *Secret design rules of nature;* Verlag Forschungszentrum Karlsruhe: Karlsruhe, Germany, 2007.
8. Mattheck, C. *Denkwerkzeuge nach der Natur;* Verlag Karlsruher Institut für Technologie (KIT): Karlsruhe, Germany, 2010.
9. Jungnikl, K.; Goebbels, J.; Burgert, I.; Fratzl, P. *Trees* **2009,** *23,* 605–610. doi:10.1007/s00468-008-0305-9
10. Speck, T.; Rowe, N. P.; Bruechert, F.; Haberer, W.; Gallenmüller, F.; Spatz, H.-C. How plants adjust the 'material properties' of their stems according to differing mechanical constraints during growth: an example of smart design in nature. In *Proceedings of the 3rd Biennial Engineering Systems Design and Analysis Conference,* Montpellier, France, June 9–14, 1996; Engin, A. E., Ed.; Am. Soc. Mech. Eng.: New York, 1996; pp 233–241.
11. Speck, T.; Rowe, N. P.; Spatz, H. C. Pflanzliche Achsen, hochkomplexe Verbundmaterialien mit erstaunlichen mechanischen Eigenschaften. In *Technische Biologie und Bionik 3, BIONA-Report 10;* Nachtigall, W.; Wisser, A., Eds.; Fischer Verlag: Stuttgart, Germany, 1996; pp 101–131.

12. Hoffmann, B.; Chabbert, B.; Monties, B.; Speck, T. *Planta* **2003,** *217,* 32–40. doi:10.1007/s00425-002-0967-2
13. Tomlinson, P. B. *The Structural Biology of Palms;* Clarendon Press: Oxford, U.K., 1990.
14. Tomlinson, P. B. Stem structure in arborescent monocotyledons. In *Formation of wood in forest Trees;* Zimmermann, M. H., Ed.; Academic Press: New York, 1964; pp 65–86.
15. Tomlinson, P. B.; Zimmermann, M. H. *J. Arnold Arbor., Harv. Univ.* **1969,** *50,* 159–179.
16. Tomlinson, P. B.; Zimmermann, M. H.; Simpson, P. G. *Phytomorphology* **1970,** *20,* 36–39.
17. Zimmermann, M. H.; Tomlinson, P. B. *J. Arnold Arbor., Harv. Univ.* **1970,** *51,* 478–491.
18. Stevenson, D. W.; Fisher, J. B. *Bot. Gaz. (Chicago)* **1980,** *141,* 264–268. doi:10.1086/337154
19. Rudall, P. *Bot. Rev.* **1991,** *57,* 150–163. doi:10.1007/BF02858768
20. Tomlinson, P. B.; Zimmermann, M. H. *Bull. Int. Assoc. Wood Anatom.* **1967,** *12,* 4–24.
21. Zimmermann, M. H.; Tomlinson, P. B. *J. Arnold Arbor., Harv. Univ.* **1969,** *50,* 370–383.
22. Scarpella, E.; Meijer, A. H. *New Phytol.* **2004,** *164,* 209–242. doi:10.1111/j.1469-8137.2004.01191.x
23. Rüggeberg, M.; Speck, T.; Paris, O.; Lapierre, C.; Pollet, B.; Koch, G.; Burgert, I. *Proc. R. Soc. London, Ser. B* **2008,** *275,* 2221–2229. doi:10.1098/rspb.2008.0531
24. Rüggeberg, M.; Speck, T.; Burgert, I. *New Phytol.* **2009,** *182,* 443–450. doi:10.1111/j.1469-8137.2008.02759.x
25. Rüggeberg, M.; Burgert, I.; Speck, T. *J. R. Soc., Interface* **2010,** *7,* 499–506. doi:10.1098/rsif.2009.0273
26. Tomlinson, P. B.; Esler, A. E. *N.Z. J. Bot.* **1973,** *11,* 627–644.
27. Schwager, H.; Haushahn, T.; Neinhuis, C.; Speck, T.; Masselter, T. *Adv. Eng. Mater.* **2010,** *12,* B695–B698. doi:10.1002/adem.201080057
28. Masselter, T.; Haushahn, H.; Schwager, M.; Milwich, M.; Nathanson, R.; Gude, M.; Cichy, F.; Hufenbach, W.; Neinhuis, C.; Speck, T. Biomimetic fibre-reinforced composites inspired by branched plant stems. In *Design and Nature V,* Pisa, June 28–30, 2010; Brebbia, C. A., Ed.; WIT Press: Southampton, Boston, 2010; pp 411–420. doi:10.2495/DN100361
29. Masselter, T.; Haushahn, T.; Cichy, F.; Gude, M.; Speck, T. Ramifications in Plant Stems as Concept Generators for Branched Technical Fiber-Reinforced Composites. In *WCB 2010,* IFMBE Proceedings 31, Singapore, Aug 1–6, 2010; Lim, C. T.; Goh, J. C. H., Eds.; Springer: Heidelberg, Germany, 2010; pp 36–39.
30. Masselter, T.; Barthlott, W.; Bauer, G.; Bertling, J.; Cichy, F.; Ditsche-Kuru, P.; Gallenmüller, F.; Gude, M.; Haushahn, T.; Hermann, M.; Immink, H.; Knippers, J.; Lienhard, J.; Luchsinger, R.; Lunz, K.; Mattheck, C.; Milwich, M.; Mölders, N.; Neinhuis, C.; Nellesen, A.; Poppinga, S.; Rechberger, M.; Schleicher, S.; Schmitt, C.; Schwager, H.; Seidel, R.; Speck, O.; Stegmaier, T.; Tesari, I.; Thielen, M.; Speck, T. Biologically inspired products. In *Nature based Innovation;* Bar-Cohen, Y., Ed.; CRC Press: Pasadena. In press.
31. Masselter, T.; Speck, T. Biomimetic fibre-reinforced compound materials. In *Advances in Biomimetics;* Lorkovic, I., Ed.; INTECH. In press.
32. Etzold, H. *Mikrokosmos* **1983,** *72,* 213–219.
33. Zimmermann, M. H.; Tomlinson, P. B. *Science* **1966,** *152,* 72–73. doi:10.1126/science.152.3718.72

License and Terms

Beilstein Journal of Nanotechnology

Infrared receptors in pyrophilous ("fire loving") insects as model for new un-cooled infrared sensors

David Klocke[1], Anke Schmitz[1], Helmut Soltner[2], Herbert Bousack[3] and Helmut Schmitz[*1]

Full Research Paper

Open Access

Address:
[1]Institute of Zoology, University of Bonn, Poppelsdorfer Schloss, 53115 Bonn, Germany, [2]Forschungszentrum Jülich GmbH, Zentralabteilung Technologie, 52425 Jülich, Germany and [3]Forschungszentrum Jülich GmbH, Peter Grünberg Institut, 52425 Jülich, Germany

Email:
David Klocke - dklocke@uni-bonn.de;
Anke Schmitz - ankeschmitz@uni-bonn.de;
Helmut Soltner - h.soltner@fz-juelich.de;
Herbert Bousack - h.bousack@fz-juelich.de;
Helmut Schmitz* - h.schmitz@uni-bonn.de

* Corresponding author

Keywords:
fire detection; forest fire; Golay cell; infrared sensor; pyrophilous insects

Beilstein J. Nanotechnol. **2011,** *2,* 186–197.
doi:10.3762/bjnano.2.22

Received: 05 January 2011
Accepted: 03 March 2011
Published: 30 March 2011

This article is part of the Thematic Series "Biomimetic materials".

Guest Editors: W. Barthlott and K. Koch

Abstract

Beetles of the genus *Melanophila* and certain flat bugs of the genus *Aradus* actually approach forest fires. For the detection of fires and of hot surfaces the pyrophilous species of both genera have developed infrared (IR) receptors, which have developed from common hair mechanoreceptors. Thus, this type of insect IR receptor has been termed photomechanic and shows the following two special features: (i) The formation of a complex cuticular sphere consisting of an outer exocuticular shell as well as of a cavernous microfluidic core and (ii) the enclosure of the dendritic tip of the mechanosensitive neuron inside the core in a liquid-filled chamber. Most probably a photomechanic IR sensillum acts as a microfluidic converter of infrared radiation which leads to an increase in internal pressure inside the sphere, which is measured by a mechanosensitive neuron.

A simple model for this biological IR sensor is a modified Golay sensor in which the gas has been replaced by a liquid. Here, the absorbed IR radiation results in a pressure increase of the liquid and the deflection of a thin membrane. For the evaluation of this model analytical formulas are presented, which permits the calculation of the pressure increase in the cavity, the deformation of the membrane and the time constant of an artificial leak to compensate ambient temperature changes. Some organic liquids with high thermal expansion coefficients may improve the deflection of the membrane compared to water.

Introduction

Fire loving (pyrophilous) insects depend on forest fires for their reproduction. Such insects approach ongoing fires and invade the burnt area immediately after a fire. For the long-range navigation toward a fire as well as for the short-range orientation on a freshly burnt area these insects have special sensors for smoke and infrared (IR) radiation. Whereas the olfactory receptors for smoke are located on the antennae, the IR receptors are housed in extra-antennal sensory organs, which can be found on the thorax or on the abdomen. In the pyrophilous beetle *Melanophila acuminata* infrared receptors and their associated sensory neurons are derived from mechanoreceptors [1]. Unlike other mechanosensory neurons, IR sensitive neurons directly send their information to be processed centrally (e.g., by the brain) rather than locally in their respective ganglia of origin [2]. It is suggested that smoke-derived odours and IR information converge on descending brain neurons which, in turn, control and direct flight toward the forest fire.

Two genera of jewel beetles (family Buprestidae) can be classified as pyrophilous: About a dozen species of the genus *Melanophila,* which are distributed nearly all over the world except for Australia, and the ”fire-beetle” *Merimna atrata,* which is endemic to Australia [3,4]. Despite the fact that *Melanophila* and *Merimna* show almost the same behaviour and belong to the same family of jewel beetles, their IR receptors are very different from each other.

On a freshly burnt area, the males of both genera often stay on the stems of trees close to burning or glowing wood or hot ashes. As soon as they become aware of a conspecific female, they try to copulate vigorously. After mating, the females deposit their eggs under the bark of burnt trees. The main reason for the pyrophilous behaviour is that the wood-boring larvae of *Melanophila* and *Merimna* can only develop in the wood of burnt trees [3,5]. As a morphological speciality, both pyrophilous buprestid genera are equipped with antennal smoke receptors and thoracic or abdominal IR organs [6-9].

Another pyrophilous beetle can also be found in Australia, i.e., the “little ash beetle” *Acanthocnemus nigricans* (family Acanthocnemidae). This inconspicuous beetle is only 4 mm long and highly attracted by hot ashes: Little is known about its biology. Similarly, *Acanthocnemus* also depends on fires for its reproduction and is equipped with a pair of sophisticated prothoracic IR receptors [10,11]. Recently, IR receptors have also been discovered in a few pyrophilous members of the flat bug genus *Aradus* (Heteroptera, Aradidae) [12]. With respect to morphology and function, the IR receptors of *Aradus* bugs are very similar to those described for *Melanophila* beetles. Fire detection is obviously an important requirement for the survival of all of the pyrophilous insect species noted above. However, the outbreak of a forest fire is highly unpredictable. Therefore, pyrophilous beetles and bugs must be able to detect fires from distances as large as possible. Furthermore, when flying over a burnt area in search for a place to land, the small insects have to avoid “hot spots” with dangerous surface temperatures above about 60 °C.

Melanophila beetles and *Aradus* bugs are equipped with sensory structures that allow both the detection of hot fires at considerable distances as well as being able to locate moderately hot spots close by. These insects feature so-called photomechanic IR receptors, which might serve well as models for the technical design of un-cooled IR receptors. In the present paper we focus on the structure and function of the biological model as well as on the design and theoretical evaluation of a technical photomechanic IR sensor.

Results

The photomechanic IR receptors in pyrophilous beetles and bugs

Structure and material properties of photomechanic IR receptors

Structure and function of photomechanic insect IR sensillae have been most studied in *Melanophila* beetles. As a special behavioural feature, beetles of both sexes approach forest fires because their brood depends on burnt wood as larval food [5,13-15]. Therefore, it must be postulated that the sensory organs, which are used for fire detection, have been subjected to a strong evolutionary pressure, especially with regard to sensitivity. The individual IR receptors (called sensilla in insects) are situated in two pit organs, which are located on the third thoracic segment. Each IR organ houses about 70 IR sensilla, which are closely packed together at the bottom of the pit [16] (Figure 1A). In pyrophilous bugs of the genus *Aradus*, about a dozen IR sensilla are located on the lateral sides (the so-called propleurae) of the prothorax (Figure 1B). Here, receptors are loosely interspersed between the common hair mechanoreceptors, which cover the entire outer body surface of the bug [12] (Figure 1B).

From the outside, a single IR sensillum in *Melanophila* beetles and *Aradus* bugs can be recognized by a hemispherical dome with a diameter of about 12–15 µm. The dome consists of a thin cuticle, which represents the outer boundary of a spherical internal cavity. The cavity is almost completely filled with a tiny cuticular sphere with a diameter of about 10 µm (Figure 2A and Figure 2B). Based on transmission electron microscopical observations, it has been observed that the internal sphere consists of at least two different zones: (i) An outer lamellated

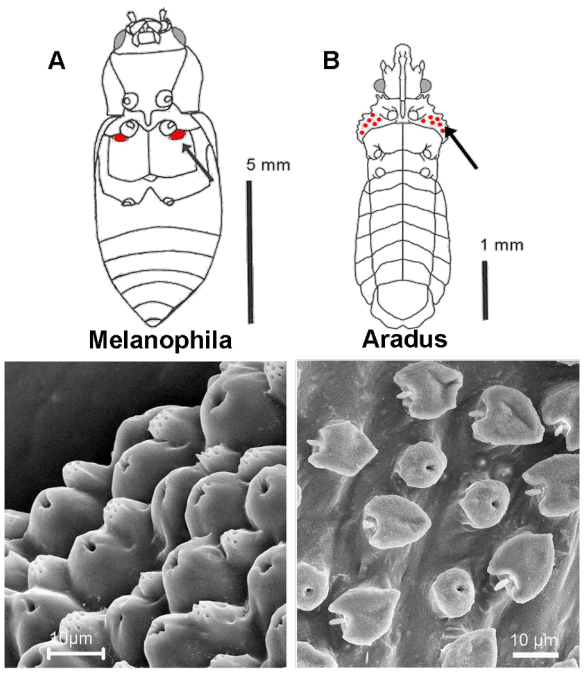

Figure 1: Infrared receptors in *Melanophila* beetles (**A**) and pyrophilous bug species of the genus *Aradus* (**B**). In *Melanophila* about 70 dome-shaped IR receptors which are accompanied by porous wax glands (shown below) are densely packed at the bottom of a thoracic pit (indicated in red and by the arrow). In *Aradus* bugs about a dozen IR receptors (indicated in red and shown below) are interspersed between mechanosensory bristles on the first thoracic segment (arrow) of the bug.

zone consisting of exocuticle. The lamellated appearance is caused by many layers of chitin fibres with a periodically changing orientation, and (ii) an internal microfluidic core. From below, the sphere is innervated by a single sensory cell. The outermost tip of the sensory dendrite is anchored in the fluidic core. All morphological as well as all physiological data available so far have demonstrated, that this cell is a ciliary mechanoreceptor [1,12,16].

Local testing of different cuticular regions of the *Melanophila* sensillum with a nanoindenter has revealed that the mechanical properties of the exocuticular shell of the sphere and the mesocuticle of the microfluidic core are different: Modulus as well as hardness of the shell are significantly higher. Interestingly, modulus and hardness of reference mesocuticle outside the IR pit organs is much higher than those of the mesocuticle inside the sphere. This points to a specialization of the material inside the sphere (Figure 2C, Figure 2D).

Receptor function

Currently, two models of sensillum function can be found in the literature. However, these models are inconsistent with each other. (i) More than 12 years ago, a so-called photomechanic principle was established [17,18]. The authors proposed that the biomolecules (i.e., proteins and chitin) in the cuticular sphere strongly absorb mid-IR radiation. In a way not described in detail, the resulting thermal expansion of the cuticular sphere is measured by the mechanoreceptor. (ii) Assuming the presence of a large air-filled cavity inside the sphere, Evans [19] proposed in a second model that IR radiation enters this cavity by a small apical waveguide with a diameter of about 1.5 µm. Due to the absorption of IR photons at the inner cuticular walls of the cavity, the enclosed air is heated up and expands. In a way not further specified the resulting increase in gas pressure should stimulate the mechanoreceptor.

Our recent findings have clearly demonstrated that the thoracic infrared (IR) sensilla of the pyrophilous jewel beetle *Melanophila acuminata* most likely have evolved from hair mechanoreceptors (sensilla trichodea) [1]. Hair mechanoreceptors, which can be found in any insect, have bristles of different length. In insects the pressure-sensitive dendrite of a single mechanosensitive sensory cell innervates the base of the bristle. As a result, even a slight bending of the bristle stimulates the tip of the dendrite [20]. Compared to a hair mechanoreceptor, a photomechanic IR sensillum in *Melanophila* beetles and *Aradus* bugs shows the following special features (Figure 2): (i) The formation of a complex cuticular sphere instead of a bristle; the sphere consists of an outer hard exocuticular shell as well as an inner relatively soft cavernous mesocuticular part forming a microfluidic core inside the sphere. (ii) The enclosure of the dendritic tip of the mechanosensitive neuron inside the inner core in a liquid-filled chamber. Most probably, IR radiation absorbed by the proteins, the chitin fibres, and the water of the sensillum heats up the sphere, which immediately causes thermal expansion especially of the liquid inside the microfluidic core. Because the shell of the sphere consists of stiff exocuticle additionally reinforced by many layers of chitin fibres, the only compliant structure in the sphere is the membrane of the tip of the mechanosensitive dendrite. Due to the air-filled tracheal system inside the body of the beetle, most of the cell body of the mechanosensitive cell is always at ambient pressure. Only the outermost tip of the sensory dendrite of the mechanosensor (Figure 2) is enclosed inside the sphere. Therefore, any increase in pressure inside the sphere will cause a cross compression of the dendritic tip which is compensated by the cell volume below the sphere. By deflection of the dendritic membrane in the range of a few nanometers, stretch-activated ion channels will be opened. A slow pressure compensation between the inner core of the sphere and the outer environment most probably is achieved by fine nanocanals which run through the outer shell of the sphere. Thus, like the integrated leak in a Golay detector (see below), relatively slow changes of the ambient temperature can be compensated. Hence, we

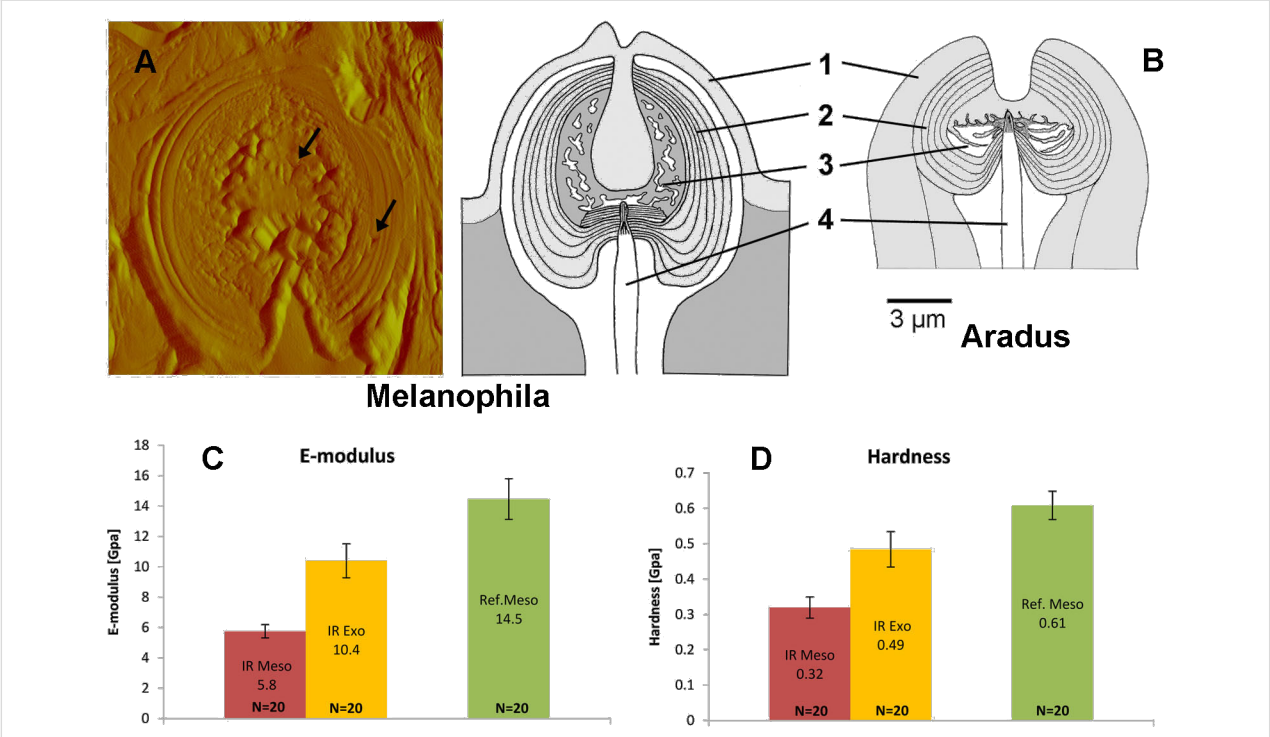

Figure 2: Schematic drawings of single IR receptors of *Melanophila* (A) and *Aradus* (B). 1: outer exocuticle; 2: exocuticular shell of the inner sphere; 3: microfluidic core; 4: tip of mechanosensory dendrite. For the *Melanophila* sensillum a topographical scan made with the tip of the nanoindenter is also shown on the left. Arrows point to indentations in the exocuticular shell of the sphere ("IR Exo" in C and D) and in the mesocuticle of the core ("IR Meso" in C and D). (C) and (D): E-modulus and hardness of different regions of the *Melanophila* sensillum measured by nanoindentation (for details see "*Experimental" section*). Twenty indents were made in each region. "Ref. Meso": reference mesocuticle outside of IR receptor.

propose that an IR sensillum acts as a microfluidic converter of infrared radiation which leads to an increase in internal pressure inside the sphere, which is measured by the mechanosensitive neuron. The principle of transforming IR radiation into a bioelectrical signal has been termed photomechanic. Most probably photomechanic IR sensilla have been developed independently in beetles and bugs. This provides strong evidence that mechanoreceptors are promising candidates for the development of IR sensors. Because the products of the evolutionary process are very similar in *Melanophila* beetles and *Aradus* bugs [12], it can be proposed that a photomechanic IR sensillum represents an optimized biological sensory system for mid IR radiation.

Model for the IR receptor

Golay sensor

After the clarification of the function of the biological IR sensor of the beetle we now analyze its principle mathematically to be able to design a technical sensor. For this purpose we investigated the pneumatic Golay sensor [21] as a simple model, see Figure 3. This sensor consists of an internal gas-filled cavity, which is closed on one side by a window and on the other side by a thin membrane. IR radiation enters through the window and heats up the gas by absorption. The deflection of the membrane caused by the expanding gas can be read by an optical system [21], a capacitive detector [22], or a tunneling displacement transducer [23]. To enhance the IR absorption in the gas, the cavity is equipped with an additional absorber. Reflecting walls of the cavity are another means to enhance the

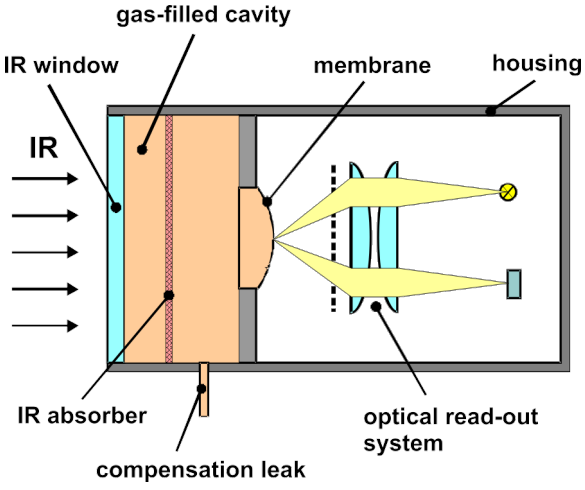

Figure 3: Principle of a gas-filled Golay sensor with optical read-out. For explanations see text.

absorption. The temperature changes of the gas caused by the absorbed IR radiation are in the range of mK. Because of slow variations of the ambient temperature in the range of a few K, it is absolutely necessary to integrate a leak, which compensates this influence due to an exchange of the gas with a reference volume.

Sensor model of the IR receptor

The model of the sensor, which we want to analyze, is shown in Figure 4. Similar to the sensillum, the sensor contains an internal water-filled cavity. A major difference between the biological sensillum and the Golay sensor is the internal medium, a gas in the traditional Golay sensor, and a fluid in the sensillum. The cavity of the technical sensor is etched into a silicon wafer and is closed on the one side by a window (Suprasil, [24]) and on the other side by a thin silicon membrane. The IR radiation being absorbed produces a change in pressure or volume due to the change of the state of the water. The deflection of the membrane caused by this pressure increase can be read out by, e.g., a capacitive detector or a tunneling displacement transducer.

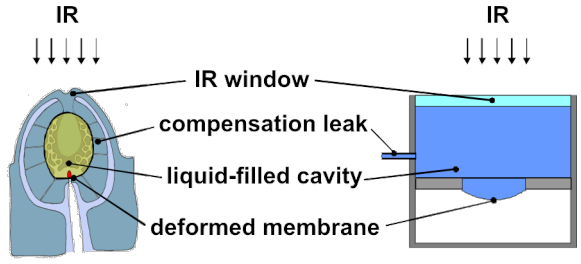

Figure 4: Comparison of the sensillum (left) with the model of the sensor (right).

Pressure increase of the cavity and deflection of the membrane

For calculating the change of the liquid pressure in the cavity based on the temperature profile, the equation of state must be solved. Because the pressure in the cavity depends upon two independent variables, temperature and volume, its total change is given by

$$\Delta P = \beta \cdot \Delta T_{\text{mean}} - \frac{1}{\kappa \cdot V} \cdot \Delta V \qquad (1)$$

with ΔP: Pressure increase, $\beta = (\partial P/\partial T)_V$: isochoric tension coefficient, ΔT_{mean}: mean temperature increase averaged over the cavity volume, $\kappa = -(1/V)\cdot(\partial V/\partial P)_T$: isothermal compression coefficient, V: volume of the cavity, ΔV: volume increase. For water (25 °C, 1 bar), $\beta = 5.68\cdot10^5$ Pa/K and $\kappa = 4.5\cdot10^{-10}$ Pa^{-1} [25].

The increase of the volume ΔV of the cavity results in a tiny deflection of the membrane. The deflection y of this membrane caused by a pressure difference can be calculated as a function of the radial distance r with the shell theory [26]

$$y(r) = \frac{\Delta P}{64 \cdot D} \cdot \left(R^2 - r^2\right)^2$$
$$D = \frac{E \cdot t_P^3}{12 \cdot (1 - \nu^2)} \qquad (2)$$

with R: radius of the membrane, D: flexural stiffness of the membrane, E: Young's modulus, t_P: thickness of the membrane, ν: Poisson's ratio.

Equation 2 is a good approximation for small membrane deflections, i.e., $y_{\max}/t_p < 1$. The volume ΔV can be calculated in relation to the pressure increase ΔP by using Equation 2

$$\Delta V = \frac{\pi \cdot R^6 \cdot \Delta P \cdot \left(1 - \nu^2\right)}{16 \cdot E \cdot t_P^3} \qquad (3)$$

The combination of Equation 2 and Equation 3 yields a relationship for ΔP, which considers the influence of temperature and volume.

$$\Delta P = \frac{\beta \cdot \Delta T_{\text{mean}}}{1 + \Omega}$$
$$\Delta T_{\text{mean}} = \frac{\int_0^{H_C} \Delta T(z) \cdot dz}{H_C} \qquad (4)$$
$$\Omega = \frac{R^4 \cdot (1 - \nu^2)}{16 \cdot E \cdot t_P{}^3 \cdot H_C \cdot \kappa}$$

with H_C: height of the cylindrical cavity, $\Delta T(z)$: temperature as a function of the axial coordinate z of the cavity and time, ΔT_{mean}: mean temperature increase averaged over the cavity.

The factor Ω characterizes the change of state of the liquid inside the cavity due to a temperature increase: For $\Omega \to 0$, which corresponds to an extremely hard membrane, the change of state is isochoric with a maximal pressure increase. For $\Omega \to \infty$, as for an extremely soft membrane, the change of state is isobaric with maximal volume increase. The transition between these two cases is at $\Omega \approx 1$. The maximal deflection $y_{\max}$ of the circular membrane can be calculated as a function of the factor Ω by using Equation 2 and Equation 4.

$$y_{\max} = \frac{3 \cdot \alpha \cdot \Omega \cdot \Delta T_{mean} \cdot H_C}{1+\Omega} \quad (5)$$

with α = β·κ: isobaric thermal expansion coefficient.

Equation 4 and Equation 5 can be also used for a gas-filled cavity. In this case the isochoric tension coefficient β and the isothermal compression coefficient κ can be calculated from the ideal gas law

$$P \cdot V_C = n \cdot R \cdot T \quad (6)$$

with n: number of moles of gas in the cavity, R: universal gas constant.

Equation 6 yields the following expression for the isochoric tension coefficient β, the isothermal compression coefficient κ and the isobaric thermal expansion coefficient α

$$\beta = \left(\frac{\partial P}{\partial T}\right)_V = \frac{P}{T}$$
$$\kappa = -\frac{1}{V}\left(\frac{\partial V}{\partial P}\right)_T = \frac{1}{P} \quad (7)$$
$$\alpha = \beta \cdot \kappa = \frac{1}{T}$$

If the change of state is small compared to the initial state T_0 = 300 K and $P_0 = 10^5$ Pa, these values result in β ≈ 330 Pa/K, κ ≈ $1.0 \cdot 10^{-5}$ Pa^{-1} and α ≈ $3.3 \cdot 10^{-3}$ K^{-1}.

The calculation of the mean temperature increase ΔT_{mean} in Equation 4 depends strongly on the boundary conditions. When an adiabatic cavity is assumed without any heat loss through the glass window or the cavity wall, the highest possible mean temperature increase ΔT_{mean} results.

$$\Delta T_{mean} = \frac{I_0 \cdot A}{m \cdot c_P} \cdot t \quad (8)$$

with: I_0: IR power density, A: cross-section surface of the cavity, m: mass of fluid inside the cavity, c_P: heat capacity of the fluid inside the cavity, t: time.

However, in reality the heat loss cannot be neglected. The heat loss through the IR window can be calculated for defined boundary conditions. A high IR absorption coefficient of the liquid in the cavity causes the absorption of the IR energy within a very small absorption zone. For water as a liquid with a very high IR absorption coefficient, a formula for the temperature profile $\Delta T(z)$ could be derived [27] on the assumption of a infinitely thin boundary layer between the glass window and the water. This allows a numerical solution of the mean temperature increase in Equation 4 taking into account the heat loss through the IR window. In the case of water as liquid up to 50% of the absorbed energy may be lost through the window by heat conduction [27]. For liquids with lower absorption coefficients than water, the mean temperature increase must be calculated numerically by finite element methods.

Gases always have a significant lower absorption coefficient which requires the application of an additional absorber such as plastic, aluminium, antimony or lead [21]. When the absorbing film is directly on the inner surface of the window, the assumption of a boundary layer as in the case of water is valid.

Evaluation of different liquids and gases as fluids inside the cavity

Water

Figure 5 shows the maximal deflection as a function of the factor Ω according to Equation 5 for an IR power density of 10 W/m^2 (IR window without absorption loss assumed) for a cavity with a height and a diameter of 0.5 mm filled with water. These values were taken as a reference. Obviously, the maximal deflection is achieved for the isobaric case with a very soft membrane. Due to the very low deflection of less than 1 nm, a capacitor for the read-out must be extremely sensitive. As an alternative an optical read-out or the use of a tunneling displacement transducer may be useful.

With regard to Equation 4 and Equation 5, the maximal deflection of the membrane can be increased by using a liquid with a high thermal expansion coefficient α and a high mean temperature increase ΔT_{mean} due to a low product of heat capacity and density in a small cavity. Additionally, the IR window and the

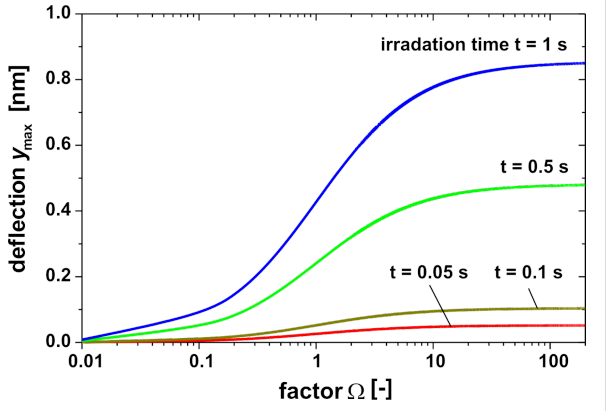

Figure 5: Maximum central deflection y_{max} of a circular membrane as function of factor Ω and irradiation time for a water-filled cavity. IR power density = 10 W/m^2, diameter and height of the cavity = 0.5 mm.

Table 1: Comparison of material properties of different hydrocarbons, water and CO_2 (300 K, 10^5 Pa). The absorption coefficients α_{OPT} were calculated in the bandwidth 3–5 µm using data from [28-30].

	α [10^{-5} K^{-1}]	κ [10^{-10} Pa^{-1}]	ρ [kg/m^3]	λ [W/(m·K)][a]	c_p [kJ/(kg·K)]	α_{OPT} [cm^{-1}]
water	26	4.5	998	0.61	4.18	1140
n-pentane	158	25.0	627	0.11	2.31	73
toluene	107	9.1	870	0.14	1.72	94
CO_2 (gas)	330	10^5	1.76	$1.64 \cdot 10^{-2}$	0.85	—[b]

[a]heat conductivity; [b]For CO_2 gas an infinitely thin absorption zone is assumed.

cavity material should have a low heat conduction to avoid heat losses during measurement.

Hydrocarbons

The inner pressure chamber of the sensillum is filled with a liquid, which consists mostly of water. Regarding the thermal expansion coefficient, water is not an optimal liquid. Hydrocarbons such as *n*-pentane and toluene, as well as methanol, which are also used as fluids in thermometers, are more appropriate. Table 1 shows the material properties of different hydrocarbons and carbon dioxide in comparison to water.

The thermal expansion coefficients of the hydrocarbons in Table 1 are about eight times higher compared to water so that the deflection of the membrane increases by this factor. The heat capacity and density of hydrocarbons is about 40–50% lower in comparison to water, which results in a higher mean temperature increase ΔT_{mean} for the same amount of stored energy.

The absorption coefficients in Table 1 were calculated in the atmospheric mid-wave window between 3–5 µm using data from [28-30]. Compared to water the absorption coefficients of hydrocarbons are up to two orders of magnitude lower. For this reason, the temperature distribution along the cavity axis is more uniform compared to water.

For the evaluation and comparison of the different liquids regarding the maximum membrane deflection in Equation 5, the mean temperature increase ΔT_{mean} has to be calculated. An IR power density of 10 W/m^2 at the outer window surface in a bandwidth of 3–5 µm and an irradiation time of 50 ms is used as a reference. For simplification it is assumed that the IR power density is independent from the wavelength in this bandwidth. Figure 6 shows the decrease of the power density as a function of the cavity axis coordinate *z* for different liquids. Obviously the decrease of the power density in water occurs only within a thin absorption zone directly behind the window, whereas in the case of hydrocarbons the entire depth of the cavity contributes to absorption. The power density profiles in Figure 6 were used to numerically calculate the temperature distribution after 50 ms in Figure 7. Due to the thin absorption zone in water, the maximum temperature appears directly behind the window resulting in heat conducting losses through the window. For hydrocarbons, however, the maximum temperature is shifted deeper into the cavity causing smaller

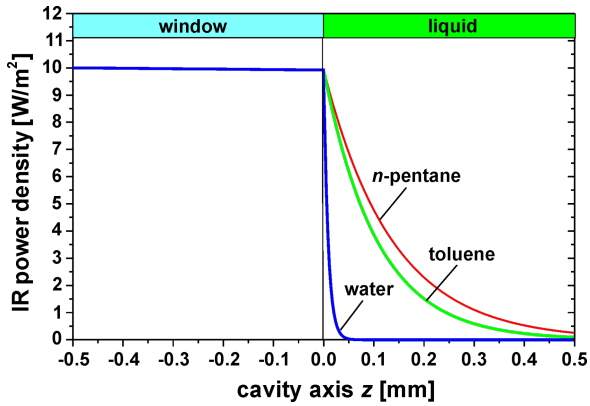

Figure 6: IR power density as function of the cavity axis for different liquids. Suprasil® 300 was used as the material for the window with an absorption coefficient of 0.16 cm^{-1} [23]. For gas, a thin absorbing film on the inner glass surface is assumed where all the radiation is absorbed.

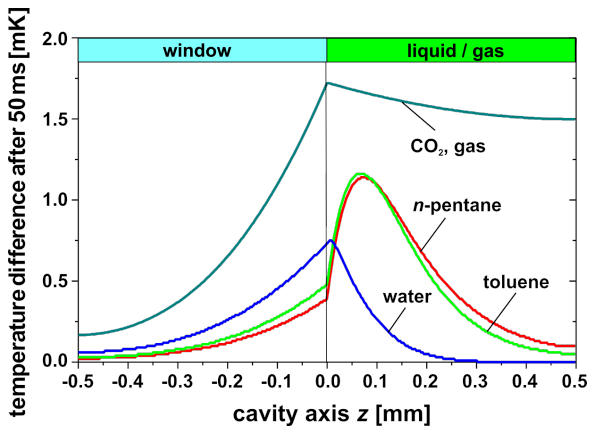

Figure 7: Temperature distribution along the cavity axis 50 ms after the onset of irradiation for different liquids with an IR power density at the outer window surface of 10 W/m^2, see Figure 6.

heat losses through the window. Based on the temperature profiles in Figure 7, the mean temperature increase ΔT_{mean} is calculated in Table 2. Here the advantage of using hydrocarbons instead of water is also obvious.

Table 2: Comparison of the mean temperature increase ΔT_{mean} , the factor Ω, and the maximum deflection y_{max} of the membrane in different liquids and CO_2 gas after 50 ms irradiation of 10 W/m^2.

	ΔT_{mean} [mK]	Ω [-]	y_{max} [nm]
water	0.14	6245	0.04
n-pentane	0.53	1126	1.26
toluene	0.64	3093	1.03
CO_2 (gas)	1.57	0.281	2.18

The silicon membrane (E = 166 GPa, ν = 0.28 [31]) has a diameter of 0.5 mm and a thickness of 1 µm, resulting in a factor Ω of 1000 to 6000 for the different liquids in Table 2. Regarding Figure 4 this is the isobaric case, and due to the high factor Ω a softer membrane will not result in a larger deflection of the membrane. With the data of the membrane, the deflection can be calculated by using Equation 5, see Table 2. A value of only about 1 nm results for the hydrocarbons. The increase of the deflection in case of the hydrocarbons by a factor 10 compared to water as liquid can be explained by an increase of the mean temperature of about factor 4–5 and an increase of the expansion coefficient by the factor 5–7. It can be assumed as a first approximation, that the deflection is proportional to the IR power density and the irradiation time.

If a pure liquid is used the thermal and optical properties are coupled, that means a liquid with an optimal product of density and heat capacity may have a low IR absorption, which makes this fluid disadvantageous for the application. A decoupling of thermal and optical properties can be achieved with a matrix of a good absorber, e.g., a meshwork of plastic or tiny plastic beads, or a dye immersed in the fluid. The plastic matrix or a dye absorbs most of the radiation and transfers the absorbed energy to the fluid, which provides optimal thermal properties and a large thermal expansion. The choice of the plastic matrix must ensure a large surface-to-volume ratio and a low product of density and heat capacity. The decoupling of the thermal and optical properties permits the determination of an optimal absorption coefficient approximately for each cavity depth to absorb the IR energy completely in the cavity without any unused fluid volume.

Gas

Using gas instead of water in the cavity as in the well known pneumatic Golay sensors yields different results due to the different material properties, in particular density ρ, heat capacity c_p and the coefficients β, κ, α in Equation 7. For a better comparison with the water-filled cavity, it is also assumed that a thin zone due to a thin absorbing film on the inner glass surface exists where all the radiation is absorbed and this energy heats up the gas by heat conduction. The resulting temperature profile for water and gas 0.5 s after the onset of IR irradiation is shown in Figure 8 based on the same IR power density 10 W/m^2. Mainly due to the lower product of density and heat capacity, the temperature increase in the gas is higher; the mean temperature increase ΔT_{mean} is in the case of water 1.2 mK and 4.8 mK in the case of gas. Using Equation 4, this causes, e.g., for Ω = 1 a pressure difference ΔP of 350 Pa in the case of water but only 0.8 Pa in the case of gas (Figure 9). However, the maximal deflection of the membrane in the case of gas is 12 nm compared to 0.2 nm in the case of water, see Figure 10. This surprising fact can be explained by the higher mean temperature increase and especially by the higher thermal

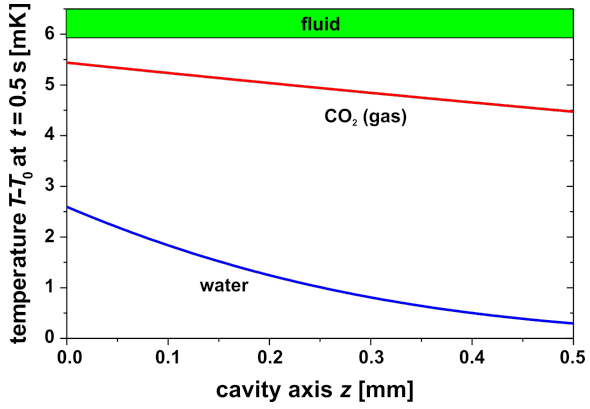

Figure 8: Temperature distribution along the cavity axis z 0.5 s after the onset of irradiation for a water-filled and a CO_2-filled cavity with an IR power density at the outer window surface of 10 W/m^2. In the case of gas, a thin IR absorber film is assumed on the inner glass surface where all the IR energy is absorbed.

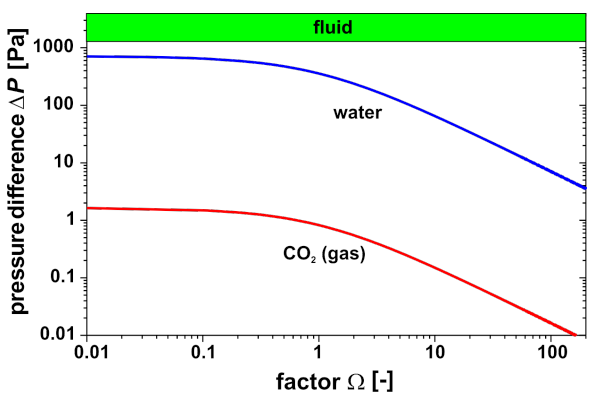

Figure 9: Pressure difference ΔP of a circular membrane at t = 0.5 s as a function of factor Ω for a water-filled and CO_2-filled cavity. IR power density 10 W/m^2, diameter and height of the cavity: 0.5 mm.

expansion coefficient in the case of gas compared to water. The temperature distribution 50 ms after the onset of IR irradiation is shown in Figure 10 comparing gas versus water and hydrocarbons. In this case the maximal deflection of the membrane is about 2 nm compared to about 1 nm in the case of hydrocarbons (Table 2).

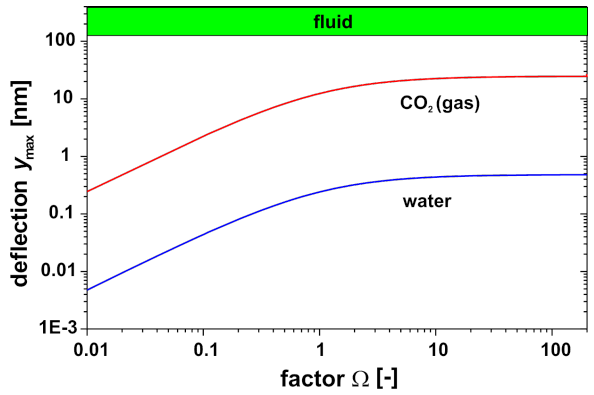

Figure 10: Maximum central deflection y_{max} of a circular membrane at t = 0.5 s as function of factor Ω for a water-filled and CO_2-filled cavity. IR power density 10 W/m^2, diameter and height of the cavity: 0.5 mm.

Using different gases will not change the result noticeably, because only the individual gas constant and the heat capacity are variable. However, using a gas with a low heat conductivity such as argon or xenon will reduce the radial heat losses in the cavity wall and yield a higher temperature increase.

Read-out of the membrane deflection

The calculated deformation of the membrane in the case of water as liquid and the deformation of the tip of the dendrite in the sensillum have the same magnitude. In mechanoreceptors such as the sensillum, deformations of the tip of the dendrite of only 0.1 nm, corresponding to an energy of 10^{-19} J, yield a receptor potential [32]. As a consequence of the tiny deformation of the membrane the technical sensor needs a read-out system that is able to detect deformations in the nm-range, such as interferometry, tunneling contacts [23], or a capacitive position sensor with nanometer resolution [33].

Compensation leak

In the IR receptor of *Melanophila acuminata* the inner sphere is enclosed by a thin layer of liquid in an outer compartment. Therefore the nanocanals in the shell of the sphere allow the exchange of liquid in and out of the microfluidic core in the sphere. Thus, any internal pressure change, which may be caused by the slowly changing ambient temperature, can be compensated. Golay sensors also use such compensation leaks for this purpose [21]. Figure 11 shows a simplified model of the sensillum with the core connected by nanocanals with the outer compartment and the geometric design of such a compensation leak. For the design of a compensation leak a formula will be derived.

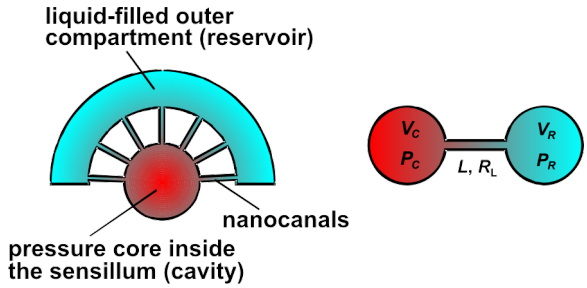

Figure 11: Left: model of the pressure core in the sensillum connected by nanocanals with the outer compartment; right: calculation model for pressure compensation between the core (cavity, volume V_C, pressure P_C) connected by a canal (length L, radius R_L) with a reservoir (volume V_R, pressure P_R) and $P_C > P_R$.

For a liquid as fluid a mass balance between the two volumes of the cavity and of the reservoir yields a system of two partial differential equations.

$$\begin{aligned} \psi_C \cdot \frac{dP_C}{dt} + \frac{1}{\kappa} \cdot (P_C - P_R) = 0 \\ \psi_R \cdot \frac{dP_R}{dt} + \frac{1}{\kappa} \cdot (P_R - P_C) = 0 \end{aligned} \tag{9}$$

with the following abbreviations:

$$\begin{aligned} \psi_C = \frac{8 \cdot V_C \cdot \eta \cdot L}{\pi \cdot R_L^4} \\ \psi_R = \frac{8 \cdot V_R \cdot \eta \cdot L}{\pi \cdot R_L^4} \end{aligned} \tag{10}$$

where η: dynamic viscosity, L: Length of canal, R_L: Radius of canal.

For the solution of the differential equations in Equation 9, a Hagen–Poiseuille flow in the canal is assumed [34,35].

$$\frac{dV_L}{dt} = \frac{\pi \cdot R_L^4}{8 \cdot \eta \cdot L} \cdot \left(P_C(t) - P_R(t) \right) \tag{11}$$

where (dV_L/dt): volumetric flow rate in the canal, $P_C(t)$, $P_R(t)$: time dependent pressures in the cavity and the reservoir.

The solution of the differential equations is given by [35]

$$P_C(t) = \frac{1}{1+\frac{V_C}{V_R}} \cdot \left[P_R(t=0) + \frac{V_C}{V_R} \cdot P_C(t=0) + \Delta P(t=0) \cdot e^{-\frac{t}{\tau}} \right]$$

$$P_R(t) = \frac{1}{1+\frac{V_C}{V_R}} \cdot \left[P_R(t=0) + \frac{V_C}{V_R} \cdot \left(P_C(t=0) - \Delta P(t=0) \cdot e^{-\frac{t}{\tau}} \right) \right] \quad (12)$$

with

$$\Delta P(t=0) = P_C(t=0) - P_R(t=0)$$

$$\tau = \frac{\psi_C \cdot \kappa}{1+\frac{V_C}{V_R}}$$

with t: time, $P_C(t = 0)$, $P_R(t = 0)$: initial pressure in the cavity and the reservoir at $t = 0$.

With N similar canals between the cavity and the reservoir, the time constant τ in Equation 12 is reduced by this number

$$\tau = \frac{\psi_C \cdot \kappa}{N \cdot \left(1+\frac{V_C}{V_R}\right)} \quad (13)$$

By assuming only little changes of the liquid density, $\Delta\rho/\rho \cong 0$, Equation 12 and Equation 13 can be used with $\kappa = 1/P$ for a gas. This assumption is justified when $P_C(t = 0)$ is similar to $P_R(t = 0)$. With $V_C << V_R$, i.e., an infinite reservoir, and with gas as the fluid, the time constant τ in Equation 10 is equal to the time constant described by Chevrier et al. in [22] derived with an electrical circuit analogy. Three examples of the pressure release between a cavity V_C (diameter 0.5 mm, depth 0.5 mm) connected by two compensation leaks to reservoirs V_R with different size and water as liquid are shown in Figure 12. The initial pressure difference ΔP of 100 Pa is, e.g., generated by a ΔT_{mean} in the cavity of about 1 mK. The time necessary for pressure compensation is about 0.15 s, when the cavity volume and the reservoir volume are equal, and is increased up to 0.3 s when the reservoir volume is 10 times larger than the cavity volume.

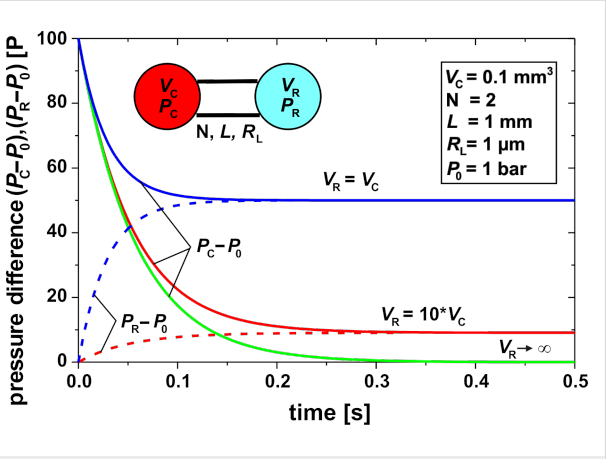

Figure 12: Pressures in the cavity, P_C, and in the reservoir, P_R, as a function of time for a cavity with a volume V_C = 0.1 mm^3 connected by two compensation leaks to a reservoir volume V_R for different values of V_R/V_C, P_0: ambient pressure.

The time constant of the compensation leak must be considerably larger than the time constant of the temperature change in the cavity due to an IR signal in order to minimize the effect of the compensation leak on the measurement. It is obvious that the time constant of the compensation leak can be tuned by the geometry and the number of the canals and the ratio of the cavity volume and the reservoir volume. Figure 13 shows the time constants of a compensation leak as function of the radius of the canal and the fluid in the cavity, water or CO_2 gas. Especially due to the higher compressibility of the gas, the time constant is in this case up to three orders of magnitude higher than in the case of water. When a time constant of 1 s is assumed, then in the case of water the compensation canal needs to have some mm length with a radius smaller than 1 µm. The use of gas instead of water will result in a simpler manufacturing procedure due to the larger radius of the canal.

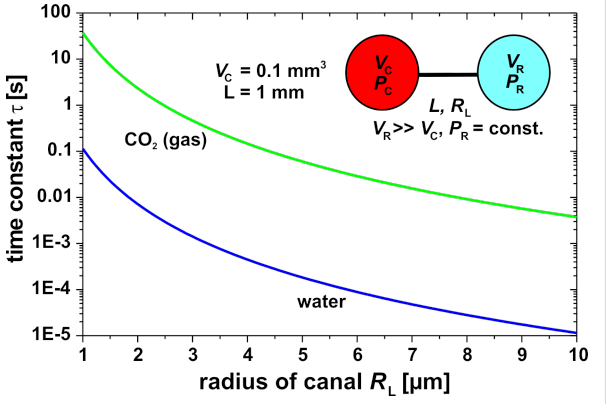

Figure 13: Comparison of time constants for a compensation leak of a cavity filled with water or with CO_2 gas as a function of the radius of the canal.

Conclusion

Just as in the photomechanic insect IR receptors, our technical model features very small displacements of the membrane in the sensing device in the range of 1 nm or less. The insects, however, have the advantage of possessing a very sensitive mechanoreceptor, the mechanosensitive neuron, which can detect minute deflections of its membrane. It seems that this sensitivity of the beetle is difficult to achieve for a technical sensor.

For our miniaturized technical sensor, an appropriate technical read-out mechanism with a high resolution of 1 nm may be necessary. Currently, a sensor with a capacitor as read-out is near completion in the *center of advanced european studies and research* (caesar), Bonn. As an alternative read-out for displacements in the nm-range, tunneling displacement transducers are under investigation. Several read-out methods will be evaluated, but it has to be stressed that this search must yield a rugged and cost-effective design in order to be able to compete with existing IR sensors.

An obvious method to enhance the displacement of the membrane is to choose liquids with optimal thermal properties, e.g., high thermal expansion coefficient and low heat capacity. Here several liquids permit an improvement. Methanol is a good candidate compared to *n*-pentane and toluene because of easier handling during the filling process of the cavity. The comparison of a liquid-filled cavity with a gas-filled cavity suggests that gas causes a larger deflection of the membrane. However, the final weighing of potential advantages or disadvantages of a miniaturized photomechanic IR sensor filled with a fluid needs further investigation.

Additionally, care has to be taken in selecting appropriate wall materials with the same low thermal conduction necessary to preserve the thermal energy inside the cell. Currently silicon is used due to its well known manufacturing technology for microsystems. As an alternative micro injection molding of plastic materials with low heat conductivity is under investigation.

Experimental

Morphological methods used are all based on well established light and electron microscopical procedures.

Mechanical tests were conducted in a nanomechanical test system capable of normal loading as well as in situ scanning probe microscopy (SPM) (TriboScope; Hysitron, Minneapolis, USA). Indentation tests were performed by using a three-sided Berkovich diamond tip with a total included angle of 142.3°. A proper area function was established by indenting in a poly(methyl methacrylate) (PMMA) test specimen with known hardness and modulus. Contact depths range from 250 to 1100 nm. The maximum load during indentation was 1,000 μN with loading and unloading rates of 100 μN/s, and a 10 s hold time at peak load to compensate for material creeping and to make sure that most of the plastic deformation was completed. It was repeatedly checked to ensure that longer holding times did not result in differing values. Hardness (H) and reduced Young´s modulus (E_r) both were calculated from the unloading portions of the load–displacement curves following well established procedures.

Acknowledgements

The authors acknowledge the measurements of absorption coefficients by Dr. Ing. V. Norkus and Dipl.-Ing. M. Schussig of the Institut für Festkörperelektronik (Technische Universität Dresden) and helpful discussions of the results. This work was funded by grants from BMBF (Grant No. 01RB0909A) and the German Science Foundation (DFG) through the Graduate Program GRK 1572.

References

1. Schmitz, A.; Sehrbrock, A.; Schmitz, H. *Arthropod. Struct. Dev.* **2007,** *36,* 291–303. doi:10.1016/j.asd.2007.02.002
2. Gronenberg, W.; Schmitz, H. *Cell Tissue Res.* **1999,** *297,* 311–318. doi:10.1007/s004410051359
3. Schmitz, H.; Schmitz, A. *Landscope* **2002,** *18,* 36–41.
4. Poulton, E. B. The habits of the Australian Buprestid "Fire-beetle", *Merimna atrata*. In *Proceedings of the Entomological Society of London 1915;* Rothschild, N. C., Ed.; Transactions of the Entomological Society of London, part V; Entomological Society of London: London, 1915; pp 3–4.
5. Apel, K.-H. *Entomol. Nachr. Ber.* **1989,** *33,* 278–280.
6. Schmitz, H.; Bleckmann, H. *Int. J. Insect Morphol. Embryol.* **1997,** *26,* 205–215. doi:10.1016/S0020-7322(97)00022-6
7. Schmitz, H.; Schmitz, A.; Bleckmann, H. *Arthropod. Struct. Dev.* **2001,** *30,* 99–111. doi:10.1016/S1467-8039(01)00028-7
8. Schmitz, H.; Trenner, S. J. *Comp. Physiol., A* **2003,** *189,* 715–722. doi:10.1007/s00359-003-0447-6
9. Schütz, S.; Weissbecker, B.; Hummel, H. E.; Apel, K.-H.; Schmitz, H.; Bleckmann, H. *Nature* **1999,** *398,* 298–299. doi:10.1038/18585
10. Schmitz, H.; Schmitz, A.; Trenner, S.; Bleckmann, H. *Naturwissenschaften* **2002,** *89,* 226–229. doi:10.1007/s00114-002-0312-4
11. Kreiss, E.-J.; Schmitz, A.; Schmitz, H. *Arthropod. Struct. Dev.* **2005,** *34,* 419–428. doi:10.1016/j.asd.2005.06.001
12. Schmitz, A.; Schätzel, H.; Schmitz, H. *Arthropod. Struct. Dev.* **2010,** *39,* 17–25. doi:10.1016/j.asd.2009.10.007
13. Champion, G. C. *Ent. Mo. Mag.* **1909,** *45,* 247–250.
14. Linsley, E. G. J. *Econ. Entomol.* **1943,** *36,* 341–342.
15. Evans, W. G. *Pan-Pac. Entomol.* **1962,** *38,* 59–62.
16. Vondran, T.; Apel, K.-H.; Schmitz, H. *Tissue Cell* **1995,** *27,* 645–658. doi:10.1016/S0040-8166(05)80020-5
17. Schmitz, H.; Bleckmann, H. J. *Comp. Physiol., A* **1998,** *182,* 647–657. doi:10.1007/s003590050210

18. Schmitz, H.; Mürtz, M.; Bleckmann, H. *Nature* **1997,** *386,* 773–774. doi:10.1038/386773a0
19. Evans, W. G. *Ann. Entomol. Soc. Am.* **2005,** *98,* 738–746. doi:10.1603/0013-8746(2005)098[0738:IRSOMA]2.0.CO;2
20. Keil, T. A. *Microsc. Res. Tech.* **1997,** *39,* 506–531. doi:10.1002/(SICI)1097-0029(19971215)39:6<506::AID-JEMT5>3.0.CO;2-B
21. Golay, M. J. E. *Rev. Sci. Instrum.* **1947,** *18,* 357–362. doi:10.1063/1.1740949
22. Chevrier, J. B.; Baert, K.; Slater, T. *J. Micromech. Microeng.* **1995,** *5,* 193–195. doi:10.1088/0960-1317/5/2/037
23. Kenny, T. W.; Reynolds, J. K.; Podosek, J. A.; Vote, E. C.; Miller, L. M.; Rockstad, H. K.; Kaiser, W. J. *Rev. Sci. Instrum.* **1996,** *67,* 112–128. doi:10.1063/1.1146559
24. Manufacturer: Heraeus Quarzglas, Hanau, Germany.
25. Section 6: Fluid Properties. In *Handbook of Chemistry and Physics,* 87th ed.; Lide, D. R., Ed.; CRC Press: Boca Raton, 2006; pp 120–121.
26. Szabo, I. *Höhere technische Mechanik: nach Vorlesungen,* 6th ed.; Springer: Berlin, 2001.
27. Soltner, H.; Bousack, H.; Schmitz, H. Zur transienten Temperaturentwicklung in einem fluidischen Infrarot-Detektor auf der Basis der infrarotempfindlichen Sensillen des Schwarzen Kiefernprachtkäfers *Melanophila acuminata*. In *Proceedings,* MikroSystemTechnik KONGRESS 2009, Berlin, Oct 12–14, 2009; VDE Verlag GmbH: Berlin, 2009; pp 401–404.
28. Wieliczka, D. M.; Wenig, S.; Querry, M. R. *Appl. Opt.* **1989,** *28,* 1714–1719. doi:10.1364/AO.28.001714
29. National Institute of Standards and Technology (NIST), Chemistry WebBook. http://webbook.nist.gov/ (accessed June 30, 2009).
30. Measurements by M. Schussig and V. Norkus, Institut für Festkörperelektronik, Technische Universität Dresden.
31. Beadle, W. E.; Tsai, J. C. C.; Plummer, R. D., Eds. *Quick reference manual for silicon integrated circuit technology;* Wiley: New York, 1985.
32. Thurm, U. Mechano-elektrische Transduktion. In *Biophysik – ein Lehrbuch;* Hoppe, W.; Lohmann, W.; Markl, H.; Ziegler, H., Eds.; Springer: Berlin, 1982; pp 681–696.
33. Capacitive Position Sensor for Nanopositioning – MicroSense Mini, MicroSense LLC, Massachusetts, USA.. http://www.microsense.net/products-position-sensors-microsense-mini.htm (accessed May 30, 2010).
34. Spurk, J. H.; Aksel, N. *Fluid Mechanics,* 2nd ed.; Springer: Berlin Heidelberg, 2008.
35. Bousack, H.; Schmitz, H.; Offenhäuser, A. Design of a fluidic infrared detector based on the infrared sensilla in the beetle *Melanophila acuminata*. In *Actuator 2008: Proceedings,* 11th International Conference on New Actuators, Bremen, June 27–30, 2008; Borgmann, H., Ed.; HVG Hanseatische Veranstaltungs-GmbH: Bremen, 2006; pp 786–789.

License and Terms

Beilstein Journal of Nanotechnology

Moisture harvesting and water transport through specialized micro-structures on the integument of lizards

Philipp Comanns[1], Christian Effertz[2], Florian Hischen[1], Konrad Staudt[1], Wolfgang Böhme[3] and Werner Baumgartner[*1]

Full Research Paper

Open Access

Address:
[1]Department of Cellular Neurobionics, RWTH-Aachen University, Lukasstr. 1, 52056 Aachen, Germany, [2]Department of Experimental Physics Ia, RWTH-Aachen University, Sommerfeldstr., 52056 Aachen, Germany and [3]Zoologisches Forschungsmuseum Alexander Koenig (ZFMK), Adenauerallee 160, 53113 Bonn, Germany

Email:
Werner Baumgartner[*] - werner@bio2.rwth-aachen.de

* Corresponding author

Keywords:
capillary; horned lizard; rain harvesting; thorny devil; water transport

Beilstein J. Nanotechnol. **2011,** *2,* 204–214.
doi:10.3762/bjnano.2.24

Received: 02 January 2011
Accepted: 19 March 2011
Published: 13 April 2011

This article is part of the Thematic Series "Biomimetic materials".

Guest Editors: W. Barthlott and K. Koch

Abstract

Several lizard species that live in arid areas have developed special abilities to collect water with their bodies' surfaces and to ingest the so collected moisture. This is called rain- or moisture-harvesting. The water can originate from air humidity, fog, dew, rain or even from humid soil. The integument (i.e., the skin plus skin derivatives such as scales) has developed features so that the water spreads and is soaked into a capillary system in between the reptiles' scales. Within this capillary system the water is transported to the mouth where it is ingested. We have investigated three different lizard species which have developed the ability for moisture harvesting independently, viz. the Australian thorny devil (*Moloch horridus*), the Arabian toadhead agama (*Phrynocephalus arabicus*) and the Texas horned lizard (*Phrynosoma cornutum*). All three lizards have a honeycomb like micro ornamentation on the outer surface of the scales and a complex capillary system in between the scales. By investigation of individual scales and by producing and characterising polymer replicas of the reptiles' integuments, we found that the honeycomb like structures render the surface superhydrophilic, most likely by holding a water film physically stable. Furthermore, the condensation of air humidity is improved on this surface by about 100% in comparison to unstructured surfaces. This allows the animals to collect moisture with their entire body surface. The collected water is transported into the capillary system. For *Phrynosoma cornutum* we found the interesting effect that, in contrast to the other two investigated species, the water flow in the capillary system is not uniform but directed to the mouth. Taken together we found that the micro ornamentation yields a superhydrophilic surface, and the semi-tubular capillaries allow for an efficient passive – and for *Phrynosoma* directed – transport of water.

Introduction

Arid environments are characterized by low precipitation and can therefore only be used as habitats if the vitally necessary water is accessible to the respective organism. To this end, two major challenges must be overcome: (1) Water (in its available form) must be collected, and (2) it must be transported to the place of ingestion. It is well known that not only insects (e.g., the famous Namibian tenebrionid beetles) but also several deserticolous and savanicolous lizards are able to collect water with their integument, and this ability has been termed "rain harvesting" [1,2]. It consists of two elements: A specific behaviour combined with special body postures, and a particular (micro-) morphology of the integument allowing the collection and transport of water towards the mouth. A translation of the German term "Feuchtigkeitsernten", i.e., "moisture harvesting", appears more appropriate to us as it describes the different kinds of water acquisition more comprehensively. It is important to note that, for the reptiles concerned, no significant water uptake is done through the integument itself. Rather, the water is transported on the integumental surface towards the mouth, performed by means of particular micro structures. As most of these lizards are unable to lick water from most parts of their body, such a water transport mechanism is essential for them. The stereotypic moisture harvesting behaviour of the Texas horned lizard *Phrynosoma cornutum* (Iguanidae: Phrynosomatinae) was extensively studied and described by [1]. However, other lizards such as the Australian thorny devil (*Moloch horridus*, Agamidae) lack such behavioural traits but nonetheless perform moisture harvesting in a successful way [2-5].

As well as *Phrynosoma* and *Moloch* [6-8], moisture harvesting has further been observed in the agamid genera *Phrynocephalus* [9] and *Trapelus* [10], and also in an arid-adapted testudinid tortoise, viz. *Psammobates tentorius trimeni* [11]. As – apart from the tortoise – the lizard species mentioned above are not closely related to each other, their ability to harvest moisture from their terrestrial environment must have evolved convergently or, in other words, has been "invented" several times during their evolution.

Generally, the integument (from Latin *integere* = to cover) is the organ system that covers the body and protects it from water loss and/or damage. The integument consists of the skin and its derivatives such as scales, feathers, hairs and nails and has a variety of functions: Next to mechanical protection and prevention of water loss from lower tissue layers, it serves also for temperature regulation and as a transmitter for tactile stimuli. The integument of lizards consists of several layers [12,13]: An outer beta-keratin layer mostly composed of beta-keratin, an inner alpha-layer built up from alpha-keratin and a meso layer separating the two former layers. The beta-layer is covered by the so-called "Oberhäutchen" which often exhibits particular micro structures (microdermatoglyphics). Several lizard species capable of moisture harvesting exhibit a honeycomb-shaped micro structure [14]. Next to the honeycomb-micro ornamentation, a special property of moisture-harvesting lizards is the existence of micro-channels (or interscalar channels) [4,15] formed by the partially overlapping (imbricate) scales. These channels have a narrow opening on their superficial side and thus form a semi-tubular capillary system over the entire lizard's body. This capillary system was believed to serve for the transport of water towards the mouth where the active water ingestion takes place [4,8].

Apart from the biological relevance, the exact functional morphology of lizard integumental structures allowing for moisture harvesting might also be of technical interest wherever efficient collection of small amounts of liquids and/or passive transport of these liquids is required. To gain a deeper insight of and understanding for moisture harvesting, we investigated the micro morphology of the skin of three lizard species known to perform moisture harvesting, viz. the iguanid *Phrynosoma cornutum*, and the two agamids *Moloch horridus* and *Phrynocephalus arabicus*. We further tried to mimic the properties and effects of the natural integument by manufacturing replicas of the surface topography. We found that in fact this micro ornamentation yields a super-wettable (superhydrophilic) surface, and the semi-tubular capillaries allow for an efficient – and in the case of *Phrynonoma cornutum* even directed! – passive transport of water.

Results and Discussion

Macroscopic morphology and wettability of the lizards' integuments

The three species under investigation were chosen because all perform moisture harvesting but developed separately in different arid areas. *Phrynosoma cornutum* developed in the deserts and steppe of North America, *Moloch horridus* is found in the Australian deserts and *Phrynocephalus arabicus* inhabits arid areas in the Near East and the Arabian peninsula. Thus we hoped that common structures among these species serve for the common goal of water acquisition.

The macroscopic body shape differs remarkably (Figure 1). While *Phrynocephalus arabicus* is an elongated smooth lizard, the bodies of *Phrynosoma cornutum* and *Moloch horridus* are covered with thorns or spikes, respectively, on their dorsal and lateral surfaces. The only common feature is a rather broad body [1]. The macroscopic morphology of the scales differs dramatically in the three species but also for one species with

Figure 1: The three lizard species under investigation. (A) *Moloch horridus* with an array of spikes covering the entire upper side of the body. The snout–vent length is about 90 mm and the total length is about 140 mm. (B) *Phrynosoma cornutum* also exhibits thorny appendages. The snout–vent length is about 95 mm. (C) *Phrynocephalus arabicus* has a velvet like surface and no apparent protuberations. The snout–vent length is about 80 mm.

respect to the exact location on the body. This is shown for *Phrynosoma cornutum* in Figure 2. Clearly the scales can be regular or irregular, polygonal or almost circular. The average scale area ranges from below 0.02 mm^2 to above 2.5 mm^2. Some scales form a spine like caudal (tailwards) end whereas others have a smooth caudal edge. Also for the other two species, the size and shape of the scales differ in dependence on the body location (data not shown).

The common feature of the scales, independent of form or species, is the wettability. Application of a water droplet onto the integument leads in all three species to an almost immediate spreading of the water as shown in Figure 3A–C and in the supplementary videos (Supporting Information Files 1–3). In contrast to the integument of lizards that do perform moisture harvesting, the droplet hardly spreads as shown in Figure 3D for a specimen of the so called sandfish (*Scincus scincus)*.

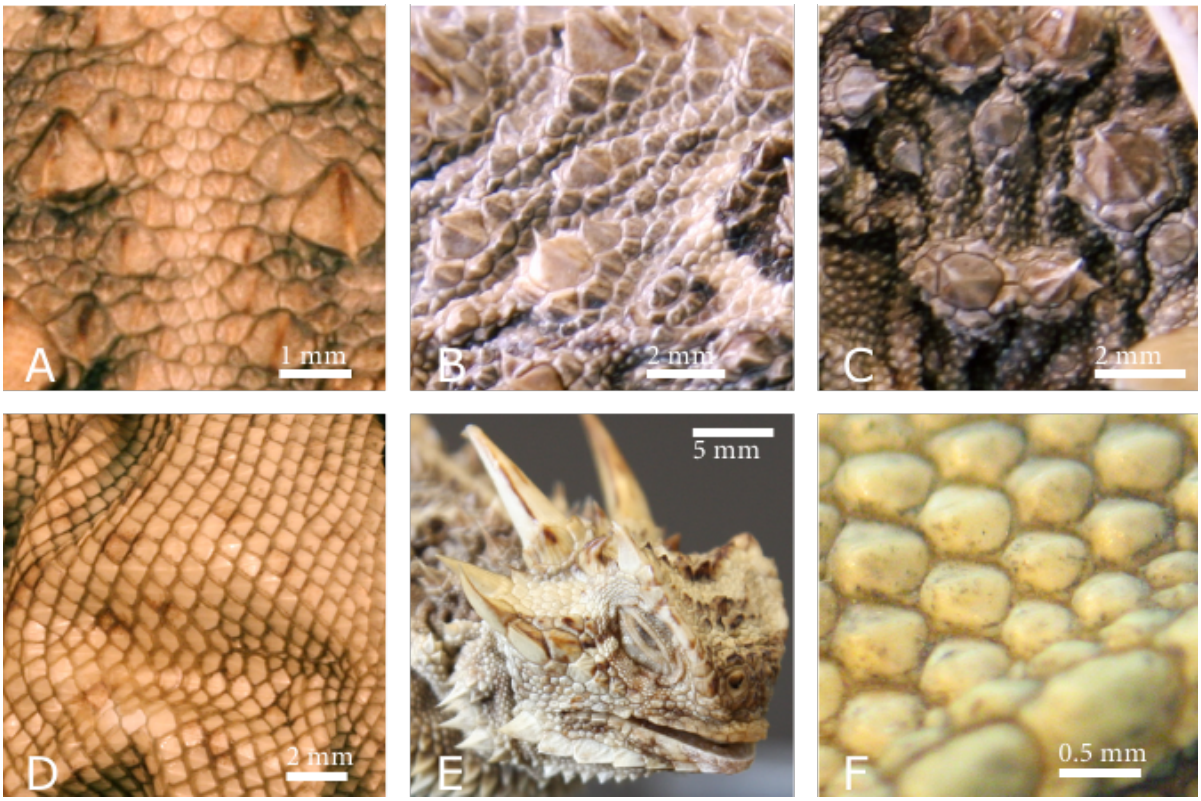

Figure 2: Different sizes and morphologies of scales of *Phrynosoma cornutum*. (A) Dorsal (back) scales along the medial line. (B) The lateral back is characterised by thorn like scales surrounded by small polygonal scales. (C) In the lateral neck region the thorns are mainly circular and are surrounded by small circular scales. (D) Ventral scales are diamond shaped and rather regular. (E) The scales on the head exhibit an enormous variety with respect to the morphology and size. (F) The scales on the chin are regular and almost circular.

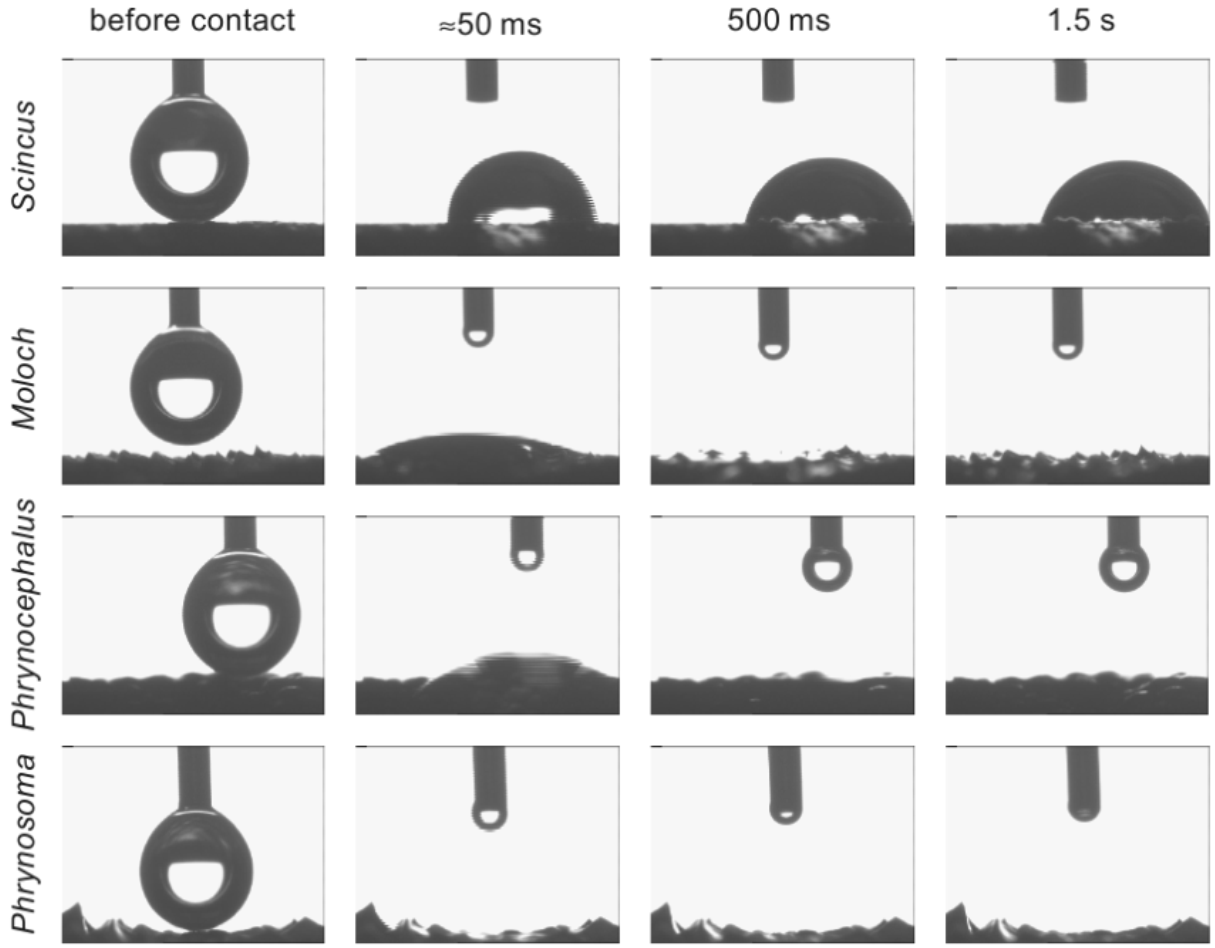

Figure 3: Water spreading on the reptiles' surfaces. A droplet of 5 µl was applied through a syringe and brought into contact with the surface by the use of a micro manipulator. While on the non-moisture harvesting lizard *Scincus scincus* the droplet hardly changes over time, an almost immediate spreading of the droplet on the moisture harvesting animals, i.e., *Moloch horridus*, *Phrynocephalus arabicus* and *Phrynosoma cornutum* can be seen. The images were recorded with a frame rate of 18 frames per second. Even in the first frame after contact, thus at about 50 ms after the droplet contacts the surface, the droplet is mostly spread and within 2 s the water is completely spread on the surface structure.

Although the velocity of the water spreading varies slightly throughout the body, we found absolutely no correlation of the wetting behaviour and any macroscopic geometric parameter of the scales in the three investigated species (data not shown). Thus, either material properties or the micro ornamentation of the scales induce the high wettability.

Contact angle and microscopic morphology

To quantify the wetting properties we attempted to measure the apparent contact angle. Measuring the apparent contact angle of the non-moisture harvesting lizards such as *S. scincus* was simply performed by using a commercially available contact angle meter and gave an apparent contact angle of 76 ± 5° (n = 7) on the dorsal and 59 ± 7° (n = 7) on the ventral scales, respectively. Other different non-moisture harvesting lizards were measured and yielded similar results (data not shown). However, the measurements on the moisture harvesting species were more difficult since water spreads out almost immediately. Thus, the measurements were performed by dipping a large scale vertically into water. For this purpose, a scale, i.e., the keratinised Oberhäutchen was removed from a dead *Phrynosoma cornutum* from the so called beard-region. There we found the largest scales of about 2.5 mm^2. This scale was dipped into water and we found asymmetric behaviour of the liquid (Figure 4A). While on the inner side of the scale a small meniscus was formed suggesting an apparent contact angle of about 60° to 70°, as measured by hand from the photo, the meniscus on the outer side is much higher forming an apparent contact angle of below 10°, rendering this surface super hydrophilic.

Interestingly, if the scale was completely dried in a desiccator containing silica gel before the experiment, the wetting was much less pronounced (Figure 4B). However, if the scale was

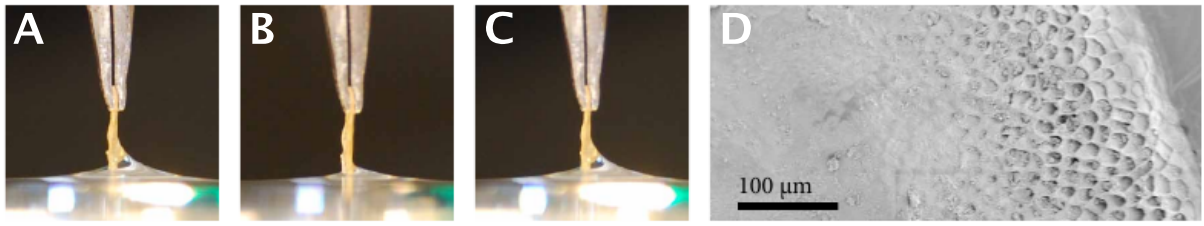

Figure 4: Scale of *Phrynosoma cornutum* dipped into deionised water. The freshly prepared scale (A) exhibits asymmetric behaviour. While on the inner side (left) a small meniscus, i.e., a large apparent contact angle of about 60° is formed, the outside of the scale (right) is wetted with an apparent contact angle of below 10°. If the experiment is repeated with a throughout dried scale (B), the difference of the inside and outside is less pronounced. After immersion of the scale in the water the scale again behaves like a freshly prepared scale (C). While the inside of this particular scale is completely flat (not shown), the outer surface exhibits a distinct micro ornamentation (D). Towards the edge (right) of the scale a honeycomb like structure is visible, while the centre of the scale is hardly structured.

completely immersed once and the experiment repeated, the same results as with the freshly removed scale could be obtained repeatedly (Figure 4C). When examined in the scanning electron microscope (SEM), the scale used for the above described experiment clearly revealed micro ornamentation on the outer side as previously described in the literature [14], whereas the inner side shows no micro ornamentation (Figure 4D). On the outer part, i.e., closer to the edge of the scale honeycomb like structures are visible on the outer surface. These structures are a more or less common feature of the scales of all three investigated species (Figure 5). Measurements with the SEM revealed that *Moloch horridus* exhibits these structures with a diameter of about 10 µm to 20 µm and a depth of about 5 µm in all scales (Figure 5A), while for *Phrynosoma cornutum* structures with a diameter of about 15 µm to 25 µm and depth of roughly 5 µm are mainly found at the scales' periphery (Figure 5B). *Phrynocephalus arabicus* has the least pronounced honeycomb structure. Here only dimples with a diameter of about 20 µm to 30 µm and a depth of about 1 µm are visible (Figure 5C). The depth was estimated from SEM-images with a viewing angle of less than 10° to the integument surface.

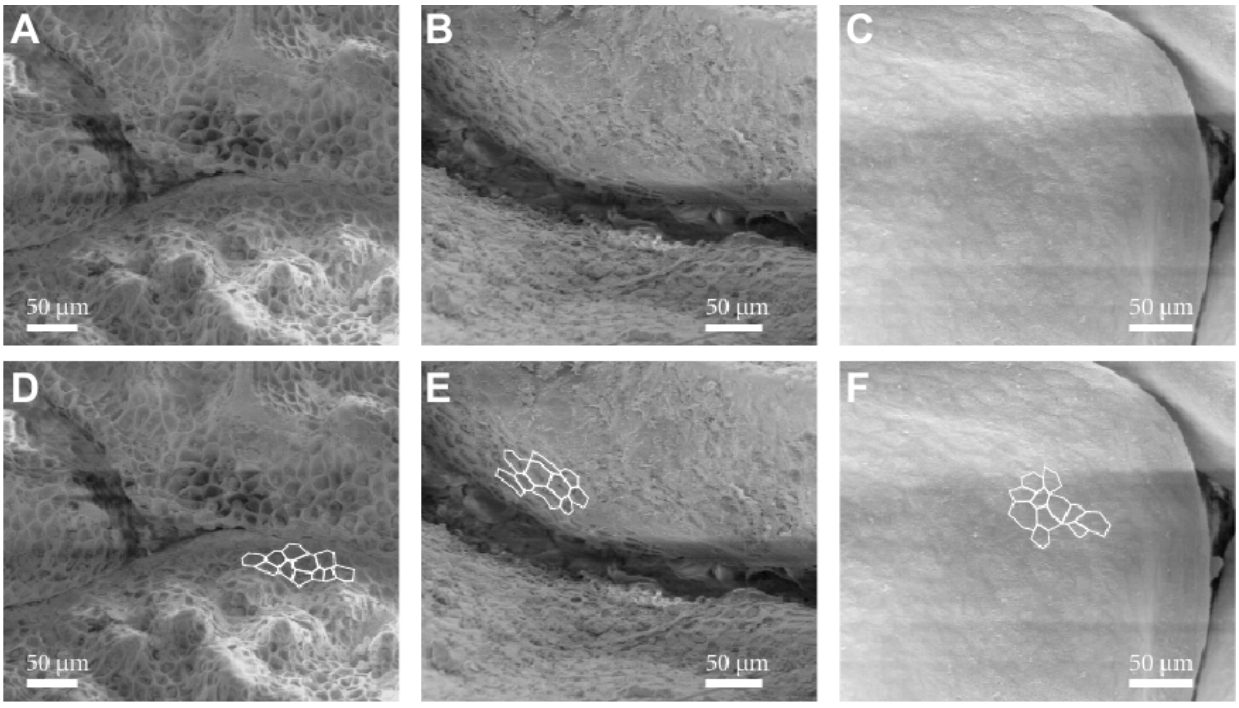

Figure 5: Micro ornamentation of the scales of the three investigated lizard species. (A) *Moloch horridus* shows the honeycomb like micro ornamentation virtually all over all scales. (B) *Phrynosoma cornutum* shows clear honeycomb like micro structures, but typically mainly at the periphery of the scales. (C) *Phrynocephalus arabicus* the only honeycomb like structures appear like dimples. (D) (E) and (F) show the images of A–C with some of the micro ornamentations marked for better orientation.

To test further whether these structures are responsible for the reduced apparent contact angle, we manufactured epoxy resin replicas of the surfaces of different body parts of the investigated species. The unstructured epoxy resin has a contact angle of 79°, which is slightly higher than the scale material. According to electron microscopy, these replicas have a good resemblance to the surface structure (see Supporting Information File 4). As expected, the replicas did not exhibit an improved wetting behaviour if they were dried before the experiment. Under these conditions the contact angle is almost identical to the contact angle of the unstructured resin (data not shown). However, if a droplet is applied for some time (ranging from several seconds to about a minute) onto the replica, the water spreads spontaneously (Figure 6). After this, if the replica is not dried throughout, the replica stays highly wettable in contrast to the unstructured resin as exemplified in the supplementary videos (Supporting Information Files 5–6).

It is generally known that structuring, i.e., increased roughness of a hydrophilic material results in a decreased contact angle [16]. Assuming a Wenzel-model [16,17] for the wetting of the lizard scales however, does not fully predict the observed effect. Structures with typical sizes significantly below the dimension of the applied water droplet would result in an apparent contact angle $\cos \varphi^* = r \cos \varphi$ where φ is the contact angle of the unstructured material and r is the ratio of the actual surface and the apparent surface. In our case the unstructured material exhibits a contact angle of about 70° and the structured material is almost perfectly wettable, i.e., the contact angle is below 10°. This would require $r > 3$ which is approximately the case for *Moloch horridus* ($r \approx 3$) but not for *Phrynosoma cornutum* ($r \approx 2.3$) or *Phrynocephalus arabicus* ($r \approx 1.4$) as estimated from the above mentioned dimensions of the honeycomb structures. So the reduction of the contact angle for these animals cannot simply be explained by increased roughness alone. Thus it is tempting to assume the Cassie-model for liquid impregnating [18] to be valid, i.e., that the honeycombs and dimples respectively, allow for the formation of a stable thin water film within a dimple so that even with a contact angle of about 60–70° as given by the scale's material, an outspread water-scale-contact is stable. The Cassie-formula for the apparent contact angle on a composite material is given by $\cos \varphi^{Cassie} = \gamma_1 \cos \varphi_1 + \gamma_2 \cos \varphi_2$. Here the effective contact angle φ^{Cassie} is dependent on the area fraction of component one (γ_1) and component two (γ_2) and the contact angles of material one (φ_1) and two (φ_2). If the dimples are filled with water, i.e., $\varphi_2 = 0$, the area fraction of water in the dimples is 73% (i.e., the fraction of pure scale material is 27%) and is sufficient to make the surface superhydrophilic and explain the described hysteresis of the contact angle.

Water condensation on the scales

It is debated in the literature whether or not condensation of water directly on the lizards' bodies plays a major role for moisture harvesting [2,4,5]. Reptiles are cold blooded, i.e., they adapt their body temperature to the surrounding air with some delay which is related to the body mass. Thus after a cold night, the body might be cold enough to allow condensation of water from warm air in the morning. The temperature difference between day and night in deserts is normally remarkably high.

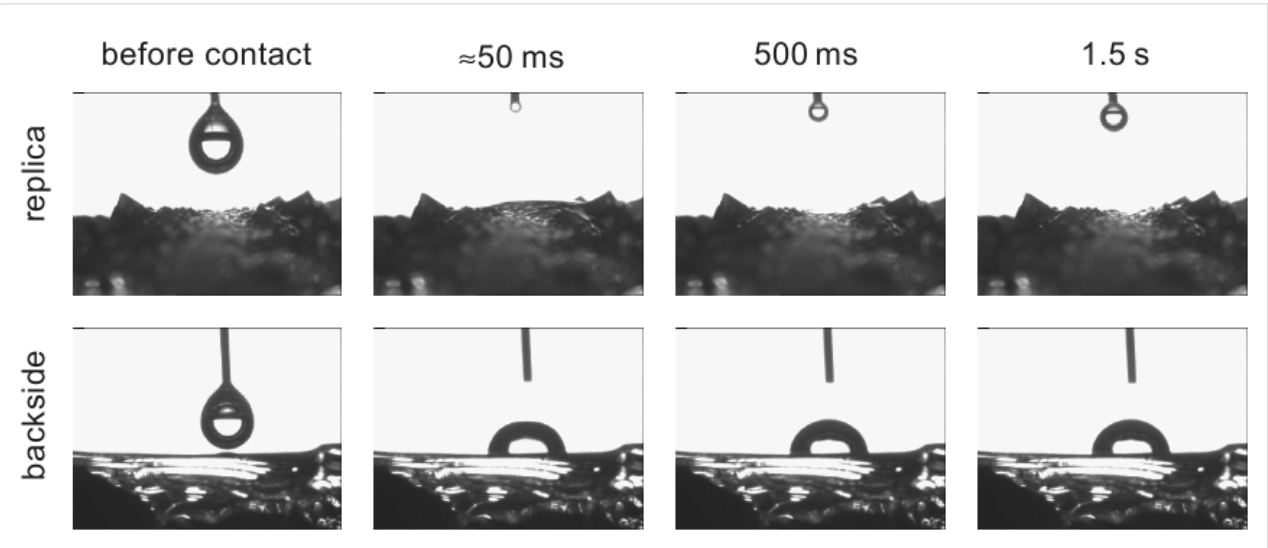

Figure 6: Water spreading on epoxy replica of moisture harvesting reptiles. A 5 µl droplet of water was applied to the epoxy replica of the medial back of the moisture harvesting species *Phrynosoma cornutum*. Similar to the situation on the native surface (see Figure 3), the water spreads at high velocity. The epoxy resin is not very wettable as can be seen when a 5 µl droplet is applied to the backside of the replica which exhibits an unstructured surface. The droplet stays perfectly constant forming a contact angle of about 80°.

Together with the typical air humidities, it was found that the temperature difference should be sufficient for significant condensation on a lizard [2]. However, experimental results show that the amount of condensed water is not sufficient to satisfy the daily water need of lizards [5,19]. It must be noted here that these experiments did not fully resemble the natural conditions.

To test the condensation behaviour, we measured the amount of condensed water on epoxy replica and on non-structured epoxy surfaces. The replicas were cut to a diameter of exactly 15 mm so all samples had about the same projected area for condensation. The replicas were thermally equilibrated at 20.5 °C. The mass was determined by weighing and then the replicas were put into 80 °C warm moisture saturated air for 15 s. After this time the mass was immediately determined again. The results are depicted in Figure 7. Clearly the total amount of water condensed on the epoxy resin is significantly higher on the replicas of the moisture harvesting lizards than on the unstructured resin as tested by an unpaired two-sided t-test. A replica of the non-moisture harvesting *S. scincus* hardly shows an improved condensation in comparison to the unstructured resin. If the resin is simply made rough (average roughness $R_a \approx 3$ µm) by means of sand paper, the condensation is improved slightly, but not significantly. Thus the honeycomb structure increases the condensation by about 100% on average for the three lizard species under investigation. This might be caused by the increased roughness only, because a rough surface supports more condensation foci. However, if condensation had taken place leading to a water film in the honeycombs, the surface exhibits the above described high wettability which would then allow for further improved moisture harvesting from other water sources like rain, fog or dew.

The experiments on the removed scale as well as the condensation behaviour clearly indicate that a minimal moisture level on the scales is necessary in order to be effective. On the living animal condensation might further improve the initial wetting of the scales by the – in fact very small – water loss of the animal through the integument [5].

Transport in the capillary network

As stated earlier, initial wetting of the scales is necessary but not sufficient for successful moisture harvesting. The collected water has to be transported to the mouth of the animals as licking off the collected water from the integument is hardly possible due to the animals' anatomy. As shown in the image sequence in Figure 8 and in the supplementary videos (Supporting Information Files 7–9) water, when applied onto the animal, is adsorbed and immediately soaked into a capillary system which then transports the water passively.

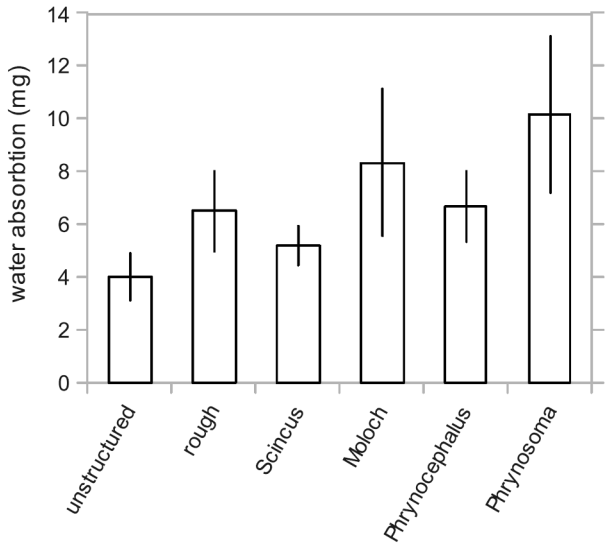

Figure 7: Water condensation on epoxy replicas of structured surfaces. The epoxy replicas were cut into disks with a diameter of 15 mm. These disks were thermally equilibrated to 20.5 °C and then held for 15 s in water-saturated air at a temperature of 80 °C. The amount of water was determined by the mass difference of each replica. Clearly structured surfaces allow for more condensation when compared with unstructured ones. Even an unspecific roughness introduced by polishing paper (roughness, $R_a \approx 3$ µm) increased the amount of water, although not significantly (p = 0.070). The replica of a non-moisture harvesting lizard *Scincus scincus* exhibits no significant increase of the condensation (p = 0.093). The replicas of the moisture harvesting lizards *Moloch horridus* (p = 0.032), *Phrynocephalus arabicus* (p = 0.034) and especially *Phrynosoma cornutum* (p = 0.007) show a significantly increased water condensation. Significance was tested by use of a two sided t-test assuming different standard deviations for the samples.

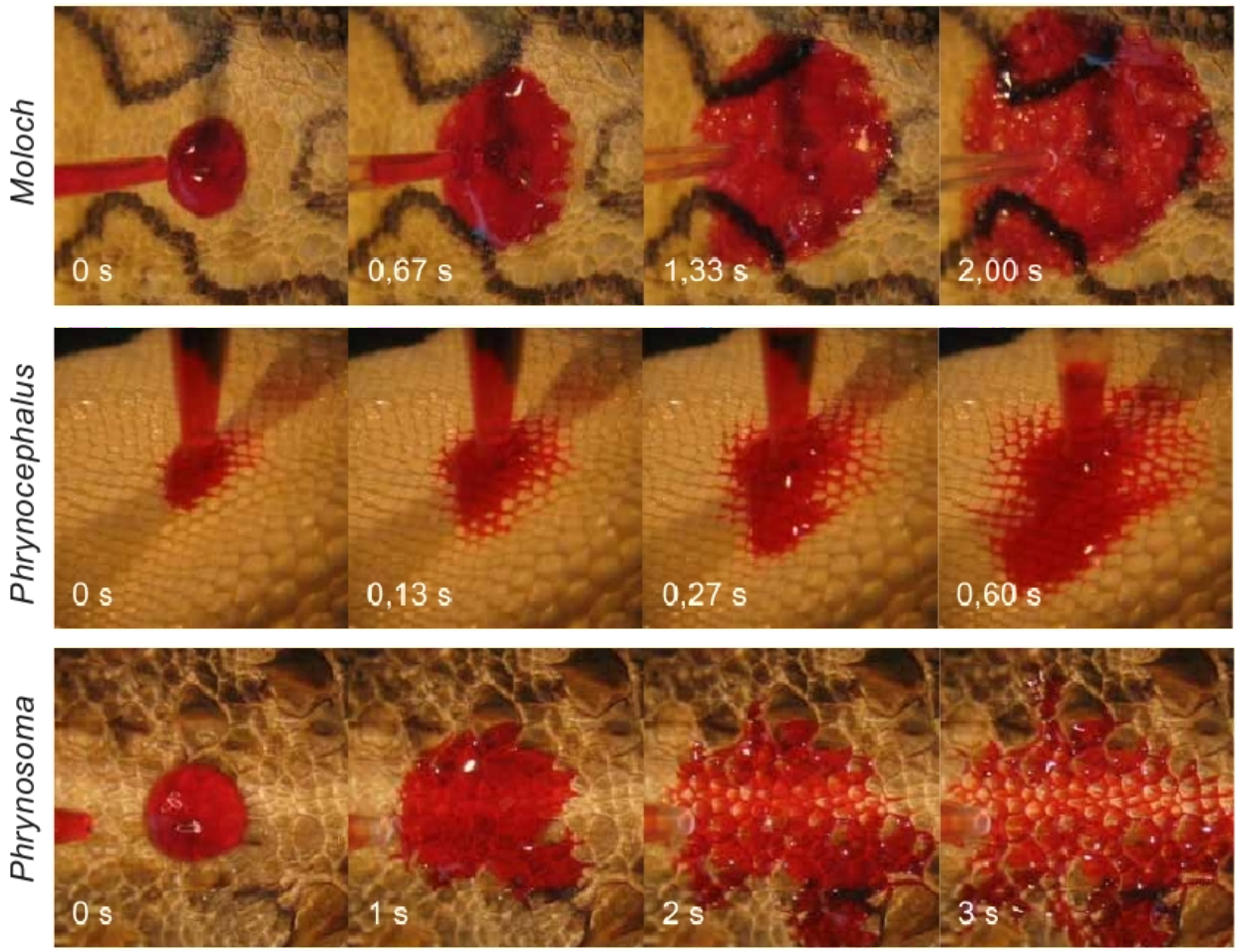

Figure 8: Water transport in interscalar capillaries. The behaviour of coloured water on the integument of the three investigated lizards is shown. The mouth is always located to the right. Note the colouring of the interscalar capillaries, best seen for *Phrynocephalus*. While the transport is about symmetrical for *Moloch* and *Phrynocephalus*, the velocity of the water transport is highest in direction to the mouth on *Phrynosoma*.

Most interestingly while *Phrynocephalus arabicus* and *Moloch horridus* clearly show an almost symmetric water flow from the point of water application, i.e., similar transport velocities rostral (forward), caudal (backward) and lateral (sidewards), *Phrynosoma cornutum* behaves differently. As already clearly evident from the supplementary videos and as depicted in detail in Table 1, the water flows with significantly higher velocity rostral, i.e., to the mouth of the animal.

Because of the highly irregular morphology of *Moloch horridus* a detailed analysis of the flow velocity over longer time intervals is time consuming. Thus we compared the flow velocity of *Phrynocephalus arabicus* and *Phrynosoma cornutum* in more detail. For this a frame-to-frame analysis of videos of water transport was performed yielding the velocity of the water in different directions over time. A typical result is depicted in Figure 9. For *Phrynocephalus arabicus* the velocity is almost

Table 1: Average water transport velocity[a].

	average velocity (mm/s)		
	rostral	lateral	caudal
P.a.	1.94 ± 0.91	2.49 ± 1.01	2.57 ± 1.91
P.c.	3.15 ± 0.94	1.84 ± 0.24	1.61 ± 0.45
M.h.	2.18 ± 0.54	1.80 ± 0.43	2.15 ± 0.35

[a]The average transport velocity within the first 333 ms after the application of 7 µl of coloured water onto the different species, i.e., *Phrynocephalus arabicus* (*P.a.*), *Phrynosoma cornutum* (*P.c.*) and *Moloch horridus* (*M.h.*) is shown. The velocity was measured on different positions on the body with n ≥ 6 independent measurements for each condition. The values are rather constant within a species except for *Phrynosoma cornutum* (*P.c.*) where the velocity towards the mouth, i.e., rostral is significantly higher than for all other directions as determined by Wilcoxon-tests when applying a significance level of $\alpha = 0.05$.

identical in all directions over time (Figure 9A). The monotonous decrease can be modelled theoretically. Generally the water flow in a capillary system can be described by the Washburn-equation [20]

$$\frac{\partial l}{\partial t} = \frac{P_O + \frac{2\gamma}{r} \cdot \cos(\varphi) \cdot (r^4 + 4\varepsilon r^3)}{8r^2\ \eta l} \quad (1)$$

Here l is the distance the fluid penetrates into the capillary tube, t is time, P_O is the total outer pressure, i.e., the atmospheric pressure plus the hydrostatic pressure acting on the liquid. γ is the surface tension, φ is the contact angle of the liquid on the unstructured capillary material, r is the radius of the capillary, η is the viscosity of the liquid, and ε is the coefficient of slip.

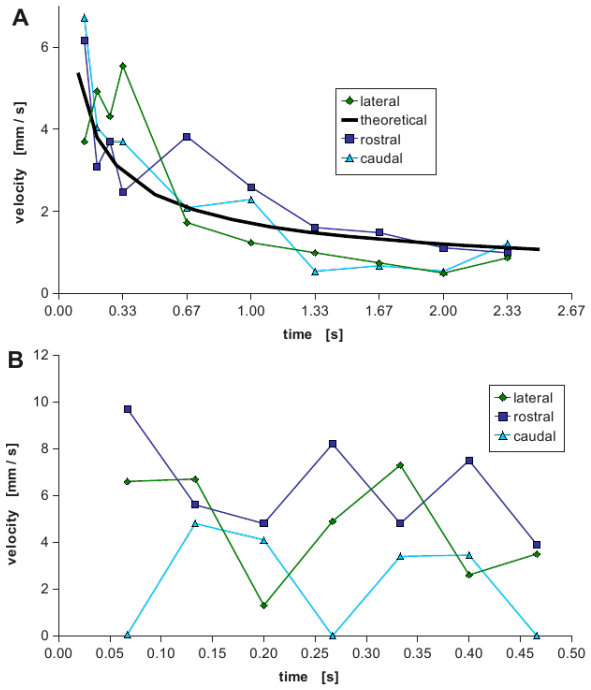

Figure 9: Water transport velocity in the capillary system. Two typical examples of results of a frame-to-frame analysis of videos showing the transport of coloured water in the capillaries are shown for *Phrynocephalus arabicus* (A) and *Phrynosoma cornutum* (B). The velocities were measured in direction to the mouth (rostral, dark blue squares), towards the tail (caudal, light blue triangles) and sidewards (lateral, green diamonds). For *Phrynocephalus arabicus* (A) no significant difference can be seen when comparing the velocities in the different directions. The theoretical behaviour described by the Washburn-equation (solid black line) fits the data quite well suggesting simple capillary transport uniformly flowing in all directions. In contrast for *Phrynosoma cornutum* the typical result is that the velocity has a highly oscillating behaviour and, most interestingly, the velocity towards the mouth is normally higher than tailwards or sideways.

The morphology of the capillaries was determined by microscopic analysis of semi-thin sections from all investigated species. We found that in between the scales semi-tubular channels are located (Supporting Information File 10) and we could measure the dimensions.

Because the total penetration length l of the liquid is hard to measure accurately in an irregular capillary system, we measured the liquid's velocity, i.e., $\partial l/\partial t$ in dependence on the time t by analysing videos on a frame-to-frame basis. For that the above ordinary differential equation was integrated numerically. By approximating the capillaries by tubes assuming the radius to be 30 µm and by introducing the parameters according to the literature and the above measurements (i.e., $P_O = 0$ as the species were almost horizontally, γ = 72.5 mN/m, φ = 60°, η = 1mPa·s) and by least square fitting the unknown coefficient of slip ε to be 0.1, one obtains the theoretical curve depicted as solid black line in Figure 9A. This curve resembles the measured values very well, thus normal capillary transport takes place in *Phrynocephalus arabicus*. The transport mechanism is homogeneous and the animal's mouth serves as a water sink. Thus when the capillary system is filled, water is ingested and thus sucked through the capillary system from all over the body, similar to the capillary system in plants where transport takes place via vessels due to evaporation of the water at the leaves which serve as a sink.

However, as depicted in Figure 9B the velocity behaviour for *Phrynosoma cornutum* differs dramatically and cannot be described by the above theory when assuming an uniform capillary system. In our microscopic analysis of semi-thin sections we found that indeed the dimensions of the capillaries' cross sections vary remarkably from 30 µm to 300 µm. Furthermore the wall structure shows some morphological details (dimples, protrusions, folds) which might be responsible for the directed flow [16] and which will have to be analysed in detail in future studies.

Conclusion

Taken together we found that the convergently evolved honeycomb like micro structures on moisture harvesting lizards render the surface superhydrophilic. The contact angle of the unstructured material is 60–70° whereas the contact angle for the structured material is below 10°. This effect could be mimicked by polymer replicas of the lizards' surfaces clearly showing that the effect is not a material property but due to the structure. The structure can be supposed to hold a thin water film stable rendering the contact energy for further water to be decreased. The initial moisture necessary for this effect can be easily obtained by condensation since on the structured surfaces condensation is improved by about 100%. The collected water is effectively transported by an interscalar capillary network towards the mouth of the lizards. The mouth serves as water sink so that water will be soaked from the whole body's surface

by capillary forces. In the case of *Phrynosoma cornutum*, the capillary effect is enhanced towards the mouth which terminates in a directed water transport.

Experimental

Photographic images of the lizards were taken with a Canon EOS 350D (Canon Inc., Tokyo, Japan) with either the original telephoto lens or a 50 mm macro lens. The auto exposure setting was used without flashlight.

For SEM-imaging, tissue samples (approx. 1 × 3 mm) from different body regions of alcohol fixed museum specimen (Zoologisches Forschungsmuseum Alexander Koenig (ZFMK) in Bonn) of the lizards under investigation were taken. These samples were fixed overnight in 4% (v/v) glutardialdehyde in 70% ethanol followed by dehydration in an ascending alcohol series (90%, 60 min; 96%, 60 min; 99.8%, 60 min twice; 100%, 2 days). After washing three times for 20 min with hexamethyldisilazane the samples were dried at room temperature for 3 days. The samples were sputter-coated without further treatment with gold and observed using a Stereoscan S604 SEM (Cambridge Instruments, UK). Images were digitally recorded with an attached i-scan digitizer (ISS Group Services Ltd., Manchester, UK) with an image acquisition time of 50 s.

For determination of water behaviour on the animals' surfaces two different approaches were used. A commercially available contact angle meter (DSA-10, Krüss, Hamburg, Germany) was used applying droplets of about 5 µl of deionised water and observing the behaviour with an integrated video camera. Alternatively, droplets of 4–7 µl of deionised water containing the red colourant 0.5% (w/v) Ponceau S Red and the behaviour of the droplet observed by a Canon camera using the video mode. The image analysis was performed using the software GIMP (version 2.6.8) which allows for the automatic recognition of the red colour and for morphometric measurements.

For production of epoxy, replicas of a negative form was obtained from the animals using dental moulding paste VPS Hydro (Henry Schein Inc., Melvolle, USA). As alcohol fixated specimen from the ZFMK were used, the animals were initially dried for 30 min. A droplet of about 2 cm diameter was applied onto the integument and pressed onto the animal by use of a 10 mL petri dish. After hardening, the negative form was removed carefully from cranial to caudal. The negative form was filled with epoxy resin (Toolcraft, Conrad Electronic, Hirschau, Germany). The ratio of resin to hardener was 10:4. The resin was degassed in a desiccator for 5 min. The quality of the replicas was checked by SEM.

For condensation measurements, replicas were cut into discs of exactly 15 mm diameter. The samples were initially weighed and equilibrated at room temperature (20.5 °C) before holding them in a moisture saturated atmosphere at 80 °C. The weight increase was determined immediately.

For histological analysis of the integument, samples of approximately 1 × 3 mm size were fixed in 70% ethanol containing 2% (v/v) glutardialdehyde and 2% (v/v) formaldehyde. The samples were dehydrated in an ascending alcohol series (3 × 15 min 70%; 15 min, 80%; 15 min, 90%; 15 min 96% and 3 × 30 min, 100%). The samples were put into LR-White resin (London Resin Company Ltd., Berkshire, London) at 4 °C overnight. The resin was changed to new LR-White and allowed to polymerise at 60 °C for 48 h. The samples were cut into 7 µm thick slices using an OM U3 microtom (Reichert, Wien, Austria) stained with Methylene Blue and investigated with a standard optical microscope.

Supporting Information

Supporting Information File 1

Application of a 5 µl droplet of deionised water onto the venter of *Moloch horridus*.
[http://www.beilstein-journals.org/bjnano/content/supplementary/2190-4286-2-24-S1.mpeg]

Supporting Information File 2

Application of a 5 µl droplet of deionised water onto the back of *Phrynocephalus arabicus*.
[http://www.beilstein-journals.org/bjnano/content/supplementary/2190-4286-2-24-S2.mpeg]

Supporting Information File 3

Application of a 5 µl droplet of deionised water onto the back of *Phrynosoma cornutum*.
[http://www.beilstein-journals.org/bjnano/content/supplementary/2190-4286-2-24-S3.mpeg]

Supporting Information File 4

SEM-image of *Moloch horridus* and the corresponding epoxy replica. Clearly the general morphology as well as the honeycomb-like micro ornamentation are well reproduced.
[http://www.beilstein-journals.org/bjnano/content/supplementary/2190-4286-2-24-S4.tif]

Supporting Information File 5

Application of 5 µl of deionised water onto a epoxy replica of the back of *Phrynosoma cornutum*.
[http://www.beilstein-journals.org/bjnano/content/supplementary/2190-4286-2-24-S5.mpeg]

Supporting Information File 6

Application of 5 µl deionised water onto the flat back side of the same replica as used in File 6.
[http://www.beilstein-journals.org/bjnano/content/supplementary/2190-4286-2-24-S6.mpeg]

Supporting Information File 7

Application of a 7 µl droplet of coloured deionised water onto the venter of *Moloch horridus*.
[http://www.beilstein-journals.org/bjnano/content/supplementary/2190-4286-2-24-S7.mpeg]

Supporting Information File 8

Application of a 7 µl droplet of coloured deionised water onto the back of *Phrynocephalus arabicus*.
[http://www.beilstein-journals.org/bjnano/content/supplementary/2190-4286-2-24-S8.mpeg]

Supporting Information File 9

Application of a 7 µl droplet of coloured deionised water onto the back of *Phrynosoma cornutum*.
[http://www.beilstein-journals.org/bjnano/content/supplementary/2190-4286-2-24-S9.mpeg]

Supporting Information File 10

Semi-thin histological sections through the integument of *Phrynosoma cornutum.* Black: spaces of the capillary system, due to overlapping scales. Different dimensions and wall morphologies can be observed.
[http://www.beilstein-journals.org/bjnano/content/supplementary/2190-4286-2-24-S10.tif]

Acknowledgements

The authors thank Agnes Weth for excellent technical assistance. The Deutsche Forschungsgemeinschaft (DFG) is acknowledged for financial support within the PhD-Program (Graduiertenkolleg GRK1572).

References

1. Sherbrooke, W. C. *J. Herpetol.* **1990,** *24,* 302–308. doi:10.2307/1564398
2. Sherbrooke, W. C. *J. Herpetol.* **1993,** *27,* 270–275. doi:10.2307/1565147
3. Bentley, P. J.; Blumer, W. F. C. *Nature* **1962,** *194,* 699–700. doi:10.1038/194699a0
4. Gans, C.; Merlin, R.; Blumer, W. F. C. *Amphibia-Reptilia* **1982,** *3,* 57–64. doi:10.1163/156853882X00167
5. Withers, P. *J. Herpetol.* **1993,** *27,* 265–270. doi:10.2307/1565146
6. Peterson, C. C. *Southwest Nat.* **1998,** *43,* 391–394.
7. Sherbrooke, W. C. *Herpetol. Rev.* **2002,** *33,* 310–312.
8. Sherbrooke, W. C. *Amphibia-Reptilia* **2004,** *25,* 29–39. doi:10.1163/156853804322992814
9. Schwenk, K.; Greene, H. W. *J. Herpetol.* **1987,** *21,* 134–139. doi:10.2307/1564473
10. Veselý, M.; Modrý, D. *J. Herpetol.* **2002,** *36,* 311–314. doi:10.2307/1566009
11. Auffenberg, W. *Anim. Behav.* **1963,** *11,* 72–73. doi:10.1016/0003-3472(63)90012-5
12. Maderson, P. F. A.; Rabinowitz, T.; Tandler, B.; Alibardi, L. *J. Morphol.* **1998,** *236,* 1–24. doi:10.1002/(SICI)1097-4687(199804)236:1<1::AID-JMOR1>3.0.CO;2-B
13. Alibardi, L.; Maderson, P. F. A. *J. Morphol.* **2003,** *256,* 111–133. doi:10.1002/jmor.10079
14. Peterson, J. A. *J. Herpetol.* **1984,** *18,* 437–467. doi:10.2307/1564106
15. Sherbrooke, W. C.; Scardino, A. J.; de Nys, R.; Schwarzkopf, L. *Zoomorphology* **2007,** *126,* 89–102. doi:10.1007/s00435-007-0031-7
16. Quéré, D. *Annu. Rev. Mater. Res.* **2008,** *38,* 71–99. doi:10.1146/annurev.matsci.38.060407.132434
17. Wenzel, R. N. *Ind. Eng. Chem.* **1936,** *28,* 988–994. doi:10.1021/ie50320a024
18. Gennes, P. G.; Brochard–Wyart, F.; Quéré, D. *Capillary and wetting phenomena;* Springer: Berlin, 2010.
19. Lasiewski, R. C.; Bartholomew, G. A. *Copeia* **1969,** *2,* 405–407. doi:10.2307/1442100
20. Washburn, E. W. *Phys. Rev.* **1921,** *17,* 273–283. doi:10.1103/PhysRev.17.273

License and Terms

Beilstein Journal of Nanotechnology

Sorting of droplets by migration on structured surfaces

Wilfried Konrad*[1] and Anita Roth-Nebelsick[2]

Full Research Paper

Open Access

Address:
[1]University of Tübingen, Institute for Geosciences, Sigwartstrasse 10, D-72076 Tübingen, Germany and [2]State Museum of Natural History Stuttgart, Rosenstein 1, D-70191 Stuttgart, Germany

Email:
Wilfried Konrad* - wilfried.konrad@uni-tuebingen.de

* Corresponding author

Keywords:
microdroplets; microfluidics; surface; surface energy; surface structures

Beilstein J. Nanotechnol. **2011,** *2,* 215–221.
doi:10.3762/bjnano.2.25

Received: 03 January 2011
Accepted: 29 March 2011
Published: 20 April 2011

This article is part of the Thematic Series "Biomimetic materials".

Guest Editors: W. Barthlott and K. Koch

Abstract

Background: Controlled transport of microdroplets is a topic of interest for various applications. It is well known that liquid droplets move towards areas of minimum contact angle if placed on a flat solid surface exhibiting a gradient of contact angle. This effect can be utilised for droplet manipulation. In this contribution we describe how controlled droplet movement can be achieved by a surface pattern consisting of cones and funnels whose length scales are comparable to the droplet diameter.

Results: The surface energy of a droplet attached to a cone in a symmetry-preserving way can be smaller than the surface energy of a freely floating droplet. If the value of the contact angle is fixed and lies within a certain interval, then droplets sitting initially on a cone can gain energy by moving to adjacent cones.

Conclusion: Surfaces covered with cone-shaped protrusions or cavities may be devised for constructing “band-conveyors” for droplets. In our approach, it is essentially the surface structure which is varied, not the contact angle. It may be speculated that suitably patterned surfaces are also utilised in biological surfaces where a large variety of ornamentations and surface structuring are often observed.

Introduction

Manipulation of droplets is an issue of great interest in microfluidics. The underlying motivation is the design of microdevices that are able to perform various fluidic processes within dimensions on the micrometer scale [1]. “Lab-on-a-chip” concepts aim at integrating chemical and biochemical processes into chip-like designs that enable the user to carry out tasks in analytical chemistry or bioassay applications [2]. The design of microfluidic batch processes requires a continuous and controlled flow and cycling of suspended droplets of reactants without contamination. Single droplet movement can be

achieved with different techniques, such as thermal Marangoni flow, electrowetting and vibration techniques [1]. Specifically designed surfaces can lead to spontaneous droplet movement, even uphill [3].

It is well known [1,4-8] that liquid droplets move towards areas of minimum contact angle if placed on a flat solid exhibiting a gradient of contact angle. Yang et al. [2] devised a hydrophobic micropatterned surface with a gradient in density of the microstructures that lead to droplet movement with maximum speeds of about 60 mm/s. This effect can be obtained by varying 1) chemical contact angle, 2) surface texture, or 3) both parameters.

In this contribution we describe how a controlled droplet movement can be achieved by a surface pattern consisting of cones and funnels whose length scales are comparable to the droplet diameter. In our approach, it is essentially the surface structure which is varied, not the contact angle. The actual movement of the droplet on the continuously varying solid surface pattern depends both on the surface pattern and on the contact angle between droplet and solid. Therefore, it is possible to devise surface patterns which are able to direct droplets differently, depending on their chemical nature.

Results

First, we derive the surface formation energy of droplets attached to cone shaped protrusions or cavities. Afterwards, we discuss the properties of specific surface patterns composed of cones with varying apex angles.

Properties of droplets attached to cone shaped protrusions or cavities

Consider a sphere-like droplet of radius R attached to an axially symmetric, cone shaped protrusion or cavity with apex half-angle $\varepsilon = 0\ldots180°$ forming a contact angle $\theta = 0\ldots180°$ (see Figure 1). We assume that the droplet is attached in a symmetry preserving way (i.e., the symmetry axes of cone and droplet coincide). We further assume that the droplet consists of a fluid ("fluid #1" in what follows) and is surrounded by a second fluid ("fluid #2" in what follows). One of the fluids must be a liquid, if both fluids are liquids they should be immiscible.

In order to form a droplet in contact with a solid, a surface formation energy W has to be provided. If we consider only droplets with constant volume this energy is given by the expression [9]

$$\begin{aligned} W &= \sigma_{12}M + \sigma_{s1}S + \sigma_{2s}(S_{\text{tot}} - S) + \text{const.} \\ &= \sigma_{12}M + (\sigma_{s1} - \sigma_{2s})S \end{aligned} \tag{1}$$

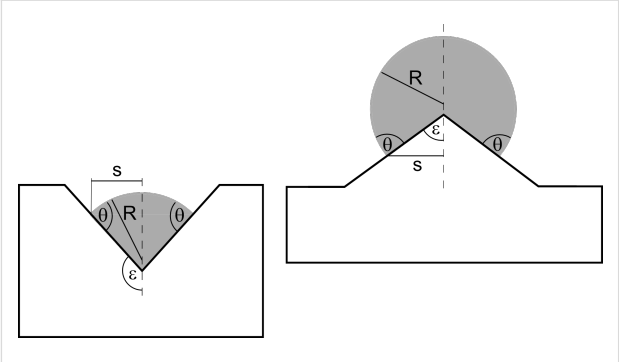

Figure 1: Sphere like droplets of fluid #1 (grey) attached to an axially symmetric solid cone (the broken line represents the symmetry axis). θ: contact angle, *R*: droplet radius, *s*: radius of contact circle (= line where solid, fluid #1 and fluid #2 are in contact), ε: apex half-angle of protrusion (for 0° < ε < 90°, right) or cavity (for 90° < ε < 180°, left).

where S denotes the attachment area between droplet and solid, M is that part of the droplet surface which is in contact with fluid #2 and $S_{\text{tot}} - S$ is the area where plane and fluid #2 are in contact.

$\sigma \equiv \sigma_{12}$, σ_{s1} and σ_{2s} denote the surface tensions (or surface energies) with respect to fluid #1/fluid #2, solid/fluid #1 and fluid #2/solid interfaces, respectively. The product $\sigma_{2s}S_{\text{tot}}$ yields a constant value. Since W is defined only up to an arbitrary constant, we can ascribe to it the value $-\sigma_{2s}S_{\text{tot}}$ which yields the second version of Equation 1. This choice is equivalent to ascribing a vanishing droplet (i.e., $M \to 0$, $S \to 0$) zero surface energy.

Droplets of constant volume in equilibrium with respect to the surface tensions pulling at them obey the Young Law

$$\sigma\cos\theta = \sigma_{2s} - \sigma_{s1} \tag{2}$$

Inserting this relation into Equation 1 we obtain the surface energy W of a droplet of fixed volume V in equilibrium with respect to surface tensions:

$$W = \sigma(M - S\cos\theta) \tag{3}$$

Expressing the surface segments M and S as well as the contact circle radius s and the droplet volume V in terms of the quantities R, ε and θ, we find from Figure 1

$$M = 2\pi R^2[1 - \sin(\varepsilon - \theta)] \tag{4}$$

$$S = \pi R^2 \frac{\cos^2(\varepsilon - \theta)}{\sin\varepsilon} \tag{5}$$

$$s = R\cos(\varepsilon-\theta) \tag{6}$$

$$V = \frac{\pi R^3}{3}\left\{2-2\sin(\varepsilon-\theta)-\frac{\cos^2(\varepsilon-\theta)\cos\theta}{\sin\varepsilon}\right\} \tag{7}$$

Since the formulas in Equation 4 through Equation 7 encompass cone shaped protrusions and cavities, we designate them both in what follows by the common term "cone".

Inserting Equation 4 and Equation 5 into Equation 3, we obtain for the surface energy W of an equilibrated droplet

$$\begin{aligned} W(\varepsilon,\theta) &= \sigma\pi R^2\left\{2-2\sin(\varepsilon-\theta)-\frac{\cos^2(\varepsilon-\theta)\cos\theta}{\sin\varepsilon}\right\} \\ &= \sigma\sqrt[3]{9\pi V^2\left\{2-2\sin(\varepsilon-\theta)-\frac{\cos^2(\varepsilon-\theta)\cos\theta}{\sin\varepsilon}\right\}} \\ &= W_{\text{float}}\sqrt[3]{\frac{1}{4}\left\{2-2\sin(\varepsilon-\theta)-\frac{\cos^2(\varepsilon-\theta)\cos\theta}{\sin\varepsilon}\right\}} \end{aligned} \tag{8}$$

where we have employed equation Equation 7 to replace the droplet radius R in favour of the (constant) droplet volume V in the second expression.

$$W_{\text{float}} := \sigma\sqrt[3]{36\pi V^2} \tag{9}$$

denotes the surface formation energy of a spherical droplet of volume V which consists of fluid #1 and floats (i.e., without contact to the solid) within fluid #2.

A closer look at the terms in the braces of expression Equation 7 reveals that certain (ε, θ)-combinations have to be excluded because they represent (non-physical) negative droplet volumes. The admissible (ε, θ)-ranges (equivalent to droplets with $V \geq 0$) are given by (see also Figure 2):

$$\Theta_0(\varepsilon) < \theta < 180° \tag{10}$$

where (see Equation 11)

The function $\Theta_0(\varepsilon)$ is calculated by setting $V = 0$ in Equation 7. Comparison of Equation 7 and Equation 8 shows the equivalence of the conditions $V \geq 0$ and $W(\varepsilon, \theta) \geq 0$.

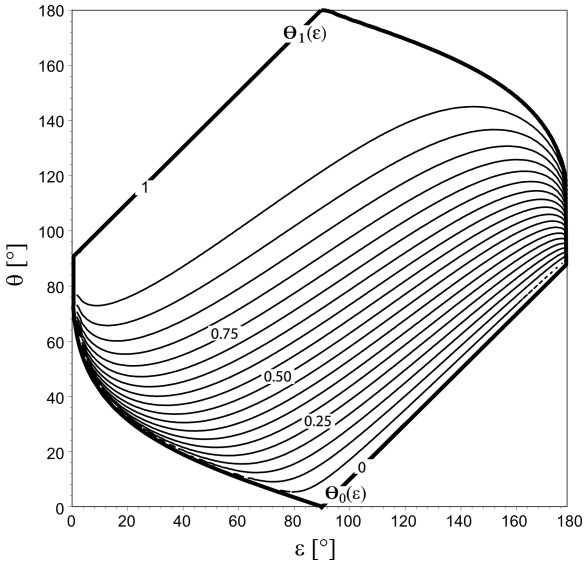

Figure 2: Thin lines: Curves of constant surface formation energy $W(\varepsilon, \theta)$ of an equilibrated droplet of volume V, according to Equation 8. Values of W are given as multiples of the surface energy W_{float} of an unattached spherical droplet (see Equation 9). The lines represent the values W/W_{float} = 0.00, 0.05, 0.10,…0.95, 1.00, starting from the lowermost line.
Thick lines: the functions $\theta = \Theta_0(\varepsilon)$ and $\theta = \Theta_1(\varepsilon)$ (defined in Equation 11 and Equation 13, resp.) envelop the (ε, θ)-pairs related to equilibrated droplets of volume V attached to a cone. The region below $\theta = \Theta_0(\varepsilon)$ has to be excluded because combinations of apex half-angle ε and contact angle θ in this region lead to $V < 0$. The curve $\theta = \Theta_1(\varepsilon)$ indicates droplets with the same surface energy as freely floating droplets without contact to the solid.

Below, the question will arise whether a freely floating droplet of surface energy W_{float} gains energy if it attaches to a cone defined by a given (ε, θ)-pair or whether this process consumes energy. The answer is found by equating the expressions in Equation 8 and Equation 9: Solving for θ, one obtains a curve

$$\Theta_1(\varepsilon) = \theta \tag{12}$$

with (see Equation 13)

$$\Theta_0(\varepsilon) := \begin{cases} \varepsilon - \arcsin\left(\sqrt[3]{\sin^2\varepsilon(1+\cos\varepsilon)} + \dfrac{\sin^2\varepsilon}{\sqrt[3]{\sin^2\varepsilon(1+\cos\varepsilon)}} - 1\right) & \text{if } 0° < \varepsilon < 90° \\ \varepsilon - 90° & \text{if } 90° < \varepsilon < 180° \end{cases} \tag{11}$$

$$\Theta_1(\varepsilon) := \begin{cases} \varepsilon + 90° & \text{if } 0° < \varepsilon < 90° \\ \varepsilon + \arcsin\left(\sqrt[3]{\sin^2\varepsilon(1-\cos\varepsilon)} + \dfrac{\sin^2\varepsilon}{\sqrt[3]{\sin^2\varepsilon(1-\cos\varepsilon)}} - 1 \right) & \text{if } 90° < \varepsilon < 180° \end{cases} \quad (13)$$

The curve $\Theta_1(\varepsilon) = \theta$ (Figure 2) divides the (ε, θ)-plane into two regions: Cones that are generated by (ε, θ)-pairs below it imply $W(\varepsilon, \theta) < W_{float}$, that is, a freely floating droplet of surface energy W_{float} gains surface energy if it chooses to attach to such a cone. Cones characterised by (ε, θ)-pairs above $\Theta_1(\varepsilon) > \theta$ require for attachment the energy $W(\varepsilon, \theta) > W_{float}$, i.e., attachment of a freely floating droplet would consume energy.

If ε is held constant, $W(\varepsilon, \theta)$ is a continuous and increasing function of θ, i.e., $\theta_2 \geq \theta_1$ implies $W(\varepsilon, \theta_2) \geq W(\varepsilon, \theta_1)$. This can be seen by calculating the slope of Equation 8 with respect to θ which is positive for ε, θ = 0…180°.

Figure 3 illustrates the behaviour of $W(\varepsilon, \theta)$ if θ is kept constant: $W(\varepsilon, \theta)$ exhibits extrema with respect to ε whose positions depend on the value of θ. For $0° \leq \theta \leq 90°$, the curves $W(\varepsilon, \theta = \text{const.})$ show *maxima* within the range ε = 0°…90°, more precisely

$$0° \leq \theta \leq 90° \Rightarrow \text{ maximum at}$$
$$\varepsilon_{max} = \arctan\left(\frac{1}{2\tan\theta}\right) \quad (14)$$

whereas the curves with $90° \leq \theta \leq 180°$ have *minima* within a range ε = 90°…180°, i.e.,

$$90° \leq \theta \leq 180° \Rightarrow \text{ minimum at}$$
$$\varepsilon_{min} = \arctan\left(\frac{-\cos\theta}{\sqrt{1+3\sin\theta}}\right) \quad (15)$$

Curves with $90° \leq \theta \leq 180°$ have also saddle points at $\varepsilon_{saddle} = \theta - 90°$. For $\varepsilon \to 90°$ both protrusions and cavities degenerate to flat surfaces.

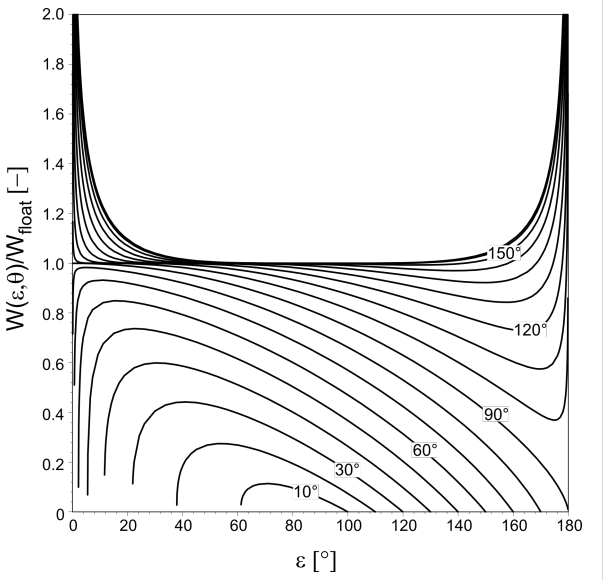

Figure 3: Surface formation energy $W(\varepsilon, \theta)$ of an equilibrated droplet of volume V. Values of W are given as multiples of the surface energy $W_{float} = \sigma\sqrt[3]{36\pi V^2}$ of a floating spherical droplet of volume V. The curves are distinguished by the value of the contact angle, namely θ = 10°, 20°, 30°…170°. Curves related to 0° < θ < 90° show *maxima* which lie all within the range 0° < ε < 90°, whereas curves with 90° < θ < 180° show *minima* all of which are located within the range 90° < ε < 180°.

Hypothetical applications

The main results of the previous section are as follows (see also Figure 2 and Figure 3):

1. The surface energy $W(\varepsilon, \theta)$ of a droplet attached to a cone of apex half-angle ε in a symmetry-preserving way is smaller than the surface energy W_{float} of a freely floating droplet, provided that the (ε, θ)-pair lies between the curves $\Theta_0(\varepsilon) = \theta$ and $\Theta_1(\varepsilon) = \theta$ (Figure 2).

2. If the value of the contact angle is fixed and lies within the interval 0° < θ < 90°, the surface energies of droplets sitting on cones whose apex half-angle ε are close to the value ε_{max} given in Equation 14 are higher than the surface energies of droplets attached to cones with greater or smaller apex half-angles.

3. If the value of the contact angle is fixed and lies within the interval 90° < θ < 180°, $W(\varepsilon, \theta)$ exhibits a minimum at $\varepsilon = \varepsilon_{min}$ (Equation 15). Thus, the surface energies of droplets sitting on cones which are very differently shaped (in terms of apex half-angle ε) are higher than the surface energies of droplets attached to cones whose shape is more similar to ε_{min}.

The features just discussed permit speculation about constructing "band-conveyors" for droplets. Such a "band-

conveyor", capable of "passing down" droplets from cone to cone, might be generated by arranging cones with increasing values of ε (but fixed θ) in one- or two-dimensional patterns. Figure 4 illustrates the basic idea: Upper and lower part of the figure show the same line-up of cones. The apex half-angle ε increases from left to right. If the fixed contact angle lies within $0° < \theta < 90°$ (upper part of Figure 4), the function $W(\varepsilon, \theta)$ has a maximum at point B (i.e., $\varepsilon_{max}(\theta)$). Thus, the energy difference $\Delta W := W_{float} - W(\varepsilon, \theta)$ which is required to detach a droplet from a cone has its minimum at point B. With increasing distance from B, droplets are increasingly stronger bound to their substrate, that is, ΔW increases towards A and D. If the fixed contact angle lies between $90° < \theta < 180°$ (lower part of Figure 4), the minimum of $W(\varepsilon, \theta)$ is located at point C (i.e., $\varepsilon_{min}(\theta)$). Hence, ΔW increases if point C is approached from A or D.

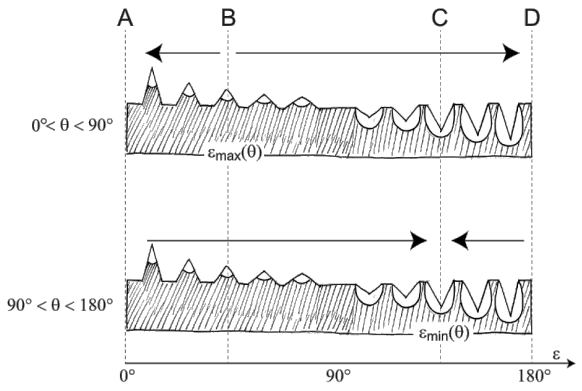

Figure 4: Line-up of cones. The apex half-angle ε increases from left to right. For θ = const. and $0° < \theta < 90°$ (upper part), the surface energy $W(\varepsilon, \theta)$ has a maximum at point B and for $90° < \theta < 180°$ (lower part) a minimum at point C. The arrows indicate directions of decreasing surface energy. In section B–C they point into the same, in sections A–B and C–D, however, into opposite directions (drawing: Birgit Binder, Tübingen).

If both lyophilic (i.e., $0° < \theta < 90°$) and lyophobic droplets (i.e., $90° < \theta < 180°$) reside on the landscape of cones of Figure 4, it appears that both droplet species experience an increase of ΔW from point B towards C. In sections A–B and C–D, however, the variation of ΔW points into opposite directions for the two droplet species.

Perhaps, these findings can be utilised to construct a "band-conveyor" for droplets. We present two ideas how this might be achieved:

1. Consider Figure 5. The double line-up of cones similar to a zip fastener is constructed from the left part of Figure 4. The apex half-angle ε of the cones increases from point A ($\varepsilon \approx 0°$) to point B ($\varepsilon = \varepsilon_{max}$). According to Equation 14, a lyophilic droplet attached to cone #2 is in a lower state of surface energy than a droplet at cone #1, but in a higher energetic state than the droplet at cone #3. If the dimensions of droplet and cones, the contact angle between them and the temperature of the arrangement are suitably chosen, thermal oscillations of the droplet around its position of symmetry at cone #2 may bring it in contact with cone #1 or cone #3. Due to the gradient of $W(\varepsilon, \theta)$ with respect to ε, for a lyophilic droplet it is energetically attractive to move to cone #3 (towards lower values of $W(\varepsilon, \theta)$), but not to cone #1. Thus, lyophilic droplets should finally get to point A. For lyophobic droplets, a similar reasoning applies, which starts, however, from Equation 15 instead of Equation 14. Hence, lyophobic droplets should migrate towards point B.

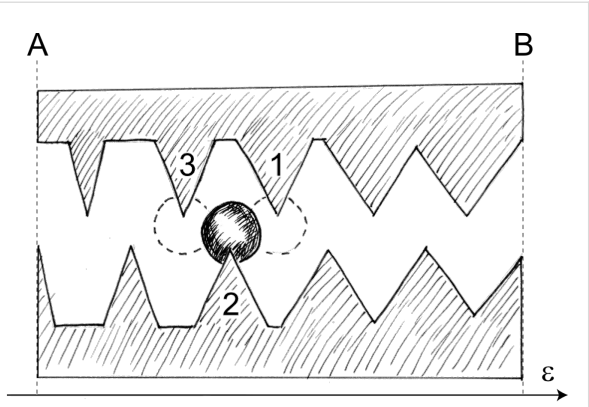

Figure 5: Double line-up of cones similar to a zip fastener constructed from the left part of Figure 4. The apex half-angle ε of the cones increases from point A ($\varepsilon \approx 0°$) to point B ($\varepsilon = \varepsilon_{max}$). Apart from one or two cones, the droplet does not touch the solid substrate (drawing: Birgit Binder, Tübingen).

2. If the cones are farther apart than in Figure 5 (more like in Figure 4), the droplets have to detach completely from a cone before they come in contact with the next one. Similarly as above, if droplet and cone dimensions, contact angle and temperature are favourable, the interaction of the droplet with the thermally agitated particles constituting fluid #2 may outweigh the binding energy $\Delta W = W_{float} - W(\varepsilon, \theta)$ between droplet and solid substrate. Since the thermal agitation fluctuates randomly, the transfer of low amounts of energy onto the droplet occurs more frequently than the transfer of high amounts of energy, on an average. Consequently, the mean residence time of a droplet sitting on a cone increases with increasing binding energy ΔW. Therefore, lyophilic droplets attached to cones close to point B (see upper part of Figure 4) leave the cones more often than droplets farther away from B. Doing so, a droplet may jump – with equal probability – either to the left or to the right: In case its next attachment is closer to

B, its residence time is shorter than before, if it moves to a cone farther away from B, it will remain there longer, on an average. The overall effect of this is a (net) movement of lyophilic droplets towards B.

Lyophobic droplets behave similarly, they move also in the direction of decreasing binding energy ΔW. This means, in terms of the lower part of Figure 4, that they move away from point C, towards points A and D.

Up to now, we have simply assumed that detached droplets re-attach to the tips of the cones. Of course, this cannot be taken for granted. One may exclude this eventuality by assembling the landscape of cones of Figure 4 from two materials with different contact angles: (a) bulk material with a very high contact angle (dotted areas in Figure 4), implying a very small ΔW, and (b) employing material with smaller contact angle for the cones (white areas in Figure 4). Alternatively, one might apply hair- or pillar-like structures which are smaller than the cones by an order of magnitude or so to the dotted areas in Figure 4. Droplets coming in contact with these structures should experience a Cassie state, leading also to very high effective contact angles [8].

Notice that the mechanisms depicted in Figure 4 and Figure 5 predict droplet migration in opposite directions. Concentrating on Figure 4, a possible application of the suggested mechanism arises, for example, from exploiting only parts of Figure 4: Arranging the landscape of cones in a twodimensional, radial pattern such that point A is close to the centre and B represents the outer fringe of a circular disc, lyophilic droplets would migrate towards the centre whereas lyophobic droplets would migrate away from it. A reverse migration order should result if the roles of A and B are interchanged or if point C is chosen as the centre and point D as the periphery.

Discussion

The specific surface patterning is not only able to initiate a spontaneous and directed movement of droplets. According to the actual surface energy, droplets with different chemical content will move to different directions. This effect thus enables not only droplet transport but also droplet sorting. According to the surface pattern, different motion patterns and behaviour can be achieved. For example, different chemical reactants can be directed to different “assembly” lines. Also the speed of the droplets can be controlled.

Surfaces similar to our patterns are not uncommon in nature. Insects show a wide variety of ornamentations of their cuticle, their compound eyes and wings [10]. Plant surfaces are also known to develop a huge variety of patterns on different length scales [11]. A prominent example are the leaf wax structures leading to superhydrophobicity and the Lotus-effect [12]. Larger structures are also common, e.g., trichomes (leaf hairs) or wart-like structures. Stomata, the micropores for gas exchange on leaves, are often particularly decorated. The stomata of *Equisetum* (horse-tail), for example, show wart-like protuberances around the central slit, while the stomata of *Gingko* are surrounded by cone-shaped structures. It might be speculated that directed transport of tiny droplets may also be involved in these cases: Stomata have to be protected from being covered by a water film, and therefore the development of water-repellent structures should be beneficial. This applies not only to large drops, as are delivered by rain precipitation, but also to droplets in the μm-range which are deposited during fog or mist events. Specifically shaped surface patterns may be able to repel not only large water drops but also direct microdroplets according to specific strategies.

Acknowledgements

We wish to thank two anonymous reviewers for constructive comments. One of them suggested the idea depicted in Figure 5. We also want to thank Birgit Binder, Tübingen, for drawing Figure 4 and Figure 5, and James H. Nebelsick for critically reading the English manuscript.

References

1. Daniel, S.; Chaudhury, M. K.; de Gennes, P.-G. *Langmuir* **2005,** *21,* 4240–4248. doi:10.1021/la046886s
2. Yang, J.-T.; Yang, Z.-H.; Chen, C.-Y.; Yao, D.-J. *Langmuir* **2008,** *24,* 9889–9897. doi:10.1021/la8004695
3. Chaudhury, M. K.; Whitesides, G. M. *Science* **1992,** *256,* 1539–1541. doi:10.1126/science.256.5063.1539
4. Greenspan, H. P. *J. Fluid Mech.* **1978,** *84,* 125–143. doi:10.1017/S0022112078000075
5. Brochard, F. *Langmuir* **1989,** *5,* 432–438. doi:10.1021/la00086a025
6. Marmur, A. *Langmuir* **2008,** *24,* 7573–7579. doi:10.1021/la800304r
7. Patankar, N. A. *Langmuir* **2003,** *19,* 1249–1253. doi:10.1021/la026612+
8. Quéré, D. *Annu. Rev. Mater. Res.* **2008,** *38,* 71–99. doi:10.1146/annurev.matsci.38.060407.132434
9. Adamson, A. W.; Gast, A. P. *Physical chemistry of surfaces;* Wiley-Interscience: Hoboken, USA, 1997.
10. Gorb, S. N., Ed. *Functional Surfaces in Biology: Little Structures with Big Effects, Volume 1;* Springer: Berlin, Germany, 2009.
11. Shirtcliffe, N. J.; McHale, G.; Newton, M. I. *Langmuir* **2009,** *25,* 14121–14128. doi:10.1021/la901557d
12. Koch, K.; Bhushan, B.; Barthlott, W. *Soft Matter* **2008,** *4,* 1943–1963. doi:10.1039/b804854a

Beilstein Journal of Nanotechnology

Detection of interaction between biomineralising proteins and calcium carbonate microcrystals

Hanna Rademaker and Malte Launspach*

Full Research Paper

Open Access

Address:
Institute of Biophysics, University of Bremen, Bremen, Germany

Email:
Hanna Rademaker - hr@biophysik.uni-bremen.de;
Malte Launspach* - ml@biophysik.uni-bremen.de

* Corresponding author

Keywords:
biomineralisation; biomineralising proteins; Haliotis; nacre; protein–mineral interaction

Beilstein J. Nanotechnol. **2011,** *2,* 222–227.
doi:10.3762/bjnano.2.26

Received: 03 January 2011
Accepted: 24 March 2011
Published: 27 April 2011

This article is part of the Thematic Series "Biomimetic materials".

Guest Editors: W. Barthlott and K. Koch

Abstract

The natural composite nacre is characterised by astonishing mechanical properties, although the main constituent is a brittle mineral shaped as tablets interdispersed by organic layers. To mimic the natural formation process which takes place at ambient conditions an understanding of the mechanism responsible for a defined microstructure of nacre is necessary. Since proteins are assumed to be involved in this mechanism, it is advantageous to identify distinct proteins interacting with minerals from the totality of proteins contained in nacre. Here, we adopted and modified a recently published approach given by Suzuki et al. [1] that gives a hint of specific protein–mineral interactions. Synthesised aragonite or calcite microcrystals were incubated with a protein mixture extracted from nacre of *Haliotis laevigata*. After incubation the mineral phase was dissolved and investigated for attached proteins. The results give a hint of one protein that seems to bind specifically to aragonite and not to calcite. The presented protocol seems to be suitable to detect mineral binding proteins quickly and therefore can point to proteins whose mineral binding capabilities should be investigated further.

Introduction

Biological synthesised materials from various organisms such as nacreous shells have attracted the attention of many researchers from different disciplines over a number of years. Nacre as an integral part of the protective shell of some marine organisms is characterised by its astonishing mechanical properties and beautiful iridescence. Although composed only of brittle calcium carbonate mineral platelets embedded in a mechanically weak organic layer, nature has created a tough material. For recent reviews dealing with biomineralisation and especially nacre consult [2] and [3].

The fracture resistance of the whole shell and especially nacre, which consists of about 95 wt % of a brittle mineral, is achieved by a defined microstructure and a complex interaction between the mineral and the organic constituents. The microstructure of nacre can be thought of as a brick-and-mortar structure where

polygonal aragonite platelets with a height of approximately 0.5 µm and a lateral extension in the micrometer range represent the bricks, whilst the organic layers around the platelets act like a kind of glue. The main toughening mechanisms in nacre include: Increasing the crack surface by crack deflection at interfaces, resistance to platelet sliding due to a rough platelet surface, platelet interlocking mechanisms and reduction of peak stresses due to crack tip blunting in the organic layer.

The organic layer between the mineral platelets comprises a chitin core with an attached protein layer. In combination with solubilised proteins, the organism is capable of producing aragonite platelets of distinct dimensions. Consequently, there must exist some kind of control mechanism for the crystal polymorph, morphology and orientation as well as crystal nucleation induction and prevention of uncontrolled crystallisation. Since proteins are assumed to play a major role in this mechanism, it would be advantageous to characterise the different proteins purified from bio-composites by their ability to bind to different minerals selectively. Such a characterisation assay or protocol is even useful for the design of peptides mimicking the biomineralisation process. It would be possible to evaluate the synthesis results of different peptides in terms of their mineral or ceramic binding capability.

Turning to proteins purified from nacre from a marine shell or of a shell forming animal, it would be helpful to determine which proteins are involved in nacre or shell formation. Recently, Suzuki and co-workers [1] described an assay to detect whether a protein binds to aragonite or calcite microcrystals specifically. Here, we wish to report how to modify the protocol given by Suzuki et al. and apply it to a mixture of soluble proteins extracted from nacre from *Haliotis laevigata*. Briefly, the experimental approach comprises the following steps: Growth of aragonite or calcite microcrystals with evaluation of the purity of the mineral phase, demineralisation of a shell from *Haliotis laevigata*, removal of the proteins from the chitin core of the remaining organic matrix from the preceding step, incubation of this protein mixture with aragonite or calcite microcrystals and finally, determination whether proteins are attached to the crystals.

Results and Discussion

Light microscopy and scanning electron microscopy (SEM) images show that aragonite precipitated as needles up to 20 µm long, and calcite as rhombohedrons (Figure 1) with an edge length of about 20 µm. The purity of the microcrystal powder measured by X-ray diffraction (Figure 2) was 97 wt % for aragonite (the remaining 3 wt % are calcite impurities) and 100 wt % for calcite, with an uncertainty of 1 wt %. Thus, the protocol used for crystallization produced different polymorphs with reasonable purities. Determination of the specific surface area of aragonite and calcite by evaluation of light microscopy images and gas adsorption (BET method, see, e.g., [4]) both showed a roughly ten times larger specific surface area for aragonite. The actual values were different though, the BET method giving 4.07 m^2/g for argonite and 0.40 m^2/g for calcite, while the geometric estimate from the light microscopy images was 0.78 m^2/g to 1.72 m^2/g for aragonite and 0.10 m^2/g to 0.19 m^2/g for calcite. The values from the light microscopy

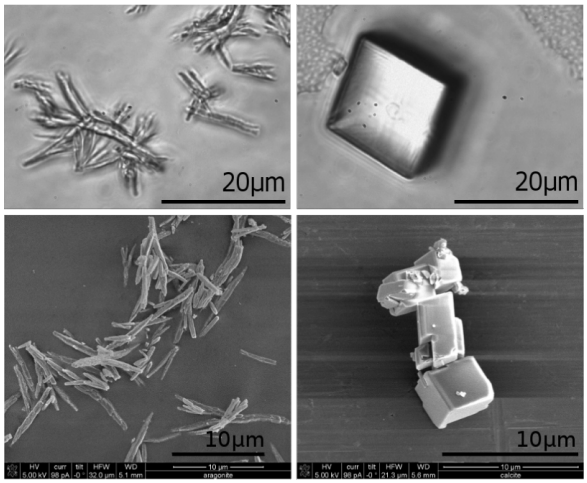

Figure 1: Precipitated aragonite needles (left) and calcite rhombohedrons (right). Upper: light microscopy images. Lower: scanning electron microscopy images.

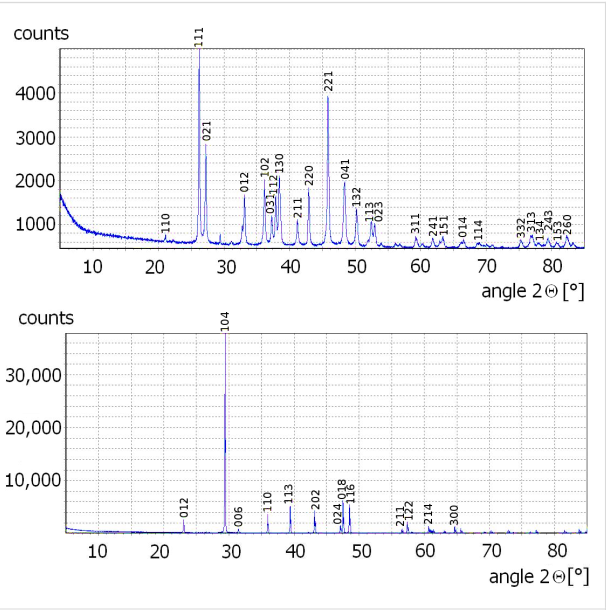

Figure 2: X-ray diffraction patterns of precipitated aragonite (upper) and calcite rhombohedrons (lower). Purity is 96–98 wt % for aragonite and 99–100 wt % for calcite as evaluated with the BRASS software suite [6]. Indexing according to data from [7] (aragonite) and [8] (calcite).

images were estimated from 20 aragonite microcrystals assumed to be cylinders, neglecting top and bottom area, and ten calcite microcrystals assumed to be rhombohedrons with all twelve edges of equal length. The density for aragonite is 2.95 g/cm^3 and 2.71 g/cm^3 for calcite [5].

Figure 3 shows the result of the protein–crystal binding experiment. The proteins in the shell from *Haliotis laevigata* that were insoluble in 6% acetic acid were removed from the chitin core with an SDS/DTT/Tris buffer as described in the experimental section. This protein solution contained several proteins or protein fragments visible in lane P on sodium dodecyl sulfate polyacrylamide gel electrophoresis (SDS-PAGE) in Figure 3. The protein solution was gel-filtered to remove the SDS and DTT. The obtained gel-filtered protein solution (lane gfP) shows the major bands on SDS-PAGE. The gel-filtered protein solution was incubated with aragonite or calcite microcrystals. After incubation, the supernatant liquid from the aragonite or calcite microcrystals was removed and subjected to SDS-PAGE at two different concentrations (AS, AS* and CS, CS*). The crystals were washed 3 times with a NaCl/Tris solution. The washing solution was retained and combined for aragonite (AW) and calcite (CW), respectively, and also subjected to SDS-PAGE. The most dominant bands were still observable. The washed crystals were dissolved in 6% acetic acid. The proteins that were attached to the aragonite crystals (A) or to the calcite crystals (C) were obtained by removing the acetic acid by dialysis.

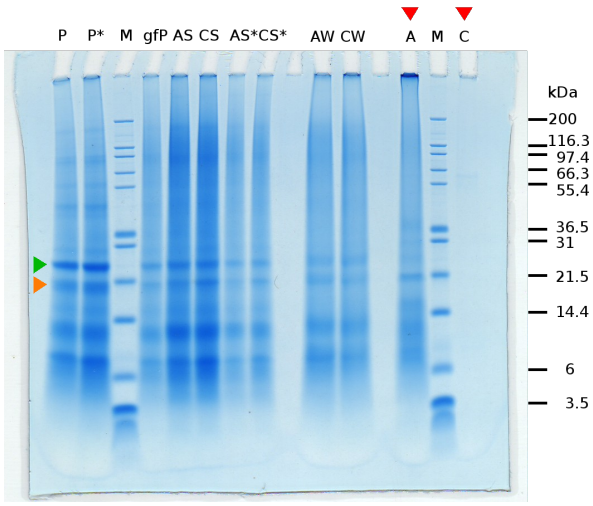

Figure 3: SDS-PAGE of proteins after different preparational steps as follows. **M:** marker proteins of known size. **P**, **P*:** protein solution of proteins that are insoluble in 6% acetic acid (chitin associated proteins), at two different concentrations. Orange marked band is less intensive than the green marked one. **gfP:** gel filtered protein solution. **AS**, **CS**, **AS***, **CS*:** supernatant of incubated aragonite and calcite crystals, contains unbound proteins, at two different concentrations. **AW**, **CW:** combined washings of aragonite and calcite. **A**, **C:** acetic acid dissolved crystals after dialysis in sodium citrate buffer. Lane A now shows higher intensity of the orange marked band relative to green marked band, which may indicate specific binding of the orange marked protein to aragonite.

Lanes A and C show the important difference between aragonite and calcite. In contrast to lane C, there are still proteins detectable by SDS-PAGE in lane A. This indicates that more protein was attached to the aragonite microcrystals. Generally, this could be expected due to the greater specific surface area of the aragonite microcrystals used compared to the calcite microcrystals. Nonetheless a lysozyme control experiment shows that unspecific binding cannot be the only reason for the larger amount of protein in lane A (here lane A from Figure 3). This control experiment shows the influence of the greater specific surface area of aragonite on the SDS-PAGE results, assuming unspecific binding of lysozyme to both, aragonite and calcite. A difference in intensities in lanes A and C from Figure 3 due only to unspecific binding seems unlikely, since lanes A and C (Figure 4) show no difference in intensity.

Verification of a specific binding would be most interesting, because this would be evidence that protein–mineral interaction guide polymorph selection and morphology of the calcium carbonate crystals. This would require a competitive assay. However, there is a suggestion of specific binding of one protein to aragonite in our results. Looking at the two protein

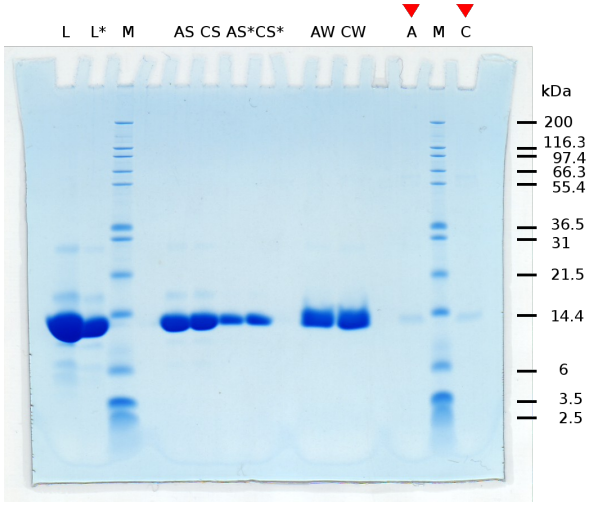

Figure 4: SDS-PAGE of control experiment with lysozyme. **M:** marker proteins of known size. **L**, **L*:** high concentrated lysozyme solution, at two different concentrations. **AS**, **CS, AS***, **CS*:** supernatant of incubated aragonite and calcite crystals, at two different concentrations. **AW**, **CW:** combined washings of aragonite and calcite. **A**, **C:** acetic acid dissolved crystals after dialysis in sodium citrate buffer. Comparing bands in lanes A and C shows no difference in intensity.

bands indicated by the orange and green arrows in Figure 3 and then comparing the relative intensity of these two protein bands in lane P (entity of chitin associated proteins) and their relative intensity in lane A (aragonite associated proteins) shows an increased relative concentration of the one indicated by the orange arrow in lane A.

To estimate the detection limit for proteins in this experiment, different quantities of lysozyme were subjected to SDS-PAGE (data not shown). While for 50 ng lysozyme the band is still visible, it is not for 5 ng. So for calcite there was less than 50 ng of each protein on 10 µg crystal powder. In the protein–crystal binding experiment 15 to 20 µL of protein solution was subjected to SDS-PAGE per lane. Assuming that the detection limit for different proteins is the same, we estimate the minimum protein concentration in the subjected solution for a visible band to be 2.5 to 3.3 µg/mL.

Conclusion

In this study a protocol given by Suzuki et al. [1] to estimate the selective mineral binding capabilities of proteins was successfully adopted and modified for nacre proteins. Firstly, the morphology, purity and specific surface area of our synthesised calcite and aragonite microcrystals was determined. After confirming the appropriate purity of the crystals, aragonite and calcite crystals were incubated with proteins that were chemically removed from the acetic acid insoluble part of nacre. The supernatant liquid of incubated aragonite and calcite crystals, washings of these aragonite and calcite samples and the acetic acid dissolved crystals were subjected to SDS-PAGE (Figure 3). The washings and the supernatant liquid contained unbound proteins. Two protein bands appeared to be present in the dissolved aragonite sample and not in the calcite sample (within the detection limit of the SDS-PAGE). It seems that the 19 kDa protein favours interactions with aragonite crystal surfaces compared to the 25 kDa one.

These two protein bands (one at approx. 19 kDa and the other at about 25 kDa) belong to the protein perlucin [10]. The corresponding fractions of purified protein showing these two bands on SDS-PAGEs had been subjected to N-terminal amino acid sequence analysis [11] in several different experiments. They always turned out to be perlucin. There might be several explanations for the different running behaviour. As perlucin has glycosylation sites there might be a subspecies of protein molecules which are glycosylated and another one which is not. There might even be the possibility that a subspecies of perlucin has saccharide oligomers bound to these sites. In MALDI-MS (matrix-assisted laser desorption/ionization mass spectroscopy) of perlucin [10] variable molecular weights of perlucin are detectable, which can be related to a 10 amino acid repeat at the C-terminus being present in various numbers of repeats. Another explanation might be that perlucin as an extracellular protein, which is incorporated in a mineral matrix, is not fully denatured by the usual procedures and therefore would have a kind of "bulky" running behaviour.

Our investigations might be a hint of specific binding of one protein to a distinct mineral polymorph. From the BET measurements and light microscopy image estimations it is known that the specific surface of the aragonite needles is approximately tenfold higher than the specific surface of calcite rhombs. Consequently, the same experimental procedure was performed with lysozyme as a control. As can be seen in Figure 4 the lysozyme bands in the dissolved aragonite and calcite sample respectively, show the same intensity indicating a non specific binding for the control protein.

We are aware that our modified protocol taken from Suzuki and co-workers can only give preliminary information about potential mineral binding proteins. Nonetheless, this fast method makes it possible to select certain proteins for further investigations. As in the case of perlucin, it is worth regarding this protein as an important model system for (theoretical) simulations of this interaction on the molecular to atomic scale and conducting further experiments.

Experimental

As we stated several times above, the detection of interaction between biomineralising proteins and calcium carbonate microcrystals in this study is based on a modified approach from [1]. The main differences between the previously published protocol and our approach are summarised in the following. In this study, the microcrystals are freshly synthesised and not purchased. BET gas adsorption measurements were used to determine the specific surface area of the different calcium carbonate polymorphs. This information is important to distinguish between unspecific and specific binding of proteins to the different crystal polymorph surfaces. Protein solutions were concentrated by vacuum centrifugation instead of ultracentrifugation. A further difference was the composition of the washing solution for removal of proteins unspecifically attached to crystal surfaces and other proteins. Here, a slightly basic buffer solution was used to prevent crystal dissolution during washing.

Preparation of microcrystals

Calcium carbonate microcrystals were obtained by a similar method as described by Wray and Daniels [9], using $CaCl_2$ instead of $Ca(NO_3)_2$. Adding 20 mL 1.0 M $CaCl_2$ to 200 mL 0.1 M Na_2CO_3 after pre-heating of both solutions and stirring at constant temperature results in the precipitation of aragonite, calcite and vaterite. The aragonite/calcite ratio of the precipi-

tated polymorphs depends on reaction temperature and digestion time. For aragonite the precipitation reaction was conducted at 70 °C for 6 min, for calcite at 30 °C for 18 h. After filtration (Filter Discs (Quant.) Grade: 389, Sartorius Stedim) and washing with deionised water the microcrystals were dried at their respective reaction temperature for at least 12 h and loosened with a glass rod from time to time. The purity of the microcrystal powder was first checked with a light microscope (ZEISS Axiovert 135), then analyzed by X-ray diffraction (X'Pert Pro, PANalytical). The crystal samples were ground with a mortar and a pestle prior to the X-ray measurement. The specific surface area of the microcrystals was determined by the BET gas adsorption method (see, e.g., [4]) with N_2 as adsorptive at a temperature of 77 K (BELsorp-miniII).

Preparation of proteins

Shells of *Haliotis laevigata* were sand blasted (Sigg Strahlmittel, WA 70, with Al_2O_3) to remove the calcite layer. After 2 min in 6% NaClO and thorough washing with deionised water, the shells were dried overnight at 4 °C and crushed into pieces smaller than 0.5 cm in diameter. 40 g of one crushed shell was placed in a dialysis tube (Spectra/Por Dialysis Membrane) with molecular weight cut-off (MWCO) of 3.5 kDa and treated with 5 liters of 6% acetic acid, which was replaced two times over one week to dissolve the mineral components. The remaining flakes of acetic acid insoluble matrix were washed with deionised water and then treated for 10 min at 100 °C with 50 mL solution of 6% sodium dodecyl sulfate (SDS), 10 mM dithiothreitol (DTT), and 10 mM Tris-HCl (pH 8.0). 2.5 mL of the supernatant liquid (protein solution, P) was filtered (NALGENE syringe filters with nylon membranes, pore size: 0.2 μm) and divided into 12 parts (first one 1.0 mL, the others 0.5 mL) with a PD-10 gel column (Sephadex TMG-25 M, GE Healthcare) to remove the SDS and DTT from the solutions. Beforehand the gel columns had been equilibrated with 25 mL 10 mM Tris-HCl (pH 8.0). After determining the fractions of highest protein concentration by a Bradford Assay (Bio-Rad), fractions 5 to 9 of two gel filtration runs were combined and concentrated in a vacuum centrifuge (Savant SpeedVac SPD121P) to 250 μL (gel-filtered protein solution, gfP).

Incubation of the microcrystals with protein solution

10 mg of the microcrystal powder were incubated with 100 μL gel-filtered protein solution for 12 h at room temperature with constant shaking. The supernatant liquid (AS for aragonite or CS for calcite) was retained and the microcrystals were washed 3 times with 100 μL solution of 240 mM NaCl, 10 mM Tris-HCl (pH 8.0). The washing solutions were retained and combined (W). After washing, the crystals (A: aragonite, C: calcite) were dissolved in 1 mL of 6% acetic acid, which was removed afterwards by dialysis (Spectra/Por Dialysis Membrane, MWCO: 3.5 kDa) in 5 mM sodium citrate buffer at pH 4.8 with 0.02% NaN_3. After concentrating protein solution P, gel-filtered protein solution gfP, supernatant S, washing solution W and crystal solutions A and C in a vacuum centrifuge (Savant SpeedVac SPD121P) to a volume of about 20 μL, each solution was subjected to SDS-PAGE. For SDS-PAGE 12% Bis-Tris gels (Invitrogen) were used with MES (2-(*N*-morpholino)ethanesulfonic acid) as running buffer (Invitrogen). For the lysozyme control experiment, commercially available lyophilisated lysozyme was dissolved in deionised water to a concentration of 1 g/L. The microcrystals were incubated with this solution as stated above.

Acknowledgements

The authors thank Monika Fritz and Manfred Radmacher (Biophysics Institute, University of Bremen) for helpful discussions and continuous support as well as the Deutsche Forschungsgemeinschaft (DFG) and the University of Bremen for funding. The authors thank Katharina Gries (Solid State Physics Institute, Biophysics Institute, University of Bremen) for the SEM images, Hanna Lührs (Crystallography Group, Geosciences, University of Bremen) for the X-ray measurements and Tanja Klein (Advanced Ceramics Group, University of Bremen) for the BET measurements.

References

1. Suzuki, M.; Saruwatari, K.; Kogure, T.; Yamamoto, Y.; Nishimura, T.; Kato, T.; Nagasawa, H. *Science* **2009,** *325,* 1388–1390. doi:10.1126/science.1173793
2. Heinemann, F.; Launspach, M.; Gries, K.; Fritz, M. *Biophys. Chem.* **2011,** *153,* 126–153. doi:10.1016/j.bpc.2010.11.003
3. Meyers, M. A.; Chen, P.-Y.; Lin, A. Y.-M.; Seki, Y. *Prog. Mater. Sci.* **2008,** *53,* 1–206. doi:10.1016/j.pmatsci.2007.05.002
4. Adamson, A. W. *Physical Chemistry of Surfaces,* 5th ed.; Wiley: New York, 1990.
5. Dana, J. D. *Manual of Mineralogy,* 20th ed.; Wiley: New York, 1985.
6. *BRASS, The Bremen Rietveld Analysis and Structure Suite,* 1.0 beta; Zentrallabor für Kristallographie und Angewandte Materialwissenschaften, Fachbereich Geowissenschaften: University of Bremen, 2003.
7. Antao, S. M.; Hassan, I. *Can. Mineral.* **2009,** *47,* 1245–1255. doi:10.3749/canmin.47.5.1245
8. Sitepu, H.; O'Connor, B. H.; Li, D. *J. Appl. Crystallogr.* **2005,** *38,* 158–167. doi:10.1107/S0021889804031231
9. Wray, J. L.; Daniels, F. *J. Am. Chem. Soc.* **1957,** *79,* 2031–2034. doi:10.1021/ja01566a001
10. Mann, K.; Weiss, I. M.; André, S.; Gabius, H.-J.; Fritz, M. *Eur. J. Biochem.* **2000,** *267,* 5257–5264. doi:10.1046/j.1432-1327.2000.01602.x
11. Weiss, I. M.; Kaufmann, S.; Mann, K.; Fritz, M. *Biochem. Biophys. Res. Commun.* **2000,** *267,* 17–21. doi:10.1006/bbrc.1999.1907

Beilstein Journal of Nanotechnology

Hierarchically structured superhydrophobic flowers with low hysteresis of the wild pansy (*Viola tricolor*) – new design principles for biomimetic materials

Anna J. Schulte*[1], Damian M. Droste[1], Kerstin Koch[2] and Wilhelm Barthlott[1]

Full Research Paper

Open Access

Address:
[1]Nees Institute for Biodiversity of Plants, University of Bonn, Meckenheimer Allee 170, Bonn, Germany and [2]Rhine-Waal University of Applied Sciences, Landwehr 4, Kleve, Germany

Email:
Anna J. Schulte* - a.schulte@uni-bonn.de

* Corresponding author

Keywords:
anti-adhesive; petal effect; petal structures; polymer replication; superhydrophobic

Beilstein J. Nanotechnol. **2011,** *2,* 228–236.
doi:10.3762/bjnano.2.27

Received: 27 December 2010
Accepted: 07 April 2011
Published: 04 May 2011

This article is part of the Thematic Series "Biomimetic materials".

Guest Editors: W. Barthlott and K. Koch

Abstract

Hierarchically structured flower leaves (petals) of many plants are superhydrophobic, but water droplets do not roll-off when the surfaces are tilted. On such surfaces water droplets are in the "Cassie impregnating wetting state", which is also known as the "petal effect". By analyzing the petal surfaces of different species, we discovered interesting new wetting characteristics of the surface of the flower of the wild pansy (*Viola tricolor*). This surface is superhydrophobic with a static contact angle of 169° and very low hysteresis, i.e., the petal effect does not exist and water droplets roll-off as from a lotus (*Nelumbo nucifera*) leaf. However, the surface of the wild pansy petal does not possess the wax crystals of the lotus leaf. Its petals exhibit high cone-shaped cells (average size 40 μm) with a high aspect ratio (2.1) and a very fine cuticular folding (width 260 nm) on top. The applied water droplets are in the Cassie–Baxter wetting state and roll-off at inclination angles below 5°. Fabricated hydrophobic polymer replicas of the wild pansy were prepared in an easy two-step moulding process and possess the same wetting characteristics as the original flowers. In this work we present a technical surface with a new superhydrophobic, low adhesive surface design, which combines the hierarchical structuring of petals with a wetting behavior similar to that of the lotus leaf.

Introduction

Plant surfaces provide a large diversity of hierarchically designed structures with various functions [1,2]. Different types of epidermal cells (micro-roughness) exist in combination with cuticular folds or epicuticular waxes (nano-roughness), or both, on top [1,3]. Hierarchy in surface sculpture can cause water repellent and self-cleaning properties ("Lotus effect") [4-6] or cause air retention under water ("Salvinia effect") [7,8]. Superhydrophobic, self-cleaning surfaces possess a static contact angle (CA) equal to or above 150°, and a low hysteresis angle, where water droplets roll-off at surface inclinations equal to or below 10° [6,9]. One of the most important biological water repellent and self-cleaning surfaces is the lotus

(*Nelumbo nucifera)* leaf [4,5]. Its water repellence is based on two factors: Surface roughness and a hydrophobic surface chemistry. The micro-morphological characteristics of lotus leaves are papillose cells covered with a dense layer of small hydrophobic wax tubules. In plants, surface waxes occur as thin films (two-dimensional waxes) or as wax tubules, platelets, rodlets or other three-dimensional waxes [1,10]. In lotus leaves, air remains trapped below a water droplet and the contact area between the water and the leaf surface is thereby minimized [1]. This micro- and nanostructured surface, composed of low surface energy materials, leads to a high CA (163°) and a low hysteresis and tilt angle (2–3°). Additionally, lotus leaves show low adhesive properties to adhering particles. Thus, contamination by dust, pollen or even hydrophilic particles such as grime are carried away by water droplets which results in a clean surface [4].

Two distinct models are proposed to explain the wetting behavior of rough surfaces. In the Wenzel model [11] roughness increases a solid surface area; this geometrically enhances its hydrophobicity. In the Cassie–Baxter model [12] air remains trapped below the droplet in the surface cavities, which also leads to a superhydrophobic behavior, because the droplet sits partially on air [13].

The Wenzel model describes homogeneous wetting by the following equation,

$$\cos\theta = r\cos\theta_0 \quad (1)$$

where θ is the static CA for a rough surface and θ_0 is the static CA for a smooth surface. The surface roughness r is defined as the ratio of the actual over the apparent surface area of the substrate. The Cassie–Baxter model describes heterogeneous wetting by the equation,

$$\cos\theta = r\cos\theta_0 - f_{\mathrm{la}}(r\cos\theta_0 + 1) \quad (2)$$

where f_{la} is the fraction of solid in contact with the liquid and is dimensionless.

Further important factors in surface wetting are the static contact angle hysteresis (CAH) and the tilt angle (TA). The CAH describes the difference between the advancing and receding CAs of a moving droplet, or of one increasing and decreasing in volume. The CAH occurs due to surface roughness and heterogeneity [14,15]. Low CAH results in a low TA, which describes the TA of a surface at which an applied water droplet starts to move [15].

Nowadays, transitional states between the Wenzel and Cassie–Baxter states have been discovered. Wang and Jiang [16] proposed five different states for superhydrophobic surfaces, where the lotus and gecko states are treated as special cases in the Cassie–Baxter model. Feng et al. [17] proposed a sixth superhydrophobic state, called the "Cassie impregnating wetting state" or "petal effect". Both describe superhydrophobic surfaces with high adhesive forces to water, and this means that the wetted surface area is smaller than in the Wenzel model but larger than in the Cassie–Baxter model. Feng et al. [17] demonstrated this effect on rose flowers (petals). The surfaces of petals are often morphologically characterized by micro papillae with cuticular folds on top. In contrast to the lotus surface with air pocket formation between cell papilla, wax crystals and salient water droplets [18], the petal surface seems to prevent air pocket formation and droplets penetrate into the cuticular folds by capillary forces. It is proposed that the sizes of both micro- and nanostructures are larger than those found on the lotus leaves. Water droplets are expected to penetrate into the larger grooves of the petals, but not into the smaller ones and, thus, cause the Cassie impregnating wetting state [17].

The structure-based wetting characteristics of petals seem to offer a great alternative for the development of biomimetic superhydrophobic materials for micro droplet transport in micro fluidic systems, sensors or optical devices [19,20]. These hierarchically designed petal surfaces, with micropapillae and cuticular folds on the papillae top, can be precisely reproduced and are suitable for the industrial production in large area foil imprinting processes. In contrast, the hierarchically organized structures of the lotus leaf are composed of micropapillae with randomly distributed tubules on top. The development of such a surface architecture requires two production steps. Firstly, the microstructures must be produced by moulding, lithography or in-print-techniques. Secondly, the nanostructure production requires expensive lithographic techniques, or self-assembling materials, such as metal oxides [9,21].

Some attempts have been made to fabricate superhydrophobic surfaces with high adhesion properties inspired by rose petals [20,22-25]. Bhushan and Her [25], for example, replicated dried and thereby collapsed, micropapillae, and examined the wetting behavior of these structurally changed petals. Bormasheko et al. [24] or Shi et al. [22] fabricated "petal effect" surfaces by impregnating a polyethylene film with *Lycopodium* particles (spores) or with techniques such as electromechanical deposition of metal aggregates, which show the same wetting behavior as rose petals, but showed a different surface design than the native petals used as biological models. Xi and Jiang [23] replicated native rose petals with polydimethylsiloxane (PDMS),

and fabricated surfaces that are topographically very similar to those of the original rose petals. However, their replicas possessed high adhesive forces to small (2 µl) water droplets, which cannot provide self-cleaning properties.

One simple and precise method to transfer petal surface structures into an artificial material is a soft lithography technique called replica moulding [26]. Specifically, for the replication of biological surfaces Koch et al. [27,28] introduced a cost-efficient, two-step replication technique. This precise method prevents shrinking and damaging of the biological master during the replication process by avoiding a vacuum preparation step or critical temperatures as are used in most other techniques, and biological surface structures with an extremely high aspect ratio (ar) can be replicated [29].

In this study, we present the superhydrophobic surface of the wild pansy *Viola tricolor* (Figure 1), with a low TA and discuss the influence of papillae morphology and the dimensions of cuticular folding on the petal wetting state. To this end biomimetic replicas of four petals, differing in their surface morphology, were generated and their wetting behavior was examined by measuring the static CA and the TA. Finally, the contact area between a water droplet and the *Viola* petal surface was examined and superhydrophobic artificial petal replicas with low adhesive properties were generated.

Figure 1: Macro photo of a water droplet on a flower of the wild pansy *(Viola tricolor)*.

Results and Discussion

Micromorphological characteristics of the surfaces

Scanning electron microscope (SEM) investigations were made to characterize the micro- and nanostructures of the petals and their replicas. Petals of four different species which differ in their cell shape and dimension as well as in their wetting behavior were chosen. Figure 2 illustrates the SEM micrographs of the petal surfaces and their uncoated and coated polymer replicas [in the following the uncoated replicas are marked with a subscript *r* (= *replicas*), the coated replicas with a *cr* (= *coated replicas*) and the original petals are unmarked].

Petal surfaces of all four species are characterized by micropapillae with a cuticular folding on top (Figure 2; 1a–4a). As the pictures show, the replicas possess the same surface structures as the original petals. Minor deviations between the papillae shape of the original petals and the replicas may arise from critical point preparation of the petals (Figure 2; 1a–4a). The replicas were made from fresh turgescent flowers and the replication material used can mould a master structure to a high precision (replica deviations <2 nm from a master structure; Supporting Information File 1, Figure S1). Because of this, one may assume that the replicas display the real shape of the fresh petal surface structures. SEM pictures also show that antispread coated replicas (Figure 2; 1c–4c) possess the same surface structures as the uncoated replicas (Figure 2; 1b–4b). Accordingly, the structural parameters were collected on the uncoated replicas. Differences between the petal structures could be found in the dimensions of papillae and folds. $Rosa_r$ and $Viola_r$ are characterized by relatively sharp micropapillae (Figure 2; 3b, 4b), while $Dahlia_r$ and $Cosmos_r$ possess micropapillae with rounded tops (Figure 2; 1b, 2b). Furthermore, the micropapillae of the four different species vary from about 14 µm ($Rosa_r$) to 40 µm ($Viola_r$) in height, from 17 µm ($Rosa_r$) to 33 µm

Table 1: Micropapillae characteristics of the petal polymer replicas: average values (av) and their standard deviation (σ) values are shown (*n* = 30).

Replica	Micropapillae						
	Height [µm]		Midwidth [µm]		Aspect ratio (ar)	Papillae peak to peak distance [µm]	
	av	σ	av	σ	av	av	σ
$Cosmos_r$	20.3	4.7	19.6	3.7	**1.0**	41.0	11.8
$Dahlia_r$	21.8	5.6	32.7	4.2	**0.7**	48.4	10.1
$Rosa_r$	13.8	3.2	16.5	3.0	**0.8**	31.1	8.9
$Viola_r$	40.2	13.1	18.9	3.9	**2.1**	24.9	3.8

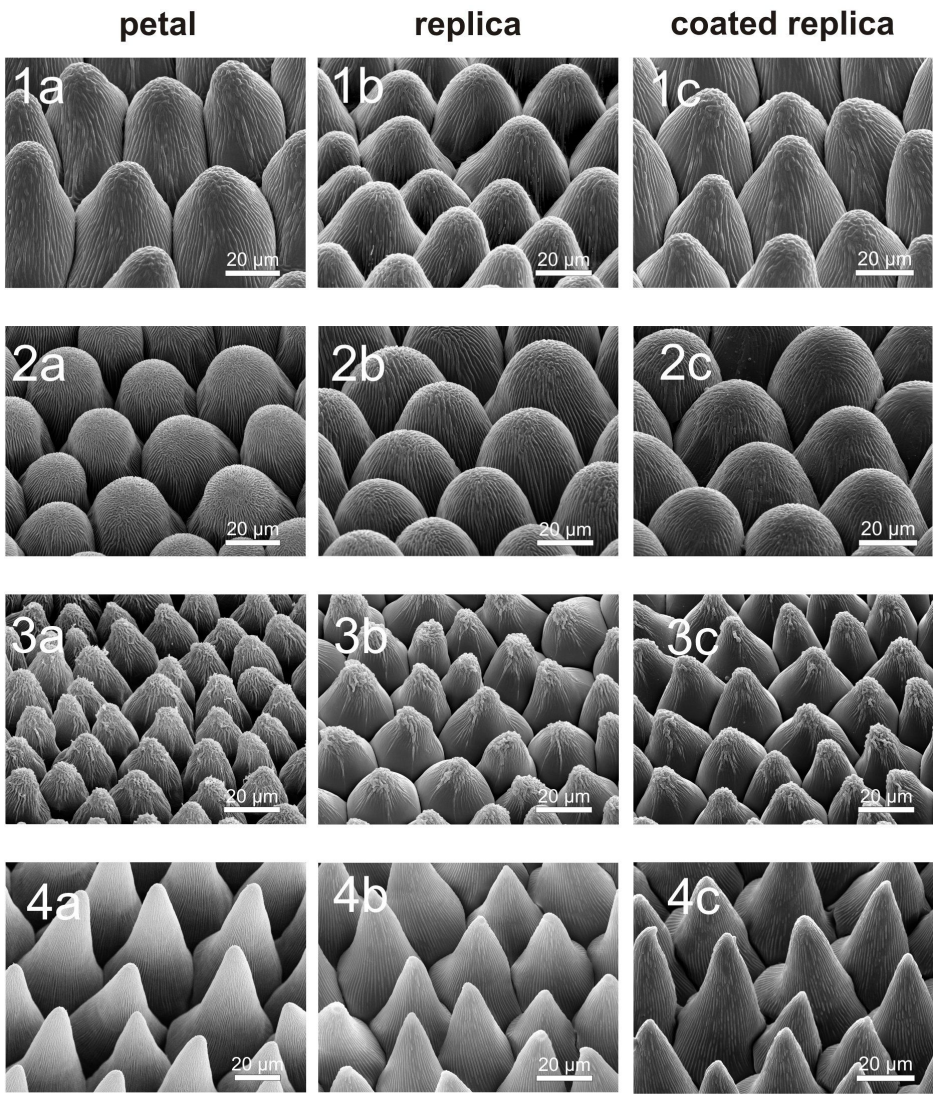

Figure 2: SEM micrographs of the petal surfaces (1a–4a), the uncoated polymer replicas (1b–4b) and the coated replicas (1c–4c) of *Cosmos atrosanguineus* (1a–1c), *Dahlia pinnata* (2a–2c), *Rosa chinensis* (3a–3c) and the wild pansy *Viola tricolor* (4a–4c).

($Dahlia_r$) in their midwidth (papillae diameter at half of the papillae height) and from 25 µm ($Viola_r$) to 48 µm ($Dahlia_r$) in their peak-to-peak distance (Table 1).

The average aspect ratio (ar) of the papillae shows similar values for the $Cosmos_r$, $Dahlia_r$ and $Rosa_r$ papillae (ar 1.0; 0.7; 0.8). In contrast, the average ar of the $Viola_r$ papillae is much larger (ar 2.1). In this context it is noted that the standard deviation (σ) of $Viola_r$ papillae height is also higher than the standard deviation of the other species. The micropapillae dimensions are shown schematically in Figure 3.

Differences between the four species were also found in the distribution and dimensions (width and distance) of the cuticular folds (Table 2). While the micropapillae of $Dahlia_r$ and $Viola_r$ are completely covered with folds, the $Cosmos_r$ and $Rosa_r$ papillae only exhibit dense folding on top of the papillae and some single folds at the papillae side (Supporting Information File 1, Figure S2). Combinations of relatively thick folds separated by a small distance and thin folds separated by a large distance were found. The width of the folds varied from 260 nm ($Viola_r$) to 600 nm ($Cosmos_r$) and the distance between the single folds varied from 210 nm ($Dahlia_r$) to 460 nm ($Cosmos_r$).

Wettability of the petals and their replicas

Static CA and the TA measurements were performed to compare the surface structures with the wettability. Two super-

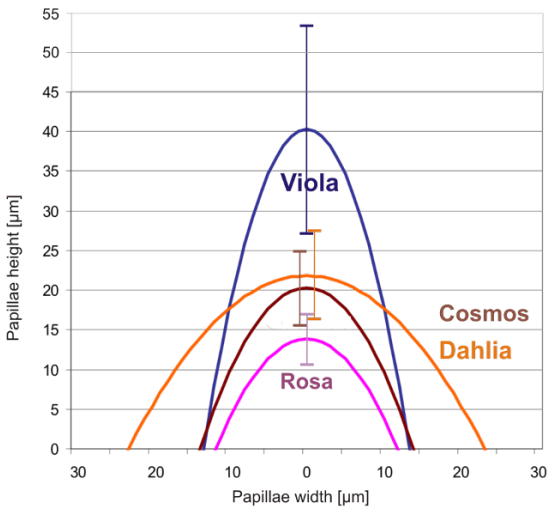

Figure 3: Diagram of the micropapillae dimensions of the average papilla shape on the upper surface of the $Cosmos_r$, $Dahlia_r$, $Rosa_r$ and $Viola_r$ petals. Also shown is the standard deviation of the papillae height (colored bars).

Table 2: Characteristics of cuticular folds found in the replicas of the petals: average values (av) and standard deviation (σ) values of the fold width and distance in µm (n = 30).

Replica	Cuticular folds			
	Width [µm]		Distance [µm]	
	av	σ	av	σ
$Cosmos_r$	0.60	0.09	0.46	0.10
$Dahlia_r$	0.39	0.08	0.21	0.06
$Rosa_r$	0.41	0.09	0.21	0.09
$Viola_r$	0.26	0.07	0.45	0.12

hydrophobic petals (*Rosa* CA 155.6° and *Viola* CA 169°) and two hydrophobic petals (*Cosmos* CA 118.3° and *Dahlia* CA 136.4°) were found (Figure 4).

The static CA of the rose petals correlates well with the CA of roses previously measured by Feng et al. [17] (CA 152.4°), Xi at al. [23] (CA 154.3°) and Bhushan et al. [25] (CA 155°). The CA of the *Cosmos* petal was only 118°, thus, the *Cosmos* surface was more hydrophilic than the other petal surfaces. Except for *Cosmos*, all uncoated polymer replicas feature a lower CA than their biological model and thus did not show the same wetting behavior. This suggests that the replica material is more hydrophobic than the cuticle of the *Cosmos* petal and more hydrophilic than the cuticles of the other species investigated. The flat uncoated polymer had a CA of 79.3°, which is by definition a hydrophilic surface [9]. With respect to the Wenzel equation (Equation 1) a CA decrease through structuring of the hydrophilic polymer was expected [11]. In contrast to that, an increase of surface roughness has led to an increase of the CA of the structured polymers. After covering the replicas with a hydrophobic fluorine polymer (CA of the flat fluorine polymer: 106.5°), the CA values increased conspicuously (Figure 4). These results emphasize that a hydrophobic material in combination with surface roughness is the basis for the fabrication of superhydrophobic surfaces.

While the CA values of the coated replicas of $Cosmos_{cr}$, $Dahlia_{cr}$ and $Rosa_{cr}$ were very similar (CA 145.2°; 141.9°; 140.0°), the CA of $Viola_{cr}$ was much higher (CA 168.9°). A similar tendency was found for the TAs (Figure 5). The petals of *Cosmos, Dahlia* and *Rosa* possess high adhesion to water droplets (*Cosmos* and *Dahlia* TA >90°; *Rosa*: TA 44°), thus, water droplets do not roll-off from the petals or the coated and

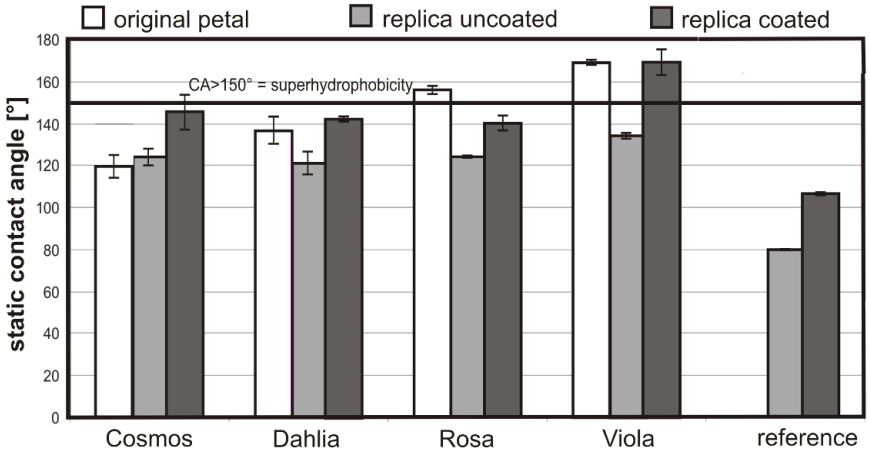

Figure 4: Static CAs of 5 µl water droplets on the surfaces of fresh (original) petals, their uncoated and coated polymer replicas and of the reference (uncoated and coated flat polymer; n = 10).

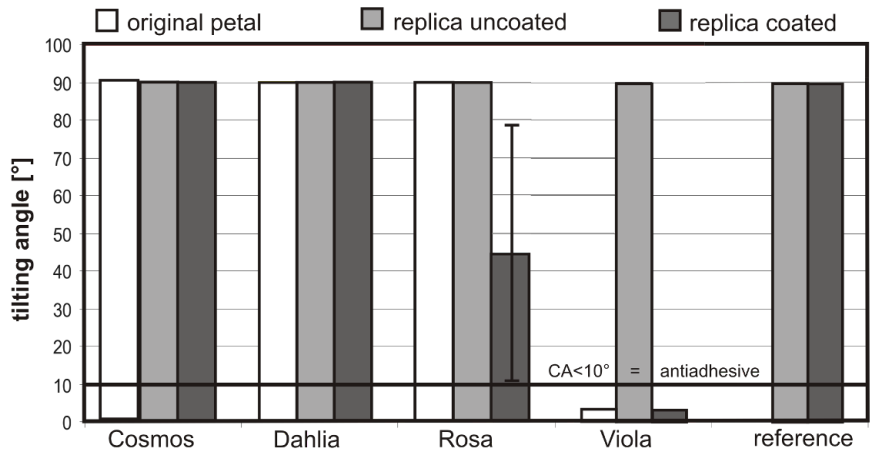

Figure 5: TAs of 5 µl water droplets on the surfaces of fresh (original) *Cosmos*, *Dahlia*, *Rosa* and *Viola* flowers, their uncoated and coated polymer replicas and the TA of the reference (uncoated and coated flat polymer*; n* = 10).

uncoated replicas. These data correlate well with the reported "petal effect". Feng et al. [17] showed that *Rosa* petal surface structures impart special properties to the flowers, in that small water droplets (1–10 µl) adhere to the petals whilst larger droplets (>10 µl) roll-off. On *Viola* petals and their coated replicas, applied droplets rolled off at TAs of <5°, even when droplets with a volume smaller than 10 µl (here 5 µl) were used (Figure 5).

The TA of the coated $Rosa_{cr}$ was very inhomogeneous. The average TA was 44° with high standard deviation (±34.4°). *Rosa* petals possess sharp micropapillae, the folds are relatively thick (410 ± 9 nm) and the micropapillae are only 13.8 ± 3.2 µm in height. With respect to wetting stages, air pocket formation on surfaces is important. By comparison of the microstructure of *Rosa* and *Viola*, we expect larger air pocket formation in *Viola,* based on the much higher micropapilla in *Viola* (40.2 µm in height). However, in roses sometimes air pocket formation might exist because some droplets rolled-off the surface at low inclination angles (TA 10°). These observations are in contrast to those of Feng et al. [17]. Over millions of years of co-evolution, different morphological adaptations have evolved in petals. Scanning electron microscopy studies also revealed large structural variations in petal microstructures. These surface microstructures cause optical signals [30,31] or function as a tactile cue for bees [32]. For us the "petal effect" or the repellence of petals seems to be a side effect and not the primary aim of the flower. A petal is a relatively short lived organ of plants, developed for pollinator attraction, but the short duration of petal lifetime makes a self-cleaning property for pathogen defence expendable. The last point might explain why water repellence is not widespread in petals.

Viola petals as a model for superhydrophobic, water repellent surfaces

Viola petals do not possess the "petal effect" and are anti-adhesive for water droplets. It is well known that hierarchical surface architecture represents optimized structures for superhydrophobic surfaces [11,33-36]. Based on the data presented here, we can describe two main superhydrophobic surface architectures for plant surfaces, the micropapillae with wax crystals [6] and micropapillae with cuticle folds. Some remarkable differences exist between the surface architecture of the lotus leaf and *Viola* petals. In *Viola* petals microstructures are larger (average height of 40.2 µm) than those of lotus leaves, which have microstructures with an average height of 15 µm [37]. The nanofolds in *Viola* have an average thickness of 0.26 µm, while the wax tubules of lotus are only 100 nm thick and ~0.5–3 µm in length [38]. Thus, the *Viola* petal possesses no three dimensional wax crystals, but a hydrophobic two dimensional wax film covering the micropapillae and nanofolds.

The distances between the structures also have an influence on the wetting stage. The average pitch value (peak to peak distances) of the lotus micropapillae is 22.6 ± 1.9 µm [37,38]. This is lower than the average pitch value of the *Rosa* micropapillae (31.1 ± 8.9 µm), but similar to the value of the *Viola* micropapillae (24.9 ± 3.8 µm). The dried rose petals investigated by Bhushan et al. [25] showed microstructures with larger pitch values than those found for the lotus leaf. On such petals water droplets seem to partially penetrate into the petal microstructures leading to a "Cassie impregnating wetting state". The low TA found for *Viola* petals indicates a Cassie–Baxter wetting regime, in which water droplets do not penetrate into the grooves of the micropapillae. Furthermore,

hysteresis can also be affected by the shape of the microstructures and adequate nano-sculpting on top. The combination of high (40.2 µm) and extremely peaked micropapillae with very fine folds (260 nm) on top apparently prevents water from penetrating into the structures by capillary force (Supporting Information File 1, Figure S2).

A high standard deviation in *Viola* micropapillae heights (σ: ±13.1 µm ≙ 33%, Table 1) demonstrates that large variations in cell height do exist. The percentage standard deviation of the micropapillae height of the other investigated species $Cosmos_r$ (σ: ±4.7 µm ≙ 23%), $Dahlia_r$ (σ: ±5.6 µm ≙ 26%) and $Rosa_r$ (σ: ±3.2 µm ≙ 23%) is much smaller. The higher standard deviation of the micropapillae height is correlated to a large reduction in papilla contact with the applied water droplet. Cryo-SEM-investigations (Figure 6) indicated that smaller micropapillae are not in contact with the applied liquid. Thus, cell height variations further decrease the liquid–solid contact area and consequently decrease the adhesion of the liquid to the surface. Additionally, a sharp papillae tip benefits more from a lower contact area than a flat, rounded papilla tip. For the "petal effect" Feng et al. [17] proposed that water droplets penetrate into the grooves between the micropapillae. *Viola* prevents water penetration into the micropapillae grooves by reducing the papillae peak to peak distance, which is on average 24.9 µm. Much larger peak to peak distances were found in $Rosa_r$ (31.1 µm), $Cosmos_r$ (41.0 µm) and $Dahlia_r$ (48.4 µm). The results presented here show that the combination of high micropapillae with high ar, sharp tips and small peak to peak distances is required for the design of biomimetic superhydrophobic petal surfaces with low hysteresis.

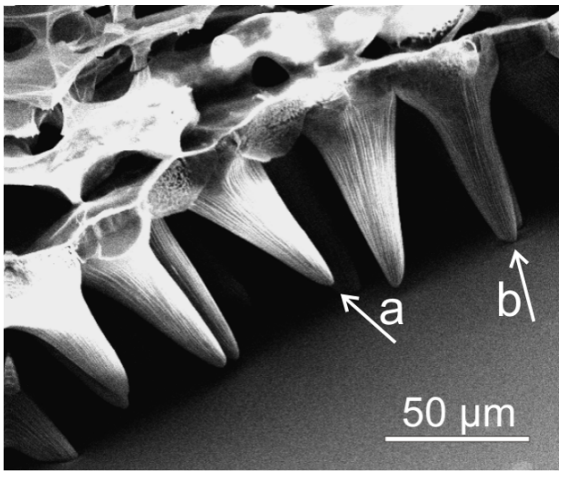

Figure 6: Cryo-SEM micrograph of the micropapillae of a *Viola* petal in contact with the surface of a water-glycerol droplet. Many micropapillae are not in contact with the droplet surface (a) while others are in contact with the droplet surface (b).

The cuticular folds also have an influence on the wetting stage. On $Viola_r$ the micropapillae are completely covered with fine nano-folds (260 ± 70 nm), arranged at a separation of 450 ± 120 nm, whilst the micropapillae of the $Rosa_r$ petals are only partially covered with broader folds (410 ± 90 nm), arranged at a separation of 210 ± 90 nm. Feng et al. [17] noted folds of 730 nm width on the micropapillae with an average diameter of 16 µm and a height of 7 µm (the differences probably result from the usage of different species). Their rose petals possess a CA of 152.4° and a TA of >90°. By replicating the flowers, they developed a polymer film with a CA of 154.6° and a high adhesion to water droplets (TA >90°). Hydrophobic replicas of the *Viola* petals have a CA of 169° and a TA of <5°. These results show that finer folds arranged at small separation seem to prevent the penetration of water into the folds by capillary forces.

Conclusion

Flower petals provide a new design strategy for the development of superhydrophobic, biomimetic materials. In contrast to superhydrophobic petals, where water droplets adhere, and which have been described before, we found a biological model (*Viola tricolor*) with a superhydrophobic, water repellent petal surface. Indeed, these flowers provide the typical surface architecture of petals (micropapillae with a folding on top), but a similar wetting behavior as that described for lotus leaves. By an easy and fast replication technique and subsequent hydrophobic coating, biomimetic replicas were fabricated. These replicas possessed the same surface structures and wettability as the biological models. The petal surface design of *Viola*, introduced here, seems to be easier and much more favourably to produce, e.g., by imprint processes, than the hierarchically organized structures which are found on the lotus leaf. In contrast to the lotus leaf structuring with randomly distributed nanocrystals the surface structures of *Viola* could be qualified, for example, for large area foil imprinting processes. Thus, a new surface design for the development of superhydrophobic, water repellent biomimetic materials is presented.

Experimental

Plant material

The upper surface (adaxial) sides of the petals of four different plant species were investigated. Plants were cultivated in the Botanic Gardens of the Rheinische Friedrich–Wilhelms-University of Bonn (BGB). Their scientific names are given together with their registration numbers of the BGB. Investigated species are the Chocolate Cosmos (*Cosmos atrosanguineus;* BGB 29614-8-2008), *Dahlia pinnata* (BGB 7960-9-1990), the China Rose (*Rosa chinensis;* BGB 3089-9-1979) and the Wild Pansy *Viola tricolor* (BGB 27262-4-2004).

Fabrication of the replicas

For the fabrication of the biomimetic polymer replicas, the replication technique introduced by Koch et al. [28] was used. Here, we briefly introduce the technique and mention the modifications made. The replication technique is a two-step moulding process, in which at first a negative is generated and then a positive. For generating the negative replicas, the master (biological sample) is moulded with polyvinylsiloxane dental wax (President light body Gel, ISO 4823, PLB; Coltene Whaldent, Hamburg, Germany). In the second step, the negative replicas were filled with a two-component epoxy resin (RECKLI Injektionsharz EP, RECKLI GmbH, Herne, Germany). The use of this material is a modification in the replication process introduced by Koch et al. [28] (replication performance of the RECKLI material; Supporting Information File 1, Figure S1). After spilling the negative replicas, the epoxy resin was dried for 48 h at 25 °C. After hardening, the positive replicas were peeled off from the negative replicas and further replicas were fabricated. In total, five petals of each species were replicated and examined afterwards.

Hydrophobization of the replicas

The replicas were dip-coated (30 sec) in a fluorine polymer (Antispread, E2/50 FE 60, Dr. Tillwich GmBH Werner Stehr) and then dried for 20 min at room temperature. Antispread is a commercially available Fluorocarbon 60 for surface hydrophobization. It forms approximately 40 nm thin layers on the substrate (producer information) and causes no additional nanostructuring on the replica surfaces. A smooth surface, dip-coated with Antispread has a static CA of 106°.

Surface characterization

The surface structures of the biological samples and their replicas were investigated by SEM. Images were recorded using a CAMBRIDGE Stereoscan 200 SEM (Zeiss GmbH, Oberkochen, Germany), a digital image processing system (DISS 5, Version 5.4.17.0, Point Electronic GmbH, Halle, Germany) was used to visualize and measure the surface structures of the petals. Fresh plant material was dehydrated with ethanol and dried in a critical point dryer (CPD 020, Balzers Union, Balzers–Pfeifer GmbH, Aßlar). On account of their stability, the replicas did not require special preparation. All samples were sputter-coated with a 30 nm gold layer (Balzers Union SCD 040, Balzers–Pfeifer GmbH, Aßlar) prior to SEM investigations.

Cryo-SEM examinations

To display an applied droplet in contact with the petal surface, the Cryo-SEM method, developed by Ensikat et al. [18], was used. In this method a sample–droplet (glycerol–water mixture of 1:3) complex was frozen with liquid nitrogen. A water–glycerol mixture was used as the liquid to prevent crystallization patterns on the droplet surface, which occur on pure water droplets. After this the sample was separated from the droplet (5 µl) and the surface imprint of the droplet was examined under a scanning electron microscope. All examinations were performed using a CAMBRIDGE Stereoscan 200 SEM (Zeiss GmbH, Oberkochen, Germany), equipped with a digital image acquisition system (DISS 5, Point Electronic, Halle, Germany).

Static contact angle and tilt angle measurements

The wettability of the biological samples and the replicas was characterized by CA and TA measurements with a computer controlled goniometer OCA 30 (Dataphysics SCA 2.02, Filderstadt, Germany). Five microliters of demineralized water droplets were automatically applied to the samples via syringe and CAs were automatically determined using the Laplace–Young fitting algorithm. TAs were measured by tilting the samples (with an applied droplet on the surface) and measuring the TA at which the droplets rolled off the surface. Each measurement was repeated 10 times.

Supporting Information

Supporting Information File 1

Additional figures.
[http://www.beilstein-journals.org/bjnano/content/supplementary/2190-4286-2-27-S1.pdf]

Acknowledgements

This study was supported by the German Science Foundation (Deutsche Forschungsgemeinschaft; DFG), within the Graduiertenkolleg 1572 “Bionics – Interactions across Boundaries to the Environment”. The authors thank Professor Matthias Frentzen of the Poliklinik für Parodontologie, Zahnerhaltung und Präventive Zahnheilkunde of the University of Bonn for his critical and helpful comments during the preparation of the biomimetic replicas. Further, the authors thank the German Federal Ministry of Education and Research (Bundesministerium für Bildung und Forschung; BMBF) and the Akademie der Wissenschaften und Literatur, Mainz for their financial support in correlated projects.

References

1. Koch, K.; Bhushan, B.; Barthlott, W. *Prog. Mater. Sci.* **2009,** *54,* 137–178. doi:10.1016/j.pmatsci.2008.07.003
2. Bargel, H.; Koch, K.; Cerman, Z.; Neinhuis, C. *Funct. Plant Biol.* **2006,** *33,* 893–910. doi:10.1071/FP06139
3. Barthlott, W.; Ehler, N. In *Tropische und Subtropische Pflanzenwelt;* Mainz, Akademie der Wissenschaften und der Literatur, Ed.; Steiner: Wiesbaden, 1977; Vol. 19, pp 367–467.

4. Barthlott, W.; Neinhuis, C. *Planta* **1997,** *202,* 1–8. doi:10.1007/s004250050096
5. Neinhuis, C.; Barthlott, W. *Ann. Bot. (Oxford, U. K.)* **1997,** *79,* 667–677. doi:10.1006/anbo.1997.0400
6. Koch, K.; Barthlott, W. *Philos. Trans. R. Soc. London, Ser. A* **2009,** *367,* 1487–1509. doi:10.1098/rsta.2009.0022
7. Barthlott, W.; Schimmel, T.; Wiersch, S.; Koch, K.; Brede, M.; Barczewski, M.; Walheim, S.; Weis, A.; Kaltenmaier, A.; Lederer, A.; Bohn, H. F. *Adv. Mater.* **2010,** *22,* 2325–2328. doi:10.1002/adma.200904411
8. Cerman, Z.; Striffler, B. F.; Barthlott, W. In *Functional Surfaces in Biology;* Gorb, S. N., Ed.; Springer: Berlin, Heidelberg, 2009; Vol. 1, pp 97–112. doi:10.1007/978-1-4020-6697-9_7
9. Roach, P.; Shirtcliffe, N. J.; Newton, M. I. *Soft Matter* **2008,** *4,* 224–240. doi:10.1039/b712575p
10. Barthlott, W.; Wollenweber, E. *Tropische und subtropische Pflanzenwelt* **1981,** *32,* 7–67.
11. Wenzel, R. N. *Ind. Eng. Chem.* **1936,** *28,* 988–994. doi:10.1021/ie50320a024
12. Cassie, A. B. D.; Baxter, S. *Trans. Faraday Soc.* **1944,** *40,* 546–551. doi:10.1039/tf9444000546
13. Lafuma, A.; Quéré, D. *Nat. Mater.* **2003,** *2,* 457–460. doi:10.1038/nmat924
14. Israelachvili, J. N.; Chen, Y.-L.; Yoshizawa, H. In *Fundamentals of adhesion and interfaces;* Rimai, D. S.; DeMejo, L. P.; Mittal, K. L., Eds.; VSP: Utrecht, 1994; pp 261–279.
15. Extrand, C. W. *Langmuir* **2002,** *18,* 7991–7999. doi:10.1021/la025769z
16. Wang, S.; Jiang, L. *Adv. Mater.* **2007,** *19,* 3423–3424. doi:10.1002/adma.200700934
17. Feng, L.; Zhang, Y.; Xi, J.; Zhu, Y.; Wang, N.; Xia, F.; Jiang, L. *Langmuir* **2008,** *24,* 4114–4119. doi:10.1021/la703821h
18. Ensikat, H. J.; Schulte, A. J.; Koch, K.; Barthlott, W. *Langmuir* **2009,** *25,* 13077–13083. doi:10.1021/la9017536
19. Hong, X.; Gao, X.; Jiang, L. *J. Am. Chem. Soc.* **2007,** *129,* 1478–1479. doi:10.1021/ja065537c
20. Liu, M.; Zheng, Y.; Zhai, J.; Jiang, L. *Acc. Chem. Res.* **2010,** *43,* 368–377. doi:10.1021/ar900205g
21. Bhushan, B.; Jung, Y. C.; Nosonovsky, M. In *Springer Handbook of Nanotechnology;* Bhushan, B., Ed.; Springer: Berlin, Heidelberg, New York, 2010; Vol. 3, pp 1437–1524. doi:10.1007/978-3-642-02525-9_42
22. Shi, F.; Chen, X.; Wang, L.; Niu, J.; Yu, J.; Wang, Z.; Zhang, X. *Chem. Mater.* **2005,** *17,* 6177–6180. doi:10.1021/cm051453b
23. Xi, J.; Jiang, L. *Ind. Eng. Chem. Res.* **2008,** *47,* 6354–6357. doi:10.1021/ie071603n
24. Bormashenko, E.; Stein, T.; Pogreb, R.; Aurbach, D. *J. Phys. Chem. C* **2009,** *113,* 5568–5572. doi:10.1021/jp900594k
25. Bhushan, B.; Her, E. K. *Langmuir* **2010,** *26,* 8207–8217. doi:10.1021/la904585j
26. Xia, Y.; Whitesides, G. M. *Angew. Chem., Int. Ed.* **1998,** *37,* 550–575. doi:10.1002/(SICI)1521-3773(19980316)37:5<550::AID-ANIE550>3.0.CO;2-G
27. Koch, K.; Dommisse, A.; Barthlott, W.; Gorb, S. N. *Acta Biomater.* **2007,** *3,* 905–909. doi:10.1016/j.actbio.2007.05.013
28. Koch, K.; Schulte, A. J.; Fischer, A.; Gorb, S. N.; Barthlott, W. *Bioinspir. Biomim.* **2008,** *3,* No. 04600210. doi:10.1088/1748-3182/3/4/046002
29. Schulte, A. J.; Koch, K.; Spaeth, M.; Barthlott, W. *Acta Biomater.* **2009,** *5,* 1848–1854. doi:10.1016/j.actbio.2009.01.028
30. Whitney, H.; Kolle, M.; Alvarez-Fernandez, R.; Steiner, U.; Glover, B. J. *Commun. Integr. Biol.* **2009,** *2,* 230–232. doi:10.4161/cib.2.3.8084
31. Zhang, Y.; Hayashi, T.; Inoue, M.; Oyama, Y.; Hosokawa, M.; Yazawa, S. *Acta Hort. (ISHS)* **2008,** *766,* 469–476.
32. Kevan, P. G.; Lane, M. A. *Proc. Natl. Acad. Sci. U. S. A.* **1985,** *82,* 4750–4752. doi:10.1073/pnas.82.14.4750
33. Callies, M.; Quéré, D. *Soft Matter* **2005,** *1,* 55–61. doi:10.1039/b501657f
34. Sun, C.-H.; Gonzalez, A.; Linn, N. C.; Jiang, P.; Jiang, B. *Appl. Phys. Lett.* **2008,** *92,* 0511071–0511073. doi:10.1063/1.2841818
35. Nosonovsky, M.; Bhushan, B. *Ultramicroscopy* **2007,** *107,* 969–979. doi:10.1016/j.ultramic.2007.04.011
36. Bhushan, B.; Jung, Y. C.; Koch, K. *Philos. Trans. R. Soc., A* **2009,** *367,* 1631–1672. doi:10.1098/rsta.2009.0014
37. Fürstner, R. In *Untersuchungen zum Einfluss von Struktur und Chemie auf die Benetzbarkeit und die Selbstreinigung superhydrophober Oberflächen;* Walzel, P., Ed.; Schriftenreihe Mechanische Verfahrenstechnik, Vol. 5; Shaker Verlag: Aachen, Germany, 2002; pp 151 ff.
38. Koch, K.; Dommisse, A.; Niemietz, A.; Barthlott, W.; Wandelt, K. *Surf. Sci.* **2009,** *603,* 1961–1968. doi:10.1016/j.susc.2009.03.019

License and Terms

Beilstein Journal of Nanotechnology

Recrystallization of tubules from natural lotus (*Nelumbo nucifera*) wax on a Au(111) surface

Sujit Kumar Dora* and Klaus Wandelt

Full Research Paper

Open Access

Address:
Institute of Physical and Theoretical Chemistry, Bonn University, Wegelerstrasse 12, 53115 Bonn, Germany

Email:
Sujit Kumar Dora* - sujitdora1977@googlemail.com; Klaus Wandelt - k.wandelt@uni-bonn.de

* Corresponding author

Keywords:
AFM; Au(111); lotus wax

Beilstein J. Nanotechnol. **2011,** *2,* 261–267.
doi:10.3762/bjnano.2.30

Received: 22 December 2010
Accepted: 26 April 2011
Published: 25 May 2011

This article is part of the Thematic Series "Biomimetic materials".

Guest Editors: W. Barthlott and K. Koch

Abstract

We present here the first results on the self-assembly of tubules of natural wax from lotus leaves on a single crystal Au(111) surface. A comparison of the tubule growth on Au(111) to that on HOPG is discussed. Although the tubule formation on both Au(111) and HOPG takes place on an intermediate wax film which should mask the substrate properties, the tubule orientations differ. In contrast to a vertical tubule orientation on HOPG, the tubules lie flat on Au(111). Taking into account the physical properties of HOPG and Au(111), we put forward a hypothesis which can explain the different tubule orientations on both substrates.

Introduction

Natural nonacosan-10-ol waxes derived from plant leaves have been subjected to numerous studies [1-9]. Electron micrograph studies by Barthlott et al. [7] demonstrated the tubule-like assembly of nonacosan-10-ol molecules on lotus (*Nelumbo nucifera*) leaves, whilst their crystalline nature was verified by X-ray powder diffraction (XRD) and electron diffraction (ED) techniques [10,11]. Koch and co-workers applied tapping mode AFM to study the continuous growth of nonacosan-10-ol tubules on HOPG [8]. By applying a 10 µL droplet of natural wax molecules derived from nasturtium (*Tropaeolum majus*) and lotus (*Nelumbo nucifera*) containing different concentrations of nonacosan-10-ol dissolved in chloroform onto a HOPG surface, they showed for the first time that tubule growth follows a three step mechanism, i.e., a "rodlet → curved structure → tubule", growth type behavior [8]. By comparing the vertical orientation of tubules on HOPG (non-polar) to horizontally oriented tubules on polar substrates, e.g., silicon, alumina, or glass, they concluded that surface polarity is responsible for tubule orientation. They also demonstrated an increase in the hydrophobicity of the HOPG surface covered with tubules by measuring the contact angle, which increased from 88° (freshly wax covered surface) to 129° after 14 days. A more recent study by the same group [6] demonstrated a number of factors which affect the self-assembly of nonacosan-10-ol molecules on

various substrates. By thermal vapor deposition of the wax molecules (in order to exclude solvent influence) they found that at 50 °C (substrate temperature) tubule growth on HOPG occurs rapidly, whereas at 25 °C no tubule was formed on the surface. They also demonstrated that tubules can only be formed from the *S*-enantiomer of nonacosan-10-ol with the addition of a certain amount of diol (0–5%), whereas the *R*-enantiomer produced very few tubular structures even after addition of 4% of the corresponding diol. On the other hand, chemically pure nonacosan-10-ol failed to form any tubules [6]. In addition, a spiral growth mechanism for tubule formation was also proposed in these studies.

Although self-assembly of these tubules was studied on a number of different substrates, as noted above, their growth on single crystal metals has not yet been investigated. Here we report the first study of the growth of tubules from natural wax collected from lotus leaves on a Au(111) surface. In addition, a comparison of tubule growth on Au(111) and HOPG is given in order to obtain a better understanding of the various surface properties affecting the growth kinetics and structure of these tubules. The Au(111) surface was chosen, because gold is regarded as the most chemically inert metal and is a well known substrate for the study of self-assembly of a number of different organic molecules, e.g., long chain alkanes [12,13], both aliphatic and aromatic thiols [14-16], substituted porphyrins [17,18], substituted pyridines [19], 1-nitronapthalene [20], saccharin [21], substituted carboxylic acids [22], polyaniline [23], etc., either by vapor deposition in vacuum, or from solution. The main intention of our study was to demonstrate that tubules from lotus wax can also be reconstituted on single crystal metal surfaces, and compare their kinetics and orientation with materials that have similar surface properties.

Results

Figure 1 shows a series of AFM images of wax growth on the Au(111) surface. A video sequence of all the images taken during scanning, which demonstrates the representative wax crystallization process on Au(111), is available in Supporting Information File 1. As for their polar orientation, the majority of the tubules are oriented in a parallel fashion with respect to the substrate surface: Only a minority do not lie totally flat on the substrate. In other words, these latter tubules have a height difference between their two ends, i.e., they exhibit a slope (for example, the tubule marked 'Z' in Figure 1f). The term polar orientation refers to the tubule orientation with respect to the vertical axis (see inset in Figure 1b, ψ is the polar angle). The average time for completion of tubule formation was about 3–4 hours. The term ”completion” indicates the point where the tubule growth ceases, i.e., when no further changes in dimensions (e.g., width, length) of the tubules are observed. Figure 1a,

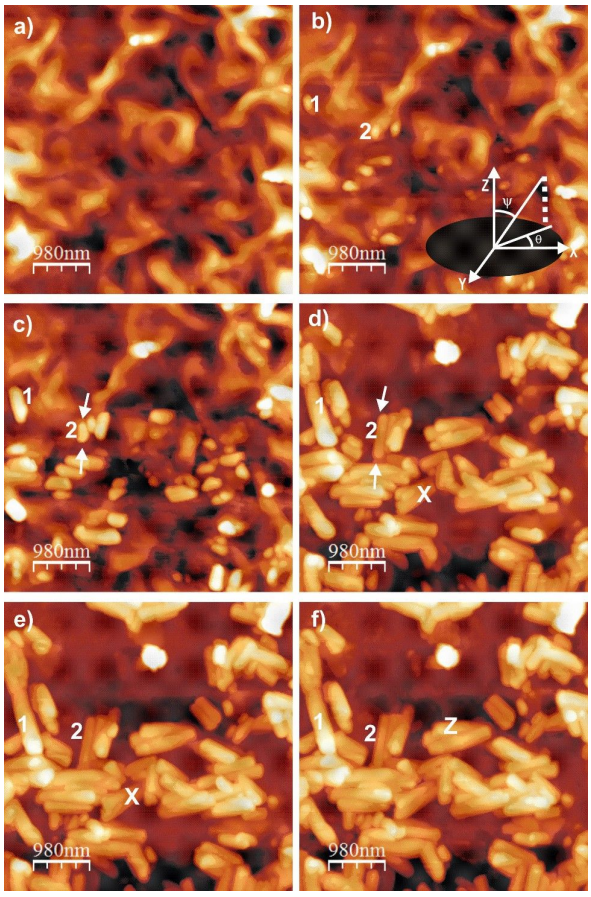

Figure 1: Consecutive AFM images showing nonacosan-10-ol wax tubule growth on a single crystal Au(111) surface about 15–759 minutes after applying 0.4 mg·mL^{-1} wax solution onto the subs trate. Tubule growth starts from a thin film (Figure 1a, 15 minutes) of irregular nature (roughness about 20–300 nm) and rodlets are formed (Figure 1b, 36 minutes) by phase separation. The rodlets then change to tubules (Figure 1c, 77 minutes) before growing longitudinally (see arrows in Figure 1b, Figure 1c and Supporting Information File 1) by the continuous accumulation of wax molecules at both ends (Figure 1d, 207 minutes). Longitudinal growth ceases at ≈4 hours (Figure 1e, 242 minutes). Further waiting up to 13 hours (Figure 1f, 759 minutes) did not result in any further morphological change. Size = 4.9 × 4.9 μm^2, scan rate = 0.619 Hz, 256 lines.

which was taken 15 minutes after application of the wax solution, shows a thin film of variable roughness (roughness varies between 20–300 nm) covering the entire surface. Figure 1b, which was recorded after 36 minutes, shows the initial phase separation and the formation of rodlets from this thin film. The term phase separation here primarily refers to the isolation of wax molecules which form rodlets (which later on are converted to tubules), from those which do not form rodlets. It is important to note here that these tubules grow on top of a non-tubule forming wax film and not on top of the Au(111) substrate itself. The average time for the onset of this phase separation is about 15–20 minutes. It is worth mentioning that the

average time period before the onset of this phase separation is reproducible from a number of experiments carried out under similar conditions which was verified in our case by repeating the experiments three times. The term rodlet used here is actually taken from previous studies by Koch et al [8]. Figure 1c, which was taken after about 77 minutes, shows rodlets undergoing bending, due the continuous incorporation of wax molecules, and hence starting to form tubules. Once the tubules are formed, they start to grow longitudinally at both sides by further addition of wax molecules to either end, as shown by arrows in Figure 1c and Figure 1d (at about 77 and 207 minutes), respectively. The longitudinal growth ceased after about 4 hours (Figure 1e, at about 242 minutes) and no further changes in the dimension of the tubule or the underlying thin film was observed, even although experiments were carried out for up to 13 hours (Figure 1f, 759 minutes). It is also important to note however, that the growth of some of the tubules ceased much earlier, for example, the tubules marked with ”X” in Figure 1d (at about 207 minutes). The reason for such premature saturation might be related to the local unavailability of further tubule forming wax molecules. The average outer diameter of the vast majority of tubules varied between 200–300 nm. Only a negligible number of tubules with an outer diameter of greater than 300 nm were found.

It is interesting to note that the outer diameter of all the tubules varied in multiples of 20 nm (e.g., 200, 220, 260, 280 and 300 nm) as observed in our experiments. Such variations in the outer diameter can also be found on a number of different substrates, e.g., glassy carbon, mica, glass, etc., as was also observed in our experiments. Figure 2a shows an initial stage of layer by layer growth of a tubule on a glassy carbon surface. A line profile across the layer (Figure 2b) clearly demonstrates that the height of a single layer is about 20 nm (standard deviation 2 nm, number of measurements = 5) which clearly agrees with the stepwise tubule outer diameter variation in multiples of 20 nm. The average length of flat lying tubules varies randomly most probably depending upon the local availability of tubule forming wax molecules, but no useful statistics could be drawn from this.

Plots of the increase in length and radial width of some tubules versus time are shown in Figure 3. The curves numbered 1 and 2 refer to the numbers 1 and 2 in Figure 1. The plot (Figure 3a) shows a logarithmic increase in the length reaching saturation after about 3.5 hours. Further waiting periods up to 6 hours (and longer - data not shown) did not result in any further measurable change of the tubule length. Comparing the growth of both tubules – 1 and 2 in Figure 1 (plotted in Figure 3a) – it is obvious that the growth rate of tubule 2 was lower and its final length was shorter, but both tubules reached their final length

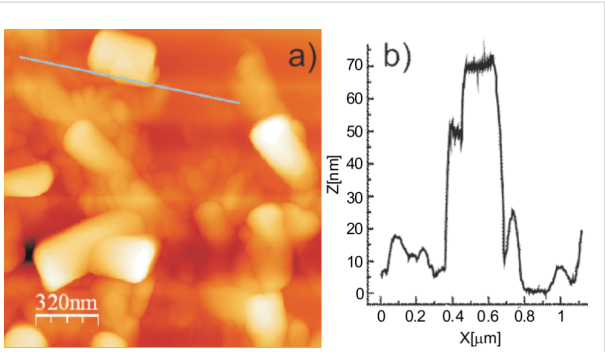

Figure 2: Initial stage formation of lotus wax tubules on a glassy carbon surface (a) and profile across the marked section (b) showing the average layer height to be about 20 nm (standard deviation 2 nm, number of measurements = 5) in agreement with the variation of outer diameters of tubules in multiples of 20 nm. Size = 1.6 × 1.6 µm^2, scan rate = 0.519 Hz, 512 lines.

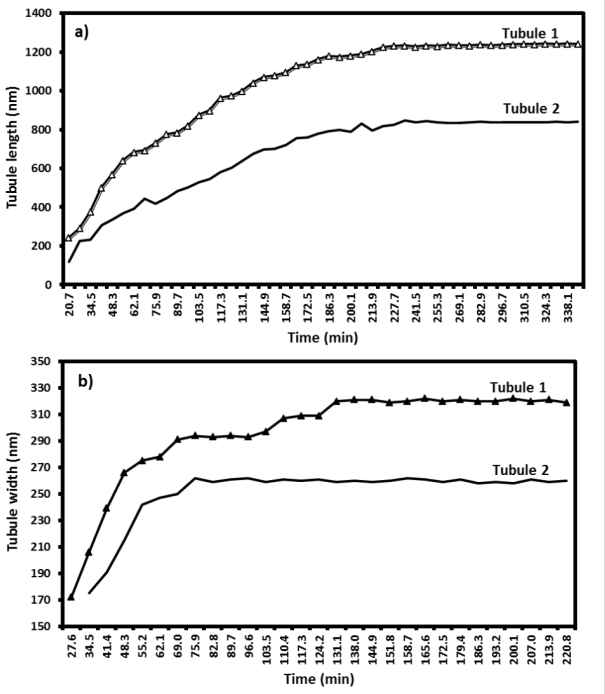

Figure 3: Change in tubule length (Figure 3a) and width (Figure 3b) versus time for two representative tubules (numbered as 1 and 2 in Figure 1) taking into account all the images shown in the video (Supporting Information File 1; partially shown in Figure 1). Tubule growth follows a logarithmic trend and saturates after ≈4 hours for longitudinal growth, and 2.2 hours or less for radial growth, respectively.

after the same time (about 3.5 hours). On the other hand, although radial growth follows a similar logarithmic increase behavior (Figure 3b), the time period of width saturation is considerably lower (about 2.2 hours for tubule 1 and 1.2 hours for tubule 2). This indicates that the tubules continued to grow

in length after they reached their final diameter. The term growth indicates increase in both longitudinal as well as radial width of the tubules. This means that tubule 1 was not only longer than tubule 2 but that its radius was also larger (about 320 nm) compared to tubule 2 (about 260 nm). In addition, in no case studied did we find a dependence of the growth kinetics on the concentration of molecules *in solution*. These two observations combined suggest that both the growth rate as well as the saturation length depends on the availability of molecules on the *surface*, or more precisely, within the "capture zone" surrounding each tubule.

Discussion

As on many other substrates such as glass, mica, and HOPG, we also observed on a Au(111) surface the recrystallization of tubular structures after application of a solution of natural lotus wax in chloroform. AFM images showed that most of the tubules with a polar orientation parallel to the surface reached their final length after approximately 3–4 hours. The reason some of the tubules had a height difference between the two ends was due to their growth over other tubules. Those tubules lying directly on the substrate (or for that matter on the non-tubule forming thin film) did indeed have a parallel orientation with respect to the substrate. This is quite different to the tubules observed by Koch et al on HOPG [9]. Although under similar conditions, the average time period for reaching saturation length is comparable for both HOPG and Au(111), the tubule orientation differs, i.e., a horizontal tubule orientation on Au(111) in comparison to the vertical orientation on HOPG (Figure 4).

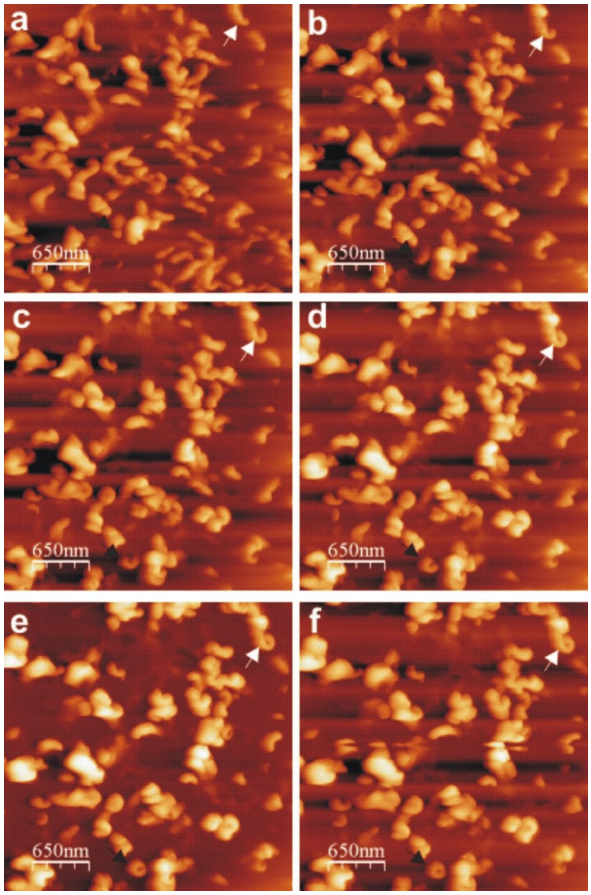

Figure 4: Consecutive AFM images of Lotus (*Nelumbo nucifera*) wax tubule growth on HOPG, about 32–230 minutes after applying 0.2 mg·mL^{-1} wax solution (chloroform solvent) to the substrate. The arrows show vertical growth of tubules in clockwise (black arrow) as well as anti-clockwise (white arrow) direction on the substrate. The average time for completion of tubule formation is about 3–4 hours. The growth of the tubules starts from rodlets (Figure 3a, 32 minutes) which form curved rodlets (Figure 3b, c, d, e, 66, 98, 148, 180 minutes) before finally forming the complete tubule (Figure 3f, 230 minutes) as marked by arrows. Size = 3.25 × 3.25 μm^2, scan rate = 0.519 Hz, 512 lines.

Taking into account the physical properties of HOPG and Au(111), where both are non-polar and crystalline in nature, this difference in the orientation of tubules is surprising. It is a well known fact that self-assembly of organic molecules with aliphatic chains results in epitaxial growth on HOPG due to their well matched atomic distances. For example, Watel et al. [24] have shown for long chain alkanes that the carbon skeleton lies parallel to the HOPG surface. On the other hand, epitaxial growth of long chain alkanes on Au(111) resulted in a vertical arrangement of the carbon skeleton [12] on the substrate. Similarly, Dorset et al. [25,26] have also demonstrated the unusual orientation of paraffin waxes by studying their epitaxial growth on organic crystals. It is important to note that epitaxial growth is limited to the first few layers attached to the substrate, however, in our case tubules were formed on top of a thin film (formed from non-tubule forming wax molecules) rather than directly on the substrate surface. The presence of such a thin film on both the Au(111) and the HOPG surface should make both surfaces behave in an equivalent manner and suppress any effect of a direct epitaxial relationship with the respective substrate. Yet, a vertical orientation of tubules could be found on HOPG compared to the horizontal tubule orientation on Au(111). To support our claim, we would also like to emphasize that even after applying a 10 μL droplet of a higher concentrated solution (10 mg·mL^{-1}) on to HOPG, vertically oriented tubules were also formed. By contrast, we have also observed rodlets of octacosan-1-ol growing only in a parallel fashion (also reported by Koch et al. [27]) on top of its thin film by applying a 10 μL droplet of 0.4 mg·mL^{-1} octacosan-1-ol in chloroform on to HOPG (Supporting Information File 2). This strongly suggests that the orientation of the three dimensional structure on top of the thin film is independent of the epitaxial behavior. Therefore we can clearly say that none of the above

mentioned substrate properties are responsible for the orientation of the tubules on these substrates. This also leads to the question, if none of these properties are responsible then what else is responsible for the vertical tubule orientation on HOPG? The answer might be found in the free standing dangling bonds on HOPG. Many authors have already reported the presence of free standing dangling bonds on the HOPG surface, which is different from metal surfaces [28-30]. The presence of such dangling bonds in HOPG might act as the preferential adsorption site for some particular constituent of the lotus wax thereby influencing the segregation behavior within the wax layer. As a consequence, the resultant surface composition of the wax film may favor vertical growth of the tubules. On the other hand, on Au(111) no such dangling bonds are available and hence the thin film might have a different surface composition upon which tubules grow horizontally. This substrate dependent segregation behavior, and hence, the different resultant concentration profile within the wax film, could be an explanation as to how the influence of the different substrates could be transferred to the surface of the wax film where the tubules actually grow. However, this "chromatographic effect" of the substrate is purely a hypothesis and no data is available yet to support this hypothesis. As for the azimuthal orientation of tubules, we would also like to make it clear that the tubules are oriented in a random manner and do not follow the symmetry found on a gold surface. The term azimuthal orientation refers to the tubule orientation with respect to the azimuthal angle in the X–Y plane (see inset in Figure 1b, θ is the azimuthal angle). Such random orientation of tubules can also be found on non-crystalline substrates, e.g., glass, glassy carbon, etc.

The next interesting behavior of the tubules is the variation of their outer diameter in multiples of 20 nm. To make sure image artefacts did not affect our measurements, we applied a very slow scanning rate of 0.619 Hz. In addition, tubule diameters were measured with respect to the flat surface and the height measurement in Figure 2 clearly demonstrates the single layer height to be about 20 nm. All these factors strongly support our measurements of outer tubule diameter as being in multiples of 20 nm. Taking into account the molecular length of nonacosan-10-ol, which is about 4 nm long (assuming all methylene groups are in trans-configuration [31]), it can be assumed that a single layer of such a tubule consists of five layers of nonacosan-10-ol (or for that matter corresponding -diol) molecules. The reason for the stability of an individual tubule layer consisting of five molecular layers of nonacosan-10-ol is still unknown, but a high resolution microscopic study might shed more light on the exact molecular architecture within the layers.

The bending of thin films to tubules most probably happens in order to release stress that arises due to the increase in length and thickness of the individual rodlets. Numerous studies have described structural transitions in thin films which contribute to the relaxation of stress at their interface [32-34].

Another interesting observation is the rather uniform and confined diameter of the completed tubules of <300 nm. This, in turn, must be an inherent property of the molecular architecture of the wax tubules. The incipient radial growth of the tubules occurs stepwise in layers of 20 nm thickness. Their molecular arrangement seems to favor a certain curvature of such a 20 nm thick layer. However, with the increasing diameter of a tubule, this curvature decreases leading to the accumulation of internal stress. As a consequence, at a tubular diameter of about 300 nm the curvature of the next added layer of 20 nm would be too low, and hence the internal stress too high, so that no further layer will grow around the tube.

To conclude we would also like to refer to the orientation of wax tubules found in previous studies of the self-assembly of natural nonacosan-10-ol wax on different substrates. Jetter and co-workers [2] showed that substrate polarity and roughness play no role in tubule crystallization by demonstrating a parallel orientation of tubules on a number of different substrates, e.g., polyethylene, polypropylene, Teflon, alumina, mica, glass, etc. However, they applied a larger volume of solution of 50–250 μL (10 mg·mL^{-1}) which effectively masks any effect of the substrate. A more recent study by Koch et al. [9] demonstrated the effect of substrate polarity on the tubule growth by showing a vertical orientation on HOPG and a horizontal orientation on silicon and alumina. However, in our study by combining various properties (e.g., polarity, crystallinity) together at two different surfaces we have demonstrated that none of these properties is directly responsible for tubule orientation. To support our data, we would also like to emphasize that the self-assembly of long chain alcohols, e.g., octacosan-1-ol, on HOPG as well as on other materials, e.g., glass, mica, or silicon, results in a totally different arrangement on HOPG compared to all other materials, as demonstrated by Dommisse [1] and Hommes [35]. This reinforces the notion that some very special properties of HOPG are responsible for the entirely different self-assembly process on its surface and a hypothetical explanation is given above. This raises also the question whether HOPG is in fact a useful substrate in order to mimic natural leaf surfaces, which is actually often done, because on natural leaves no such preferentially vertical orientation is found [7].

Conclusion

We have performed the first study of the growth of nonacosan-10-ol tubules on a single crystal Au(111) surface. By comparing the wax growth on Au(111) with that on a HOPG substrate,

being both non-polar and crystalline, we have found that none of these properties are responsible for tubule orientation. From this study, we have also concluded that HOPG most probably has some special properties that lead to the unusual upright orientation of tubules on its surface. We have proposed as a hypothesis that ultimately the presence of free-standing dangling bonds on HOPG, and thereby a substrate specific segregation behavior within the wax materials, might be responsible for this tubule orientation. Furthermore, we propose the buildup of internal stress within the layered structure of the tubules which limits the outer diameter of tubules to approximately 300 nm. Finally, we have raised the question of whether or not HOPG is a suitable material to mimic wax growth as on natural leaf surfaces.

Experimental

The nonacosan-10-ol wax materials, which were extracted with chloroform from lotus (*Nelumbo nucifera*) leaves, were obtained from the Nees Institute for Biodiversity of Plants at Bonn University. These wax materials, which were used in all our experiments, are actually a mixture of long chain hydrocarbons and their derivatives, e.g., alcohols with one or two OH-groups, aliphatic acids, as well as some unidentified components. For the exact chemical composition of this wax, the reader is referred to the following article [8]. A concentration of 0.4 $mg \cdot mL^{-1}$ of wax molecules was prepared by dissolving 2 mg of wax in 5 mL of chloroform. The Au(111) single crystal used in our experiments was bought from Mateck GmbH, Jülich, Germany. The Au(111) crystal was cleaned by flame annealing (a well established procedure in electrochemical surface science). For this purpose, the crystal was placed on a ceramic plate and annealed with a butane gas flame for 3 minutes up to faint red glow (600–700 °C). The crystal was then cooled to room temperature in an argon atmosphere for about 15 minutes. A clean HOPG surface was prepared by simply removing a few atomic layers with adhesive tape.

AFM measurements were carried out with a Picoscan AFM (Molecular Imaging, Tempe, AZ, USA) with a PicoScan controller coupled with a MAC Mode controller. The system was operated in MAC Mode AFM employing type I MAC levers under ambient conditions. The type I MAC levers are silicon cantilevers with a length of 90 µm and a typical tip radius of less than 10 nm, having a resonance frequency of 75 kHz and a force constant of 3 N/m (NanoAndMore GmbH, Wetzlar, Germany). Appropriate imaging conditions were a scan size of 4.9 × 4.9 μm^2, a scan rate of 0.5–1 lines/s, and an image size of 256 × 256 pixels. In order to minimize interaction between tip and sample, the set point was chosen close to the upper limit. All experiments were performed at room temperature (20–24 °C).

For real time observations of wax recrystallization by AFM, a 10 µL droplet of wax molecules dissolved in chloroform was applied onto the central part of both the Au(111) and a HOPG surface. The total area of wax crystallization was about 20 mm^2 for both substrates. The chloroform took ca. 30 seconds to evaporate from the surface leaving the wax molecules on the substrate. The substrates were then fixed to the AFM stainless steel base plate, and the first image acquisition started as soon as possible after the chloroform evaporation, typically after 8–10 minutes. AFM images were taken consecutively from the same substrate area over a period of several hours applying a constant scan rate (as denoted in the respective figure captions). Height and length measurements of the resultant wax crystals were made with the program WSxM (Version 3.0; Nanotec Electronica, Madrid, Spain).

Supporting Information

Supporting Information File 1

Natural nonacosan-10-ol wax crystallization on Au(111) surface.
[http://www.beilstein-journals.org/bjnano/content/supplementary/2190-4286-2-30-S1.avi]

Supporting Information File 2

Parallel orientation of 3-dimensional structures of octacosan-1-ol on HOPG by recrystallization from chloroform solution.
[http://www.beilstein-journals.org/bjnano/content/supplementary/2190-4286-2-30-S2.jpg]

Acknowledgements

The authors are grateful for financial support of their work by the German Science Foundation (Deutsche Forschungsgemeinschaft, DFG) and the German Ministry for Education and Research (BMBF).

References

1. Dommisse, A. Self-assembly and pattern formation of epicuticular waxes on plant surfaces. Ph.D. Thesis, University Bonn, 2007.
2. Jetter, R.; Riederer, M. *Planta* **1994,** *195,* 257–270. doi:10.1007/BF00199686
3. Matas, A. J.; Sanz, M. J.; Heredia, A. *Int. J. Biol. Macromol.* **2003,** *33,* 31–35. doi:10.1016/S0141-8130(03)00061-8
4. Niemietz, A.; Wandelt, K.; Barthlott, W.; Koch, K. *Prog. Org. Coat.* **2009,** *66,* 221–227. doi:10.1016/j.porgcoat.2009.07.009
5. Koch, K.; Bhushan, B.; Barthlott, W. *Prog. Mater. Sci.* **2009,** *54,* 137–178. doi:10.1016/j.pmatsci.2008.07.003
6. Koch, K.; Dommisse, A.; Niemietz, A.; Barthlott, W.; Wandelt, K. *Surf. Sci.* **2009,** *603,* 1961–1968. doi:10.1016/j.susc.2009.03.019

7. Barthlott, W.; Neinhuis, C.; Cutler, D.; Ditsch, F.; Meusel, I.; Theisen, I.; Wilhelmi, H. *Bot. J. Linn. Soc.* **1998,** *126,* 237–260. doi:10.1111/j.1095-8339.1998.tb02529.x
8. Koch, K.; Dommisse, A.; Barthlott, W. *Cryst. Growth Des.* **2006,** *6,* 2571–2578. doi:10.1021/cg060035w
9. Koch, K.; Bhushan, B.; Barthlott, W. Multifunctional Plant Surfaces and Smart Materials. In *Springer Handbook of Nanotechnology,* 3rd ed.; Bhushan, B., Ed.; Springer: Heidelberg, Dordrecht, London, 2010; pp 1399–1436. doi:10.1007/978-3-642-02525-9
10. Ensikat, H. J.; Boese, M.; Mader, W.; Barthlott, W.; Koch, K. *Chem. Phys. Lipids* **2006,** *144,* 45–59. doi:10.1016/j.chemphyslip.2006.06.016
11. Malkin, T. *Progr. Chem. Fats Other Lipids* **1952,** *1,* 1–6. doi:10.1016/0079-6832(52)90003-7
12. Cousty, J.; Marchenko, A. *Surf. Sci.* **2002,** *520,* 128–136. doi:10.1016/S0039-6028(02)02305-1
13. Marchenko, A.; Cousty, J. *Wear* **2003,** *254,* 941–944. doi:10.1016/S0043-1648(03)00296-5
14. Heinz, B.; Morgner, H. *Surf. Sci.* **1997,** *372,* 100–116. doi:10.1016/S0039-6028(96)01131-4
15. Balzer, F.; Gerlach, R.; Polanski, G.; Rubahn, H. G. *Chem. Phys. Lett.* **1997,** *274,* 145–151. doi:10.1016/S0009-2614(97)00666-0
16. Jin, Q.; Rodriguez, J. A.; Li, C. Z.; Darici, Y.; Tao, N. J. *Surf. Sci.* **1999,** *425,* 101–111. doi:10.1016/S0039-6028(99)00195-8
17. Suto, K.; Yoshimoto, S.; Itaya, K. *J. Nanosci. Nanotechnol.* **2009,** *9,* 288–294. doi:10.1166/jnn.2009.J074
18. Resta, A.; Felici, R.; Kumar, M.; Pedio, M. *J. Non-Cryst. Solids* **2010,** *356,* 1951–1954. doi:10.1016/j.jnoncrysol.2010.05.051
19. Mayer, D.; Dretschkow, T.; Ataka, K.; Wandlowski, T. *J. Electroanal. Chem.* **2002,** *524-525,* 20–35. doi:10.1016/S0022-0728(01)00754-9
20. Böhringer, M.; Morgenstern, K.; Schneider, W.; Wühn, M.; Wöll, C.; Berndt, R. *Surf. Sci.* **2000,** *444,* 199–210. doi:10.1016/S0039-6028(99)01039-0
21. Ivanova, V.; Buess-Hermann, C. *J. Electroanal. Chem.* **2003,** *552,* 45–51. doi:10.1016/S0022-0728(03)00211-0
22. Zhu, N.; Osada, T.; Komeda, T. *Surf. Sci.* **2007,** *601,* 1789–1794. doi:10.1016/j.susc.2007.02.003
23. Lee, Y.; Chang, C.; Yau, S.; Fan, L.; Yang, Y.; Yang, L.; Itaya, K. *J. Am. Chem. Soc.* **2009,** *131,* 6468–6474. doi:10.1021/ja809263y
24. Watel, G.; Thibaudau, F.; Cousty, J. *Surf. Sci.* **1993,** *281,* L297–L302. doi:10.1016/0039-6028(93)90843-9
25. Dorset, D. L. *Acta Crystallogr., Sect. B* **1995,** *51,* 1021–1028. doi:10.1107/S0108768195005465
26. Dorset, D. L.; Pangborn, W. A.; Hancock, A. J. *J. Biochem. Biophys. Methods* **1983,** *8,* 29–40. doi:10.1016/0165-022X(83)90018-0
27. Koch, K.; Barthlott, W.; Hommes, A.; Wandelt, K.; Mamdouh, W.; De-Feyter, S.; Broekmann, P. *Planta* **2005,** *223,* 258–270. doi:10.1007/s00425-005-0081-3
28. Sarraf, H.; Skarpova, L.; Louda, P. *Arch. Mater. Sci. Eng.* **2007,** *28,* 489–494.
29. Kusunoki, K.; Sakata, I.; Miyamura, K. *Anal. Sci.* **2001,** *17,* i1267–i1268.
30. Sanfelix, P. C.; Holloway, S.; Kolasinski, K. W.; Darling, G. R. *Surf. Sci.* **2003,** *532-535,* 166–172. doi:10.1016/S0039-6028(03)00161-4
31. Papadantonakis, K. M.; Brunschwig, B. S.; Lewis, N. S. *Langmuir* **2008,** *24,* 857–861. doi:10.1021/la702585e
32. Koch, R. *J. Phys.: Condens. Matter* **1994,** *6,* 9519–9550. doi:10.1088/0953-8984/6/45/005
33. Huang, M.; Boone, C.; Roberts, M.; Savage, D. E.; Lagally, M. G.; Shaji, N.; Qin, H.; Blick, R.; Nairn, J. A.; Liu, F. *Adv. Mater.* **2005,** *17,* 2860–2864. doi:10.1002/adma.200501353
34. Zang, J.; Huang, M.; Liu, F. *Phys. Rev. Lett.* **2007,** *98,* 146102. doi:10.1103/PhysRevLett.98.146102
35. Hommes, A. Untersuchungen zum Adsorptionsverhalten molekularer Filme epikutikularer Wachse auf artifiziellen Oberflächen. Ph.D. Thesis, University Bonn, 2010.

License and Terms

Beilstein Journal of Nanotechnology

Determination of object position, vortex shedding frequency and flow velocity using artificial lateral line canals

Adrian Klein* and Horst Bleckmann

Full Research Paper

Open Access

Address:
Institute for Zoology, University of Bonn, Poppelsdorfer Schloss, 53115 Bonn, Germany

Email:
Adrian Klein* - adrian@uni-bonn.de

* Corresponding author

Keywords:
artificial lateral line; biomimetics; flow sensor; mechanoreception; optical sensor

Beilstein J. Nanotechnol. **2011,** *2,* 276–283.
doi:10.3762/bjnano.2.32

Received: 27 January 2011
Accepted: 13 May 2011
Published: 06 June 2011

This article is part of the Thematic Series "Biomimetic materials".

Guest Editors: W. Barthlott and K. Koch

Abstract

The lateral line system of fish consists of superficial neuromasts, and neuromasts embedded in lateral line canals. Lateral line neuromasts allow fish to sense both minute water motions and pressure gradients, thereby enabling them to detect predators and prey or to recognize and discriminate stationary objects while passing them. With the aid of the lateral line, fish can also sense vortices caused by an upstream object or by undulatory swimming movements of fish. We show here that artificial lateral line canals equipped with optical flow sensors can be used to detect the water motions generated by a stationary vibrating sphere, the vortices caused by an upstream cylinder or the water (air) movements caused by a passing object. The hydrodynamic information retrieved from optical flow sensors can be used to calculate bulk flow velocity and thus the size of the cylinder that shed the vortices. Even a bilateral sensor platform equipped with only one artificial lateral line canal on each side is sufficient to determine the position of an upstream cylinder.

Introduction

Nature has invented a stunning diversity of sensory systems whose small size and high sensitivity is so far unmatched by man-made devices. Flow sensors based on hairs are located on the skin and are found in crustaceans [1], as well as in spiders and insects [2]. These sensors enable insects and spiders to perceive air displacements down to flow amplitudes of 30 µm/s [3]. Flow sensors are also found in fish and aquatic amphibians and are called lateral line neuromasts. With neuromasts some fish can detect water surface waves with a displacement amplitude of only 0.01 µm [4]. Most lateral line neuromasts are located on the skin (superficial neuromasts or SN), but some are located in subepidermal canals (canal neuromasts or CN).

A lateral line neuromast consists of up to several hundred or even thousand mechanosensitive hair cells, enveloped in a gelatinous cupula. Lateral line hair cells are morphologically

polarized, i.e., they have a bundle of stereovilli at their apical surface that grows longer from one edge to the other. Within the sensory epithelium of a neuromast, lateral line hair cells are oriented into two opposing directions that define the most sensitive axis of the neuromast [5]. Although the design of the lateral line can be quite different in different fish species [6], most fish have several hundred (sometimes up to several thousand) SNs distributed over their head, body and tail fin [7].

Fish use their lateral line for prey detection, predator avoidance, schooling, intraspecific communication, rheotaxis and station holding [8,9]. In addition, with the lateral line system fish can form a spatio-temporal image of nearby objects based on their hydrodynamic signature [10].

Lateral line afferents not only respond to the sinusoidal water motions generated by a vibrating sphere [11,12] but also to more natural stimuli, such as single vortices [13] or vortex streets caused by a cylinder exposed to running water [14]. The direction of water motions inside a vortex as well as the vortex shedding frequency of a cylinder can be determined from the responses of primary lateral line afferents [13,14]. Lateral line nerve fibers also alter their discharge rate if an object passes the fish laterally. In this case the discharge pattern reflects both the position (including distance) of the object and the direction of object motion [15].

The sensory hairs of crustaceans, insects and spiders and the lateral line system of fish have inspired engineers to develop artificial air [16] and water flow sensors [17-19] based on microelectromechanical system (MEMS) technology. With individual sensors, mimicking SN or sensory hair function, the air or water motions caused by a vibrating sphere can be detected [16], and, if arrays of multiple sensors are used, a vibrating sphere can even be localized [17].

Nature alters the response properties of biological flow sensors by altering their shape and size [20]. In case of the lateral line, the canals also determine the response properties of the flow sensors. In general, lateral line canals shield CNs from DC flow [12]. In most fish species the course of the lateral line canals is clearly visible to the naked eye since lateral line canals open to the environment through a series of pores. In teleosts, CNs are located halfway between neighbouring canal pores. Drag forces, resulting from fluid motions induced inside the canal by pressure fluctuation outside of the canal, stimulate CNs. In general, CNs respond (up to a frequency of about 150 Hz) roughly in proportion to the pressure gradient between neighbouring pores and thus to the external water acceleration [21]. SNs respond (up to about 80 Hz) roughly in proportion to the water velocity [22].

There have been several attempts to design an engineering equivalent to the sensory hairs of insects and spiders [16,23] and to the superficial neuromast system of fish. However, an engineering equivalent of the fish lateral line canal system did not previously exist, and therefore we have built artificial lateral line canals (ALLCs) and equipped them with artificial neuromasts (ANs). Unlike the artificial neuromasts built by other researchers, our neuromasts use optical signals to measure water or air motions. With these optical flow sensors we measured water (air) motions inside artificial canals and thus we were able to quantify outside pressure gradients. The performance of the ALLCs was assessed by exposing them, not only to the pressure gradients caused by a stationary vibrating sphere, but also to the vortical flows caused by a cylinder placed upstream in running water. We show that ALLCs can even be used to determine the position and size of an upstream cylinder and to detect and localize a moving object.

Results

Experiment I

In experiment I we investigated whether ALLCs can be used to detect object movements in air. To stimulate the ALLC, a human finger was moved alongside the ALLC at a distance of about 2 cm. The finger movement caused responses that had a 'Mexican hat shape', i.e., a decrease in voltage amplitude was followed by an increase and another decrease (Figure 1). If the direction of finger movement was reversed, the shape of the response also reversed. A canal with only two neuromasts was sufficient to determine the velocity of finger movement. If the finger first passed AN one (AN_A), the response of AN two (AN_B) was delayed with respect to the response of AN_A. Thus artificial lateral lines (ALLs) equipped with only two neuromasts can not only be used to detect moving objects but can also determine object velocity and roughly the direction of object motion.

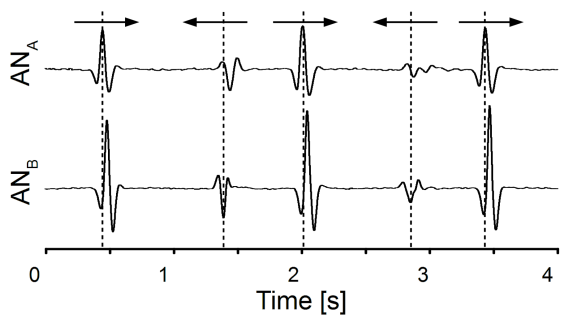

Figure 1: Responses of sensor platform I to a human finger that moved alongside the ALLC with a velocity of about 20 cm/s. Arrows indicate direction of finger motion. Responses of AN_A (upper graph) and AN_B (lower graph) are shown. Note that the responses were inverted if the direction of finger motion was reversed.

Experiment II

To examine the performance of ALLCs in water, a vibrating sphere (diameter 1 cm, p–p displacement amplitude 237 µm, vibration frequency 50 Hz, duration of vibration 200 ms) was placed adjacent to the ALLC. Within the range of distances tested (1 to 4 cm), the frequency of the voltage output of the AN equalled the frequency of sphere vibration (Figure 2). As expected [22], the output voltage of the AN decreased approximately with the third power of the sphere distance (see inset Figure 2). With respect to sphere movement, the voltage output of the AN was phase shifted by 90°.

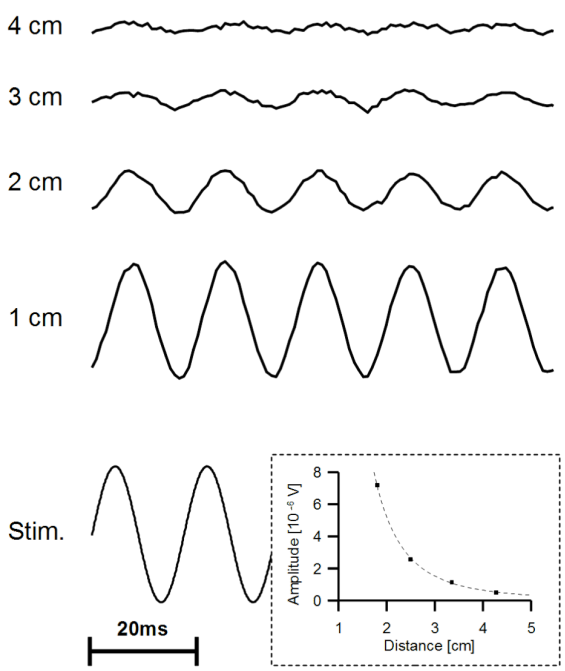

Figure 2: A typical AN response to a dipole flow field. The sinusoidal voltage used to drive the mini-shaker (bottom left) and the voltage output of the AN exposed to the vibrating sphere (top 4 traces) is shown. Distances between the ALLC and the vibrating sphere were 1, 2, 3 and 4 cm. The voltage output of the AN is plotted on the same scale. Inset: Voltage output of the AN as a function of sphere to pore distance. The fitting function (dashed line) is $f(x) = 42.66\ x^{-3.03}$. This indicates a third order decrease of sensor output with increasing sphere distance.

Experiment IIIa

This experiment tested whether ALLCs can be used to detect an upstream cylinder exposed to running water. ANs responded to such a cylinder with an oscillating voltage output (Figure 3A). The Fourier spectra of these oscillations had a peak frequency (Figure 3B) close to the calculated (see material and methods) vortex shedding frequency (VSF) of the cylinder. When the diameter of the cylinder was altered, this oscillation peak shifted in the predicted (Equation 1) direction, i.e., with increasing cylinder diameter the VSF decreased (Figure 3C).

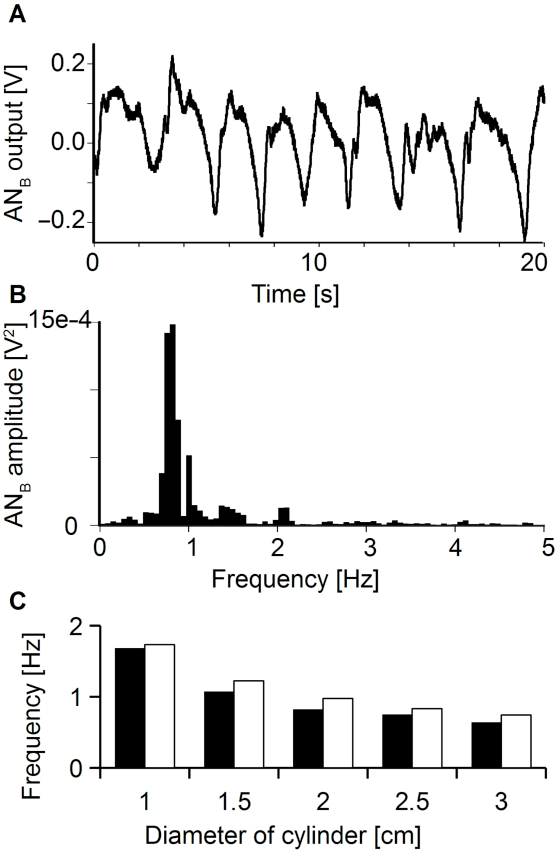

Figure 3: The response of an artificial CN exposed to the vortices shed from a stationary cylinder (diameter 2 cm) (A) and frequency spectrum of the response (B). Peak frequency (0.82 Hz) was similar to the calculated vortex shedding frequency (0.98 Hz). (C) Measured (black bars) and calculated (white bars) vortex shedding frequencies for cylinders of different diameters.

Experiment IIIb

In this experiment we tested whether ALLs can also be used to localize an upstream cylinder. When the distance between the ALLC and the cylinder was increased, the voltage output of the AN decreased, but the upstream cylinder could still be detected from a distance of 20 cm. When the cylinder was moved perpendicular to the direction of bulk water flow, the responses recorded from the ipsilateral ALLC were larger than the responses recorded from the contralateral ALLC (cf. Figure 4). In general, moving the cylinder to the left or right systematically changed the responses of the two ALLCs (Figure 4). Thus by comparing the voltage output of the two ALLCs (Figure 5) we could approximately determine the lateral position of the cylinder.

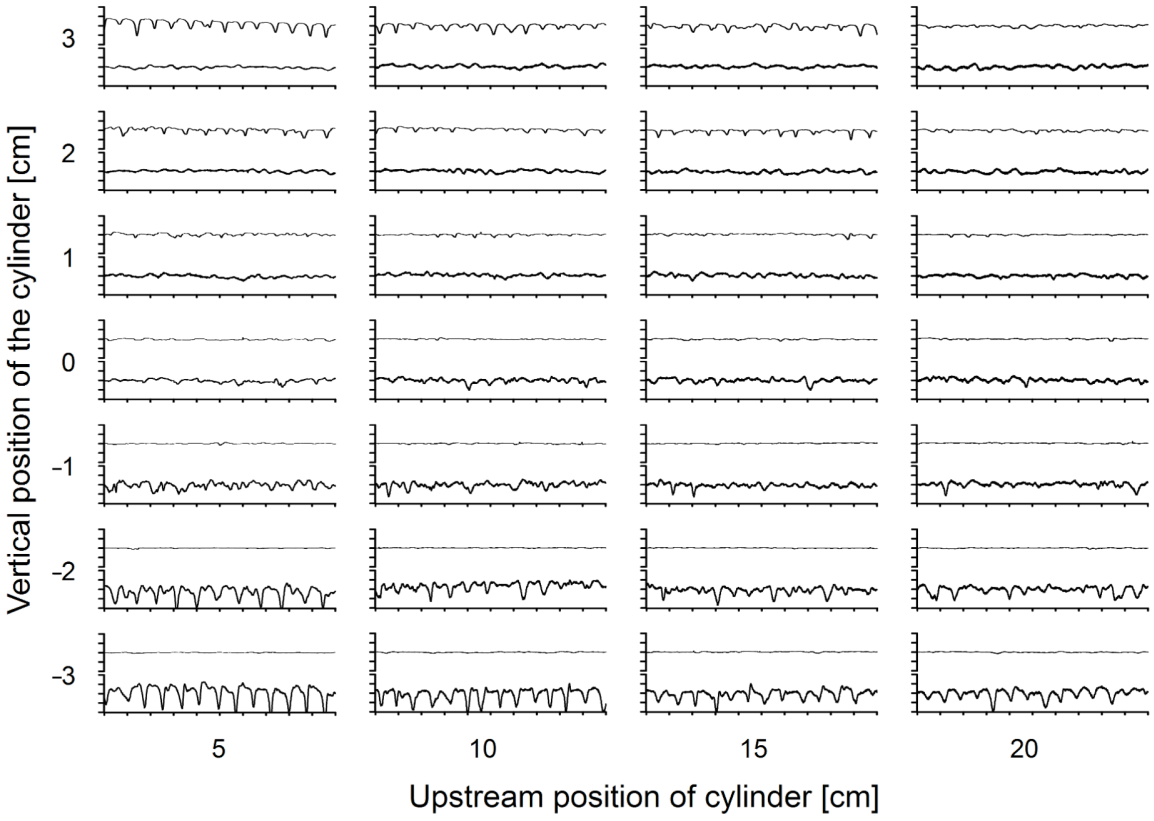

Figure 4: Responses of AN_A (upper line in each graph) and AN_B (lower line in each graph) (for AN_A and AN_B see Figure 6A) to the vortices caused by a cylinder (diameter 2 cm) placed at various positions upstream to the ALL. Note that response amplitudes decreased with increasing distance of the cylinder and that the responses were more pronounced for the AN that was ipsilateral to the cylinder.

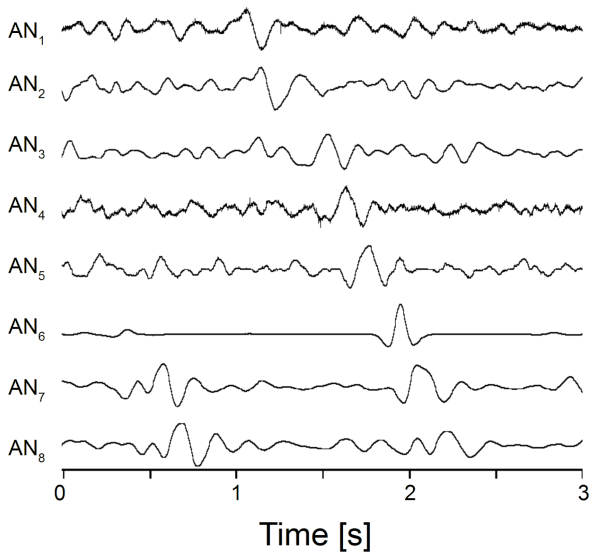

Figure 5: Responses of AN_1 to AN_8 (cf. Figure 6B) to bulk water flow. Note that the most prominent peak visible in the response of AN_1 is systematically delayed from AN_1 to AN_8. The curves are not to scale due to the manual fabrication of each AN.

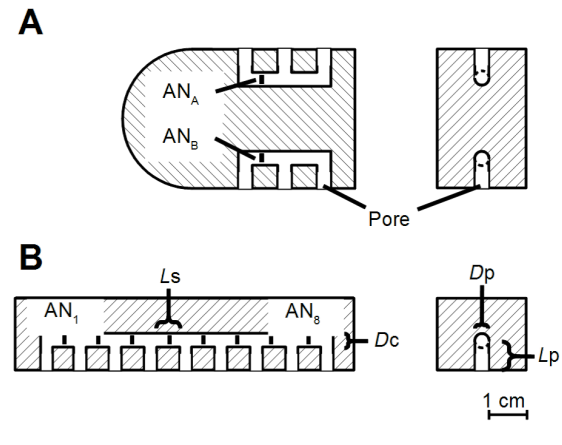

Figure 6: Horizontal (left) and vertical (right) cross sections of platforms III (A) and IV (B) that were used for the present study. Black squares indicate the positions of the ANs inside artificial lateral line canals. Platform III housed two and platform IV housed eight ANs. The length of pores (*L*p) was 1 cm, the inter pore distance (*L*s) was 1 cm and the diameter of the canal (*D*c) as well as the pore diameter (*D*p) was 3 mm in both devices.

Determination of bulk flow velocity

To determine bulk flow velocity, the responses of all eight ANs of sensor platform IV (cf. Figure 6B) were compared. If the ALLC of sensor platform IV was exposed to running water, the responses of all ANs showed characteristic peaks (e.g., Figure 7). Any particular distinctive part of the voltage output (e.g., a peak) was first generated by the specific AN that was located at the most upstream position. In ANs located more downstream, this part occurred with delays that were proportional to the downstream distance of the respective neuromast. We calculated bulk flow velocity by cross correlating the output data of neighbouring ANs (see also [24]) and dividing the pore distance by the correlation delay. Mean bulk flow velocity was determined using the calculated bulk flow velocities obtained from 7 adjacent neuromast pairs.

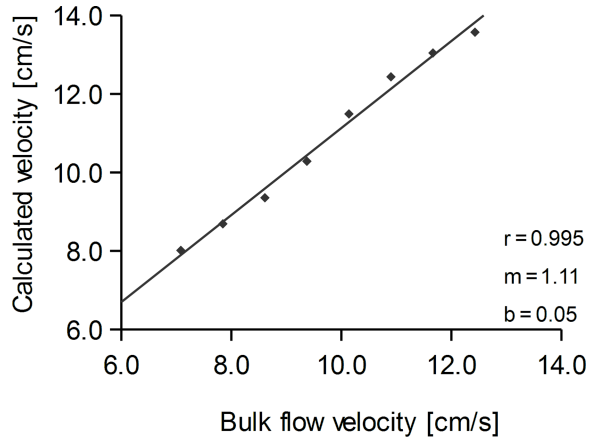

Figure 7: Velocity calculated with data obtained from AN_1 to AN_8 as function of bulk flow velocity. Note that the fitting curve intersects close to the origin (b = 0.05). Its slope (m) is larger than 1. This could be due to vibrations or a crosstalk between adjacent ANs.

Discussion

There have only been a few attempts to design an engineering equivalent to the sensory hairs of insects and spiders [16,23]. These sensors were used for air flow sensing and for aerial acoustic perception [16,18]. Researchers also have built artificial lateral line neuromasts. Campenhausen et al. [19] built an artificial SN that consisted of a needle that connected a plastic blade (the artificial cupula) with a piece of paper that partly intercepted a light beam. In standing water, this system was able to sense vertically oriented metal bars while passing. Yung et al. [25] built a monolithically integrated array of microfabricated hot wire anemometers. The hot wires had a length of 400 µm, an elevation of 600 µm and a spacing of 1 mm. This matches the dimensions of many fish lateral lines. The anemometer system exhibited a sensitivity of about 200 µm/s flow velocity, a bandwidth of about 1 kHz, and, due to its small dimensions, a reduced interference with the flow field and with the neighbouring anemometers. Unfortunately, hot wire anemometers cannot discern flow direction. As a result, they only provide a rectified reading of oscillatory flow fields. Nevertheless, arrays of hot wire anemometers were successfully used to determine the location of a moving dipole source up to a distance equalling the length of the sensor array, to access the signature of a wake caused by an upstream object and to determine the general direction to the location of that object [25]. Recently, Yan et al. [17] built an ALL that consisted of superficial microfabricated ANs wrapped around a cylinder. Each of the 15 ANs consisted of a horizontal cantilever with a vertical hair (length 500 µm) attached at the distal end. At the fixed end of the cantilever was a piezoresistor. Flow that impinged upon the vertical hair created a bending torque that acted on the cantilever to induce stress concentration at the site of the piezoresistor. The induced change of resistance was converted to a voltage and thus could be used to infer the local flow velocity. Unlike sensors based on hot-wire anemometry, these sensors were directional like lateral line neuromasts, i.e., along their dominant axis they responded to water flow in both directions with equal sensitivity but with opposite polarity. The detection limit for water flow was 100 µm/s, a value comparable to the fluid velocity detection thresholds of SNs (38 to 60 µm/s [26,27]).

Some researchers [28-30] have also studied the filter properties of ALLCs. To do so they measured optically particle displacements inside ALLCs in relation to particle displacements in the outside medium. According to these studies, particle displacements inside ALLCs are related linearly to those in the medium. Below 80 Hz, the ratio of particle displacement inside the canal to particle displacement in the medium roughly followed the velocity in the medium. Water displacements in the ALLC were proportional to the component of the external velocity parallel to the canal. If a cylinder is placed near to an ALLC, an externally exposed flow induces complicated flow patterns inside the canal that depended on the position of the cylinder relative to the ALLC [30]. There was little mechanical coupling between neighbouring parts of the canal.

The present study is the first to measure the performance of ALLCs equipped with optical ANs. This has enabled us to illustrate the potential of optical ANs and of biomimetic ALLCs. In general, ALLCs can be used to measure and quantify air and water motions, but due to the different Reynolds numbers, larger flow speeds are needed in air compared to water to obtain a signal. In comparison with a pure SN-system, a canal system has several advantages: 1) Sensors situated in canals are not

exposed to the external environment, thus they cause minimal interference to the external flow field; 2) the sensors are protected from the external environment and thus are less prone to physical damage; 3) the sensitivity, frequency response and dynamic amplitude range of ALLCs can easily be altered by changing canal morphology (e.g., the number, size and placement of canal pores, canal diameter, and canal compartmentalization) [31] and 4) by building artificial canals that have tubuli [6], the mechanical filter properties of ALLCs can be further altered in a predictable manner [32].

With the aid of ALLCs equipped with optical flow sensors, we were able to detect sinusoidal water motions. The responses were phase shifted by about 90°, i.e., as expected [22] the ALLC acted as a differentiator. According to the flow field equations [21], at a distance of 4 cm from a vibrating sphere (1 cm diameter, 50 Hz, 237 µm p–p sphere displacement) the tangential flow amplitude is about 4 µm/s (about 12.7 nm displacement). Thus a sinusoidal signal with this amplitude could be detected with our ALLCs. Besides a stationary vibrating sphere, the ALLCs responded to linear object motions and to the vortices shed by a cylinder. A stationary sensor platform equipped with two ALLCs (one on each side) was sufficient to determine the approximate upstream position of a cylinder. And a canal equipped with at least two ANs could determine bulk flow velocity. If the variables bulk flow velocity and vortex-shedding frequency are known, then the size of the cylinder can also be calculated (cf. Equation 2).

According to a recent study an artificial cupula made out of hydrogel can improve the performance of artificial sensory hairs (ANs) by about two orders of magnitude. Minimal thresholds were as low as 2.5 µm/s [33]. Thus, one should be able to increase further the sensitivity of ALLCs by attaching artificial cupulae to the artificial CNs.

Overall, our study shows that ALLCs equipped with optical flow sensors are effective for the detection and quantification of aerial or aquatic stimuli. ALLCs could potentially provide unprecedented sensing and control functions to underwater vehicles and platforms. If so they may be useful for guiding autonomous vehicles (in both air and water), tracking and identifying wake generators and for the measurement of air and water movements in pipes and canals. To improve the performance of ALLCs, one important step will be to reduce the size of the optical ANs using MEMS technology. This is currently being done in cooperation with the center for advanced studies (caesar) in Bonn. Smaller sensors will allow us to build smaller canal systems and thus to miniaturize the sensor platforms. Finally, the development of ALLs will facilitate fundamental studies on the fish lateral line.

Experimental

Sensor platforms

Half canals were milled inside opaque PVC plates. Two mirror inverted PVC plates were screwed together thereby forming a sensor platform that contained ALLCs. Four sensor platforms were built. Type I had a single linear canal that consisted of 3 segments and 4 canal pores (length Ls = 12.5 mm, pore length Lp = 5 mm, canal diameter Dc = 4 mm, pore diameter Dp = 4 mm, for definitions see Figure 6). Type II had a single linear canal that consisted of only one segment (Ls = 30 mm, Lp = 10 mm, Dp = 4 mm, Dc = 4 mm) with 2 canal pores. Type III had two linear canals (one on each side; cf. Figure 1A), each of which consisted of 2 segments and 3 pores (Lc = 10 mm, Lp = 5 mm, Dc = 3 mm, Dp = 3 mm) and type IV had one linear canal that consisted of 8 segments and 9 canal pores (Lc = 10 mm, Lp = 5 mm, Dc = 3 mm, Dp = 3 mm; cf. Figure 1B).

Artificial canal neuromasts

ALLCs were equipped with artificial canal neuromasts (artificial CNs). To build artificial CNs, transparent silicone bars (Wacker Silicones, Elastosil RT 60) were fabricated (length < Dc, width 0.4–1.0 mm) and installed inside each ALLC segment (cf. Figure 8). The density of the silicone bars was comparable to the density of water to ensure that only the motion of the fluid affected the bending of the bar. For the detection of canal fluid motion, one end of each silicone bar was illuminated with an infrared light emitting diode (LED, SFH420). Light, leaving the opposite end of the silicone bar, illuminated an optical fiber that was connected to a SMD phototransistor (PT15) (cf. Figure 8) and the output was amplified (transistor BC547). A potentiometer (100 kΩ) was placed between the emitter of the transistor and earth. The transistor output was fed into an AD converter (Power 1401, sampling rate 1 kHz) and stored on a computer (Optiplex 745, Dell). Pressure gradients between canal pores caused water (or air) flow inside the ALLCs that in turn deflected the silicone bars. In the absence of a stimulus, the silicone bars were not perfectly vertically oriented (0°) but instead were slightly deflected to one side (at about 10°, cf. Figure 8). The degree of deflection

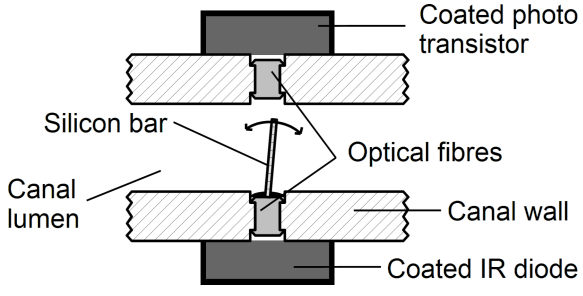

Figure 8: Scheme of an artificial CN. The drawing is not to scale.

modulated, i.e., increased (flow in one direction) or reduced (flow in the opposite direction), the amount of light that reached the SMD phototransistor. Thus, the artificial CNs were directionally sensitive.

Test of sensor performance

To test the performance of the sensor platforms, four experiments were performed:

Experiment I

Sensor platform I (not shown) was used. A human finger moving in air alongside the platform (the ALLC) served as a stimulus source.

Experiment II

Hydrodynamic stimuli were generated with a vibrating sphere (diameter 1 cm, 50 Hz, 237 μm peak to peak displacement) that was attached to a stainless steel rod (length 10 cm, diameter 1.6 mm). The rod was mounted on a mini-shaker (Ling Dynamic System LTD, model V 101) that rested on a sliding bar assembly allowing for manual adjustment of the sphere distance to the type II sensor platform (also not shown). The sphere was positioned at the height of the ALLC midway between two canal pores. The distance between the surface of the sphere and the sensor platform was 1, 2, 3 or 4 cm. The vibration direction of the sphere was parallel to the long axis of the ALLC.

Experiment III

The sensor platform was submerged in a flow tank that had a cross section of 10 × 15 cm^2 and a water depth of 12 cm. It contained a flow collimator upstream of the working section holding the sensor platform. Flow (7.9 cm/s) was produced by a propeller (Schottelantrieb Aeronaut 100) coupled to a d.c. motor (Conrad Electronic) that was driven by a power supply (Voltcraft DIGI 35, Conrad Electronic). The propeller was suspended from a holder on the side of the tank opposite to the section that housed the sensor platform. For experiment III sensor platform III (cf. Figure 6B) was used.

Experiment IIIa

The sensor platform was positioned horizontally in the middle of the working section of the flow tank. In this way both canals of the platform were exposed to bulk water flow. To generate vortices, a half-cylinder (diameter 1.5 cm, hereafter referred to as the cylinder; Reynolds number 1200) was placed vertically in the working section of the flow tank. The distance between the cylinder and the upstream edge of the sensor platform was 5, 10, 15 or 20 cm. The lateral distance of the cylinder with respect to the midline of the sensor platform was −3, −2, −1, 0, +1, +2 or +3 cm.

Experiment IIIb

One side of sensor platform III was attached to the wall of the flow tank, i.e., only one canal was exposed to bulk water flow. Cylinders with a diameter of 1, 2 or 3 cm were placed 10 cm upstream from the sensor platform. The lateral distance between the cylinders and the midline of the sensor platform was 2.5 cm.

Experiment IV

Sensor platform IV was used (cf. Figure 6B). A cylinder (diameter 2 cm) was placed 10 cm upstream from the sensor platform. The in-plane curved head (radius 1.5 cm) of the platform served to minimize any fluctuations that may have been caused by the upstream edge of the sensor platform. Bulk flow velocity was varied between 3.3 and 12.4 cm/s.

The generation of defined vortex streets

Over a certain range of Reynolds numbers (typically above 140), a cylinder placed in running water will generate a Kármán vortex street. The frequency of vortex detachment (f) is a function of the Strouhal number S_t (a dimensionless index), the diameter d of the cylinder and the actual flow velocity (v) [34]:

$$f = S_t \cdot v / d \quad (1)$$

The Strouhal number for the cylinder depends on the Reynolds number; however, it remains at an almost constant value of 0.2 for Re > 2000 [33]. To account for flow constrictions near the cylinder due to blocking effects, the VSF was calculated using the actual flow velocity (v) in the region of the cylinder, according to a method typically used for vortex flow meters [35,36]:

$$v = U \cdot W / (W - d) \quad (2)$$

where (U) is the nominal flow velocity (7.9 $cm \cdot s^{-1}$ in our experiments) and W the width of the flow tank (10 cm). For the experiments a Reynolds number between 800 and 2400, based on the diameter of the cylinder, was chosen.

Bulk flow velocity was measured with particle image velocimetry (experiment 1, 2, and 3, cf. [37]) or with an impeller (P670).

Acknowledgements

This paper is dedicated to the memory of Joseph Humphrey, a brilliant scientist, friend and exceptional human being. We thank V. Schlüssel for editorial assistance and J. Mogdans for carefully reading and commenting on the MS. The authors gratefully acknowledge the financial support provided by the DFG and by the DARPA BioSenSE AFOSR Grant #FA9550-05-0459.

References

1. Bender, M.; Gnatzy, W.; Tautz, J. *J. Comp. Physiol., A* **1984,** *154,* 45–47. doi:10.1007/BF00605388
2. Humphrey, J.; Barth, F. Medium Flow-Sensing Hairs: Biomechanics and Models. In *Advances in Insect Physiology;* Casas, J.; Simpson, S. J., Eds.; Academic Press: New York, 2007; Vol. 34, pp 1–80.
3. Shimozawa, T.; Murakami, J.; Kumagai, T. Cricket wind receptors: thermal noise for the highest sensitivity known. In *Sensors and Sensing in Biology and Engineering;* Barth, F.; Humphrey, J.; Secomb, T., Eds.; Springer, 2003; pp 145–158.
4. Bleckmann, H. *J. Comp. Physiol., A* **1980,** *140,* 163–172. doi:10.1007/BF00606308
5. Flock, Å.; Wersäll, J. *J. Cell Biol.* **1962,** *15,* 19–27. doi:10.1083/jcb.15.1.19
6. Coombs, S.; Janssen, J.; Webb, J. In *Sensory Biology of Aquatic Animals,* 1st ed.; Atema, J.; Fay, R.; Popper, A.; Tavolga, W., Eds.; Springer-Verlag: New York, 1988; pp 83–130.
7. Schmitz, A.; Bleckmann, H.; Mogdans, J. *J. Morphol.* **2008,** *269,* 751–761. doi:10.1002/jmor.10621
8. Bleckmann, H. Reception of hydrodynamic stimuli in aquatic and semiaquatic animals. In *Progress in Zoology;* Rathmayer, W., Ed.; Gustav Fischer-Verlag: Stuttgart, Jena, New York, 1994; Vol. 41, pp 1–115.
9. Faucher, K.; Aubert, A.; Lagardere, J.-P. *Brain Behav. Evol.* **2003,** *62,* 223–232. doi:10.1159/000073274
10. Windsor, S. P.; Tan, D.; Montgomery, J. C. *J. Exp. Biol.* **2008,** *211,* 2950–2959. doi:10.1242/jeb.020453
11. Coombs, S.; Hastings, M.; Finneran, J. *J. Comp. Physiol., A* **1996,** *178,* 359–371. doi:10.1007/BF00193974
12. Engelmann, J.; Hanke, W.; Bleckmann, H. *J. Comp. Physiol., A* **2002,** *188,* 513–526. doi:10.1007/s00359-002-0326-6
13. Chagnaud, B. P.; Bleckmann, H.; Engelmann, J. *J. Exp. Biol.* **2006,** *209,* 327–342. doi:10.1242/jeb.01982
14. Chagnaud, B. P.; Bleckmann, H.; Hofmann, M. H. *J. Comp. Physiol., A* **2007,** *193,* 753–763. doi:10.1007/s00359-007-0230-1
15. Mogdans, J.; Bleckmann, H. *J. Comp. Physiol., A* **1998,** *182,* 659–676. doi:10.1007/s003590050211
16. Krijnen, G. J. M.; Dijkstra, M.; van Baar, J. J.; Shankar, S. S.; Kuipers, W. J.; de Boer, R. J. H.; Altpeter, D.; Lammerink, T. S. J.; Wiegerink, R. *Nanotechnology* **2006,** *17,* S84. doi:10.1088/0957-4484/17/4/013
17. Yang, Y.; Nguyen, N.; Chen, N.; Lockwood, M.; Tucker, C.; Hu, H.; Bleckmann, H.; Liu, C.; Jones, D. L. *Bioinspir. Biomim.* **2010,** *5,* 016001. doi:10.1088/1748-3182/5/1/016001
18. Dagamseh, A. M. K.; Bruinink, C. M.; Droogendijk, H.; Wiegerink, R. J.; Lammerink, T. S. J.; Krijnen, G. J. M. Engineering of Biomimetic Hair-Flow Sensor Arrays Dedicated to High-Resolution Flow Field Measurements. IEEE Sensors 2010 conference, Hawaii, USA, Nov 1–4, 2010; pp 2251–2254.
19. Campenhausen, C.; Riess, I.; Weissert, R. *J. Comp. Physiol., A* **1981,** *143,* 369–374. doi:10.1007/BF00611175
20. McHenry, M. J.; Strother, J. A.; van Netten, S. M. *J. Comp. Physiol., A* **2008,** *194,* 795–810. doi:10.1007/s00359-008-0350-2
21. van Netten, S. M. *Biol. Cybern.* **2006,** *94,* 67–85. doi:10.1007/s00422-005-0032-x
22. Kalmijn, A. In *Sensory Biology of Aquatic Animals,* 1st ed.; Atema, J.; Fay, R. R.; Popper, A. N.; Tavolga, W. N., Eds.; Springer-Verlag: New York, 1988; pp 83–130.
23. Dijkstra, M.; van Baar, J. J.; Wiegerink, R. J.; Lammerink, T. S. J.; de Boer, J. H.; Krijnen, G. J. M. *J. Micromech. Microeng.* **2005,** *15,* S132. doi:10.1088/0960-1317/15/7/019
24. Chagnaud, B. P.; Bleckmann, H.; Hofmann, M. H. *Zoology (Munich, Ger.)* **2008,** *111,* 204–217. doi:10.1016/j.zool.2007.07.009
25. Yang, Y.; Chen, J.; Engel, J.; Pandya, S.; Chen, N.; Tucker, C.; Coombs, S.; Jones, D. L.; Liu, C. *Proc. Natl. Acad. Sci. U. S. A.* **2006,** *103,* 18891–18895. doi:10.1073/pnas.0609274103
26. Oman, C. M.; Frishkopf, L. S. Neural responses of lateral-line organs. *Necturus maadosus to direct mechanical stimulation;* Quart. Progr. Rep., Vol. 108; Research Laboratory of Electronics, M.I.T., 1973; pp 332–338.
27. Kroese, A. B. A.; Zalm, J. M.; Bercken, J. *Pfluegers Arch.* **1978,** *375,* 167–175. doi:10.1007/BF00584240
28. Denton, E. J.; Gray, J. *Proc. R. Soc. London, Ser. B* **1983,** *218,* 1–26. doi:10.1098/rspb.1983.0023
29. Weber, T.; Bleckmann, H.; Münz, H. *Verh. Dtsch. Zool. Ges.* **1991,** 461–462.
30. Barbier, C.; Pillapakkam, S. B.; Humphrey, J. A. C.; Rüter, A.; Otto, B.; Bleckmann, H.; Hanke, W. In *Proceedings of the 5th International Symposium on Turbulence and Shear Flow Phenomena,* TU München, 2007; pp 1017–1022.
31. Denton, E. J.; Gray, J. In *Sensory Biology of Aquatic Animals,* 1st ed.; Atema, J.; Fay, R.; Popper, A.; Tavolga, W., Eds.; Springer: New York, 1988; pp 595–617.
32. Klein, A; Bleckmann, H. unpublished results.
33. McConney, M. E.; Chen, N.; Lu, D.; Hu, H. A.; Coombs, S.; Liu, C.; Tsukruk, V. V. *Soft Matter* **2009,** *5,* 292–295. doi:10.1039/b808839j
34. Vogel, S. *Life in Moving Fluids;* Princeton University Press: Pinceton, N.J., 1994; p 467.
35. Liao, J. C.; Beal, D. N.; Lauder, G. V.; Triantafyllou, M. S. *J. Exp. Biol.* **2003,** *206,* 1059–1073. doi:10.1242/jeb.00209
36. Igarashi, T. *JSME Int. J., Ser. B* **1999,** *42,* 586–595.
37. Przybilla, A.; Kunze, S.; Rudert, A.; Bleckmann, H.; Brücker, C. *J. Exp. Biol.* **2010,** *213,* 2976–2986. doi:10.1242/jeb.041632

License and Terms

Beilstein Journal of Nanotechnology

The effect of surface anisotropy in the slippery zone of *Nepenthes alata* pitchers on beetle attachment

Elena V. Gorb* and Stanislav N. Gorb

Full Research Paper

Open Access

Address:
Department of Functional Morphology and Biomechanics, Zoological Institute, University of Kiel, Am Botanischen Garten 1–9, D-24098 Kiel, Germany

Email:
Elena V. Gorb* - egorb@zoologie.uni-kiel.de; Stanislav N. Gorb - sgorb@zoologie.uni-kiel.de

* Corresponding author

Keywords:
adhesive pads; claws; *Coccinella septempunctata*; insect–plant interactions; traction force

Beilstein J. Nanotechnol. **2011,** *2,* 302–310.
doi:10.3762/bjnano.2.35

Received: 01 April 2011
Accepted: 24 May 2011
Published: 16 June 2011

This article is part of the Thematic Series "Biomimetic materials".

Guest Editors: W. Barthlott and K. Koch

Abstract

The slippery zone in pitchers of the carnivorous plant *Nepenthes alata* bears scattered prominent lunate cells and displays continuous epicuticular crystalline wax coverage. The aim of this study was to examine the influence of the surface anisotropy, caused by the shape of lunate cells, on insect attachment ability. Traction tests with ladybird beetles *Coccinella septempunctata* were performed in two types of experiments, where surface samples of (1) intact pitchers, (2) chemically de-waxed pitchers, and (3) their polymer replicas were placed horizontally. Beetle traction forces were measured when they walked on test surfaces in either an upward (towards the peristome) or downward (towards the pitcher bottom) direction, corresponding to the upright or inverted positions of the pitcher. On intact pitcher surfaces covered with both lunate cells and wax crystals, experiments showed significantly higher forces in the direction towards the pitcher bottom. To distinguish between the contributions, from claw interlocking and pad adhesion, to insect attachment on the pitcher surfaces, intact versus claw-ablated beetles were used in the second type of experiment. On both de-waxed plant samples and their replicas, intact insects generated much higher forces in the downward direction compared to the upward one, whereas clawless insects did not. These results led to the conclusion that, (i) due to the particular shape of lunate cells, the pitcher surface has anisotropic properties in terms of insect attachment, and (ii) claws were mainly responsible for attachment enhancement in the downward pitcher direction, since, in this direction, they could interlock with overhanging edges of lunate cells.

Introduction

Pitcher-shaped trapping organs produced at the tips of tendrils are characteristic for carnivorous plants from the genus *Nepenthes* [1,2]. These traps, using a passive pitfall mechanism for capturing, mainly, invertebrates, consist of several functional zones specialized for prey attraction, capture, retention, digestion, and uptake of nutrients [3-6]. During the

past few decades, different aspects of *Nepenthes* biology, among them the structure and functions of pitchers, especially with respect to their trapping efficiency, have been the focus of numerous structural and experimental studies and field observations (review in [7]). For example, the importance of the pitcher rim, the peristome, for initial prey capture due to its specific microstructure combined with both surface hydrophilicity and secretion of hygroscopic nectar, was recently discovered [8-11]. In addition, the digestive fluid collected in the lower part of the pitcher was recently found to be highly viscous thus preventing trapped insects from escaping [12,13].

Although the slippery zone, situated inside the pitcher just below the peristome in the majority of *Nepenthes* species, was recognised long ago as an important structure for insect trapping and retention, due to its particular downward-directed lunate cells and thick crystalline wax coverage [14-16], the contribution of the microstructure to the anti-adhesive function of this surface is still being actively discussed. Numerous studies were recently performed to investigate the micromorphology, chemistry, properties of pitcher waxes, and their effect on insect attachment ability in several *Nepenthes* species (e.g., [17-26]). Using different experimental approaches, the authors explained the prevention of insect adhesion via contamination of adhesive pads by wax crystals and/or reduction of the real contact area caused by surface micro-roughness [19,22,25,26]. Also, due to the fragile and brittle nature of wax crystals and their small dimensions, insects cannot apply their claws for interlocking with crystals in order to climb up the pitcher wall [22,25,26].

As for the potential role of lunate cells in hindering insect attachment, the effect of surface anisotropy caused by these cells was postulated for the first time more than a century ago [15,27]. The authors suggested that these cells should be turned upside down to allow claw clinging by insects. However, the experiments performed by Knoll [15] could not show such an effect on insect locomotion. Whereas the morphology, distribution and origin of lunate cells, considered to be transformed stomatal guard cells, were later widely discussed in the literature [16,17,26,28,29], the experimental study to test the above hypothesis was only recently carried out. It was found that ants *Iridomyrmex humilis* moved faster and escaped more successfully when de-waxed pitchers of *N. alata* were inverted [18]. What still remains unclear is (1) the effect of the surface anisotropy of intact plant surfaces on insect attachment and (2) the contact mechanism responsible for this effect, although these issues have been repeatedly raised in discussions by recent authors (e.g., [25,26]).

This study was undertaken in order to directly examine the influence of the lunate cells causing surface anisotropy in the slippery zone on insect attachment force. We performed traction tests with ladybird beetles *Coccinella septempunctata* (L.) in two different experiments on (1) intact pitchers of *N. alata* Blanco, (2) de-waxed pitchers, and (3) their polymer replicas. Forces on tethered beetles were measured when they walked in the upward (towards the peristome) or downward (towards the pitcher bottom) directions corresponding to the upright or inverted positions of the pitcher. In order to distinguish between the contribution from claw interlocking and from adhesion using tarsal adhesive pads to insect attachment on these surfaces, the performances of intact and clawless (the claws were amputated) beetles were compared in the second experiment.

Results

Structure of test surfaces and insect attachment organs

The intact slippery zone of the *N. alata* pitcher bears relatively large, prominent lunate cells scattered between tabular epidermal cells and microscopic epicuticular wax crystals on top of both cell types (Figure 1A and Figure 1D). Numerous lunate cells (477.3 ± 46.02 per mm^2, N = 3) are regularly distributed singly over the surface, whereas wax crystals form a continuous coverage. Lunate cells have a special crescent shape with their ends pointed toward the pitcher bottom (Figure 1A, Figure 2A and Figure 2C). The exposed upper side of the cell is sloped towards the pitcher mouth so that the lower cell margin becomes prominent and hangs over the adjoining cell (Figure 2B). Data on lunate cell dimensions and their distribution over the surface are given in Figure 2. These cells are responsible for the anisotropic surface relief of up to 10 μm in height, whereas crystalline wax coverage creates an additional roughness in the range of about 1 μm.

De-waxed pitcher samples and their polymer replicas displayed a very similar surface structure with a clear pattern of lunate cells (Figure 1B and Figure 1C). Wax crystals were completely removed by chloroform and the surface of lunate cells, as well as areas between them, became smooth (Figure 1E and Figure 1F). These samples additionally showed some waviness caused by the corrugation of tabular epidermal cells due to the drying process.

The tarsus of the *C. septempunctata* beetle ends distally with two ventrally curved claws having tip diameters of 3.7 ± 0.64 μm (N = 10, Figure 3). Attachment pads belong to the hairy type of locomotory organs in insects. Pads and types of adhesive setae in this beetle species have been previously described in detail by [30].

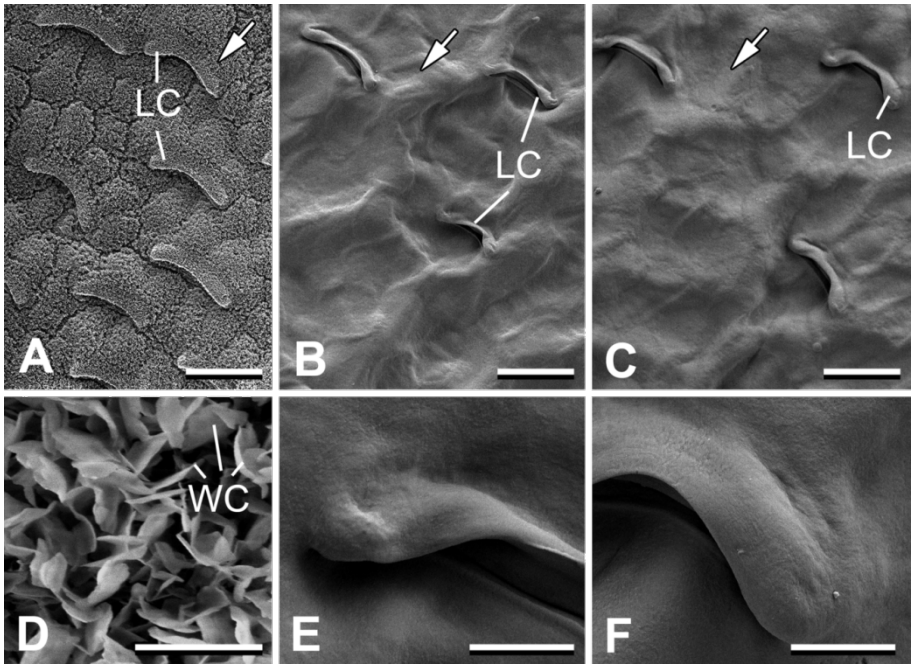

Figure 1: Cryo-SEM micrographs of intact *Nepenthes alata* pitchers (A, D) and SEM micrographs of de-waxed pitcher samples (B, E) and their polymer replicas (C, F) used for traction experiments. LC: lunate cells; WC: wax crystals. White arrows indicate direction to the pitcher bottom. Scale bars = 50 µm (A–C), 2 µm (D), 10 µm (E, F).

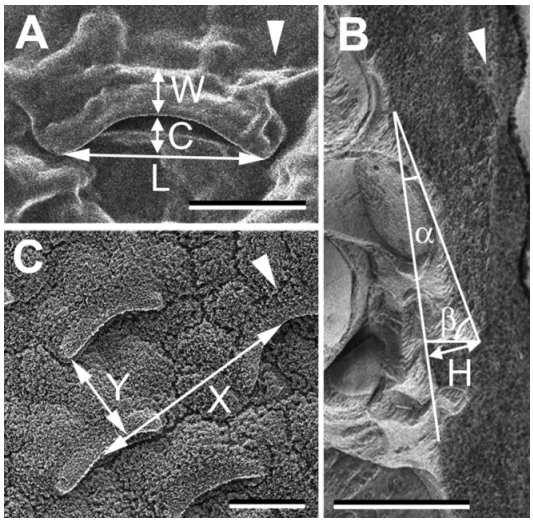

Figure 2: Morphometrical variables and distribution of lunate cells measured in SEM micrograph of a de-waxed surface (A) and cryo-SEM micrographs of an intact surface (B, C) of the slippery zone in *Nepenthes alata* pitchers: α = 19.53 ± 3.92°, β = 68.12 ± 17.01°, *C* = 6.95 ± 1.46 µm, *H* = 9.41 ± 2.08 µm, *L* = 35.51 ± 6.02 µm, *W* = 7.21 ± 1.01 µm, *X* = 84.90 ± 29.39 µm, *Y* = 51.16 ± 16.05 µm, N = 10–20. A, C: Top view of the surfaces. B: Fractured sample, used to measure variables α and β (angles between the exposed side of the lunate cell and its adjoining sides). White arrowheads indicate direction to the pitcher bottom. Scale bars = 20 µm. [B: courtesy of M. Benz (Department of Functional Morphology and Biomechanics, Zoological Institute, Christian Albrecht University of Kiel, Germany).]

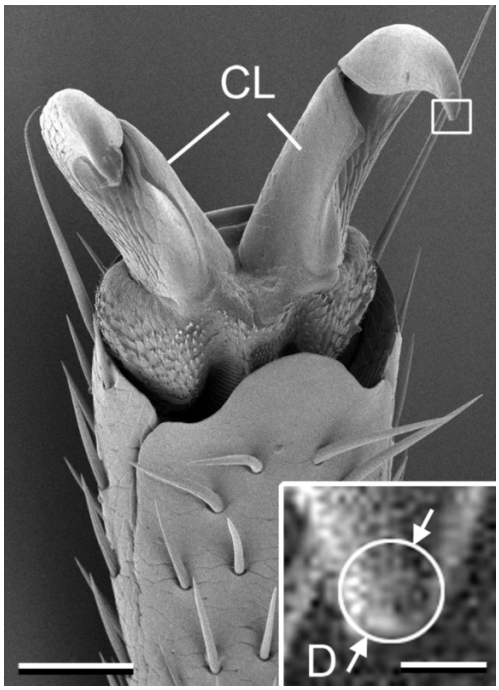

Figure 3: SEM micrographs of the distal part of the tarsus in the *Coccinella septempunctata* beetle. Inset shows magnified claw tip, where the white inscribed circle was used to measure the diameter of the claw tip. CL: claws; D: diameter of the claw tip. Scale bar = 50 µm. Scale bar of the inset = 5 µm.

Traction forces of beetles on different surface samples

On intact pitcher surfaces bearing both lunate cells and epicuticular crystalline waxes, traction forces of insects were drastically reduced compared to those measured on a glass sample (glass versus pitcher upward: t = 6.400; glass versus pitcher downward: t = 6.045, d.f. = 14, $p < 0.001$, paired t-test) (Figure 4A, Table 1). Beetles showed significantly lower force values when they moved in the upward direction compared to the downward one (upward versus downward: t = −4.271, d.f. = 14, $p < 0.001$, paired t-test).

In experiments with treated de-waxed pitchers and their replicas, insects both intact and clawless generated statistically different forces on tested surfaces, with forces on glass being higher and more variable than on other substrates (intact: $H_{4,74} = 30.033$; clawless: $H_{4,74} = 38.003$, $p < 0.001$, Kruskal–Wallis one way ANOVA on ranks) (Figure 4B and Figure 4C, Table 1).

Intact beetles exhibited high traction forces in the downward direction than in the upward one in both cases, on de-waxed pitchers and their replicas (de-waxed pitcher, upward versus

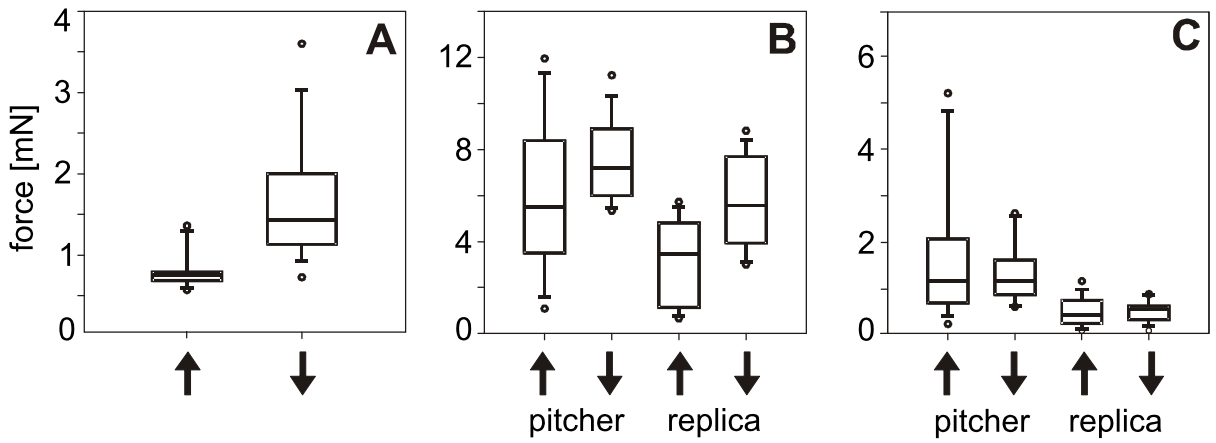

Figure 4: Results of traction force tests with *Coccinella septempunctata* beetles on different surfaces. (A) Experiments with both pitchers and insects intact. (B) Experiments with intact insects on de-waxed pitchers and their replicas. (C) Experiments with clawless insects on de-waxed pitchers and their replicas. Arrows pointing up indicate movement toward the pitcher peristome; arrows pointing down indicate movement towards the pitcher bottom.

Table 1: Traction forces (in mN) generated by *Coccinella septempunctata* beetles.

experiment	surface and run direction	mean value	st. dev.	N
both intact pitchers and beetles	glass	7.56	4.282	30
	intact pitcher upward	0.29	0.220	15
	intact pitcher downward	1.20	0.721	15
intact beetles on de-waxed pitchers and their replicas	glass	9.17	3.868	15
	de-waxed pitcher upward	5.78	3.252	15
	de-waxed pitcher downward	7.58	1.711	15
	replica upward	3.00	1.843	15
	replica downward	5.65	2.050	15
clawless beetles on de-waxed pitchers and their replicas	glass	2.27	1.854	15
	de-waxed pitcher upward	1.68	1.486	15
	de-waxed pitcher downward	1.29	0.614	15
	replica upward	0.51	0.315	15
	replica downward	0.51	0.229	15

downward: t = −2.327, p = 0.036; replica, upward versus downward: t = −3.060, p = 0.003, d.f. = 14, paired t-test) (Figure 4B, Table 1). In experiments with these beetles, forces on polymer replicas were lower compared to those on de-waxed pitchers (de-waxed pitcher upward versus replica upward: t = 4.006, p = 0.001; de-waxed pitcher downward versus replica downward: t = 2.834, p = 0.013, d.f. = 14, paired t-test).

Tests with clawless insects showed no significant differences in force values between upward and downward directions on either de-waxed plant samples or replicas (de-waxed pitcher, upward versus downward: W = −14.000, T+ = 53.000, T− = −67.000, p = 0.720, Wilcoxon signed rank test; replica, upward versus downward: t = 0.079, d.f. = 14, p = 0.938, paired t-test) (Figure 4C, Table 1). Just as in experiments with intact insects, clawless ones also produced lower forces on replicas than on de-waxed pitchers (de-waxed pitcher upward versus replica upward: W = −116.000, T+ = 2.000, T− = −118.000, p < 0.001, Wilcoxon signed rank test; de-waxed pitcher downward versus replica downward: t = 4.966, p < 0.001, d.f. = 14, paired t-test).

Discussion

Texture of natural and artificial pitcher surfaces

As in many other *Nepenthes* species, the slippery zone of *N. alata* represents a hierarchically structured surface created by the combination of several structural elements: Idioblasts (lunate cells) between tabular epidermal cells and superimposed crystalline wax coverage [31]. Pitchers lacking both lunate cells and wax were found only in a few species from this genus, such as *N. ampularia* [29], *N. bicalcarata* [8,16,32-35], *N. rafflesiana* [13,36], and *N. veitchii* [37].

The slippery zone in test pitchers displayed a surface morphology typical for *N. alata* and is described in detail in a series of recent studies [18,20,22,24-26]. Lunate cells in our pitcher samples were 1.5 times shorter than and half as wide as those reported in [26]. The heights of prominent margins of lunate cells were only 70% of those measured previously, whereas the density of cells exceeded twice the previously reported one. Here, we do not discuss the complex structure of the wax coverage. It is only important to note that the shapes, dimensions, and arrangement of uppermost wax crystals were in line with those previously observed.

De-waxed pitcher samples and their replicas had slightly corrugated surfaces with interspersed lunate cells, but still rather smooth at the micrometer scale. Similarly to previously reported data [18], no strong geometric artefacts in the pitcher surface, caused by the chloroform treatment, were found. Only some small changes in the increased waviness of the surface in de-waxed samples and their replicas were observed compared to the intact pitchers. Taking into account the relatively low height and aspect ratio of this waviness, it seemed to have no effect on the anisotropic properties of plant surfaces as discussed below.

Anisotropy effect on insect attachment

Insect attachment ability in the slippery zone of the *N. alata* pitcher was previously studied in experiments designed to test the anti-adhesive effect of the wax coverage. It was shown in behavioural experiments that intact surfaces covered with wax crystals hindered the locomotion of ants *Iridomyrmex humilis*, as compared to de-waxed pitchers [18]. Traction experiments [22] demonstrated a significant reduction in the force generated by beetles *Adalia bipunctata* on two wax layers, as compared to both de-waxed pitchers and smooth hydrophilic glass used as a control. In slightly modified traction tests with locusts *Locusta migratoria*, forces on the pitcher surface were smaller than those on the smooth steel reference plate [26]. In all these studies, insects were tested walking in the upward direction of the pitcher.

Our present data on beetles walking in both upward and downward directions on the intact pitcher are consistent with the results of previous authors and also show drastically decreased traction force on wax-bearing surfaces compared to those measured on smooth glass. The decrease of insect attachment ability on the waxy pitcher surface can be explained by contamination of adhesive pads with wax crystals [1,2,19,22] and by reduction of the real contact area between the surface and insect attachment organs due to the surface micro-roughness [18,22,25,26]. A recently proposed model of the interactions of *N. alata* pitcher surface with insect pads and claws demonstrated that both stick insects *Carausius morosus* and ants *Lasius niger* can apply neither their pads nor claws for attachment to the crystalline wax surface with such a micro-roughness [25]. Due to the assumed mechanical stability of wax crystals, the hindering of insect attachment is explained solely by the reduction of the contact area caused by the surface micro-roughness. However, our previous theoretical study on the fracture behaviour of wax crystals, based on data on the crystal geometry in seven plant species and data on the mechanical properties of plant waxes, shows that crystals with very small cross sections and high slenderness ratios can break under the weight of middle-sized or even small-sized insects [38]. These results can also be applied to platelet-shaped crystals in *Nepenthes* plants.

Force measurements on insects running in different directions (upward versus downward) on the intact pitcher surface were

performed here for the first time. In spite of the general large reduction of insect attachment ability on waxy surfaces, we detected a significant difference between forces generated in different directions: Beetles performed more strongly moving downwards than upwards. Similar results were obtained in tests with intact beetles on de-waxed pitchers and their polymer replicas, where force values were higher than on intact plant surfaces. These data concur with previous findings showing that ants *Iridomyrmex humilis* climbed up the surface much more successfully and faster on inverted de-waxed pitchers [18]. In unprecedented tests with clawless beetles, conducted to confirm experimentally the contribution made by claws in clinging to the pitcher surface, no differences between traction forces measured in different directions of the pitcher were found on either de-waxed pitchers or their replicas. This result indicates to us the principal role of claws in interlocking to inverted lunate cells. Furthermore, the slippery effect of the pitcher in the upright position is partially due to the failure of claw interlocking.

According to [39], successful attachment of an insect by claw interlocking is provided when the diameter of the claw tip is smaller than the size of surface asperities (or cavities). Since the height of overhanging edges in lunate cells (> 9 μm) exceeds the claw tip diameter (about 4 μm) in the tested beetle species, sufficient attachment of the beetle to the slippery zone should occur. This effect was observed in the present study in the experiments with intact insects on inverted surfaces, where inverted lunate cells served as anchorage sites for claws. Moving in an upward direction, as in a natural situation where an insect tries to escape from the pitcher, the beetles were unable to employ their claws, because of the downward orientation of the overhanging cell edges. Thus, the anisotropic morphology of the lunate cells causes the anisotropic tribological properties of the slippery pitcher zone. The effect of cell shape on the prevention of claw anchorage has also been previously reported for another pitcher surface, the peristome [8], where insect locomotion is also promoted in the downward pitcher direction and prevented in the upward one.

Since de-waxed pitchers and polymer replicas showed very similar topographies, better performance of beetles on de-waxed pitcher surfaces than on their replicas may be explained by the different mechanical and physicochemical properties of both substrates. We surmise that the softer and more compliant material of the plant tissue promotes insect interlocking due to easier indentation of claw tips into a softer substrate. This effect is reinforced by the higher surface energy of de-waxed plant samples (compared with epoxy replicas) presumably leading to some increase in pad adhesion. In an experimental study on frictional properties of the adhesive pads of locusts *Oedaleus infernalis* on several artificial substrates having similar roughness but different stiffness, lower insect attachment ability on zinc plates (stiff) compared to polyvinyl chloride substrates (soft) was also demonstrated [40].

Based on the data presented here, we may conclude that, due to the particular shape of the lunate cells, the slippery pitcher zone has anisotropic frictional properties in terms of insect attachment. Claws are primarily responsible for attachment enhancement on inverted pitchers, since they could interlock with the overhanging edges of the lunate cells. Due to the failure of the claw interlocking on upright pitchers, insects can slide more easily inside the pitcher. In intact pitchers, the latter effect is reinforced by a strong reduction of adhesion by adhesive pads due to the crystalline wax coverage.

Outlook: biomimetic potential and implementation

The anisotropic properties of the slippery zone in *N. alata* pitchers and their polymer replicas make these surfaces suitable as possible prototype materials for technical implementations requiring frictional anisotropy. Possible applications range from braking systems of cars to haptic security signs in banknotes. There is only very limited information on the anisotropic tribological properties of natural surfaces in general, and the present paper opens a new field in the biomechanics and biomimetics of this kind of system. Here, we were able to establish the first artificial prototypes of anisotropic surface structures by a two-step replicating process. In the framework of a joint project within the DFG priority program SPP 1420, whose members include the Department of Functional Morphology and Biomechanics at the University of Kiel and the Institute for Chemistry at the University of Osnabrück, the hierarchical structure of the slippery zone is currently being analysed at different levels of organization, in order to use estimated geometrical variables to mimic the surface in technical materials using various available micro- and nanofabrication technologies. The moulding technique applied here has clearly demonstrated that the structural anisotropy of a certain dimension affects the frictional anisotropy (at least for crawling insects). However, the implementation of such anisotropy in industrial polymer foils, especially on a large production scale, still remains a rather challenging task.

Experimental

Plant and insect species

Mature upper pitchers of the tropical pitcher plant *N. alata* were harvested from plants grown in the greenhouse of the Botanical Garden at the University of Hohenheim (Stuttgart, Germany) and kept in plastic bags in a refrigerator for the duration of the experiments.

Seven-spotted ladybird beetles *C. septempunctata* were used in traction experiments because of their appropriate size (6–8 mm in body length), availability, and robustness in traction experiments. The capture of coleopteran insects by pitchers of several *Nepenthes* species has been previously reported [3,4,6]. Adult beetles were collected from plants along roadsides near Kronshagen (Germany). They were kept in small ventilated cages at a temperature of 22–24 °C and relative humidity of 60–75% for four days and fed with a weak solution of honey in tap water. Water was changed daily and the cages were sprayed with water twice a day.

Test surfaces

Three types of substrates were used for traction tests with insects: (1) intact slippery zone of *N. alata* pitchers, (2) de-waxed slippery zone, and (3) polymer replicas of the de-waxed slippery zone.

Three strips, each 7–8 cm long and 1.5–2 cm wide, were cut with a razor blade from the slippery zone of three pitchers from three *Nepenthes* plants and directly used in the first type of experiments. Three other similar strips, cut from the same pitchers, were rinsed for 20 s in warm chloroform to remove the crystalline wax coverage from the surface, air dried and used as (i) de-waxed pitcher samples and (ii) for making high-resolution polymer replicas of this surface. Replicas were additionally used because treatment of plant surfaces with chloroform leads to the removal not only of epicuticular waxes, but also intracuticular ones and therefore changes the chemical and physical properties of the plant surface [21]. To eliminate these effects on insect attachment and examine the contribution of surface topography, we prepared replicas of the de-waxed pitchers and tested them together with de-waxed plant samples in the second type of traction experiments. Replicas were obtained by applying the two-component dental wax (Coltène President light body, Coltène Whaledent Dentalvertriebs Ltd., Konstanz, Germany) and Spurr resin [41] according to the two-step moulding method [42].

Microscopy

The microstructure of the above described intact and de-waxed pitcher samples was studied by scanning electron microscope (Hitachi S-4800, Hitachi High-Technologies Corporation, Tokyo, Japan) equipped with a cryo-preparation system (Gatan ALTO 2500 cryo-preparation system, Gatan Inc., Abingdon, UK). The cryo-SEM method employed for studying intact pitcher samples was previously introduced in detail [24]. De-waxed pitcher samples and their polymer replicas were examined using a conventional SEM method as described in [22]. Morphometrical variables of the surface structures, such as lunate cell width W, length L, and height C of the span in the pendent cell margin, height H of the prominent cell margin relative to the adjoining cell, slopes of two free cell sides α and β, as well as intervals between lunate cells in vertical Y and side X directions (Figure 2) were measured from digital images using SigmaScan Pro 5 software (SPSS Inc., Chicago, USA). Additionally, the density of lunate cells on the surface was estimated.

The attachment organs of beetles were studied in the SEM at an acceleration voltage of 3 kV. For this purpose, insects were air-dried, mounted with their dorsal side to aluminium holders, sputter-coated with gold-palladium (thickness 6 nm), and examined in SEM, as described above. The diameter of the claw tip (D) was estimated from digital images (Figure 3) using SigmaScan Pro 5 software according to [39].

Traction experiments

Traction force measurements were performed with both male and female beetles (see [30] for a detailed method description). Two types of experiments were carried out with tethered beetles on horizontally placed substrates. Firstly, traction forces were measured on intact pitcher surfaces while intact insects walked either upwards (towards the peristome) or downwards (towards the pitcher bottom) corresponding to the upright or inverted positions of the pitcher. The test on a smooth hydrophilic glass surface, used as a reference substrate, was carried out prior to each test on the plant surface, in order to eliminate disabled insects and select only strong healthy ones for experiments. To exclude the effect of possible contamination of insect attachment organs by wax crystals on the force measured, the second experiment on the pitcher surface (in the opposite pitcher direction) was executed after the beetles had recovered overnight from the first experiment performed on the pitcher surface.

In the second type of experiment, we compared the performances of intact insects with those of insects having amputated claws. With each individual insect, two sets of tests were performed on the following, horizontally placed, substrates: (1) Smooth solid glass plate; (2) de-waxed pitcher surface in the upward (towards the peristome) running direction; (3) de-waxed pitcher surface in the downward (towards the pitcher bottom) running direction; (4) polymer replica of the de-waxed pitcher surface in the upward running direction; (5) polymer replica of the de-waxed pitcher surface in the downward running direction.

Tests on a glass surface were always conducted first for the same reason as in the first type of experiment. The use of the other surface samples was randomized to avoid any systematic artefacts due to testing the surfaces in a given order. At first, we tested intact insects on the five substrates mentioned above. The claws were then amputated and, after overnight recovery, the

same insects were used in the second set of experiments. For claw amputation, the beetles were narcotised with CO_2 for about 1 min, and then the claws were excised with small scissors.

The force-time curves obtained were used to calculate the maximal traction force of individual beetles. Tests were performed at a room temperature of 22–24 °C and 55–60% relative humidity. Fifteen beetles were tested in each type of experiment. In all, 210 force measurements were carried out.

Data are presented in the text as a mean value ± standard deviation. Kruskal-Wallis one way ANOVA on ranks was used to evaluate the differences in traction force values between substrate samples (software SigmaStat® 3.1.1, Systat Software Inc., Richmond, California, USA). To compare forces between upward and downward running directions and between de-waxed pitchers and replicas, data were statistically analysed using paired t-test and Wilcoxon signed rank test (software SigmaStat® 3.1.1).

Acknowledgements

The assistance of Mr. A. Baran with traction experiments is greatly acknowledged. We wish to thank the staff of the Botanical Garden at the University of Hohenheim (Stuttgart, Germany) for providing plant material. Ms. V. Kastner (Max Planck Institute for Metals Research, Stuttgart, Germany) helped with editing of the manuscript. This study was partly supported by the SPP 1420 priority program of the German Science Foundation (DFG) 'Biomimetic Materials Research: Functionality by Hierarchical Structuring of Materials' (project GO 995/9-1) to SG.

References

1. Juniper, B. E.; Burras, J. K. *New Sci.* **1962,** *13,* 75–77.
2. Juniper, B. E.; Robins, R. J.; Joel, D. M. *The Carnivorous Plants;* Academic Press: London, U.K., 1989.
3. Kato, M.; Hotta, M.; Tamin, R.; Itino, I. *Trop. Zool.* **1993,** *6,* 11–25.
4. Moran, J. A. J. *Ecol.* **1996,** *84,* 515–525. doi:10.2307/2261474
5. Adam, J. H. *Pertanika J. Trop. Agric. Sci.* **1997,** *20,* 121–134.
6. Moran, J. A.; Booth, W. E.; Charles, J. K. *Ann. Bot. (Oxford, U. K.)* **1999,** *83,* 521–528. doi:10.1006/anbo.1999.0857
7. Moran, J. A.; Clarke, C. M. *Plant Signal. Behav.* **2010,** *5,* 644–648. doi:10.4161/psb.5.6.11238
8. Bohn, H. F.; Federle, W. *Proc. Natl. Acad. Sci. U. S. A.* **2004,** *101,* 14138–14143. doi:10.1073/pnas.0405885101
9. Bauer, U.; Bohn, H. F.; Federle, W. *Proc. R. Soc. London, Ser. B* **2008,** *275,* 259–265. doi:10.1098/rspb.2007.1402
10. Bauer, U.; Willmes, C.; Federle, W. *Ann. Bot. (Oxford, U. K.)* **2009,** *103,* 1219–1226. doi:10.1093/aob/mcp065
11. Bauer, U.; Federle, W. *Plant Signal. Behav.* **2009,** *4,* 1019–1023. doi:10.4161/psb.4.11.9664
12. Gaume, L.; Forterre, Y. *PLoS One* **2007,** *2,* e1185. doi:10.1371/journal.pone.0001185
13. Gaume, L.; Di Gusto, B. *Ann. Bot. (Oxford, U. K.)* **2009,** *104,* 1281–1291. doi:10.1093/aob/mcp238
14. Macfarlane, J. M. *Ann. Bot. (Oxford, U. K.)* **1893,** *7,* 401–458.
15. Knoll, F. *Jahrb. Wiss. Bot.* **1914,** *54,* 448–497.
16. Lloyd, F. E. *The Carnivorous Plants;* The Ronald Press Company: New York, U.S.A., 1942.
17. Owen, T. P.; Lennon, K. A. *Am. J. Bot.* **1999,** *86,* 1382–1390. doi:10.2307/2656921
18. Gaume, L.; Gorb, S.; Rowe, N. *New Phytol.* **2002,** *156,* 476–489. doi:10.1046/j.1469-8137.2002.00530.x
19. Gaume, L.; Perret, P.; Gorb, E.; Gorb, S.; Labat, J.-J.; Rowe, N. *Arthropod. Struct. Dev.* **2004,** *33,* 103–111. doi:10.1016/j.asd.2003.11.005
20. Riedel, M.; Eichner, A.; Jetter, R. *Planta* **2003,** *218,* 87–97. doi:10.1007/s00425-003-1075-7
21. Riedel, M.; Eichner, A.; Meimberg, H.; Jetter, R. *Planta* **2007,** *225,* 1517–1534. doi:10.1007/s00425-006-0437-3
22. Gorb, E.; Haas, K.; Henrich, A.; Enders, S.; Barbakadze, N.; Gorb, S. J. *Exp. Biol.* **2005,** *208,* 4651–4662. doi:10.1242/jeb.01939
23. Gorb, E. V.; Gorb, S. N. *Plant Biol. (Hoboken, NJ, U. S.)* **2006,** *8,* 841–847. doi:10.1055/s-2006-923929
24. Gorb, E. V.; Gorb, S. N. Functional surfaces in the pitchers of the carnivorous plant *Nepenthes alata*: A cryo-SEM approach. In *Functional Surfaces in Biology;* Gorb, S. N., Ed.; Springer: Dordrecht, The Netherlands, 2009; Vol. 2, pp 205–238. doi:10.1007/978-1-4020-6695-5_9
25. Scholz, I.; Bueckins, M.; Dolge, L.; Erlinghagen, T.; Weth, A.; Hischen, F.; Mayer, J.; Hoffmann, S.; Riederer, M.; Riedel, M.; Baumgarten, W. J. *Exp. Biol.* **2010,** *213,* 1115–1125. doi:10.1242/jeb.035618
26. Wang, L.; Zhou, Q. *Adv. Nat. Sci.* **2010,** *3,* 152–160.
27. Bobisut, O. *Sitzungsber. Akad. Wiss. Wien, Math.-Naturwiss. Kl., Abt. 1* **1910,** *119,* 3–10.
28. Adams, R. M., II; Smith, G. W. *Am. J. Bot.* **1977,** *64,* 265–272. doi:10.2307/2441969
29. Pant, D. D.; Bhatnagar, S. *Phytomorphology* **1977,** *27,* 13–34.
30. Gorb, E.; Hosoda, N.; Miksch, C.; Gorb, S. J. R. *Soc., Interface* **2010,** *7,* 1571–1579. doi:10.1098/rsif.2010.0081
31. Poppinga, S.; Koch, K.; Bohn, H. F.; Barthlott, W. *Funct. Plant Biol.* **2010,** *37,* 952–961. doi:10.1071/FP10061
32. Clarke, C. M.; Kitching, R. L. J. *Trop. Ecol.* **1995,** *11,* 589–602. doi:10.1017/S0266467400009160
33. Cheek, M.; Jebb, M. *Flora Malesiana. Series I – Seed Plants;* National Herbarium Nederland: Leiden, The Netherlands, 2001; Vol. 15.
34. Merbach, M. A.; Zizka, G.; Fiala, B.; Maschwitz, U.; Booth, W. E. *Flora (Jena)* **2001,** *196,* 153–160.
35. Moran, J. A.; Hawkins, B. J.; Gowen, B.; Robbins, S. *J. Exp. Bot.* **2010,** *61,* 1365–1374. doi:10.1093/jxb/erq004
36. Di Gusto, B.; Gueroult, M.; Rowe, N.; Gaume, L. The waxy surfaces in *Nepenthes* pitcher plants: Variability, adaptive significance and developmental evolution. In *Functional Surfaces in Biology;* Gorb, S. N., Ed.; Springer: Dordrecht, The Netherlands, 2009; Vol. 2, pp 183–203. doi:10.1007/978-1-4020-6695-5_8
37. Benz, M. J. Comparative study of the ultrastructure of the slippery zone in nine carnivorous *Nepenthes* species. Diploma Thesis, University of Stuttgart, Germany, 2009.
38. Borodich, F. M.; Gorb, E. V.; Gorb, S. N. *Appl. Phys. A* **2010,** *100,* 63–71. doi:10.1007/s00339-010-5794-x
39. Dai, Z.; Gorb, S. N.; Schwarz, U. J. *Exp. Biol.* **2002,** *205,* 2479–2488.

40. Wang, L.; Zhou, Q.; Xu, S.; Niu, H. *Chin. Sci. Bull.* **2009,** *54,* 4549–4554. doi:10.1007/s11434-009-0576-6
41. Spurr, A. R. J. *Ultrastruct. Res.* **1969,** *26,* 31–43. doi:10.1016/S0022-5320(69)90033-1
42. Gorb, S. N. *Microsc. Today* **2007,** *15,* 44–46.

License and Terms